Faculteit Farmaceutische, Biomedische en Diergeneeskundige Wetenschappen

Departement Biomedische Wetenschappen

The versatile nature of cytoglobin, the Swiss-army knife among globins, with a preference for oxidative stress

De veelzijdigheid van cytoglobine, het Zwitsers zakmes onder de globines, met een voorkeur voor oxidatieve stress

Proefschrift voorgelegd tot het behalen van de graad van
Doctor in de Biomedische Wetenschappen
Aan de Universiteit Antwerpen te verdedigen door

Joey DE BACKER

Promotoren: Prof. Dr. Wim Vanden Berghe
Prof. Dr. Annemie Bogaerts
Prof. Dr. David Hoogewijs

Antwerpen, 2023

Internal doctoral committee

Chair

Prof. dr. Guy Van Camp
Department of Medical Genetics, Antwerp University Hospital University of Antwerp

Jury-member

Prof. dr. An Wouters
Center for Oncological Research (CORE), Integrated Personalized and Precision Oncology Network (IPPON)
University of Antwerp

Promotors

Prof. dr. Wim Vanden Berghe
Protein Chemistry, Proteomics and Epigenetic Signaling Department of Biomedical Sciences
University of Antwerp

Prof. dr. Annemie Bogaerts
Plasma Lab for Applications in Sustainability and Medicine-Antwerp (PLASMANT), Department of Chemistry
University of Antwerp

Prof. dr. David Hoogewijs
Section of Medicine, Department of Endocrinology, Metabolism and Cardiovascular System
University of Fribourg

External doctoral committee

Prof. dr. Cristina Canal
Plasmas for BioMedical Applications laboratory, Universitat Politècnica de Catalunya

Prof. dr. Bart Braeckman
Research group Aging Physiology and Molecular Evolution, Ghent University

Prof. dr. em. Luc Moens
Protein Chemistry, University of Antwerp

Table of contents

ACTB	β-actin
Adgb	androglobin
AI	allelic imbalance
AP-1	activator protein 1
APCs	antigen presenting cells
APE-1	human apurinic/apyrimidinic (AP) endonuclease
ATP	adenosine triphosphate
B2M	β -2-microglobulin
BRAF	v-Raf murine sarcoma viral oncogene homolog B
CAIX	carbonic anhydrase 9
CAP	cold atmospheric plasma
CASP1	caspase 1
CCS	collision cross section
CD	circular dichroism
CD74	cluster of differentiation
ceRNA	competing endogenous RNA
CID	collision induced dissociation
CL	cardiolipin
CRT	calreticulin
CTLA4	cytotoxic T-lymphocyte-associated protein 4
CXCR4	C-X-C chemokine receptor type 4
Cygb	cytoglobin
CYGB	human cytoglobin
$CYGB_{S-S}$	monomeric cytoglobin with intramolecular disulfide bridge
$CYGB_{SH-SH}$	monomeric cytoglobin with reduced thiol groups
Cyt c	cytochrome c
DAMPs	Damage associated molecular patterns
DBD	dielectic barrier discharge
DCs	dendritic cells
DEGs	differentially expressed genes
DMBA	7, 12-dimethylbenz[a]anthracene
DTT	dithiothreitol
EDTA	ethylenediaminetetraacetic acid
EMT	epithelial-to-mesenchymal transition
EPR	electron paramagnetic resonance
Erastin	small molecule eradicator of RAS and ST
ERK	extracellular signal regulated kinase
ESI	electrospray ionization
FBS	fetal bovine serum
FCCP	carbonyl cyanide-4-trifluoromethoxy phenylhydrazone
fGSEA	Fast gene set enrichment analysis
FITC	fluorescein isothiocyanate
FSP1	ferroptosis-suppressor protein 1
GAPDH	glyceraldehyde-3-phosphate dehydrogenase
Gb E, -X, -Y	Globin E, X, Y
GLUT1	glucose transporter 1
GPx	glutathione peroxidase

GR	glutathione reductase
GSH	glutathione
GST	glutathione S-transferase
GUS	β-glucuronidase
Hb	hemoglobin
HIF-1	hypoxia-inducible factor 1
HIF-2α	hypoxia inducible factor 2 α
HIF-α	hypoxia inducible factor alpha
HMBS	Hydroxymethylbilane synthase
HMGB1	high-mobility group box 1
HO-1	heme-oxygenase 1
HPRT1	Hypoxanthine phosphoribosyltransferase 1
ICD	immunogenic cell death
IL-1 β	interleukin 1 β
IMM	inner mitochondrial membrane
IRC	inter-run calibrator
LC-MS/MS	liquid chromatography – ion trap tandem mass spectrometry
lncRNA	long non-coding RNA
LUCA	Last universal common ancestor
Mb	Myoglobin
MCR1	melanocortin receptor 1
MD	molecular dynamics
MEG3	maternally expressed 3
MEK	mitogen-activated protein kinase kinase
MIF	macrophage migration inhibitory factor
miRNA	micro-RNA
MITF	microphthalmia associated transcription factor
mRNA	messenger RNA
MS	mass spectrometry
NAC	N-acetyl cysteine
NFAT	Nuclear factor of activated T-cells
NFκB	nuclear factor-κB
Ngb	neuroglobin
NLRP3	NOD-, LRR- and pyrin domain-containing protein 3
NOD	nitric oxide dioxygenase
NOS	nitric oxide synthase
NR	nitrite reductase
NRF2	nuclear factor erythroid 2–related factor 2
NSCLC	non-small cell lung carcinoma
NTP	non-thermal plasma
OCR	oxygen consumption rate
OMM	outer mitochondrial membrane
PAMPs	pathogen associated molecular patterns
PBS	phosphate-buffered saline
PD-1	programmed cell death protein 1
PEF	pulsed electric fields
PHD	prolyl hydroxylase domain

PHD2	prolyl hydroxylase domain 2
PI	propidium iodide
pPBS	plasma-treated phosphate buffered saline
PTS	non-thermal plasma-treated solutions
PUFAs	polyunsaturated fatty acid-containing phospholipids
qPCR	real-time quantitative polymerase chain reaction
rCYGB	recombinant human cytoglobin
RIN	RNA integrity number
RNA-seq	RNA sequencing
RNS	reactive nitrogen species
RONS	reactive oxygen and nitrogen species
ROS	reactive oxygen species
RR	resonance raman
RSL3	(1S, 3R)-RAS-selective lethal small molecule
SDHA	Succinate dehydrogenase complex flavoprotein subunit A
SDS-PAGE	sodium dodecyl sulphate polyacrylamide gel-electrophoresis
SEM	standard error of the mean
shRNA	short hairpin RNA
siRNA	small-interfering RNA
SOD	superoxide dismutase
SYK	spleen tyrosine kinase
TBP	TATA-box binding protein
TBS	Tris-buffered saline
TCEP	tris (2-carboxyethyl) phosphine
TLRs	toll-like receptors
TNFα	tumor necrosis factor α
TOC	tylosis with esophageal cancer syndrome
TR	thioredoxin reductase
TRIS	tris(hydroxymethyl)aminomethane
TUBB	β-tubulin
UBC	ubiquitin C
UV	ultraviolet
UVR	ultraviolet radiation
VSMCs	vascular smooth muscle cells
YWHAZ	Tyrosine 3-monooxygenase/tryptophan 5-monooxygenase activation protein ζ
α-MSH	α-melanocyte stimulating hormone

SUMMARY

Summary

Since its discovery 20 years ago, many comparative, functional, and structural studies have been performed to gain insight into the functional role of cytoglobin (Cygb). However, instead of identifying one specific function, Cygb has been proven to be a promiscuous protein. Yet, there is a consensus that Cygb is a cytoprotective protein involved in redox homeostasis. CYGB is a ubiquitously expressed hexacoordinated globin that is highly expressed in melanocytes and is often found to be downregulated during melanocyte-to-melanoma transition.

In Chapter III, we investigated the molecular mechanism through which CYGB could be involved in redox regulation. Here, we showed that CYGB contains two redox-sensitive cysteine residues that enable the formation of intra- and/or intermolecular disulfide bridges. The formation of an intramolecular disulfide bridge led to a minor shift of the E- and F-helix and substantially changed the position of the His117 residue, which resulted in the heme group becoming more accessible to external ligands. This supports the hypothesis that Cys38 and Cys83 serve as sensitive redox sensors that modulate the distal heme pocket reactivity and ligand binding of Cygb.

In Chapter IV we showed the need for the proper selection and validation of reference genes for gene expression analysis using real-time qPCR. In A375 and Malme-3M melanoma cells, CYGB mRNA levels were elevated upon exposure to hypoxia. Differences in response between A375 and Malme-3M originated from different endogenous expression levels of CYGB. Immunoblotting confirmed that CYGB is strongly upregulated under hypoxic conditions in A375 cells. Interestingly, this upregulation in A375 cells was most likely HIF-2α-dependent. We propose that in A375 cells, HIF-2α, rather than HIF-1α, by recruitment and binding of other transcription factors, positively regulates *CYGB* under hypoxic conditions in a cell type specific way.

In Chapter V, we investigated the cytotoxic effect of indirect NTP treatment in two melanoma cell lines with divergent endogenous CYGB expression levels, and we explored the role of CYGB in determining treatment outcome. We confirmed that the treatment of PBS with NTP endows cytotoxicity that induces cell death in melanoma cells through apoptosis and that this cytotoxicity was mediated through the production of ROS. Moreover, we showed that CYGB protects melanoma cells from ROS-induced apoptosis by the scavenging of ROS, possibly through its superoxide dismutase (SOD) activity. Interestingly, CYGB expression influenced the expression of NRF2 and HO-1. We identified the lncRNA MEG3 as a possible mechanism through which NRF2

expression and its downstream target HO-1 can be regulated by CYGB. Therefore, the correlation between CYGB and MEG3 expression sheds a new light on the tumor-suppressive function of CYGB.

The evidence that CYGB protects melanoma cells from ROS-induced apoptosis encouraged us to investigate the potential effect of CYGB on the cellular sensitivity towards RSL3-mediated ferroptosis. In chapter VI, we showed that an increased basal ROS level and higher degree of lipid peroxidation upon RSL3 treatment contributes to the increased sensitivity of CYGB knockdown G361 cells to ferroptosis. Furthermore, transcriptome analysis demonstrates the enrichment of multiple cancer malignancy pathways upon CYGB knockdown, supporting a tumor-suppressive role for CYGB. Remarkably, CYGB expression regulation was identified as a critical determinant of the ferroptosis–pyroptosis therapy response. Collectively, this suggests that CYGB is involved in the regulation of multiple modes of programmed cell death, including apoptosis, ferroptosis, and pyroptosis. How exactly CYGB is involved in determining the type of programmed cell death remains to be seen.

In the last Chapter, we performed a thorough examination of the RONS generated by DBD plasma and sought to delineate the RONS that are responsible for plasma-induced ICD. Our results show that alone, persistent RONS are not sufficient for DBD plasma-induced ICD and highlight the importance of the short-lived species. Furthermore, we are first to demonstrate that NTP-created vaccine is safely prepared and offers complete protection. Moreover, we provide conclusive evidence that direct application of NTP induces ICD in melanoma.

SAMENVATTING

Samenvatting

Sinds de ontdekking van cytoglobine (Cygb) 20 jaar geleden hebben verscheidene vergelijkende, functionele en structurele studies getracht de fysiologische functie te achterhalen. Dit leidde echter niet tot het bepalen van één specifieke functie. In de plaats daarvan werden verschillende functies voorgesteld die allen wijzen naar een rol voor Cygb in de redox-regulatie van de cel. CYGB wordt alom geëxpresseerd in verschillende celtypes maar is in grote hoeveelheden aanwezig in melanocyten en wordt vaak neergereguleerd tijdens de transitie naar melanoom.

In Hoofdstuk III werd het moleculair mechanisme waarmee CYGB betrokken kan zijn in de redox-regulatie onderzocht. CYGB beschikt over twee redox-sensitieve cysteine residu's die in staat zijn intra- en/of intermoleculaire disulfide bruggen te vormen. De formatie van een intramoleculaire disulfide brug leidt tot een kleine verschuiving van de E- en F-helix en verandert de positie van het His117 residu aanzienlijk, wat resulteert in een meer toegankelijke heemgroep voor externe liganden. Dit ondersteunt de hypothese dat de twee cysteine residu's dienen als redox-sensitieve sensoren die de heemreactiviteit en ligandbinding van Cygb moduleren.

In Hoofdstuk IV werd de nood voor de correcte selectie en validatie van referentiegenen voor genexpressie analyse met behulp van real-time qPCR verder aangetoond. Onder blootstelling aan hypoxie werden CYGB mRNA niveaus opgereguleerd In A375 en Malme-3M melanoomcellen. Verschillen tussen A375 and Malme-3M waren te wijten aan een verschil in endogene hoeveelheden aan CYGB. Naast mRNA werd ook CYGB eiwit opgereguleerd in A375 cellen onder hypoxische omstandigheden. Deze opregulatie was hoogstwaarschijnlijk HIF-2α afhankelijk. Wij stellen voor dat in A375 cellen voornamelijk HIF-2α *CYGB* onder hypoxische omstandigheden positief reguleert in een celtype-specifieke manier.

Het cytotoxische effect van indirecte NTP behandeling werd in Hoofdstuk V onderzocht. Hiervoor werden twee melanoom cellijnen met een verschillende endogene expressie van CYGB gebruikt. Er werd bevestigd dat de behandeling van PBS met NTP leidt tot de verwerving van cytotoxiciteit die ROS-gemedieerde apoptotische celdood induceert in melanoom cellen. Bovendien beschermde CYGB melanoomcellen van ROS-gemedieerde apoptose door het neutraliseren van ROS via zijn superoxide dismustase activiteit. Bovendien beïnvloedde CYGB de expressie van NRF2 en HO-1. Mogelijks reguleert CYGB NRF2 en HO-1 expressie via lncRNA MEG3. De correlatie tussen MEG3 en CYGB werpt een nieuw licht op de tumor-suppressieve functie van CYGB.

Het bewijs dat CYGB bescherming biedt tegen apoptose zette ons ertoe aan om het potentiële effect van CYGB op de cellulaire sensitiviteit voor RSL3-gemedieerde ferroptose te onderzoeken. In Hoofdstuk VI werd aangetoond dat CYGB knockdown melanoomcellen gevoeliger waren voor RSL3 en dat deze verhoogde gevoeligheid voor ferroptose correleerde met een hogere mate van lipide peroxidatie en basale hoeveelheid intracellulaire ROS. Verder demonstreerde analyse van het transcriptoom de verrijking van meerdere kankerpathways in de CYGB knockdown melanoomcellen, wat opnieuw wijst op een mogelijke tumor-suppressor rol voor CYGB. Opmerkelijk genoeg werd de regulatie van de expressie van CYGB aangeduid als een kritische determinant van de ferroptose-pyroptose therapie respons. Gezamenlijk suggereert dit dat CYGB betrokken is bij de regulatie van meerdere vormen van geprogrammeerde celdood, waaronder apoptose, ferroptose en pyroptose. Verder onderzoek zal moeten uitwijzen hoe CYGB precies betrokken is bij het bepalen van het type celdood.

In het laatste hoofdstuk (Hoofdstuk VIII) werd er een grondige analyse uitgevoerd naar de specifieke RONS die worden geproduceerd door DBD plasma alsook welke van die RONS verantwoordelijk zijn voor plasma-geïnduceerde immunogene celdood. Onze resultaten benadrukken het belang van de kortlevende RONS voor het induceren van immunogene celdood. Verder werd er aangetoond dat een NTP-gegenereert vaccin veilig kan worden voorbereid en volledige bescherming biedt. Bovendien leveren we overtuigend bewijs dat directe toediening van NTP immunogene celdood induceert in melanoom.

CHAPTER I

GENERAL INTRODUCTION

The Discovery of Oxygen

In the 1600s, John Mayow performed an experiment that demonstrated that some aspect of air was essential for life and that this component could be removed both by a flame and mouse respiration [1]. In 1779, Joseph Priestley performed similar experiments, where he showed that mice were able to survive for longer in air heated by mercury oxide, compared to air heated using a flame, again pertaining to the fact that fire required an element in air, and by utilizing this element, its depletion directly resulted in the demise of a mouse [2]. This work was repeated by Antoine Lavoisier who called the air “eminently breathable air” and later coined the term “oxygen” [3].

Evolution of oxygen and life

Complex life on Earth, i.e., the emergence and expansion of eukaryotic cells and their aggregation into multicellular organisms, began approximately 500 million years ago. Geologically, the planet was formed 4.5 billion years ago. In the ensuing 1.5 billion years the first organisms, mainly bacteria, had to develop systems for energy metabolism under anoxic conditions. These systems were based on anoxygenic photosynthesis, which used hydrogen or sulfur as electron donors instead of water. About 2.7-2.5 billion years ago the first traces of oxygenic photosynthesis were found, stemming from the precursors of cyanobacteria [4, 5]. This ushered in the Proterozoic ‘Great Oxidation Event’ and caused the rise of oxygen levels to a maximum of 2% [6]. The rise in oxygen to present atmospheric levels happened however relatively late in the history of the Earth with the emergence of land plants approximately 500 million years ago [7, 8], stemming from the deposition of cellulose on land by the terrestrial descendants of streptophytes [9]. The arrival of terrestrial photosynthesis and biomass production, accompanied by carbon burial, initiated the further rise in oxygen and the emergence of complex life [10]. It was not so much that land plants generated large amounts of oxygen, rather that they removed carbon from oxidation through burial [11].

All photosynthesizing organisms (cyanobacteria, green algae, modern plants) have been found to use the same inorganic core and similar reaction center core proteins to split water into oxygen, protons, and electrons [3, 5]. During photosynthesis, photons of light fall onto chlorophyll thereby enhancing its energy level to a degree that makes it possible to drive the splitting of water enzymatically in photosystem II (PSII) to create oxygen and hydrogen through

the extraction of electrons from water, leading to the production of adenosine triphosphate (ATP) [12]. This reaction is catalyzed in PSII by a catalyst containing four manganese and one calcium (Mn_4Ca). The photon-induced excitation of chlorophyll is used to extract four electrons from Mn_4Ca, which are subsequently replaced by four electrons from two molecules of water [13].

The creation of a photosynthetic apparatus was the pivotal innovation in the evolution of life on Earth. The increased presence of oxygen in the atmosphere led to the biological innovation of aerobic respiration, which harnesses a more efficient energy source in the form of aerobic metabolism, producing 18 times more energy, i.e., ATP, per hexose sugar than anaerobic metabolism [5, 14]. Since aerobic metabolism generates more energy, approximately 1000 reactions more can occur than under anaerobic metabolism [15]. When this remarkable energetic capacity of molecular oxygen is being harnessed by mitochondria in eukaryotes the energy flux increases enormously, potentially contributing to a vastly expanded repertoire of novel protein folds, protein interactions and regulatory cascades [16]. These fascinating series of evolutionary steps enabled the emergence of complex, multicellular, energy-efficient, eukaryotic organisms.

The physiological role of oxygen in metazoan species pertains not only to mitochondrial respiration. Oxygen is also a crucial component in a myriad of metabolic and biosynthetic pathways, contributing to the synthesis of regulatory membrane lipids [17] and structural proteins [18]. For example, the oxygen-dependent synthesis of sterols and polyunsaturated fatty acids, important elements of cell membranes, might have been involved in the development of early organelles and cellular compartmentalization [19]. Furthermore, oxygen is essential for the posttranslational hydroxylation of proline (and lysine), one of the principal components of the most abundant protein in Metazoa, collagen [20]. Moreover, protein hydroxylation is involved in cellular oxygen sensing. During this process, prolyl-4-hydroxylase domain enzymes covalently modify hypoxia-inducible transcription factor-α (HIF-α) subunits [21, 22]. In the presence of sufficient oxygen, two distinct HIF-α prolyl residues within an oxygen-dependent degradation domain are hydroxylated in a nonreversible reaction involving oxygen, 2-oxoglutarate, ferrous iron, and probably vitamin C.

Although oxygen-dependent biosynthetic reactions and aerobic respiration have significant advantages, the electronic structure of oxygen makes it potentially toxic to cells. Atmospheric oxygen is paramagnetic and contains two unpaired electrons with parallel spin states, which renders reactions with oxygen difficult [19, 23]. Therefore, oxygen is either combined with a paramagnetic metal (e.g. Cu or Fe) or is reduced by a univalent pathway [23]. The reduction through successive transfers of a single electron requires the formation of superoxide anion radical ($\cdot O_2^-$), hydrogen peroxide (H_2O_2) and hydroxyl radical ($\cdot OH$), reactive free radical intermediates that can cause damage to cellular macromolecules such as proteins, lipids, and DNA. To counteract the toxicity of these so-called reactive oxygen species (ROS) all aerobic species possess conserved cellular defense mechanisms such as the antioxidant enzymes superoxide dismutase, catalase, peroxiredoxins, and glutathione peroxidase [1].

The emergence of large(r) animals during the Cambrian explosion made oxygen supply by simple diffusion inefficient. Hence, proteins evolved that facilitated oxygen supply by transporting and/or storing oxygen. Of the three known respiratory proteins (hemocyanins, hemerythrins, and globins) that exist, globins are the most widespread and can be found in all three domains of life: Bacteria, Archaea, and Eukarya [24-27].

The globin superfamily

Globins are small (around 150 amino acids) globular metalloproteins characterized by the globin fold (Figure 1.1), a 3/3 sandwich of α-helical segments (A, B, C, and E over F, G, and H), and the presence of a heme prosthetic group (Fe^{2+}-protoporphyrin IX) [28-30]. Although their overall structures are conserved, globin primary sequences are much less conserved. In fact, the proximal heme-coordinating histidine at position 8 of helix F (HisF8) is the only residue present in all globins [30, 31].

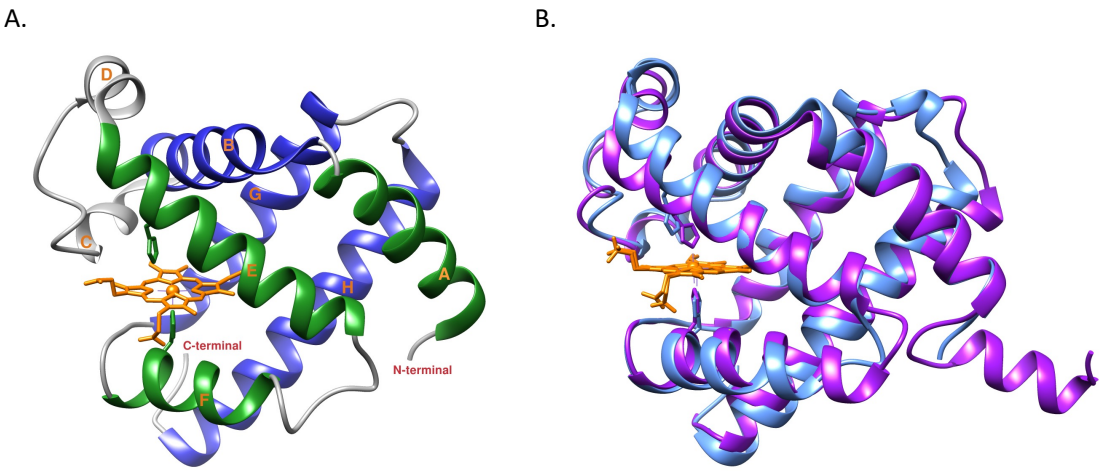

Figure 1.1. The globin fold. (A) The classical 3-over-3 α-helical sandwich structure with the helices labelled according to the conventional globin nomenclature (A to H) based on the sperm whale Mb (PDB: 1VXA). Sandwich layers (colored green and blue) are linked by the C and D loop (in grey). The heme group (in orange) is located in the hydrophobic pocket. (B) Superimposition of Cygb (in purple; PDB: 2DC3) and Mb (in blue) protein structures, demonstrating the conserved globin fold among different globins. The 20 amino acid N-terminal extension in Cygb is clearly noticeable. Modified using Chimera software.

Each globin incorporates a single molecule of heme in the hydrophobic pocket generated by the globin fold. The central iron of the heme can form six coordinative bonds. Heme iron is coordinated by four N-atoms, one from each of the four pyrrole rings of the porphyrin. Furthermore, the heme is bound to the protein through a coordinate covalent bond between the heme iron and the N-atom of the proximal HisF8 residue. The plane of the porphyrin divides the heme pocket into two regions: the Fe-coordinating HisF8 side chain occupies the proximal heme pocket, leaving diatomic ligands to bind on the opposite face of the porphyrin, which is the distal heme pocket.

The state of the sixth iron binding site divides globins into two subgroups. In the deoxygenated (Fe^{2+}) state, penta-coordinated globins possess an empty distal binding site that can form a coordinate covalent bond with diatomic gaseous ligands such as oxygen, carbon monoxide, nitric oxide, and hydrogen sulfide. In hexa-coordinated globins however, the iron atom is bound to the distal residue at position 7 of helix F, usually a His or Gln [32].

For many decades, the oxygen-binding hemoglobin (Hb) and myoglobin (Mb) were considered the only globin types present in vertebrates. However, genomic analyses have revealed an unprecedented structural and functional diversity of vertebrate globins through the discovery of 6 novel globin types. 20 years ago, neuroglobin (Ngb) and cytoglobin (Cygb) were discovered in rapid succession in nerve cells and fibroblasts, respectively [33-36]. More recently, Hoogewijs et

al. discovered androglobin (Adgb), a family of large chimeric proteins predominantly expressed in testis tissue. Finally, globin E (GbE) [38], globin Y (GbY) [39] and globin X (GbX) [40] complete the vertebrate globin family.

Their widespread occurrence in bacteria, fungi, plant, protists, and animals demonstrate that globins are derived from an ancient protein already present in the last universal common ancestor (LUCA) of all living organisms more than 1.5 billion years ago (Figure 1.2) [41]. In Metazoa, Ngb, GbX and Adgb represent major clades distinct from other globin types as they have been identified in both vertebrates and invertebrates indicating their early evolutionary origin [33, 37, 42, 43]. Cygb diverged from the vertebrate globin clade (consisting of Hb, Mb, GbE and GbY) before the separation of Agnatha and Gnathostomata, evidenced by the presence of Cygb in the sea lamprey *Petromyzon marinus* [44]. Remarkably, Ngb, GbX, Adgb, and Cygb are all hexa-coordinated, suggesting that hexa-coordination was the original heme iron coordination state [30]. Moreover, this indicates that penta-coordination, typical for globins involved in oxygen transportation, evolved later. Hb, Mb, GbE and GbY have therefore been proposed to belong to a separate clade of globins. The duplication and gene diversification of these penta-coordinated globin types took place in a relatively short time frame in the Cambrian or Precambrian period that coincided with the rise in atmospheric oxygen and the evolution of complex life forms [30].

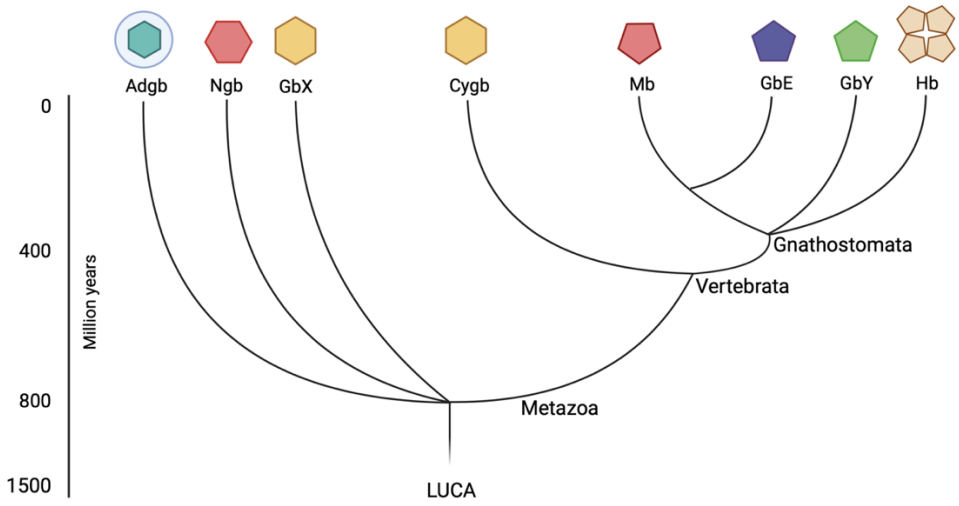

Figure 1.2. Metazoan evolution of globins. Globins are derived from a protein that was already present in the last universal common ancestor (LUCA) of all living organisms more than 1.5 billion years. Ngb, GbX and Adgb represent major clades that are distinct from the other globin types as they emerged before the separation of Deuterostomia and Protostomia around 800 million years ago. Cygb diverged from the vertebrate globin clade before Agnatha and Gnathostomata separated. The last common ancestor of Gnathostomata had a globin ancestor that subsequently gave rise to Hb, Mb, GbE and GbY. Created with Biorender.com.

The function of the ancient globin of the LUCA is unknown. However, it is likely that the last common ancestor had a role in oxygen sensing, the detoxification of ROS/RNS, or was another type of oxygen-dependent enzyme [45].

Cytoglobin: an enigmatic protein

Cygb was first described in rat liver stellate cells by Kawada et al. Shortly thereafter, two independent studies reported that Cygb was expressed in many tissues and provided an initial biochemical characterization of the protein [35, 36]. The human cytoglobin gene (*CYGB*) is a single copy gene located at chromosome 17. It is proposed that Cygb and Mb share a common phylogenetic clade, and that respective regions 17q25 and 22q12 represent paralogous regions of genomic DNA that resulted from a duplication event 450 million years ago [45]. With its 190 amino acids long primary structure, and a molecular weight of 21kDa, CYGB is a relatively large globin (Figure 1.3A). This is due to two distinct 20 amino acid extensions at the N- and C-terminal ends.

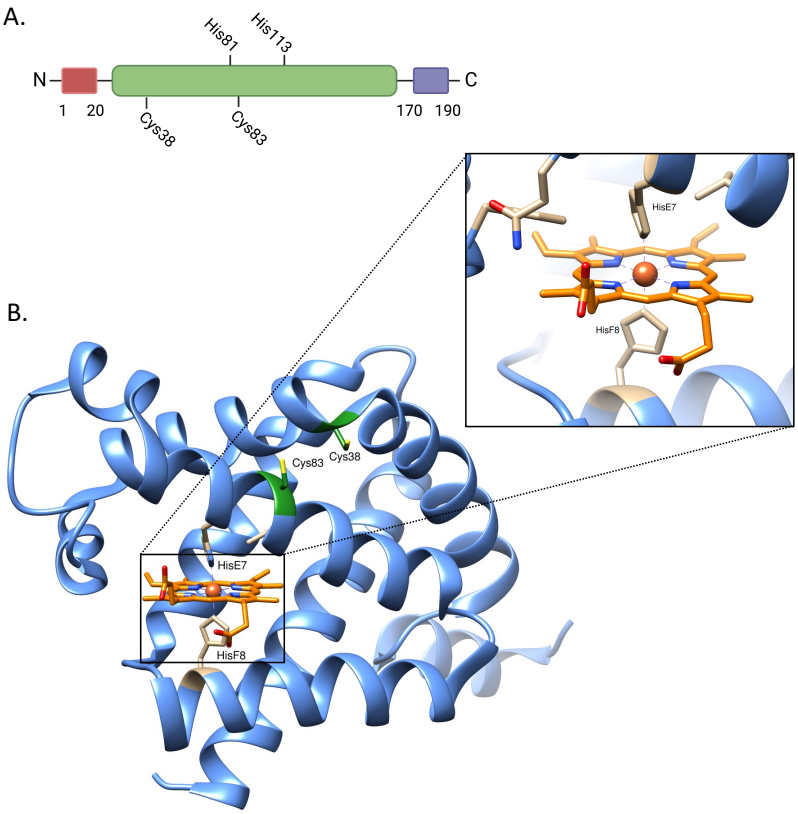

Figure 1.3. **Cygb structure.** A) Primary structure of cytoglobin. A globin domain (green) is flanked with distinct N- (red, amino acids 1 to 20) and C- (purple, amino acids 170 to 190) terminal ends. Position of the proximal (His113) and distal (His81) histidine residues and surface cysteine residues (Cys38 and Cys83) are shown. B) Ribbon view of the tertiary structure of Cygb (PDB 2DC3). In Cygb, the heme (orange) is hexa-coordinated in both the ferrous (Fe^{2+}) and ferric (Fe^{3+}) state. Inset: More detailed view of the heme group. The heme iron is coordinated by the proximal HisF8 (His113) and distal HisE7 (His81). The two cysteine residues Cys38 and Cys83 are depicted in green. Structure adapted with Chimera software.

CYGB exhibits the canonical 3/3 α-helical globin fold that forms a hydrophobic pocket around the heme (Figure 1.3B). Interestingly, the heme is hexa-coordinated in both the ferrous (Fe^{2+}) and ferric (Fe^{3+}) state. In hexa-coordinated globins, the distal HisE7 (or Gln) must first dissociate from the heme for diatomic gaseous ligands to bind to the heme iron. In CYGB, the distal HisE7 residue rotates out of the heme pocket similar to the repositioning observed in Mb [46]. Although the ability of CYGB to undergo hexa- to penta-coordination allows for the reversible binding with external ligands, the hexa-coordination imposes redox properties distinct from penta-coordinated (hemo)globins.

The initial crystallographic structures of CYGB were described as dimers [47-49]. However, later studies revealed that at micromolar concentrations, which resemble the physiological concentration much better, recombinant CYGB (rCYGB) appears predominantly as a monomer [50, 51]. Interestingly, CYGB possesses two cysteine residues (Cys38 and Cys83) that can form intramolecular and/or intermolecular disulfide bridges, which affect ligand binding properties [50-52]. More specifically, an intramolecular disulfide bridge formation creates a significant stress on the E-helix, resulting in a change in the distal histidine end-position, which increases the dissociation rate from the iron and increases the rate of ligand binding to the heme. As such, the oxidation and reduction of the cysteine residues might function as a redox switch and provide additional functionalities to CYGB [53].

1.4.1 CYGB as a regulator of NO levels

Nitric oxide is a membrane-permeable, freely diffusible paracrine transmitter that is the central regulator of vascular homeostasis [54]. In humans, nitric oxide is produced by various isoforms of nitric oxide synthase (NOS) heme-containing enzymes which use L-arginine, oxygen, and NADPH as substrates to produce aerobic NO and L-citrulline [55]. NO acts on its targets at nM concentrations but is also toxic at similar concentrations through inhibiting many other heme- or iron-containing enzymes, including cytochrome c oxidase, the terminal oxidase of the electron transport chain [56, 57]. Furthermore, NO contributes to nitrosative stress through radical chemistry. Therefore, NO availability is tightly regulated by enzymes with nitric oxide dioxygenase (NOD) activity.

It is well established that NO dioxygenation, whereby NO is metabolized to nitrate (NO_3^-) in the presence of oxygen, can occur in Hb and Mb [58, 59]. In fact, Hb and Mb play an important role in NO degradation in the blood and in skeletal and cardiac muscles, respectively. Like Hb and Mb, Cygb has been shown to regulate NO signaling in the vasculature system. Remarkably, of all mammalian globins, Cygb displays the highest rate of NO dioxygenation and is efficiently reduced by reducing agents such as ascorbate, P450 reductase or b_5/cytochrome b_5 reductase, satisfying multiple criteria for a genuine NOD enzyme [60-63].

Cygb expression was first demonstrated to be concurrent with Mb in cardiomyocytes [64]. Shortly after, Halligan et al. discovered Cygb in vascular smooth muscle cells (VSMCs) of various species, including human. Knockdown of Cygb expression in NIH-3T3 cells attenuated NO degradation and nitrate formation, whereas the restitution of Cygb reversed this effect. The presence of Cygb in VSMCs was later confirmed by others [66, 67]. Notably, VSMCs have little or no Hb or Mb expression [63]. Therefore, it seems that Cygb is the main NOD enzyme in smooth muscle cells and thus would be expected to have a major role in vascular NO metabolism and regulation of vascular tone. Consistently, Liu et al. demonstrated that Cygb-deficient mice have a decreased blood pressure and systemic vascular resistance as well as increased cardiac output.

Interestingly, under anaerobic conditions, Cygb switches to a nitrite reductase (NR) activity by reducing nitrite (NO_2^-) to NO, thereby promoting perfusion and tissue oxygenation [66]. Noteworthy, due to its pre-dominantly hexa-coordinated state, the NR activity of Cygb is much weaker than Hb and Mb. Additionally, Cygb's concentration in smooth muscle cells, is too low to significantly contribute to NO production. However, the hypoxia-dependent regulation would dramatically increase Cygb-mediated NO production [69, 70]. Moreover, Reeder et al. have shown that NR activity is increased by as much as 50-fold upon intramolecular disulfide bridge formation, again highlighting the potential of the cysteine residues to act as a redox switch. Taken together, this supports a role for Cygb as a major regulator of NO bioavailability and decay and subsequently vascular homeostasis. Cygb is ubiquitously expressed (Figure 1.4C) and might as such have a general role in protecting electron transport proteins from NO toxicity.

1.4.2 The antioxidative function of Cygb

Throughout the years, a cytoprotective function for Cygb through an innate ability to scavenge ROS has been proposed [72-74]. Cygb has been shown to scavenge ROS and provide protection against oxidative stress in multiple normal and malignant cellular models including renal fibroblasts [75], keratinocytes [76], hepatic stellate cells [77], neuronal cells [74], podocytes [78], pancreatic cancer [79], oral squamous cell carcinoma [80], glioma cells [81], and melanoma [82]. Moreover, the antioxidant function of Cygb was investigated in a Cygb-deficient mouse model developed by Thuy le et al., which developed multiple organ abnormalities in aged mice [83]. The same group also developed a Cygb transgenic mouse model. In this model, thioacetamide-mediated membrane damage and oxidative stress was decreased compared to wildtype mice, demonstrating Cygb's role as an antioxidant protein [84]. In concordance, injection of 7, 12-dimethylbenz[a]anthracene (DMBA) into the pancreatic tail in wild-type mice resulted in time-dependent induction of severe pancreatitis, fibrosis, and oxidative damage, which was rescued by Cygb overexpression in transgenic mice [79].

Although a considerable number of studies demonstrate a prominent role for Cygb in the antioxidant defense, the molecular basis for this is not well understood. Cygb can be considered a pseudo-peroxidase: the active sites are not specifically designed to catalyze the H_2O_2 reduction to water but, due to changes in external conditions, the characteristics of their active center can change, and they can display peroxidase-like activity [85].

As previously mentioned, ligand binding properties of the heme are controlled by formation of a disulfide bridge between the redox-sensitive Cys38 and Cys83 residues of the protein [52, 71, 86]. In an oxidative environment, the heme shifts from a hexa- towards a penta-coordinated state upon formation of an internal disulfide bridge. In this conformation, Cygb possesses peroxidase activity [87]. Interestingly, the redox status of Cys38/Cys83 determines the binding affinity of the heme towards fatty acids and may act either as a co-activator of the peroxidase activity, or as a substrate for Cygb [88].

Although the second order reaction rate constant for the reaction of H_2O_2 with monomeric cytoglobin containing an internal disulfide bridge is similar to reaction rates measured for penta-coordinated hemoglobins [89], it is several orders of magnitude lower than other heme- or

cysteine-based peroxidases [53]. Therefore, it seems unlikely that Cygb would significantly affect cellular H_2O_2 concentrations upon oxidative insult. Yet, it is feasible that Cygb is involved in the peroxidation of lipids that could serve as lipid signaling molecules in specific redox-sensitive signaling networks [90].

Additionally, Cygb can exert its antioxidative effect through the scavenging of superoxide ($O_2^{\bullet-}$). rCYGB has been shown to decrease lipopolysaccharide-induced NO and $O_2^{\bullet-}$ production in an *in vivo* chronic alcohol-induced liver disease model [91]. In the past, there has been controversy regarding the superoxide dismutase (SOD) function of Cygb [92, 93]. However, a recent study by Zweier et al. demonstrated potent SOD activity for rCYGB with a bimolecular dismutation rate constant only five-fold less than Cu,Zn-SODs and similar to that of Mn-SOD. Remarkably, in comparison to other globins, the dismutation rate of $O_2^{\bullet-}$ is much faster. Moreover, in isolated VSMCs, endogenous levels of Cygb largely quenched the $O_2^{\bullet-}$ produced by the uncoupler menadione [94]. In contrast, siRNA-mediated knockdown of Cygb increased the $O_2^{\bullet-}$ levels approximately threefold. Furthermore, following menadione treatment, $O_2^{\bullet-}$ levels were markedly increased in the aorta of Cygb-deficient mice compared to their wild-type counterparts, unequivocally demonstrating Cygb's SOD function. Combined with its potent NOD activity, Cygb would be highly effective in decreasing both $O_2^{\bullet-}$ and NO levels, thereby serving as a key protective mechanism to prevent the formation of the potent oxidant peroxynitrite ($ONOO^-$) and subsequent oxidative stress.

1.4.3 Cygb as a tumor suppressor

An association and potential role for Cygb in cancer was originally described by Shaw et al. in tissue samples obtained from human patients with oral squamous cell carcinoma. In this study, methylation profiling of cancer tissue found a significant increase in CpG methylation of the *CYGB* gene promoter compared to normal tissue. DNA methylation is the primary and most studied epigenetic modification and plays an important role in normal mammalian development [96]. However, aberrant methylation patterns are correlated with several diseases, including many types of human cancers.

In tissue obtained from patients with tylosis with esophageal cancer (TOC) syndrome, *CYGB* expression was markedly reduced and coincided with promoter hypermethylation [97]. TOC has

been mapped to a 42.5 kb region on chromosome 17q25 which contains the entire *CYGB* gene. Allelic imbalance (AI) occurs frequently in this locus. Therefore, hypermethylation of the *CYGB* promotor may constitute the 'second hit' of tumorigenesis in TOC. A similar mechanism has been proposed in non-small cell lung carcinoma (NSCLC) [98]. Chromosome 17q is among the chromosomal regions strongly implicated in the molecular pathogenesis of NSCLC and has been shown in several studies to demonstrate AI in lung tumors [99]. Investigation of the expression, promoter methylation, and AI status of *CYGB* in surgically excised lung tissue samples from patients with NSCLC, demonstrated the significant reduction of *CYGB* and excessive hypermethylation of the promoter in tumor tissue. Moreover, frequent AI was detected at the 17q25 locus in tumor-derived tissues. Interestingly, *CYGB* expression was further decreased when both AI and hypermethylation coincided.

In agreement, *CYGB* promoter hypermethylation and associated mRNA downregulation was reported in head and neck squamous cell carcinoma [100], oral epithelial dysplasia [101], leukemia, breast, colon, and bladder cancer [102]. The high frequency of *CYGB* promoter hypermethylation in these diverse tumor types and stages possibly implies a role in early tumorigenesis. Considering that hypermethylation of CpG islands located in the promoter regions of genes is an important mechanism for the inactivation of tumor suppressor genes [103], Shivapurkar et al. proposed a tumor suppressor role for Cygb. In this study, RNA interference-mediated knockdown of CYGB resulted in increased colony formation in a lung cancer cell line, whereas the forced expression of CYGB led to a reduction in colony formation capacity in lung and breast cancer cell lines. Throughout the years, several other *in vitro* studies have shown that Cygb silencing or overexpression affects migration, cell cycle progression, colony formation, proliferation, and cell death in multiple cancer cell types [79, 104-106].

Evidence for a tumor suppressor function for Cygb also exists *in vivo.* In the Cygb-deficient murine model developed by Thuy le et al., the absence of Cygb resulted in an increased incidence of tumor development in liver and lungs upon N, N-diethylnitrosamine-induced tumorigenesis. Additionally, non-alcoholic steatohepatitis in Cygb-deficient mice almost certainly led to hepatocellular carcinoma development [108]. Moreover, incidence of pancreatic cancer upon DMBA injection into the pancreatic tail of Cygb expressing transgenic mice was reduced to 55% compared to 93% in wild-type mice [79]. In an independent murine Cygb knockout model, the

absence of Cygb exacerbated chemically induced colitis and increased colonic tumor formation [109].

Despite the large amount of data supporting a tumor suppressing function for Cygb, several studies have shown that Cygb might also be considered an oncogene, dependent on the cell type and microenvironment [100, 110]. Accordingly, Olekciewicz et al. showed that CYGB has a tumor suppressor capacity in lung cancer cells during normoxia but will protect the tumor when it is upregulated in response to hypoxia, thereby promoting the tumorigenic potential of the tumor.

This bimodal role for Cygb makes it difficult to delineate the underlying molecular mechanisms. However, it can be speculated that Cygb's role as a tumor suppressor stems from its involvement in the antioxidant response. Oxidative stress is defined as an imbalance between the production of RONS and their elimination by antioxidants. This imbalance can lead to DNA, protein, and lipid damage that over time might induce somatic mutations and neoplastic formation which can lead to the initiation and progression of cancer [111]. Cancer cells exhibit aberrant redox homeostasis, but while RONS are pro-tumorigenic, high RONS levels are cytotoxic [112]. Therefore, tumors have adapted to thrive in oxidative conditions by increasing their antioxidant status to optimize RONS-mediated proliferation, while at the same time avoiding excessive RONS levels that would trigger senescence, or cell death [111]. Cygb, as an antioxidant could reduce the oxidative stress in normal cells, thereby protecting normal cells from cellular damage. However, the loss or reduction of Cygb expression during tumor initiation or progression would lead to increased RONS and inflammation, promoting angiogenesis, migration, and invasion. Yet, in tumor cells where Cygb expression is not diminished, Cygb could facilitate tumor progression and aggressiveness.

1.4.4 Cygb in melanocytes and melanoma

Melanocytes are specialized pigmented cells predominantly found in the skin and eyes that are responsible for the pigmentation of the skin and hair [113]. Cutaneous melanocytes are derived from a group of highly migratory embryonic cells called the neural crest. In the skin, melanocytes reside in the basal layer of the epidermis and in the hair follicles where they play an important photoprotective role in response to ultraviolet (UV) exposure via melanin synthesis. The production of melanin takes place in specific organelles called melanosomes. Mediated by

multiple keratinocyte-derived paracrine factors, melanin is transported via dendrites to adjacent keratinocytes where it accumulates in the perinuclear area as supranuclear caps, protecting nuclear DNA from UV irradiation and preventing DNA damage [114, 115].

The synthesis of melanin requires repeated oxidation steps from tyrosine to quinone [116]. Polymerization of these reactive quinones leads to the formation of the black/brownish eumelanin. In contrast, the reddish/brownish pheomelanin requires the incorporation of cysteines and its synthesis involves the production of cysteinyl-dopa instead of dopa. It is this difference that accounts for the higher (UV-induced) pro-oxidant property of pheomelanin compared to eumelanin. The sequence of oxidation reactions involved in melanogenesis results in a continuous generation of ROS including O_2^- and H_2O_2 that subject melanocytes to increased levels of oxidative stress [117]. The balance between the pro-oxidant and antioxidant properties of melanin are dependent on the redox state of the melanocytes, the relative eumelanin and pheomelanin contents, the levels of melanin intermediates, and the presence of reactive metals within the melanosome microenvironment [118, 119].

There is increasing evidence for the significance of oxidative stress in the initiation and progression of melanoma, supported by findings that mutations in several melanoma-associated genes result from, or exacerbate, oxidative stress [116, 120-122]. To maintain redox homeostasis melanocytes possess a highly efficient antioxidant network comprising of both enzymatic (e.g. SOD, catalase, glutathione peroxidase (GPx), glutathione reductase (GR), and thioredoxin reductase (TR)), and non-enzymatic (e.g. ascorbic acid, glutathione) antioxidants [123] . Furthermore, paracrine factors are instrumental in maintaining the homeostasis of melanocytes. For instance, endothelin-1 is a melanogenic factor that reduces H_2O_2 generation in UV-irradiated melanocytes [115]. Additionally, the melanocortin α-melanocyte stimulating hormone (α-MSH), through activation of the melanocortin 1 receptor (MCR1), reduces the induction of 8-oxo-2'-deoxyguanosine and enhances its repair upon UV-exposure [115, 124]. Moreover, activation of MCR1 by α-MSH regulates the intracellular redox status by upregulating the expression of various antioxidant genes, including heme-oxygenase 1, ferritin, and peroxiredoxin 1, and transcription factors MITF, NRF2, and APE-1 [118, 125].

In an attempt to assess the correlation between CYGB loss and tumor malignancy, Fujita et al. performed an extensive screening in several cancer cell lines and found that some melanoma

cells (but not all) abundantly express CYGB. The subsequent investigation of melanocytes revealed melanocytes as a prominent cell type with high endogenous CYGB levels. The expression level of CYGB mRNA surpassed those observed in skin and various other normal tissues and protein levels in human keratinocytes and dermal fibroblasts were almost undetectable compared to melanocytes [126].

Meta-analysis of the whole genome bead array dataset (GSE29359) comparing human primary melanocyte cell lines and 82 patient-derived metastatic melanoma samples identified CYGB as a differentially expressed gene in melanoma (Figure 1.4). However, when comparing CYGB expression between metastatic melanoma samples, ~18% had comparable levels to that of the primary melanocytes, demonstrating that although CYGB is mostly lost during melanocyte-to-melanoma transition, some melanoma cells retain their endogenous CYGB levels. Additionally, CYGB transcription levels of melanoma cells with diminished expression were found to be downregulated through hypermethylation of the promoter region. In contrast, promoter regions of melanoma cells with high endogenous CYGB expression were unmethylated. Moreover, knockdown of CYGB in melanoma cells increased proliferation and intracellular ROS levels and protected cells from oxidative stress-induced cell death [126].

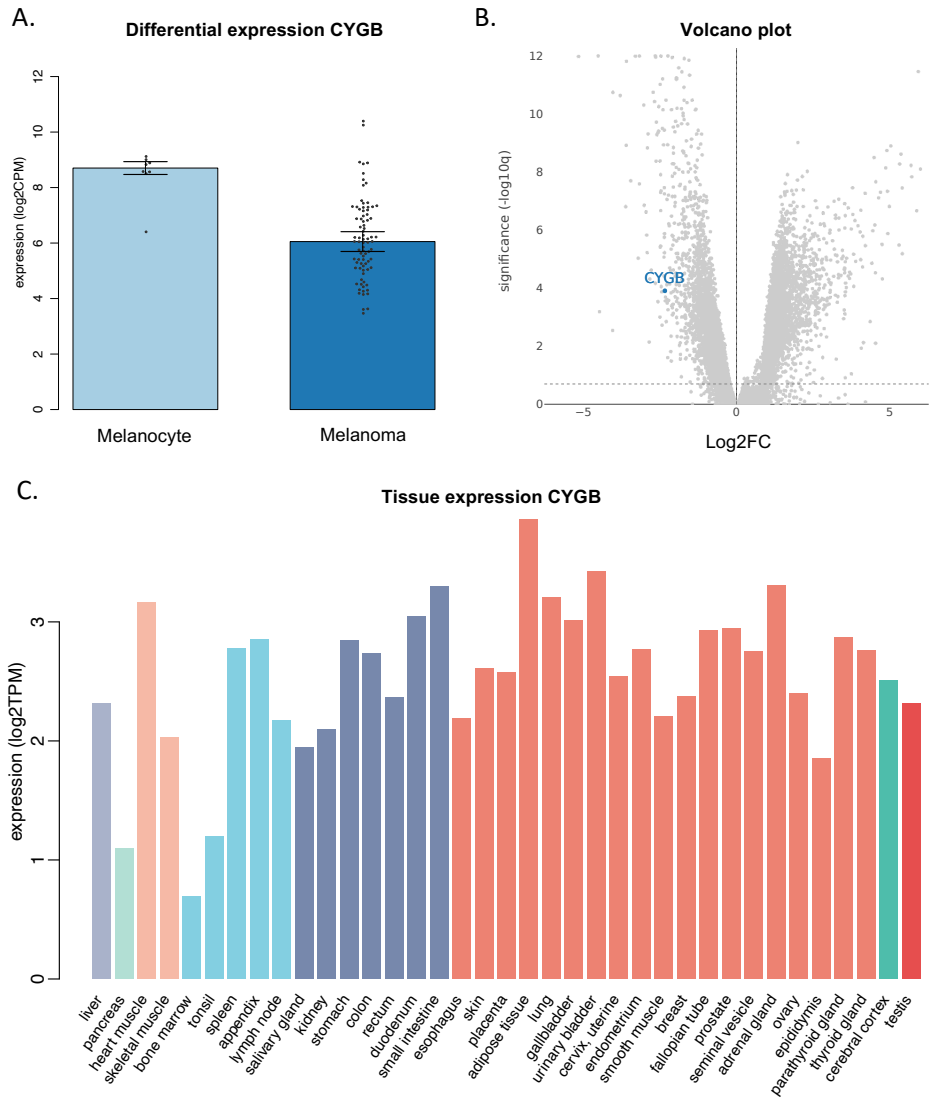

Figure 1.4. CYGB expression in melanoma. A) Differential gene expression analysis of CYGB using the whole genome bead array dataset (GSE29359) comparing 8 human primary melanocyte cell lines and 82 patient-derived metastatic melanoma samples. CYGB is differentially expressed in melanoma cells. Expression is represented as Log2 values of copies per million (Log2CPM). B) Volcano representation of the differential expression analysis of melanoma samples. CYGB has been highlighted in blue. Differentially expressed genes were represented based on their Log2 fold change (Log2FC) and −Log10 *p*-adjusted value (-Log10q). C) Tissue-specific expression of CYGB collected from the Genotype-Tissue Expression (GTEx) dataset. Gene expression is shown as the log2 values of transcripts per million (TPM). Colors correspond to "tissue-clusters as computed by unsupervised clustering. Meta-analysis was executed using Omics Playground (v2.8.8).

Taken together, CYGB seems to play a tumor suppressor role in melanocytes and melanoma cells through its antioxidant function(s). However, considering that some melanoma cells retain high CYGB expression levels, CYGB could also protect melanoma cells from cytotoxic levels of oxidative stress, thereby facilitating tumor progression and malignancy. Furthermore, CYGB could also influence the outcome of melanoma treatments focused at increasing oxidative stress.

1.4.5 Non-thermal plasma anti-cancer therapy

In addition to solid, liquid, and gas, plasma is the fourth state of matter. Non-thermal plasma (NTP) is a partially ionized gas that consists of a plethora of components, including electrons and ions, electric fields, thermal and UV radiation, and RONS [127, 128]. Of those, RONS are hypothesized to mediate the effects observed in biological systems as they are known to be involved in rapid reactions with important biomolecules such as proteins, lipids, and nucleic acids [129-131]. RONS are formed upon reaction with molecules (oxygen, nitrogen, water) present in the ambient air [131], leading, on the one hand, to the formation of ROS, such as ozone, superoxide anion, singlet delta oxygen, atomic oxygen, hydroxyl radical and hydrogen peroxide, and on the other hand, RNS such as nitrogen dioxide radical, peroxynitrite, and nitric oxide [132, 133]. The physical components produced by NTP such as UV radiation and electromagnetic fields have a negligible cellular impact [134].

The biomedical applications of NTP consist of (but are not restricted to) wound healing [135], blood coagulation [136], sterilization [137], treatment of skin diseases [138], and recently anticancer treatment. NTPs use as an anticancer treatment was first reported more than a decade ago, where they showed the inactivation of melanoma cells following NTP treatment [139]. Subsequently, more evidence emerged of NTPs antitumoral effect in numerous cancer types such as head and neck [140], pancreatic [141], brain [142], skin [143], breast [144], colorectal [145], cervical [146], and liver cancer [147]. Furthermore, NTP has been suggested to be selective towards cancer cells due to overall increase in RONS levels, altered expression of aquaporins [148], and reduced amount of cholesterol in the cell membrane [131].

There are two major types of plasma sources that are suitable for medical purposes: dielectric barrier discharges (DBD) and plasma jets (Figure 1.5A & B) [149]. DBDs generate plasma in atmospheric air directly onto the treatment target, which acts as the second electrode. Plasma jets ionize a stream of noble or inert gas (or a mixture) that subsequently interacts with oxygen and nitrogen in ambient air [128]. The generated plasma protrudes from the aperture of the device and is brought in contact with the biological target for treatment. Recently, the atmospheric pressure argon plasma jet kINPen MED has been successfully employed as cancer treatment in palliative patients with advanced head and neck cancer [137].

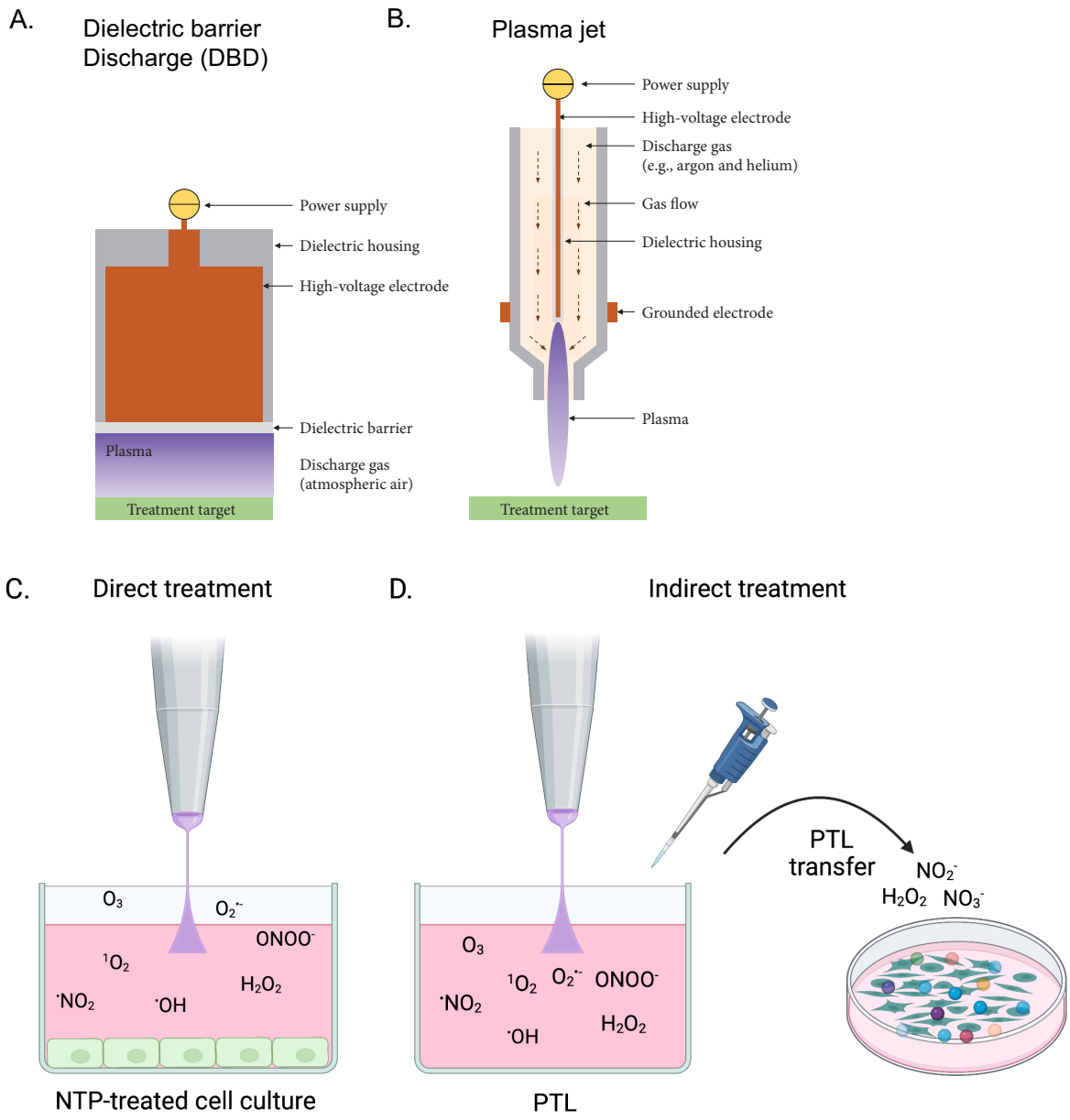

Figure 1.5 **Non-thermal plasma devices and treatment.** Schematic of two commonly used plasma devices for medical application: A) dielectric barrier discharges (DBD) and B) plasma jets. With DBD, plasma is generated in atmospheric air directly onto the biological target, while in plasma jets, plasma is generated inside the device and delivered to the treatment target through the gas flow. Figures adapted from [149]. Non-thermal plasma (NTP) can be applied C) directly or D) indirectly. Direct NTP treatment benefits from the presence of highly active, short-lived species that are delivered directly to the target cells or tissue. With indirect treatment, plasma-treated liquids (PTL) are produced by exposing a solution to the plasma gas phase. Afterwards, PTL is transferred to a target cell culture (or injected *in vivo*). Created with BioRender.com.

NTP can exert its biomedical effects either by direct treatment of cancer cells or by indirect treatment, i.e., by applying NTP-treated solutions (PTS), rich in long-lived reactive species (Figure 1.5C & D) [132, 148]. During this process, NTP-derived RONS are delivered from the plasma gas phase into the liquid phase. Most RONS produced by the NTP device have very short half-lives

which leads to their degradation before reaching the liquid phase. Therefore, long-lived species such as hydrogen peroxide, nitrite, and nitrate are considered the major components in PTS [132]. This mixture of long-lived species might recombine, react with components in the solution, or react with cellular short-lived species, further contributing to the anticancer capacity of PTS [150]. Although direct NTP treatment has been shown to be more effective in the treatment of some cancer types, PTS holds promise for future clinical applications, as it can be administered as injections in the peritoneal cavity or bulk tumor. PTS has proven to be effective in inhibiting the dissemination of ovarian cancer [151] and reduced the tumor burden, promoted macrophage recruitment, and increased T cell activation in murine colon and pancreatic tumors [152, 153].

Interestingly, NTP treatment has been demonstrated to induce immunogenic cell death (ICD) through the generation of RONS, and to increase tumor immunogenicity [154, 155]. When ICD occurs, damage associated molecular patters (DAMPs) are released from, or displayed on the outer surface of, the dying cell [156]. Once externalized, DAMPs initiate an immunologic response by attracting antigen presenting cells (APCs) (e.g., macrophages, dendritic cells) to the tumor. Presenting tumor antigens to T cells result in the expansion of tumor-specific effector and memory T cells. NTPs ability to induce ICD has been thoroughly investigated in multiple murine *in vivo* models. NTP-treatment was shown to induce the expression of DAMPs adenosine triphosphate and calreticulin along with the recruitment of APCs to the tumor region in a CT26 murine colorectal tumor model [157]. Moreover, application of a vaccination protocol verified NTP as a genuine ICD inducer. Vaccination of syngeneic mice provided protective immunity against CT26 tumor challenge in BALB/c mice immunized with NTP-treated CT26 cells [157] and C57BL/6 mice vaccinated with B16-F10 melanoma cells treated with a DBD plasma source [158].

REFERENCES

1. Lenton, T.M., *3 - The coupled evolution of life and atmospheric oxygen*, in *Evolution on Planet Earth*, L.J. Rothschild and A.M. Lister, Editors. 2003, Academic Press: London. p. 35-53.
2. Severinghaus, J.W., *Priestley, the furious free thinker of the enlightenment, and Scheele, the taciturn apothecary of Uppsala.* Acta Anaesthesiol Scand, 2002. **46**(1): p. 2-9.
3. Lindahl, Sten G.E., *Oxygen and Life on Earth: An Anesthesiologist's Views on Oxygen Evolution, Discovery, Sensing, and Utilization.* Anesthesiology, 2008. **109**(1): p. 7-13.
4. Castresana, J. and M. Saraste, *Evolution of energetic metabolism: the respiration-early hypothesis.* Trends Biochem Sci, 1995. **20**(11): p. 443-8.
5. Dismukes, G.C., et al., *The origin of atmospheric oxygen on Earth: The innovation of oxygenic photosynthesis.* Proceedings of the National Academy of Sciences, 2001. **98**(5): p. 2170.
6. Javaux, E.J. and K. Lepot, *The Paleoproterozoic fossil record: implications for the evolution of the biosphere during Earth's middle-age.* Earth-Science Reviews, 2018. **176**: p. 68-86.
7. Lenton, T.M., et al., *Earliest land plants created modern levels of atmospheric oxygen.* Proc Natl Acad Sci U S A, 2016. **113**(35): p. 9704-9.
8. Stolper, D.A. and C.B. Keller, *A record of deep-ocean dissolved O(2) from the oxidation state of iron in submarine basalts.* Nature, 2018. **553**(7688): p. 323-327.
9. Martin, W.F. and J.F. Allen, *An Algal Greening of Land.* Cell, 2018. **174**(2): p. 256-258.
10. Daines, S.J., B.J. Mills, and T.M. Lenton, *Atmospheric oxygen regulation at low Proterozoic levels by incomplete oxidative weathering of sedimentary organic carbon.* Nat Commun, 2017. **8**: p. 14379.
11. Zimorski, V., et al., *Energy metabolism in anaerobic eukaryotes and Earth's late oxygenation.* Free Radic Biol Med, 2019. **140**: p. 279-294.
12. Allen, J.F. and W. Martin, *Out of thin air.* Nature, 2007. **445**(7128): p. 610-612.
13. Yano, J., et al., *Where water is oxidized to dioxygen: structure of the photosynthetic Mn4Ca cluster.* Science, 2006. **314**(5800): p. 821-5.
14. Jiang, Y.Y., et al., *How does oxygen rise drive evolution? Clues from oxygen-dependent biosynthesis of nuclear receptor ligands.* Biochem Biophys Res Commun, 2010. **391**(2): p. 1158-60.
15. Raymond, J. and D. Segrè, *The effect of oxygen on biochemical networks and the evolution of complex life.* Science, 2006. **311**(5768): p. 1764-7.
16. Lane, N. and W. Martin, *The energetics of genome complexity.* Nature, 2010. **467**(7318): p. 929-934.
17. Summons, R.E., et al., *Steroids, triterpenoids and molecular oxygen.* Philosophical transactions of the Royal Society of London. Series B, Biological sciences, 2006. **361**(1470): p. 951-968.
18. Towe, K.M., *Oxygen-collagen priority and the early metazoan fossil record.* Proc Natl Acad Sci U S A, 1970. **65**(4): p. 781-8.
19. Thannickal, V.J., *Oxygen in the evolution of complex life and the price we pay.* American journal of respiratory cell and molecular biology, 2009. **40**(5): p. 507-510.
20. Shoulders, M.D. and R.T. Raines, *Collagen structure and stability.* Annual review of biochemistry, 2009. **78**: p. 929-958.
21. Wenger, R.H. and D. Hoogewijs, *Regulated oxygen sensing by protein hydroxylation in renal erythropoietin-producing cells.* American Journal of Physiology-Renal Physiology, 2010. **298**(6): p. F1287-F1296.
22. Kaelin, W.G., Jr. and P.J. Ratcliffe, *Oxygen sensing by metazoans: the central role of the HIF hydroxylase pathway.* Mol Cell, 2008. **30**(4): p. 393-402.
23. Fridovich, I., *Oxygen: how do we stand it?* Medical principles and practice : international journal of the Kuwait University, Health Science Centre, 2013. **22**(2): p. 131-137.
24. Hardison, R., *Hemoglobins from bacteria to man: evolution of different patterns of gene expression.* J Exp Biol, 1998. **201**(Pt 8): p. 1099-117.
25. Vázquez-Limón, C., et al., *The evolution of land plant hemoglobins.* Plant Sci, 2012. **191-192**: p. 71-81.

26. Vinogradov, S.N., et al., *Chapter Nine - Microbial Eukaryote Globins*, in *Advances in Microbial Physiology*, R.K. Poole, Editor. 2013, Academic Press. p. 391-446.
27. Weber, R.E. and S.N. Vinogradov, *Nonvertebrate hemoglobins: functions and molecular adaptations.* Physiol Rev, 2001. **81**(2): p. 569-628.
28. Kapp, O.H., et al., *Alignment of 700 globin sequences: extent of amino acid substitution and its correlation with variation in volume.* Protein Sci, 1995. **4**(10): p. 2179-90.
29. Gell, D.A., *Structure and function of haemoglobins.* Blood Cells Mol Dis, 2018. **70**: p. 13-42.
30. Burmester, T. and T. Hankeln, *Function and evolution of vertebrate globins.* Acta Physiol (Oxf), 2014. **211**(3): p. 501-14.
31. Freitas, T.A., et al., *Ancestral hemoglobins in Archaea.* Proc Natl Acad Sci U S A, 2004. **101**(17): p. 6675-80.
32. de Sanctis, D., et al., *Structure-function relationships in the growing hexa-coordinate hemoglobin sub-family.* IUBMB Life, 2004. **56**(11-12): p. 643-51.
33. Burmester, T., et al., *A vertebrate globin expressed in the brain.* Nature, 2000. **407**(6803): p. 520-3.
34. Kawada, N., et al., *Characterization of a Stellate Cell Activation-associated Protein (STAP) with Peroxidase Activity Found in Rat Hepatic Stellate Cells*.* Journal of Biological Chemistry, 2001. **276**(27): p. 25318-25323.
35. Burmester, T., et al., *Cytoglobin: A Novel Globin Type Ubiquitously Expressed inVertebrate Tissues.* Molecular Biology and Evolution, 2002. **19**(4): p. 416-421.
36. Trent, J.T. and M.S. Hargrove, *A Ubiquitously Expressed Human Hexacoordinate Hemoglobin*.* Journal of Biological Chemistry, 2002. **277**(22): p. 19538-19545.
37. Hoogewijs, D., et al., *Androglobin: a chimeric globin in metazoans that is preferentially expressed in Mammalian testes.* Mol Biol Evol, 2012. **29**(4): p. 1105-14.
38. Kugelstadt, D., et al., *Neuroglobin, cytoglobin, and a novel, eye-specific globin from chicken.* Biochem Biophys Res Commun, 2004. **325**(3): p. 719-25.
39. Fuchs, C., T. Burmester, and T. Hankeln, *The amphibian globin gene repertoire as revealed by the Xenopus genome.* Cytogenet Genome Res, 2006. **112**(3-4): p. 296-306.
40. Roesner, A., et al., *A globin gene of ancient evolutionary origin in lower vertebrates: evidence for two distinct globin families in animals.* Mol Biol Evol, 2005. **22**(1): p. 12-20.
41. Vinogradov, S.N., et al., *A model of globin evolution.* Gene, 2007. **398**(1-2): p. 132-42.
42. Blank, M. and T. Burmester, *Widespread occurrence of N-terminal acylation in animal globins and possible origin of respiratory globins from a membrane-bound ancestor.* Mol Biol Evol, 2012. **29**(11): p. 3553-61.
43. Dröge, J., et al., *Comparative genomics of neuroglobin reveals its early origins.* PLoS One, 2012. **7**(10): p. e47972.
44. Schwarze, K., et al., *The globin gene repertoire of lampreys: convergent evolution of hemoglobin and myoglobin in jawed and jawless vertebrates.* Mol Biol Evol, 2014. **31**(10): p. 2708-21.
45. Keppner, A., et al., *Lessons from the post-genomic era: Globin diversity beyond oxygen binding and transport.* Redox Biol, 2020. **37**: p. 101687.
46. Makino, M., et al., *Crystal structure of the carbon monoxide complex of human cytoglobin.* Proteins, 2011. **79**(4): p. 1143-53.
47. de Sanctis, D., et al., *Crystal structure of cytoglobin: the fourth globin type discovered in man displays heme hexa-coordination.* J Mol Biol, 2004. **336**(4): p. 917-27.
48. Fago, A., et al., *Allosteric regulation and temperature dependence of oxygen binding in human neuroglobin and cytoglobin. Molecular mechanisms and physiological significance.* J Biol Chem, 2004. **279**(43): p. 44417-26.
49. Sugimoto, H., et al., *Structural basis of human cytoglobin for ligand binding.* J Mol Biol, 2004. **339**(4): p. 873-85.
50. Lechauve, C., et al., *Cytoglobin conformations and disulfide bond formation.* The FEBS Journal, 2010. **277**(12): p. 2696-2704.

51. Astudillo, L., et al., *Reduction of the internal disulfide bond between Cys 38 and 83 switches the ligand migration pathway in cytoglobin.* J Inorg Biochem, 2013. **129**: p. 23-9.
52. Beckerson, P., B.J. Reeder, and M.T. Wilson, *Coupling of disulfide bond and distal histidine dissociation in human ferrous cytoglobin regulates ligand binding.* FEBS Lett, 2015. **589**(4): p. 507-12.
53. Mathai, C., et al., *Emerging perspectives on cytoglobin, beyond NO dioxygenase and peroxidase.* Redox Biology, 2020. **32**: p. 101468.
54. Moncada, S., R.M. Palmer, and E.A. Higgs, *Nitric oxide: physiology, pathophysiology, and pharmacology.* Pharmacol Rev, 1991. **43**(2): p. 109-42.
55. Förstermann, U. and W.C. Sessa, *Nitric oxide synthases: regulation and function.* Eur Heart J, 2012. **33**(7): p. 829-37, 837a-837d.
56. Gardner, P.R., *Hemoglobin: A Nitric-Oxide Dioxygenase.* Scientifica, 2012. **2012**: p. 683729.
57. Brunori, M., et al., *Control of cytochrome c oxidase activity by nitric oxide.* Biochimica et Biophysica Acta (BBA) - Bioenergetics, 2004. **1655**: p. 365-371.
58. Flögel, U., et al., *Myoglobin: A scavenger of bioactive NO.* Proc Natl Acad Sci U S A, 2001. **98**(2): p. 735-40.
59. Kuhn, V., et al., *Red Blood Cell Function and Dysfunction: Redox Regulation, Nitric Oxide Metabolism, Anemia.* Antioxid Redox Signal, 2017. **26**(13): p. 718-742.
60. Amdahl, M.B., et al., *Efficient Reduction of Vertebrate Cytoglobins by the Cytochrome b(5)/Cytochrome b(5) Reductase/NADH System.* Biochemistry, 2017. **56**(30): p. 3993-4004.
61. Liu, X., et al., *Characterization of the Function of Cytoglobin as an Oxygen-Dependent Regulator of Nitric Oxide Concentration.* Biochemistry, 2012. **51**(25): p. 5072-5082.
62. Liu, X., et al., *Differences in oxygen-dependent nitric oxide metabolism by cytoglobin and myoglobin account for their differing functional roles.* The FEBS Journal, 2013. **280**(15): p. 3621-3631.
63. Zweier, J.L. and G. Ilangovan, *Regulation of Nitric Oxide Metabolism and Vascular Tone by Cytoglobin.* Antioxidants & Redox Signaling, 2019. **32**(16): p. 1172-1187.
64. Singh, S., et al., *Calcineurin activates cytoglobin transcription in hypoxic myocytes.* (0021-9258 (Print)).
65. Halligan, K.E., F.L. Jourd'heuil, and D. Jourd'heuil, *Cytoglobin is expressed in the vasculature and regulates cell respiration and proliferation via nitric oxide dioxygenation.* J Biol Chem, 2009. **284**(13): p. 8539-47.
66. Li, H., et al., *Characterization of the mechanism and magnitude of cytoglobin-mediated nitrite reduction and nitric oxide generation under anaerobic conditions.* J Biol Chem, 2012. **287**(43): p. 36623-33.
67. Straub, A.C., et al., *Endothelial cell expression of haemoglobin α regulates nitric oxide signalling.* Nature, 2012. **491**(7424): p. 473-477.
68. Liu, X., et al., *Cytoglobin regulates blood pressure and vascular tone through nitric oxide metabolism in the vascular wall.* Nat Commun, 2017. **8**: p. 14807.
69. Avivi, A., et al., *Neuroglobin, cytoglobin, and myoglobin contribute to hypoxia adaptation of the subterranean mole rat Spalax.* Proceedings of the National Academy of Sciences, 2010. **107**(50): p. 21570-21575.
70. Schmidt, M., et al., *Cytoglobin is a respiratory protein in connective tissue and neurons, which is up-regulated by hypoxia.* J Biol Chem, 2004. **279**(9): p. 8063-9.
71. Reeder, B.J. and J. Ukeri, *Strong modulation of nitrite reductase activity of cytoglobin by disulfide bond oxidation: Implications for nitric oxide homeostasis.* Nitric Oxide, 2018. **72**: p. 16-23.
72. McRonald, F.E., J.M. Risk, and N.J. Hodges, *Protection from intracellular oxidative stress by cytoglobin in normal and cancerous oesophageal cells.* PLoS One, 2012. **7**(2): p. e30587.
73. Li, D., et al., *Cytoglobin up-regulated by hydrogen peroxide plays a protective role in oxidative stress.* Neurochem Res, 2007. **32**(8): p. 1375-80.
74. Hodges, N.J., et al., *Cellular protection from oxidative DNA damage by over-expression of the novel globin cytoglobin in vitro.* Mutagenesis, 2008. **23**(4): p. 293-8.

75. Nishi, H., et al., *Cytoglobin, a Novel Member of the Globin Family, Protects Kidney Fibroblasts against Oxidative Stress under Ischemic Conditions.* The American Journal of Pathology, 2011. **178**(1): p. 128-139.
76. Latina, A., et al., *ΔNp63 targets cytoglobin to inhibit oxidative stress-induced apoptosis in keratinocytes and lung cancer.* Oncogene, 2016. **35**(12): p. 1493-503.
77. Xu, R., et al., *Cytoglobin Overexpression Protects against Damage-Induced Fibrosis.* Molecular Therapy, 2006. **13**(6): p. 1093-1100.
78. Randi, E.B., et al., *The Antioxidative Role of Cytoglobin in Podocytes: Implications for a Role in Chronic Kidney Disease.* Antioxid Redox Signal, 2020. **32**(16): p. 1155-1171.
79. Hoang, D.V., et al., *Cytoglobin attenuates pancreatic cancer growth via scavenging reactive oxygen species.* Oncogenesis, 2022. **11**(1): p. 23.
80. Thorne, L.S., et al., *Cytoglobin protects cancer cells from apoptosis by regulation of mitochondrial cardiolipin.* Sci Rep, 2021. **11**(1): p. 985.
81. Fang, J., I. Ma, and J. Allalunis-Turner, *Knockdown of cytoglobin expression sensitizes human glioma cells to radiation and oxidative stress.* Radiat Res, 2011. **176**(2): p. 198-207.
82. De Backer, J., et al., *Cytoglobin inhibits non-thermal plasma-induced apoptosis in melanoma cells through regulation of the NRF2-mediated antioxidant response.* Redox Biol, 2022. **55**: p. 102399.
83. Thuy, L.T.T., et al., *Absence of cytoglobin promotes multiple organ abnormalities in aged mice.* Scientific Reports, 2016. **6**(1): p. 24990.
84. Thi Thanh Hai, N., et al., *Selective overexpression of cytoglobin in stellate cells attenuates thioacetamide-induced liver fibrosis in mice.* Sci Rep, 2018. **8**(1): p. 17860.
85. Vlasova, II, *Peroxidase Activity of Human Hemoproteins: Keeping the Fire under Control.* Molecules, 2018. **23**(10).
86. Tsujino, H., et al., *Disulfide bonds regulate binding of exogenous ligand to human cytoglobin.* J Inorg Biochem, 2014. **135**: p. 20-7.
87. Ascenzi, P., et al., *Non-covalent and covalent modifications modulate the reactivity of monomeric mammalian globins.* Biochim Biophys Acta, 2013. **1834**(9): p. 1750-6.
88. Reeder, B.J., D.A. Svistunenko, and M.T. Wilson, *Lipid binding to cytoglobin leads to a change in haem co-ordination: a role for cytoglobin in lipid signalling of oxidative stress.* Biochem J, 2011. **434**(3): p. 483-92.
89. Beckerson, P., D. Svistunenko, and B. Reeder, *Effect of the distal histidine on the peroxidatic activity of monomeric cytoglobin.* F1000Res, 2015. **4**: p. 87.
90. Tejero, J., et al., *Peroxidase activation of cytoglobin by anionic phospholipids: Mechanisms and consequences.* Biochim Biophys Acta, 2016. **1861**(5): p. 391-401.
91. Wen, J., et al., *Protective effects of recombinant human cytoglobin against chronic alcohol-induced liver disease in vivo and in vitro.* Sci Rep, 2017. **7**: p. 41647.
92. Trandafir, F., et al., *Neuroglobin and cytoglobin as potential enzyme or substrate.* Gene, 2007. **398**(1-2): p. 103-13.
93. Hanai, S., et al., *Roles of N- and C-terminal domains in the ligand-binding properties of cytoglobin.* J Inorg Biochem, 2018. **179**: p. 1-9.
94. Zweier, J.L., et al., *Cytoglobin has potent superoxide dismutase function.* Proc Natl Acad Sci U S A, 2021. **118**(52).
95. Shaw, R.J., et al., *Promoter methylation of P16, RARbeta, E-cadherin, cyclin A1 and cytoglobin in oral cancer: quantitative evaluation using pyrosequencing.* Br J Cancer, 2006. **94**(4): p. 561-8.
96. Li, E. and Y. Zhang, *DNA methylation in mammals.* Cold Spring Harbor perspectives in biology, 2014. **6**(5): p. a019133-a019133.
97. McRonald, F.E., et al., *Down-regulation of the cytoglobin gene, located on 17q25, in tylosis with oesophageal cancer (TOC): evidence for trans-allele repression.* Hum Mol Genet, 2006. **15**(8): p. 1271-7.
98. Xinarianos, G., et al., *Frequent genetic and epigenetic abnormalities contribute to the deregulation of cytoglobin in non-small cell lung cancer.* Hum Mol Genet, 2006. **15**(13): p. 2038-44.

99. Abujiang, P., et al., *Loss of heterozygosity (LOH) at 17q and 14q in human lung cancers.* Oncogene, 1998. **17**(23): p. 3029-33.
100. Shaw, R.J., et al., *Cytoglobin is upregulated by tumour hypoxia and silenced by promoter hypermethylation in head and neck cancer.* Br J Cancer, 2009. **101**(1): p. 139-44.
101. Hall, G.L., et al., *p16 Promoter methylation is a potential predictor of malignant transformation in oral epithelial dysplasia.* Cancer Epidemiol Biomarkers Prev, 2008. **17**(8): p. 2174-9.
102. Shivapurkar, N., et al., *Cytoglobin, the newest member of the globin family, functions as a tumor suppressor gene.* Cancer Res, 2008. **68**(18): p. 7448-56.
103. Esteller, M., *CpG island hypermethylation and tumor suppressor genes: a booming present, a brighter future.* Oncogene, 2002. **21**(35): p. 5427-5440.
104. Rowland, L.K., et al., *Putative tumor suppressor cytoglobin promotes aryl hydrocarbon receptor ligand-mediated triple negative breast cancer cell death.* J Cell Biochem, 2019. **120**(4): p. 6004-6014.
105. Zhang, J., et al., *Cytoglobin ameliorates the stemness of hepatocellular carcinoma via coupling oxidative-nitrosative stress signals.* Mol Carcinog, 2019. **58**(3): p. 334-343.
106. John, R., et al., *DNA damage induced activation of Cygb stabilizes p53 and mediates G1 arrest.* DNA Repair (Amst), 2014. **24**: p. 107-112.
107. Thuy le, T.T., et al., *Promotion of liver and lung tumorigenesis in DEN-treated cytoglobin-deficient mice.* Am J Pathol, 2011. **179**(2): p. 1050-60.
108. Thuy le, T.T., et al., *Cytoglobin deficiency promotes liver cancer development from hepatosteatosis through activation of the oxidative stress pathway.* Am J Pathol, 2015. **185**(4): p. 1045-60.
109. Yassin, M., et al., *Cytoglobin affects tumorigenesis and the expression of ulcerative colitis-associated genes under chemically induced colitis in mice.* Sci Rep, 2018. **8**(1): p. 6905.
110. Oleksiewicz, U., et al., *Cytoglobin has bimodal: tumour suppressor and oncogene functions in lung cancer cell lines.* Hum Mol Genet, 2013. **22**(16): p. 3207-17.
111. Hayes, J.D., A.T. Dinkova-Kostova, and K.D. Tew, *Oxidative Stress in Cancer.* Cancer Cell, 2020. **38**(2): p. 167-197.
112. Reczek, C.R., et al., *A CRISPR screen identifies a pathway required for paraquat-induced cell death.* Nat Chem Biol, 2017. **13**(12): p. 1274-1279.
113. Gray-Schopfer, V., C. Wellbrock, and R. Marais, *Melanoma biology and new targeted therapy.* Nature, 2007. **445**(7130): p. 851-7.
114. Kobayashi, N., et al., *Supranuclear melanin caps reduce ultraviolet induced DNA photoproducts in human epidermis.* J Invest Dermatol, 1998. **110**(5): p. 806-10.
115. Kadekaro, A.L., et al., *alpha-Melanocortin and endothelin-1 activate antiapoptotic pathways and reduce DNA damage in human melanocytes.* Cancer Res, 2005. **65**(10): p. 4292-9.
116. Denat, L., et al., *Melanocytes as instigators and victims of oxidative stress.* J Invest Dermatol, 2014. **134**(6): p. 1512-1518.
117. Simon, J.D., et al., *Current challenges in understanding melanogenesis: bridging chemistry, biological control, morphology, and function.* Pigment Cell Melanoma Res, 2009. **22**(5): p. 563-79.
118. Liu, Y., et al., *Comparison of structural and chemical properties of black and red human hair melanosomes.* Photochem Photobiol, 2005. **81**(1): p. 135-44.
119. Di Donato, P., A. Napolitano, and G. Prota, *Metal ions as potential regulatory factors in the biosynthesis of red hair pigments: a new benzothiazole intermediate in the iron or copper assisted oxidation of 5-S-cysteinyldopa.* Biochim Biophys Acta, 2002. **1571**(2): p. 157-66.
120. Jenkins, N.C., et al., *The p16(INK4A) tumor suppressor regulates cellular oxidative stress.* Oncogene, 2011. **30**(3): p. 265-74.
121. Cassidy, P.B., et al., *Selenium for the prevention of cutaneous melanoma.* Nutrients, 2013. **5**(3): p. 725-49.
122. Govindarajan, B., et al., *Overexpression of Akt converts radial growth melanoma to vertical growth melanoma.* J Clin Invest, 2007. **117**(3): p. 719-29.
123. Diehl, C., *Melanocytes and Oxidative Stress.* Journal of Pigmentary Disorders, 2014. **1**.

124. Song, X., et al., *alpha-MSH activates immediate defense responses to UV-induced oxidative stress in human melanocytes.* Pigment Cell Melanoma Res, 2009. **22**(6): p. 809-18.
125. Jain, A., et al., *p62/SQSTM1 is a target gene for transcription factor NRF2 and creates a positive feedback loop by inducing antioxidant response element-driven gene transcription.* J Biol Chem, 2010. **285**(29): p. 22576-91.
126. Fujita, Y., et al., *Melanoma transition is frequently accompanied by a loss of cytoglobin expression in melanocytes: a novel expression site of cytoglobin.* PLoS One, 2014. **9**(4): p. e94772.
127. Graves, D.B., *Reactive Species from Cold Atmospheric Plasma: Implications for Cancer Therapy.* Plasma Processes and Polymers, 2014. **11**(12): p. 1120-1127.
128. Lu, X., et al., *Reactive species in non-equilibrium atmospheric-pressure plasmas: Generation, transport, and biological effects.* Physics Reports, 2016. **630**: p. 1-84.
129. De Backer, J., et al., *The effect of reactive oxygen and nitrogen species on the structure of cytoglobin: A potential tumor suppressor.* Redox Biol, 2018. **19**: p. 1-10.
130. Furuta, R., et al., *Intracellular responses to reactive oxygen and nitrogen species, and lipid peroxidation in apoptotic cells cultivated in plasma-activated medium.* Plasma Processes and Polymers, 2017. **14**(11): p. 1700123.
131. Hirst, A.M., et al., *Low-temperature plasma treatment induces DNA damage leading to necrotic cell death in primary prostate epithelial cells.* Br J Cancer, 2015. **112**(9): p. 1536-45.
132. Wende, K., et al., *Chemistry and biochemistry of cold physical plasma derived reactive species in liquids.* Biol Chem, 2018. **400**(1): p. 19-38.
133. Gorbanev, Y., D. O'Connell, and V. Chechik, *Non-Thermal Plasma in Contact with Water: The Origin of Species.* Chemistry, 2016. **22**(10): p. 3496-3505.
134. Graves, D.B., *Low temperature plasma biomedicine: A tutorial review.* Physics of Plasmas, 2014. **21**(8): p. 080901.
135. Dubey, S.K., et al., *Cold atmospheric plasma therapy in wound healing.* Process Biochemistry, 2022. **112**: p. 112-123.
136. Bekeschus, S., et al., *Platelets are key in cold physical plasma-facilitated blood coagulation in mice.* Clinical Plasma Medicine, 2017. **7-8**: p. 58-65.
137. Moisan, M., et al., *Plasma sterilization. Methods and mechanisms.* Pure and Applied Chemistry, 2002. **74**(3): p. 349-358.
138. Friedman, P.C., et al., *Successful treatment of actinic keratoses using nonthermal atmospheric pressure plasma: A case series.* J Am Acad Dermatol, 2017. **76**(2): p. 349-350.
139. Fridman, G., et al., *Floating Electrode Dielectric Barrier Discharge Plasma in Air Promoting Apoptotic Behavior in Melanoma Skin Cancer Cell Lines.* Plasma Chemistry and Plasma Processing, 2007. **27**(2): p. 163-176.
140. Berner, J., et al., *Medical Gas Plasma Treatment in Head and Neck Cancer—Challenges and Opportunities.* Applied Sciences, 2020. **10**(6): p. 1944.
141. Brullé, L., et al., *Effects of a non thermal plasma treatment alone or in combination with gemcitabine in a MIA PaCa2-luc orthotopic pancreatic carcinoma model.* PLoS One, 2012. **7**(12): p. e52653.
142. Almeida, N.D., et al., *Cold Atmospheric Plasma as an Adjunct to Immunotherapy for Glioblastoma Multiforme.* World Neurosurg, 2019. **130**: p. 369-376.
143. Pasqual-Melo, G., et al., *Targeting malignant melanoma with physical plasmas.* Clinical Plasma Medicine, 2018. **10**: p. 1-8.
144. Xiang, L., et al., *Cold atmospheric plasma conveys selectivity on triple negative breast cancer cells both in vitro and in vivo.* Free Radic Biol Med, 2018. **124**: p. 205-213.
145. Kim, C.H., et al., *Induction of cell growth arrest by atmospheric non-thermal plasma in colorectal cancer cells.* J Biotechnol, 2010. **150**(4): p. 530-8.
146. Feil, L., et al., *Cancer-Selective Treatment of Cancerous and Non-Cancerous Human Cervical Cell Models by a Non-Thermally Operated Electrosurgical Argon Plasma Device.* Cancers (Basel), 2020. **12**(4).

147. Li, Y., et al., *Selective Anti-Cancer Effects of Plasma-Activated Medium and Its High Efficacy with Cisplatin on Hepatocellular Carcinoma with Cancer Stem Cell Characteristics.* Int J Mol Sci, 2021. **22**(8).
148. Yan, D., et al., *Toward understanding the selective anticancer capacity of cold atmospheric plasma--a model based on aquaporins (Review).* Biointerphases, 2015. **10**(4): p. 040801.
149. Privat-Maldonado, A., et al., *ROS from Physical Plasmas: Redox Chemistry for Biomedical Therapy.* Oxid Med Cell Longev, 2019. **2019**: p. 9062098.
150. Bauer, G., *Intercellular singlet oxygen-mediated bystander signaling triggered by long-lived species of cold atmospheric plasma and plasma-activated medium.* Redox Biology, 2019. **26**: p. 101301.
151. Nakamura, K., et al., *Novel Intraperitoneal Treatment With Non-Thermal Plasma-Activated Medium Inhibits Metastatic Potential of Ovarian Cancer Cells.* Sci Rep, 2017. **7**(1): p. 6085.
152. Tanaka, H., et al., *Similarities And Differences In The Cellular Resposnses Between Plasma-Activated Medium-Treated Glioblastomas And Plasma-Activated Ringer's Lactate Solution-Treated Glioblastomas.* Clinical Plasma Medicine, 2018. **9**: p. 42-43.
153. Liedtke, K.R., et al., *A myeloid and lymphoid infiltrate in murine pancreatic tumors exposed to plasma-treated medium.* Clinical Plasma Medicine, 2018. **11**: p. 10-17.
154. Bekeschus, S., et al., *Physical Plasma Elicits Immunogenic Cancer Cell Death and Mitochondrial Singlet Oxygen.* IEEE Transactions on Radiation and Plasma Medical Sciences, 2018. **2**(2): p. 138-146.
155. Lin, A., et al., *Nanosecond-Pulsed DBD Plasma-Generated Reactive Oxygen Species Trigger Immunogenic Cell Death in A549 Lung Carcinoma Cells through Intracellular Oxidative Stress.* Int J Mol Sci, 2017. **18**(5).
156. Fucikova, J., et al., *Detection of immunogenic cell death and its relevance for cancer therapy.* Cell Death & Disease, 2020. **11**(11): p. 1013.
157. Lin, A.G., et al., *Non-thermal plasma induces immunogenic cell death in vivo in murine CT26 colorectal tumors.* Oncoimmunology, 2018. **7**(9): p. e1484978.
158. Lin, A., et al., *Non-Thermal Plasma as a Unique Delivery System of Short-Lived Reactive Oxygen and Nitrogen Species for Immunogenic Cell Death in Melanoma Cells.* Adv Sci (Weinh), 2019. **6**(6): p. 1802062.

CHAPTER II

OBJECTIVES

The vast repertoire of postulated functions of cytoglobin (Cygb), together with its ubiquitous expression in tissues and cells, makes it daunting to unravel the physiological function of Cygb, both on a cellular and molecular level. The discovery of melanocytes (and some melanomas) as a cell type possessing high endogenous expression levels of human Cygb (CYGB) makes melanocytes an ideal model to study CYGB in a biologically relevant setting. Furthermore, the frequent downregulation of CYGB during melanomagenesis makes it opportune to investigate CYGBs cytoprotective function in this cancer cell type. Additionally, the recent development of non-thermal plasma (NTP) paved the way for new approaches in the treatment of melanoma, and cancer in general. As CYGBs presence could potentially influence the outcome of therapeutic treatments aimed at elevating oxidative stress, including NTP, this project mainly focused on the sensitivity of melanoma towards the effects of NTP and the role CYGB plays in the determination of the efficiency of NTP treatment. Additionally, pertaining further to the redox-regulatory function, the influence of CYGB on ferroptosis sensitivity, and hypoxic regulation of CYGB expression was investigated in melanoma.

The **first objective** of this project was to investigate the molecular mechanism through which CYGB can function as a redox-sensitive protein involved in the cellular antioxidant response. NTP was as used as a mean of producing a multitude of reactive oxygen and nitrogen species (RONS) and treated recombinant CYGB to investigate the effect of RONS on CYGB protein structure. Relating to CYGB's role in redox homeostasis, hypoxia-dependent regulation of CYGB mRNA levels was observed in various cell types and tissues. Considering that hypoxia plays a crucial role in melanoma malignancy, the oxygen-dependent regulation of CYGB expression was therefore investigated in melanoma cells (**objective 2**). For the **third objective,** the potential influence of the presence or absence of CYGB in melanoma cells on NTP-treatment outcome was investigated. In the last objective (**objective 4**) pertaining to CYGB function, the potential effect of CYGB on the cellular sensitivity towards ferroptosis was investigated in melanoma cells that express highly abundant endogenous levels of CYGB.

Finally, we investigated the potential of NTP as an immunogenic cell death inducer in a murine melanoma model (**objective 5)**. For this purpose, we treated murine melanoma cells with a DBD plasma device. Treated cells were afterwards administered to mice and protection towards subsequent tumor challenge was assessed.

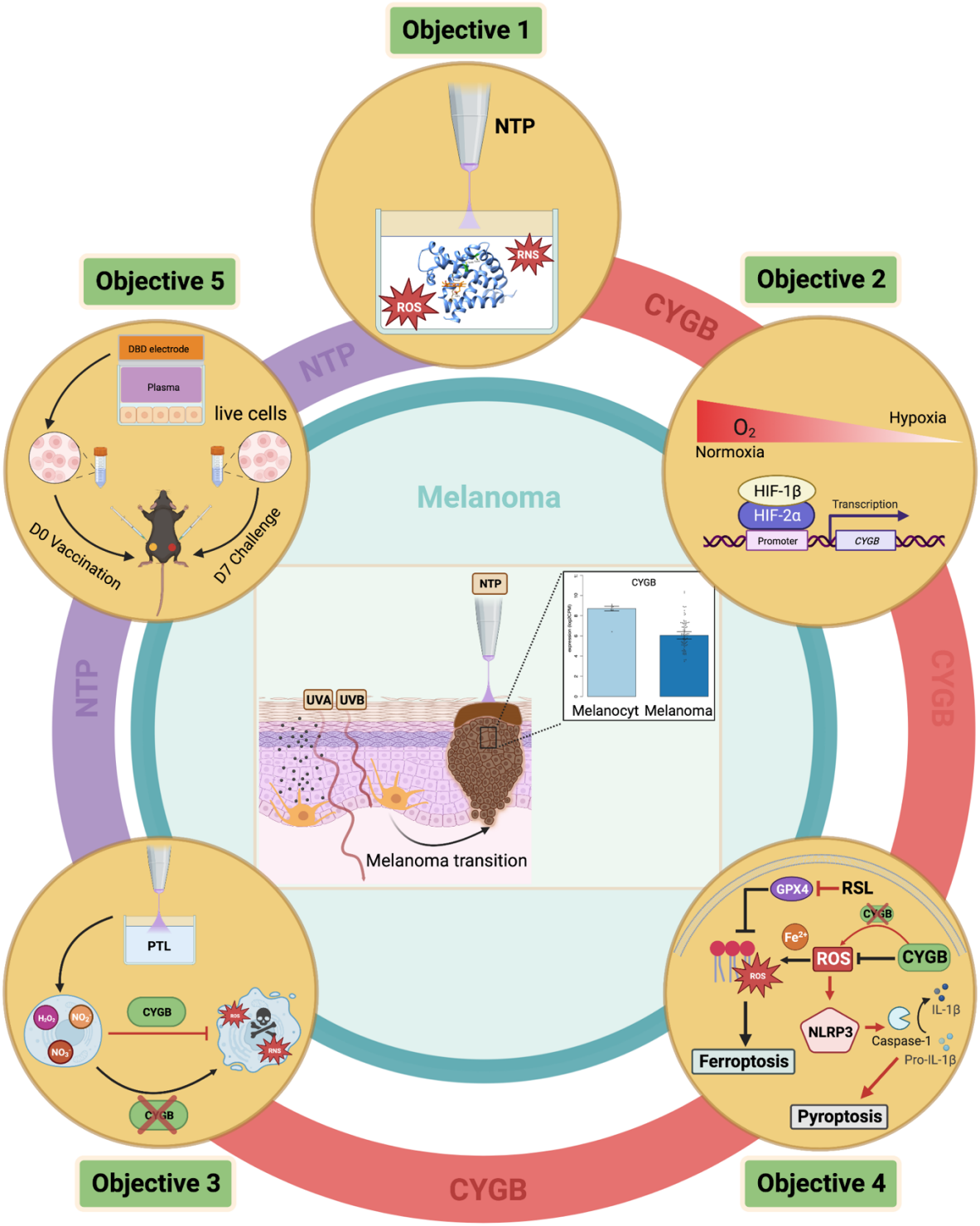
Objective 1
NTP
RNS
ROS
Objective 2
CYGB
Hypoxia
O_2
Normoxia
HIF-1β
HIF-2α
Transcription
Promoter
CYGB
Objective 5
DBD electrode
Plasma
live cells
D0 Vaccination
D7 Challenge
NTP
Melanoma
UVA
UVB
Melanocyt
Melanoma
Melanoma transition
PTL
CYGB
Objective 3
GPX4
RSL
Fe2+
ROS
NLRP3
IL-1β
Caspase-1
Pro-IL-1β
Ferroptosis
Pyroptosis
Objective 4

Chapter III

THE EFFECT OF REACTIVE OXYGEN AND NITROGEN SPECIES ON THE STRUCTURE OF CYTOGLOBIN: A POTENTIAL TUMOR SUPPRESSOR

Published as:

De Backer J, Razzokov J, Hammerschmid D, Mensch C, Hafideddine Z, Kumar N, van Raemdonck G, Yusupov M, Van Doorslaer S, Johannessen C, Sobott F, Bogaerts A, Dewilde S. *The effect of reactive oxygen and nitrogen species on the structure of cytoglobin: A potential tumor suppressor*. Redox Biol. 2018 Oct;19:1-10. doi: 10.1016/j.redox.2018.07.019.

3.1 ABSTRACT

Many current anti-cancer therapies rely on increasing the intracellular reactive oxygen and nitrogen species (RONS) contents with the aim to induce irreparable damage, which subsequently results in tumor cell death. A novel tool in cancer therapy is the use of cold atmospheric plasma (CAP), which has been found to be very effective in the treatment of many different cancer cell types *in vitro* as well as *in vivo*, mainly through the vast generation of RONS. One of the key determinants of the cell's fate will be the interaction of RONS, generated by CAP, with important proteins, *i.e.,* redox-regulatory proteins. One such protein is cytoglobin (CYGB), a recently discovered globin proposed to be involved in the protection of the cell against oxidative stress. In this study, the effect of plasma-produced RONS on CYGB was investigated through the treatment of CYGB with CAP for different treatment times. Spectroscopic analysis of CYGB showed that although chemical modifications occur, its secondary structure remains intact. Mass spectrometry experiments identified these modifications as oxidations of mainly sulfur-containing and aromatic amino acids. With longer treatment time, the treatment was also found to induce nitration of the heme. Furthermore, the two surface-exposed cysteine residues of CYGB were oxidized upon treatment, leading to the formation of intermolecular disulfide bridges, and potentially also intramolecular disulfide bridges. In addition, molecular dynamics and docking simulations confirmed, and further show, that the formation of an intramolecular disulfide bond, due to oxidative conditions, affects the CYGB 3D structure, thereby opening the access to the heme group, through gate functioning of His_{117}. Altogether, the results obtained in this study (1) show that plasma-produced RONS can extensively oxidize proteins and (2) that the oxidation status of two redox-active cysteines lead to different conformations of CYGB.

3.2 INTRODUCTION

The use of cold atmospheric plasma (CAP) has attracted a lot of attention over the past few years and has already found many biomedical applications, including wound healing [1], sterilization [2], biofilm removal [3], blood coagulation [4], and more recently cancer therapy [5]. CAP is a plasma (i.e., ionized gas) in which the high-temperature electrons are in non-equilibrium with the low-temperature heavy particles, thereby keeping the gas itself near room temperature and making it suitable for treatment of living cells and tissues. Plasma is a mixture of various components, including charged particles (ions, electrons), reactive neutral species (reactive oxygen and nitrogen species; RONS), UV radiation, and electromagnetic fields [6]. Of those, RONS are hypothesized to mediate the effects observed in biological systems as they are known to be involved in rapid reactions with important biomolecules such as proteins and lipids [7, 8]. In the last few years, CAP was shown to be able to induce apoptotic cell death in numerous different cancer cell types [9-15]. Although not fully understood, a possible mechanism of action is through: (1) the production of reactive species by CAP, which then diffuse into the cells or create extra RONS inside the cells, e.g., due to lipid peroxidation; (2) an increase in the level of intracellular RONS that oxidize proteins, lipids, and DNA; (3) oxidation exceeding the anti-oxidant capacity of the cells leads to irreversibly damaged biomolecules, which in turn induces a physiological response through cell death. Therefore, to gain further insight into these processes, it is necessary to study the interaction between CAP and cells on a molecular level.

As proteins are the main facilitators of biological functions (and account for about 50% of the gross dry weight of cells), one could hypothesize that plasma-protein interactions will be key determinants of the cell's fate after plasma treatment. Recent investigations have shown that CAP can affect infectious prion protein [16], recombinant green fluorescent protein [17], lysozyme [18], and globins, such as hemoglobin and myoglobin [19] through modification of the higher-order structure and/or heme degradation. Proteins of a particular interest to investigate the plasma-protein interactions would be redox-sensitive proteins, as they are centrally involved in regulating the redox balance inside the cell, mainly through oxidative modification of redox-sensitive cysteine residues [20]. One such protein is cytoglobin (CYGB). CYGB is a recently discovered hexa-coordinated globin with many proposed functions, including oxygen transport, NO-dioxygenase activity [21, 22], reactive oxygen species (ROS)-scavenger [23], and tumor

suppression [24]. Although some of these proposed functions are still under debate, there is a general consensus that CYGB can protect the cell from oxidative stress. This implies that CYGB is a redox-sensitive protein, of which the sensitivity has been suggested to occur through heme-coordination and/or cysteine residues (Cys_{38} and Cys_{83}) on its surface, which can form intra- or intermolecular disulfide bridges [25-27]. Treating CYGB with plasma would allow for the verification and further clarification of the proposed models on how plasma-induced RONS affect biomolecules. Furthermore, it can shed new light on recent findings [28-30] concerning how CYGB is involved in cell protection against oxidative stress.

In this study, recombinant CYGB was treated with a cold plasma jet (kINPen IND) for different treatment times. Possible structural modifications were investigated by using electronic circular dichroism (CD), UV-Vis spectroscopy, and resonance Raman spectroscopy. Additionally, mass spectrometry (MS) experiments were performed on the native form and under denaturing conditions. Finally, molecular dynamics (MD) and docking simulations were performed to assess the effect of an intramolecular disulfide bond on the structure and function of monomeric CYGB. These combined experiments and simulations allow us to gain an insight into the effect of plasma treatment, and also oxidative stress, on structural features of proteins, which should contribute to a better understanding of the above-mentioned postulated functions of CYGB.

3.3 EXPERIMENTAL

3.3.1 Expression and purification of recombinant CYGB

The expression of recombinant wild-type CYGB was performed as previously described [31]. Briefly, human cDNA of CYGB was cloned in the pET3a expression vector. Inclusion bodies were solubilized in 6M guanidinium hydrochloride and insoluble material was eliminated. Afterwards, CYGB was reconstructed by adding free hemin and dialyzed overnight. The samples were then purified with an Akta purifier system on a Hitrap DEAE-Sepharose column (both GE Healthcare, Life Sciences). The concentrated material was loaded onto a Sephacryl S-200 High resolution column (GE Healthcare). The final purity of the pooled CYGB was checked by absorbance spectra and SDS-PAGE.

3.3.2 CAP treatment of recombinant CYGB

A recombinant CYGB stock solution (19.3 mg/mL; 901 µM) was diluted either in deionized water or 50 mM Tris-buffer (pH 8) to a final concentration of 20 µM. Plasma treatment was performed on 500 µL aliquots in a 24-well plate (on ice) for different time points (30 s, 1 min, 3 min, 5 min, 10 min) using the kINPen IND plasma jet (neoplas GmbH). The applied gas flow rate and gap distance were set at 3 L/min, and 10 mm, respectively, for all treatments. Argon was used as feed gas. After treatment, the evaporated volume of the aliquots was calculated and replaced by either water or Tris-buffer. The treated samples were immediately put on ice before being handled for further analysis.

The pH of both used solvents was measured before and after treatment with CAP at different lengths of time to assess the effect of CAP treatment on the pH of the samples. The pH was measured with the pHenomenal pH 1100 H pH-meter (VWR).

3.3.3 Mass spectrometry

3.3.3.1 Native and denatured MS

Before native MS analysis, 50 µL of each sample was buffer exchanged using a Micro Bio-Spin P-6 Gel column (Bio-Rad) equilibrated with 100 mM aqueous ammonium acetate (pH 6.8), according to the manufacturer's protocol. Afterwards, the samples were further diluted to a concentration of 10 µM.

3 µL of sample solution were loaded into an in-house produced, gold coated nano-electrospray ionization (ESI) glass capillaries and mounted in the needle holder of the instrument. MS spectra were acquired on a Synapt G2 HDMS instrument (Waters, Wilmslow, UK) using the following instrument parameters: 1.6 kV spray capillary voltage; 100 V sampling cone; 3 V extractor cone; 6.3 mbar backing pressure; 15 V and 5 V collision energy in the trap (2.4×10^{-2} mbar) and transfer (2.5×10^{-2} mbar) cell, respectively; 45 V trap DC bias; 180 mL/min and 90 mL/min He and IMS gas flow, respectively. The ions were separated in the ion mobility (IM) cell, using nitrogen gas and a wave velocity of 750 m/s and a wave height of 40 V.

The samples were also measured under denaturing conditions by diluting the sample 1:1 with acetonitrile containing 1 % formic acid. The MS parameters for measuring the denatured samples were: 1.4 kV spray capillary voltage; 25 V sampling cone; 1 V extractor cone; 2.7 mbar backing

pressure; and 5 V collision energy in trap (2.00 x 10^{-2} mbar) and transfer (2.2 x 10^{-2} mbar) cell. Settings for IM separation were the same as under native conditions. Additional native and denaturing measurements on the Tris-diluted CYGB samples were also performed in 10 mM dithiothreitol (DTT).

3.3.3.2 In solution protein digestion and MS

To detect oxidative modifications at amino acid level, a tryptic digest was performed on each treated sample following our own protocol. Briefly, 40 µg of plasma-treated sample was used. 1% RapiGest SF Surfactant (Waters) was added to a final concentration of 0.1% before incubation for 5 min at 100°C. 200 mM TCEP (Tris (2-carboxyethyl) phosphine) was added to reduce the sample. After 1h incubation at 55 °C, 375 mM 2-iodocetamide was added and further incubated for 30 min in the dark to alkylate the sample. After alkylation, the sample was precipitated with pre-chilled acetone and incubated overnight at -20 °C. The acetone-precipitated pellet was resuspended in 100 mM triethylammonium bicarbonate to a final concentration of 1 µg/µL before MS grade trypsin protease (Thermo Scientific) was added to a final protease-protein ratio of 1:40 (w/w). Tryptic digest was performed overnight at 37 °C. The enzymatic reaction was stopped by freezing the samples at -20 °C. The digested samples were measured using liquid chromatography – ion trap tandem mass spectrometry (LC-MS/MS).

The peptide mixture was separated by reversed phase C18 (RP-C18) liquid chromatography on a nanoAcquity UPLC system (Waters) using a Symmetry C18 trap column (5 µm particle size; 280 µm x 20 mm) connected to a BEH C18 analytical column (1.7 µm particle size; 100 µm x 100 mm) (Waters). Before loading, each sample was dissolved in 10 µL mobile phase A (0.1% formic acid in 100% water) and in total 1 µg of protein digest was loaded onto the column. A linear gradient of mobile phase B (0.1% formic acid in 100% acetonitrile) from 5 to 55% in 50 min followed by a steep increase to 100% mobile phase B in 3 min was used at a flow rate of 400 nL/min. The nano-UPLC system was coupled online with the mass spectrometer using a PicoTip Emitter (New objective) and a nanospray ion source (Thermo Scientific). The LTQ ion trap mass spectrometer (Thermo Scientific) was set up in MS mode, where a full MS1 scan (300 to 2000 m/z) was followed by collision-induced dissociation (CID) and a subsequent MS2 scan (100 to 2000 m/z). All scans were acquired in the linear ion trap with an automatic gain control (AGC) set at 3 x 10^4 ions for MS1 and 1 x 10^4 ions for MS2 scans. The normalized collision energy was 31% in CID, and a

dynamic exclusion list of 30s for data dependent acquisition was used. Between every sample a blank run was performed to exclude any possible carry-over effect.

Proteome Discoverer (2.1 SP1) software (Thermo Scientific) was used to perform database searching against the UniProt reference human database using both the Sequest and Mascot algorithms. Following settings were applied: precursor mass tolerance of 500 ppm, fragment mass tolerance of 0.50 Da. Trypsin was specified as digesting enzyme and 2 missed cleavages were allowed. Cysteine carbamidomethylation was defined as fixed modification and oxidations (on residues M/Y/D/F/H/W/N and P) were set as variable modifications. The results were filtered using the following settings: only medium and high confident peptides with a global FDR < 5% based on a target-decoy approach [16] and first ranked peptides were included in the results.

3.3.4 UV-Vis spectroscopy

UV-Vis circular dichroism (CD) and absorption spectra were collected using a Chirascan Plus qCD (LAAPD solid-state detector) spectrometer (Applied Photophysics Ltd.) operating with a bandwidth of 1 nm, a step size of 1 nm, a scanning speed of 0.5 s/nm, a sample temperature of 20 °C and a cuvette with a path length of 0.5 mm or 2.0 mm. The spectral region sensitive to secondary structure 180-280 nm was measured using a 0.5 mm path length and the spectral region 225–600 nm comprising the Soret band and Q-bands was measured with a path length of 2.0 mm.

3.3.5 Resonance Raman spectroscopy

Resonance Raman (RR) spectra were acquired using a Dilor XY-800 spectrometer in low-dispersion mode using a liquid N_2-cooled CCD detector. The excitation source was a Spectra Physics (Mountain View) BeamLok 2060 Kr^+ laser operating at 413.1 nm. The spectra were recorded at room temperature and the protein solutions were magnetically stirred at 500 rpm in order to avoid local heating and photochemical decomposition. The slit width used during the experiments was 200 μm. In general, 10-12 spectra were acquired with an integration time of 240 s each. Spikes due to cosmic rays were removed by omitting the highest and lowest data points for each frequency and by averaging the remaining values. Typical sample concentrations were in the order of 20 μM.

3.3.6 Computer simulations (molecular dynamics and docking)

Molecular dynamics (MD) and docking simulations were performed in order to elucidate the functionality of monomeric CYGB with and without an intramolecular disulfide bridge, at the molecular level. The simulations were carried out using the GROMACS [32] program package (version 5.1), applying the GROMOS 45a3 force field [33]. The coordinate file (with the initial configuration) of monomeric CYGB was obtained from the Protein Data Bank (PDB ID: 1V5H) [34]. The structure of CYGB without an initial disulfide bond, i.e., $CYGB_{SH...SH}$, was placed in a dodecahedron box, with size chosen in such a way that there initially was 1.0 nm buffer distance between the protein and the boundary of the simulation box. This was done in order to avoid long distance interactions (i.e., Coulomb and van der Waals interactions) between $CYGB_{SH...SH}$ and its periodic images. The box was then filled with water molecules surrounding the $CYGB_{SH...SH}$ molecule, employing the SPC water model [35], and sodium counter ions were added to neutralize the system. Periodic boundary conditions were applied in all directions.
In order to study the effect of the abovementioned disulfide bond on the conformation of CYGB, this disulfide linkage was manually created using Avogadro software [36]. Subsequently, energy minimization was applied to optimize the modified structure, using the steepest descent algorithm. The measured length of the disulfide bond after the energy minimization was 2.05 Å, which is exactly the same as the disulfide bond length given in literature [37, 38]. The abovementioned MD procedure was then repeated (i.e., the creation of the box and addition of water molecules, as well as counter ions) to create the simulation system with CYGB containing a disulfide bridge, i.e., $CYGB_{S\text{-}S}$.

Thus, two model systems were used (i.e., $CYGB_{SH...SH}$ and $CYGB_{S\text{-}S}$) covered with water as a starting structure for the calculations. The systems were minimized in three steps, by applying three optimization algorithms, i.e., steepest descent, conjugate gradient and low-memory Broyden-Fletcher-Goldfarb-Shanno (L-BFGS) [39]. Subsequently, a 500 ps equilibration run was performed employing the NVT ensemble (i.e., a system with constant number of particles N, volume V and temperature T). Next, a 150 ns production run was performed using NPT dynamics (i.e., a system with constant number of particles N, pressure P and temperature T). The NPT simulations were carried out for 300 K and 1 bar pressure, employing the velocity-rescaling thermostat with a coupling constant of 0.1 ps and the isotropic Parrinello-Rahman barostat [40, 41], with a compressibility and coupling constant of 4.5×10^{-5} bar^{-1} and 2 ps, respectively. A 1.4 nm cut-off

distance was applied for the van der Waals interactions. The long range electrostatic interactions are described by the particle mesh Ewald (PME) method [42], again using 1.4 nm cut-off for the real-space interactions in combination with a 0.15 nm spaced-grid for the reciprocal-space interactions.

In the docking simulations, binding hot spots of equilibrated $CYGB_{SH...SH}$ and $CYGB_{S-S}$ were predicted using the FTMap family of the web server [43]. FTMap samples the positions of 16 small probing organic molecules and identifies potential ligand binding regions of the protein based on the lowest binding free energy. These individual probing molecules may bind at various locations of the protein, and thus their clusters specify binding hot spots (so-called binding pockets) of the protein. The probing molecules used in the FTMap server are ethane, ethanol, isopropanol, isobutanol, acetonitrile, methanamine, N,N-dimethylformamide dimethyl ether, benzaldehyde, benzene, cyclohexane, phenol, acetamide, acetone, acetaldehyde and urea. They vary in shape, size and polarity, and can be considered as drug-like molecules [43]. The hot spot of the protein was identified by means of a mapping algorithm that consisted of the following four steps: (1) each probe molecule samples on a grid around the fixed protein. The energy function considers van der Waals energy with attractive and repulsive contributions and an electrostatic as well as solvation term characterized by the Poisson–Boltzmann continuum model. The algorithm choses the 2000 best positions of each probing molecule and proceeds to the next stage. (2) These best positions of the probe molecules with the protein complex are energy minimized using the CHARMM potential [44] with an analytical continuum electrostatics model [45]. During the energy minimization run, the protein atoms are fixed while the probing molecules are free to move. (3) The minimized structures are clustered within a 4 Å radius, considering the lowest energy structure. For each probe molecule, six clusters are retained with the lowest energy, which are ranked by their Boltzmann averaged energies. (4) The clusters of the 16 different probe molecules are then clustered into consensus clusters. This clustering stage defines the center of mass for each cluster probe. The highest ranked consensus cluster is selected, using the distance between the centers of mass of the cluster centers as measure for the distance and 4 Å as the clustering radius. VMD [46], and Pymol [47] visualizing tools were used for preparation of the images.

3.4 RESULTS

3.4.1 Spectroscopic changes upon plasma treatment of CYGB

As an initial study of the structural effects of plasma treatment on CYGB, UV-Vis absorption and CD spectra were recorded and are presented in Figure 3.1. The UV-Vis absorption spectrum of the untreated sample contains a Soret (γ) band at 417 nm, and β and α bands in the visible region of the spectrum at 535 and 565 nm, respectively, indicating that the heme iron is in a ferric low-spin HisF8-Fe(III)-HisE7 hexa-coordination state [48]. The treatment of CYGB with plasma induces significant spectroscopic changes. Most noteworthy is the time-dependent disappearance of the Soret band, but also the steady decrease of the intensity of the β and α bands with longer treatment times. When comparing the spectra, acquired in the two solvents that were employed, both similarities and differences can be observed. For both, a time-dependent decrease in intensity of the Soret band can be observed. However, the Soret band of the samples diluted in Tris-buffer is still clearly visible after 5 min exposure to plasma. Even after 10 min, there is still positive intensity discernible at 417 nm in Tris-buffer, while this is not the case in water. Even more so, in water, a new peak appears at 387 nm after 5 min of treatment, indicating that free heme is present in the solution [49]. In Tris-buffer, the same peak (383 nm) only starts to appear after 10 min treatment, again indicating the presence of free heme.

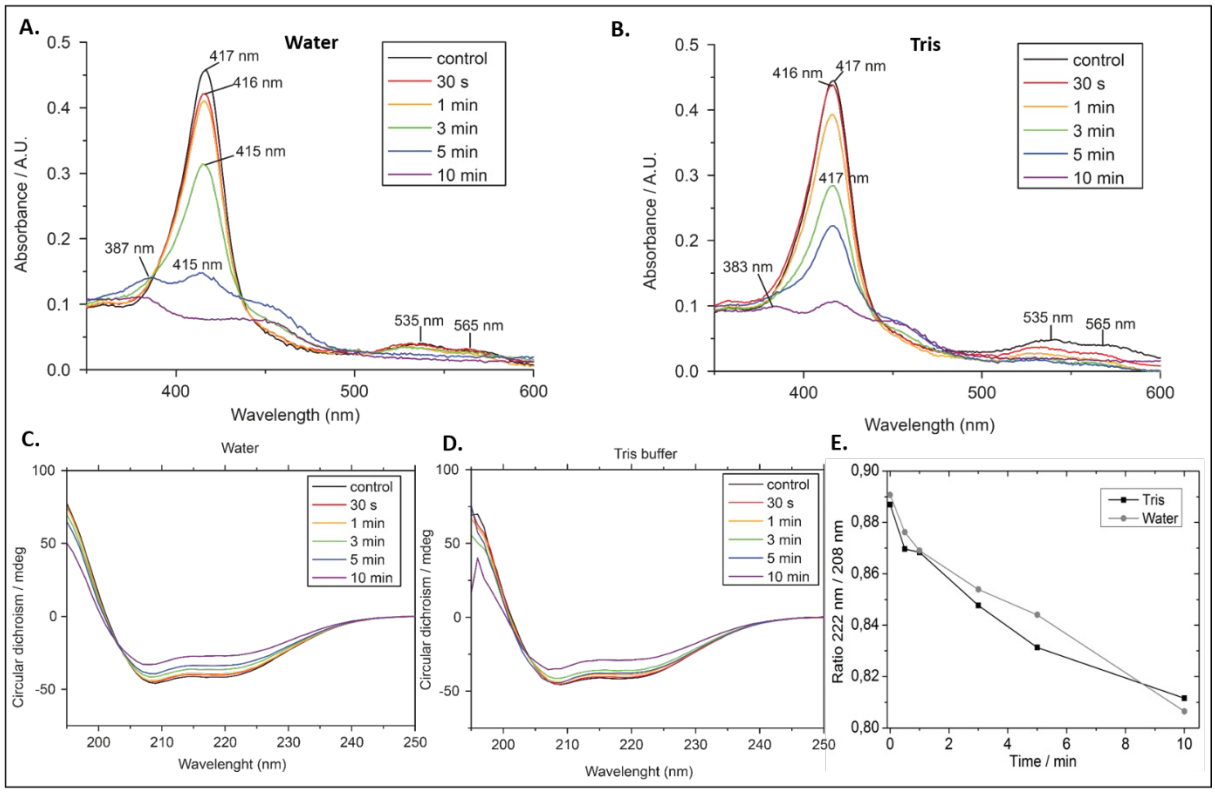

Figure 3.1. Spectroscopic changes of CYGB after plasma treatment. UV-Vis spectra of untreated and plasma-treated CYGB in (A.) water, and (B.) Tris-buffer, in the 350-600 nm region with the Soret band (417 nm) and β (535 nm) and α (565 nm) bands clearly visible. (C) and (D): CD spectra of untreated and plasma-treated CYGB samples in the 190-250 nm region, depicting the double minima at 208 nm and 222 nm typical for alpha helical structures. (E): Change of the 208/222 nm ratio in function of the treatment time with both used solvents.

The CD spectra of CYGB before and after treatment are shown in Figure 3.1C and D. All spectra display the typical double minima at 208 and 222 nm, characteristic for protein structures that are predominantly α-helical [50]. Plasma treatment, besides altering the intensity of the double minima, does not seem to influence the spectra significantly, suggesting that the secondary structure remains largely unaltered by the plasma treatment. As the $\Theta_{222}/\Theta_{208}$ ratio is sensitive to structural changes, the ratio was plotted over treatment time (Figure 3.1E) [50]. The plot shows that, with both solvents, the ratio drops depending on the treatment time. The change in the ratio, although very minor, indicates a slight unfolding of the protein.

pH measurements indicated that the pH of the samples dissolved in water significantly drops after plasma treatment, whereas with Tris-buffer, no change in pH could be observed (Figure. S3.3). As the change in pH of water could have a profound effect on CYGB, and thus on the results obtained with this solvent, we decided to focus further only on the results obtained with Tris-buffer.

3.3.4 Mass spectrometry experiments

Following the UV-Vis and CD measurements, mass spectrometry (under native and denaturing conditions) was used to assess changes in the tertiary structure of CYGB samples as well as chemical modifications after treatment with plasma.

3.4.2.1 Native MS

Figure 3.2 shows the native mass spectra of untreated and treated CYGB. The spectrum of the untreated sample ("control") clearly exhibits a charge state distribution for monomeric and dimeric species, with the monomeric species accounting for the majority of the signal (see also Figure S3.1). As can be seen, plasma treatment not only leads to peak broadening and a shift to higher m/z values, but also to a small increase of dimeric species. The peak shift and broadening is highlighted (in blue) for the monomeric +9 species in the m/z region of 2400-2600 (Figure 3.2, inset). Here, it can be seen that plasma treatment of only 30 s already causes a mass shift to higher m/z values and peak broadening, which indicates an unresolved distribution of oxidized

species. Not much change is observed up to 3 min treatment of CYGB. However, a major peak shift is visible after 5 and 10 min of treatment, which is probably caused by binding of an additional ligand to the heme (see further, Figure 3.3). In addition, a small fraction of apo-CYGB is also present, in agreement with UV-Vis data that showed heme loss after 10 min as well.

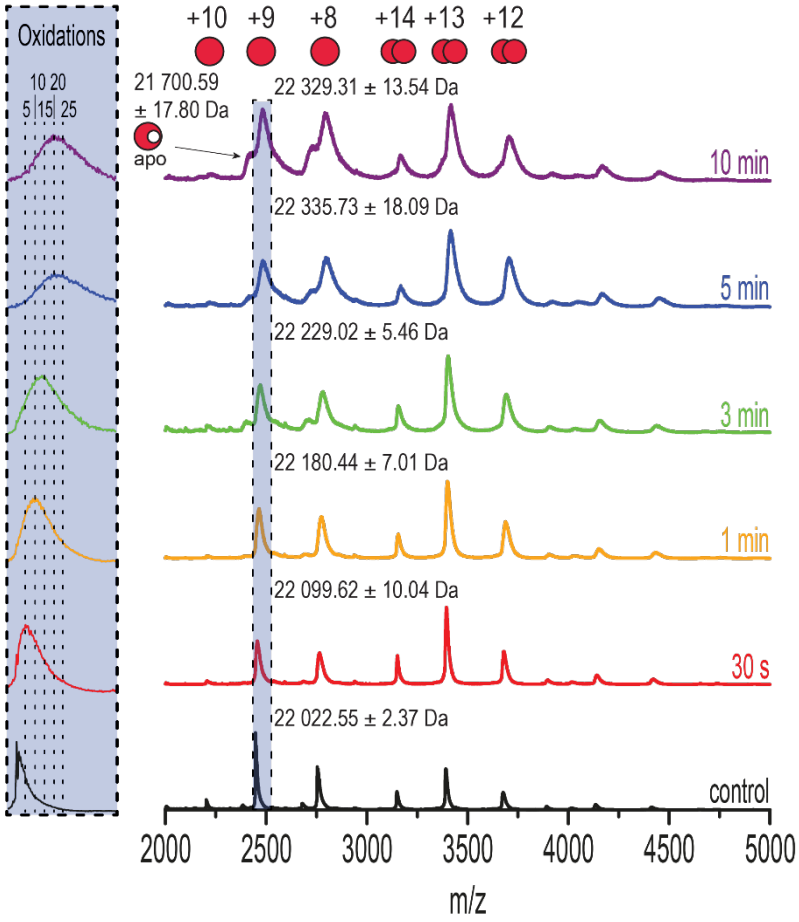

Figure 3.2. Native MS. Native MS spectra of 10 µM holo CYGB in 100 mM ammonium acetate after different duration of plasma treatment (20 µM CYGB in 50 mM Tris-buffer). Monomeric (+10, +9, +8) and dimeric (+14, +13, +12) species are identified. The monomeric +9 species are highlighted in blue. Inset: zoomed in section of the +9 monomers, highlighting mass shifts and peak broadening caused by plasma-induced oxidations. The theoretical mass of holo CYGB is 22021.11 Da.

3.4.2.2 Denatured MS

Plasma-treated samples were also measured under denaturing conditions, in order to determine if the observed dimers were noncovalent complexes, or covalently linked, e.g., via disulfide bridges (Figure 3.3). As can be seen in Figure 3.3B (bottom panel, "control") and Figure S3.2, unfolding leads to a much broader charge state distribution for the monomer that no longer contains the heme group. The spectra also show minor peaks in between the monomers (Figure 3.3B), highlighting the presence of dimeric species that still remain after denaturation. This indicates that the dimerization occurs via covalent bonds. In Figure 3.3A, the m/z region between

600 and 700 is shown with the peak corresponding to the free heme group (616 m/z). A plasma treatment time of up to 3 min does not show much effect; however after 5 min a new peak appears at 661 m/z, indicating the binding of a molecule to the heme group (while also replacing a hydrogen atom) which we interpret as $^{\bullet}NO_2$ (+45 Da).

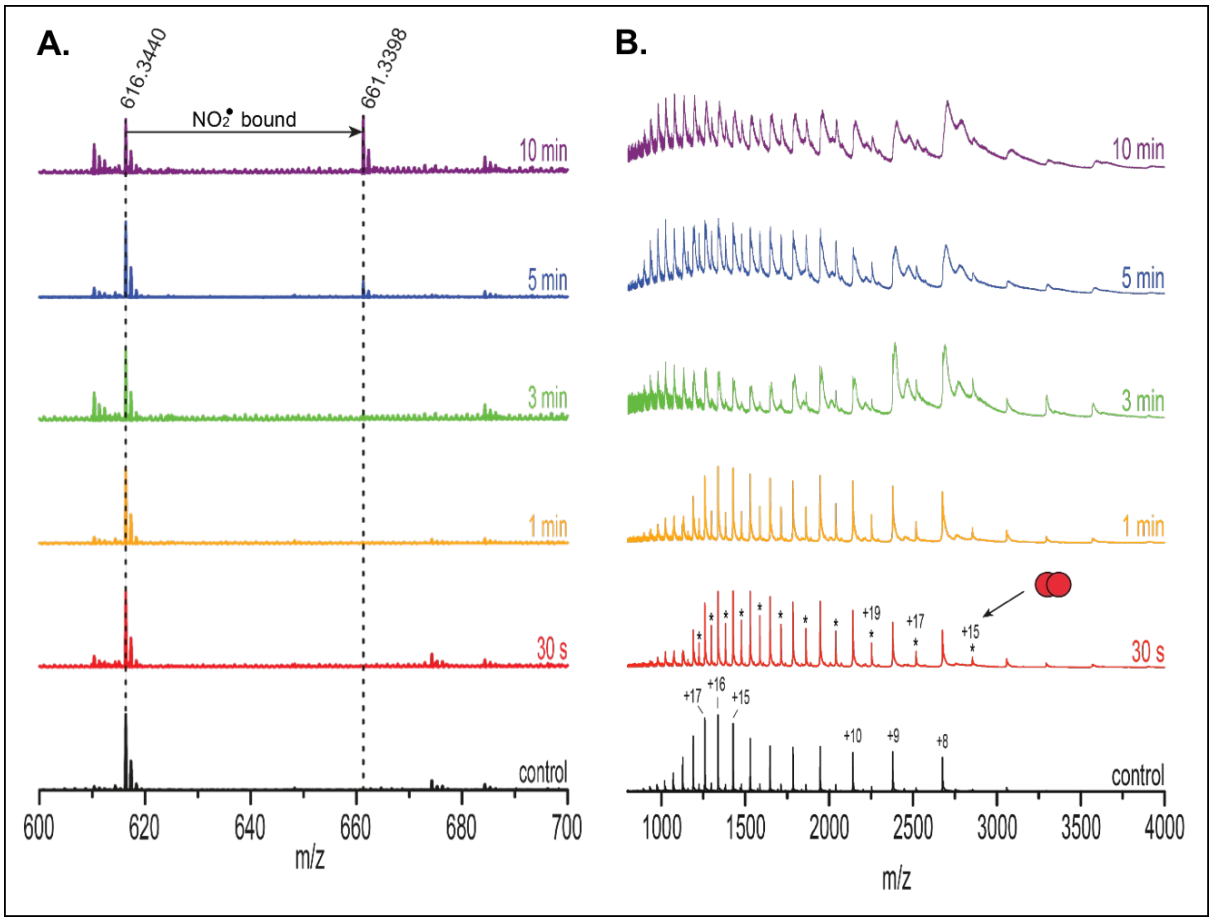

Figure 3.3 Denaturing MS of CYGB. ESI spectra of 10 µM CYGB (diluted 1:1 in acetonitrile containing 1% formic acid) after different duration of plasma treatment (20 µM CYGB in 50 mM Tris-buffer). (A.): Zoomed in m/z region from 600 to 700. The peak at 616.3440 m/z represents the free heme group. 5 to 10 min of treatment induces binding of a molecule, i.e., $^{\bullet}NO_2$ to the heme group (661.3398 m/z). (B.): Full spectrum ranging from 800-4000 m/z showing the apo-form of the protein. The appearance of smaller peaks (asterisks) in between the monomers highlights the presence of covalent dimers in the sample. The theoretical mass of CYGB in the apo-form (without heme) is 21 404.62 Da compared to the experimental mass of 21 407.29 ± 4.16 Da in the control.

We note that dimers are already present in the native spectra (Figure 3.2) without plasma treatment, but almost entirely absent in the denatured spectrum (Figure 3.3B). In order to investigate whether pre-existing noncovalent CYGB dimers are converted to covalent, disulfide-bound dimers under the influence of plasma oxidation, measurements in Tris-buffer, under native conditions, were repeated after adding 10 mM of the reducing DTT to the samples. Figure 3.4 shows the full spectra and zoomed in section of the monomeric +9 peak (inset, highlighted in blue). As can be observed, addition of DTT leads to a loss of the dimeric species, indicating that

dimerization is stabilized by disulfide bonds. Furthermore, the addition of DTT also reduces the plasma-induced oxidations. This is clearly visible when comparing the monomeric +9 peaks in Figure 3.4 with the ones depicted in Figure 3.2, under otherwise identical conditions. The peak shifts after 5 and 10 min of plasma treatment again indicate binding of an additional ligand to the heme group.

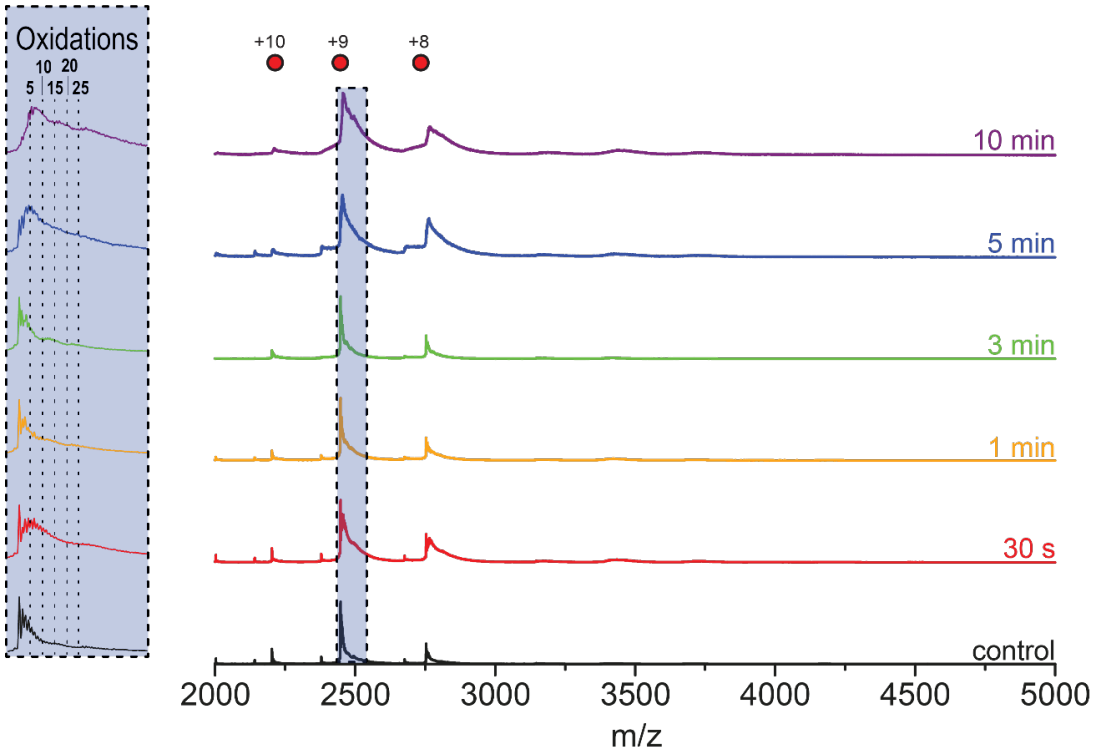

Figure 3.4. Native MS after reduction with DTT. Native MS spectra of 10 µM CYGB in 100 mM ammonium acetate after adding 10 mM DTT. Monomeric +9 is highlighted. Inset: the zoomed in section of the monomeric +9 peak. Addition of DTT leads to a loss of the dimers via reduction of disulfide bridges. DTT also seems to reduce the number of oxidations (narrowing of the peaks). See also Figure 3.2 for comparison.

3.4.3 Amino acid modification sites of CYGB

Next, we aimed to map plasma-induced oxidative modification sites using LC-orbitrap MS/MS of trypsin-digested samples. Table 3.1 gives an overview of different types of amino acids that were found to be modified after plasma treatment of a specific duration. CAP was able to oxidize all different amino acids that were selected for the analysis (Table 3.1), with some seeming to be more readily oxidized than others. Of the investigated amino acids, methionine, tryptophan, and tyrosine were the three found to be preferably oxidized, as reported previously [51]. Surprisingly, no clear treatment-time-dependent increase in the number of oxidized amino acids could be observed, indicating that oxidation may occur rapidly. In the suppl. Table S3.2, the complete

amino acid sequence of CYGB is given together with the specific location of each identified modification, for each exposure time. Table S3.2 shows that some of the amino acids, at certain locations, were never oxidized. For example, two of the six methionine and two of the five tyrosine (Met_{66}, Met_{72}, Tyr_{59}, and Tyr_{123}) were not found to be oxidized, under any condition.

Table 3.1. **Oxidative modifications of CYGB.** A list of the number of different amino acids in CYGB (# AA in sequence) and the number of oxidized amino acids of each type before (control) and after different treatment times. Eight amino acids (M, Y, D, F, H, W, N, and P) were chosen for analysis. Samples were measured with Ion trap LC-MS/MS and spectra were analyzed with Mascot and Sequest algorithms.

		Tris-buffer					
Amino Acid	# AA in sequence	Control	30s	1min	3min	5min	10min
Methionine (M)	6	2	3	4	4	3	4
Tyrosine (Y)	5	2	3	3	2	3	2
Tryptophan (W)	3		1	2	2	2	2
Phenylalanine (F)	8	1	1	1	1	1	1
Aspartic acid (D)	5			1	2	2	1
Asparagine (N)	5		3	3	1	2	
Proline (P)	13			1			3
Histidine (H)	6		1	1	1		1
TOTAL	51	5	12	16	13	13	14

Table 3.2 gives the total number of identified peptide fragments (so-called 'Peptide Spectrum Matches', PSM), together with the number of oxidized PSMs. Here, a clear treatment-time-dependent increase in oxidized peptides can be observed, illustrating the increasing oxidation potential with increasing treatment time. It is also noticeable (Tables 3.1, 3.2 & S3.2) that in the control samples some amino acids (Met, Tyr, and Phe) are also oxidized. This oxidation is likely due to the exposure of the sample to the surrounding atmosphere or may occur during electrospray.

Table 3.2. Oxidative modifications of CYGB. A list of the number of oxidized peptide fragments before and after plasma treatment. The number of Peptide Spectrum Matches (PSM) is the total number of identified peptide spectra matched for the protein. Samples were measured with Ion trap LC-MS/MS and spectra were analyzed with Mascot and Sequest algorithms.

	Sample	**# PSM in total**	**#Oxidation PSM**	**% Oxidation**
Tris-buffer	Control	90	15	17%
	30 sec	121	23	19%
	1 min	223	44	20%
	3 min	117	34	29%
	5 min	109	38	35%
	10 min	138	54	39%

3.4.4 MD and docking simulations

CYGB possesses two cysteine residues (Cys_{38} and Cys_{83}), which are known to be able to form disulfide bridges, either inter- or intramolecularly [25, 26]. As CYGB is proposed to be a monomer *in vivo* [52], and the formation of an intramolecular disulfide bridge can influence the activity of CYGB, we chose to investigate the effect of the formation of an intramolecular disulfide bridge in between the cysteine amino acids of monomeric CYGB (i.e., $CYGB_{S\text{-}S}$) with MD simulations. We have shown experimentally that an intermolecular disulfide bridge is present in the dimeric fraction. However, we can also speculate that the monomeric fraction may contain an intramolecular disulfide bridge. Figure 3.5 illustrates the last snapshots of the equilibrated $CYGB_{SH\ldots SH}$ (i.e., CYGB monomer without an initial disulfide bond) and $CYGB_{S\text{-}S}$ molecules (i.e., CYGB monomer with an intramolecular disulfide bond) depicted in yellow and green, respectively. The F-helix of CYGB is located at the proximal side of the heme group, while the E-helix is positioned at the distal side. The disulfide linkage in $CYGB_{S\text{-}S}$ clearly influences its conformation and hence, the positions of the E- and F-helices are shifted relative to $CYGB_{SH\ldots SH}$ (cf. the yellow and green dashed lines). In order to calculate the distances between the helices, residues Ala_{82} and Ala_{88} in the F helix and Ala_{107} and Ala_{112} in the E-helix were chosen. These amino acids are positioned at the end of the black dashed lines but they are not shown in the figure for the sake of clarity. The calculated distances between these amino acids located in the E- and F-helices are also given in Table S3.1, indicating the minor change in the modified $CYGB_{S\text{-}S}$. It is also obvious from Figure 3.5 that there is a negligible shift of the heme group in the modified $CYGB_{S\text{-}S}$ molecule compared to native $CYGB_{SH\ldots SH}$. Hence, the formation of the disulfide bridge between the cysteine residues does not alter the local orientation of the heme group and imidazole planes of the histidines (i.e., His_{81}, His_{113}) bound to the heme: the imidazole planes do not rotate versus each other. This was also reported in literature by experimental investigations [53].

Comparing the consecutive MD frames of both monomeric $CYGB_{SH\ldots SH}$ and $CYGB_{S\text{-}s}$, indicates that the His_{117} residue located nearby the heme group (see Figure 3.6) substantially changes its orientation in $CYGB_{S\text{-}S}$. Indeed, the calculated distance between the heme iron and one of the nitrogen atoms of His_{117} (located in the imidazole ring) almost doubled in $CYGB_{S\text{-}S}$ (see Table. S3.1), which is due to the conformational change caused by the intramolecular disulfide bond. Besides the change in orientation of His_{117}, it is noticeable that the propionate group of the heme

closest to His_{117} flips its position upon disulfide bond formation (facing downward in $CYGB_{S\text{-}S}$; see Figure 3.6 (b) and (d)). To get more insight into the structural changes caused by the intramolecular disulfide bond, the binding hot spots of both $CYGB_{SH\ldots SH}$ and $CYGB_{S\text{-}S}$ were investigated as described in the 'Experimental' section.

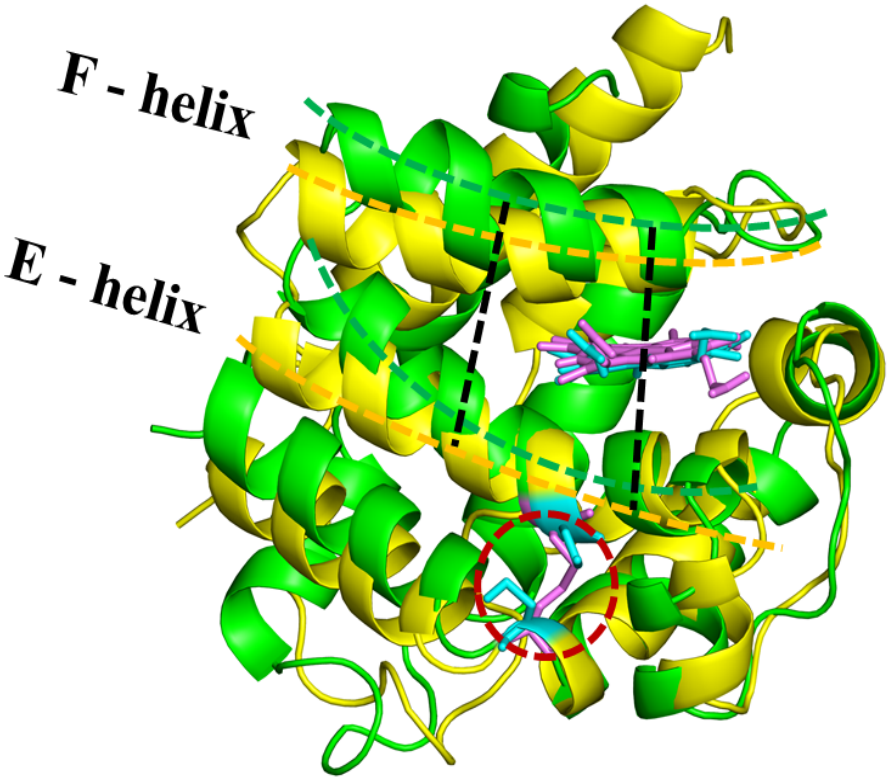

Figure 3.5. Aligned structures of $CYGB_{SH\ldots SH}$ (yellow) and $CYGB_{S\text{-}S}$ (green). The distances between Ala_{88}-Ala_{107} and Ala_{82}-Ala_{112} are depicted by black dashed lines. The yellow and green dashed lines are plotted to indicate shifted positions of the E-and F-helices. The heme group and cysteine residues of both $CYGB_{SH\ldots SH}$ and $CYGB_{S\text{-}S}$ are presented in licorice view in blue and pink, respectively. The disulfide (S-S) bridge is shown within the red dashed circle.

10 CYGB structures with 1 ns time interval were extracted using the last 10 ns trajectory of the equilibrated (so-called production) run. These structures were employed to examine the structural dependencies of the binding hot spots of CYGB. Here, only one of the results out of ten are presented, as the other nine results were very similar. Three different pockets (with lowest binding energies) were obtained in both $CYGB_{SH\ldots SH}$ and $CYGB_{S\text{-}S}$, which are depicted as meshed regions in Figure 3.6. The other two meshed regions are not shown as we are focusing on the catalytic site of CYGB (i.e., the heme pocket). As mentioned above, the formation of a disulfide bond between the cysteine residues leads to a change of the CYGB conformation, which results in a doubling of the distance between the highly localized His_{117} residue and the heme group in $CYGB_{S\text{-}S}$ (see Table S3.1 and cf. Figure 3.6 (a) and (c) or Figure 3.6 (b) and (d)). Accordingly, this results in the heme group to become more accessible to the probing molecules (see overlap

between heme group and meshed regions in Figure 3.6 (c) and (d)). In addition, the flipping of the position of the heme propionate upon disulfide formation further contributes to the accessibility of the heme pocket (Figure 3.6 (b) and (d)). Our binding hot spot analysis indeed shows that in the case of $CYGB_{S\text{-}S}$ the binding pocket is located around the heme group, whereas in $CYGB_{SH\ldots SH}$ it is found with limited access to the heme group, i.e., around the helices (cf. Figure 3.6 (a) and (c), or Figure 3.6 (b) and (d)). This again confirms that in $CYGB_{SH\ldots SH}$ the access to the heme group is more limited than in $CYGB_{S\text{-}S}$.

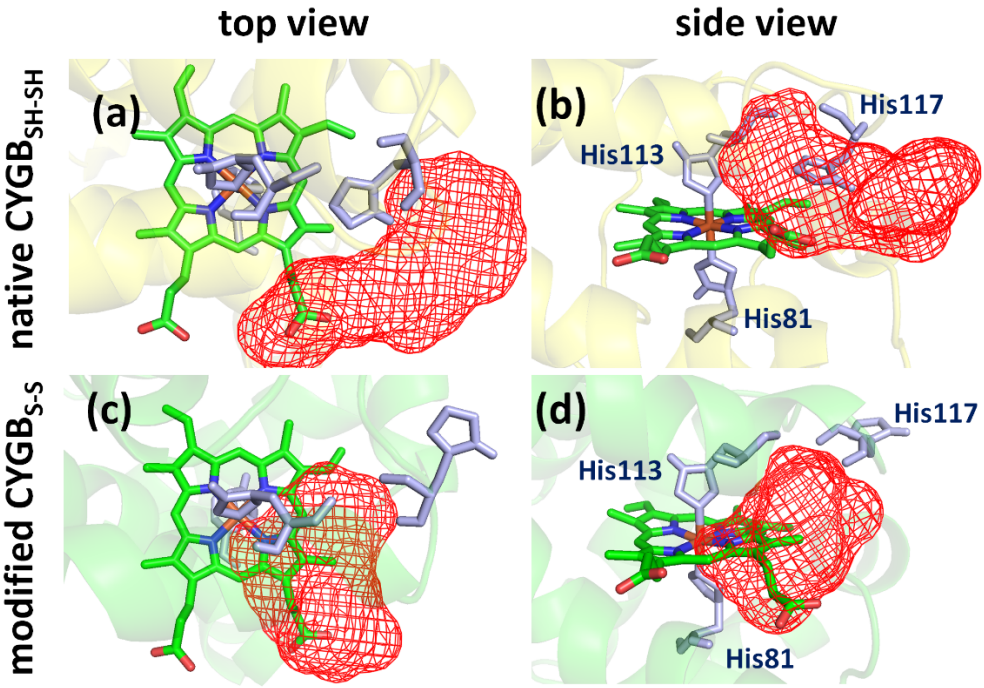

Figure 3.6. Binding hot spots. Binding hot spot of $CYGB_{SH\ldots SH}$ (a-b) and (c-d) $CYGB_{S\text{-}S}$ presented as red meshed regions. The helices in the structures are represented in pale colors, for the sake of clarity. The heme group and the histidine residues (81, 113, 117) are shown in green and light purple colors and licorice views, respectively. It is clear that in $CYGB_{SH\ldots SH}$ the access to the heme group is more limited than in $CYGB_{S\text{-}S}$.

3.5 DISCUSSION

In this study, it was shown that the treatment of recombinant CYGB with CAP resulted in chemical modifications of the protein. The spectral characteristics described for the untreated recombinant CYGB are identical to the ones described previously, showing that the protein is in the hexacoordinated ferric form [48]. Upon plasma treatment, spectral changes occur, which appear to be dependent on the duration of the treatment. These changes were more prominent when water was used as a solvent than in Tris-buffer. This suggests that in water, the effect of plasma, which is mainly through reactive species production, is greater than in Tris-buffer.

However, there is one main difference between the two solvents that were employed: deionized water has no buffering capacity, whereas Tris-buffer does. As plasma treatment induces many different reactive species (i.e. $^{\bullet}OH$, H_2O_2, $^{\bullet}NO$, O_2^{-}, ONOOH, $^{\bullet}NO_2$, NO_2^{-}, NO_3^{-}) [54], these species can contribute to the acidification of liquids. Indeed, pH measurements highlighted that plasma treatment induces a significant drop in the pH of deionized water, whereas no such effect could be observed with Tris-buffer (Figure S3). Thus, with water, there is a secondary effect of plasma treatment, through the acidification of the sample. Low pH can, depending on the protein, lead to protein denaturation and aggregation. In Figure 3.1A, after 5 min treatment, the Soret peak at 415 nm has almost completely disappeared, and a new peak has emerged at 387 nm, indicating free heme in the solution [49]. Additionally, the ultracentrifugation of the 5 min treated sample showed a clear brown precipitate, indicating the aggregation and denaturation of the sample upon plasma treatment. In Tris-buffer, on the other hand, no clear precipitate after ultracentrifugation of the 5 min treated sample could be observed, yet still, clear spectral changes were observed. Altogether, this confirms that in water, plasma treatment acidifies the solution, leading to structural changes in the protein, and the eventual (partial) denaturation of the protein sample. This has some implications for the further interpretation of the results from this study. As the main aim of this study was to investigate the effects of plasma-generated RONS on CYGB, the results obtained from treating CYGB with plasma in Tris-buffer are of higher relevance and will be discussed further in more detail (see supplementary Figures S3.6 & S3.7 for MS spectra in water).

From the absorption spectra of the samples treated in Tris-buffer, it can be concluded that plasma induces a decrease in intensity of the Soret band at 417 nm. This could indicate two things: the first option would be that the protein is continuously degrading more with longer treatment times, with the eventual, almost complete denaturation of the protein at 10 min treatment time. Although the appearance of a peak at 383 nm (after 10 min treatment) indicates the leaking of the heme out of the protein (and thus denaturing of the protein), CD and MS data (Figure 3.1E & 3.2) however shows that the largest fraction of the protein is still folded and contains the heme group. The slight unfolding we see in the CD-spectra may be explained by the MD data where it is shown that the formation of an intramolecular disulfide bridge in $CYGB_{S\text{-}S}$ induces a minor shift of the E-and F-helices, relative to $CYGB_{SH\ldots SH}$ (see Table S3.1 & Figure 3.5). Furthermore, measurement of the drift time of the monomeric (+9 peak) species showed that

there was no significant alteration of the collision cross section (CCS) of the treated protein (Figure S3.4), indicating that the three-dimensional shape, i.e., the tertiary structure, is not significantly affected upon plasma treatment, and thus excluding this option.

The second option would be that plasma treatment induces specific chemical modifications in the protein that lead to the observed spectral changes. The Soret band is emblematic for heme-containing proteins such as globins and various cytochromes, and arises primarily due to π-π* transitions in the heme group [55]. Binding of molecules to the heme structure or close environment could affect the (electronic) structure and lead to a decrease and/or shift of the Soret peak. From the MS data, it is clear that there is indeed covalent modification of CYGB upon plasma treatment. In Figure 3.2, it can be seen that there is a peak shift and broadening, indicating that plasma treatment induces numerous oxidations, either at specific amino acids, or at the heme group. Moreover, the MS spectra of the denatured sample (Figure 3.3) clearly show that, with 5 or 10 min treatment, there is binding of a molecule, most likely $^{\bullet}NO_2$, to the protein bound heme group. Binding of $^{\bullet}NO_2$ has already been shown to occur *in vitro* in other globins, i.e. myoglobin [56], hemoglobin [57], and more recently leghemoglobin [58], by exposing the proteins to excess $NaNO_2$. In these studies, it was shown that heme nitration originated from the substitution of a proton by $^{\bullet}NO_2$ from one of the vinyl groups. The subsequent formation of a nitrovinyl group results in a modified visible spectrum (a Soret band with lower intensity) and a heme group with *m/z* 661, similar to the results that were obtained in this study. Addition of a 1000-fold excess of $NaNO_2$ to CYGB (data not shown) led to the same modified spectra observed after plasma treatment of 5 and 10 min, confirming the nitration of the heme. Furthermore, resonance Raman (RR) experiments further confirmed the binding of $^{\bullet}NO_2$ to the heme (Figure S3.5). The high-frequency region of the RR spectra revealed the appearance of a strong band at ~1325 cm^{-1}, which is specific for a nitroaromatic group [59-61], again indicating the binding of $^{\bullet}NO_2$ to the vinyl groups of the heme. Plasma treatment of liquids does indeed yield the formation of $^{\bullet}NO_2$ [62-64]. Thus, upon plasma treatment for 5 min and longer, $^{\bullet}NO_2$, and most probably other related nitrogen species, are sufficiently produced in order to induce the binding of $^{\bullet}NO_2$ to the heme. Furthermore, the fact that $^{\bullet}NO_2$ can bind to the CYGB heme could implicate that it also performs a similar biological role, i.e., the involvement of CYGB in NO homeostasis. Previous reports already proposed a role for CYGB in NO regulation through its NO dioxygenase activity [26]. However, under conditions of oxygen deprivation, CYGB could act as a source of NO by

switching to a nitrite reductase function. The switching between these two functions is regulated through the oxidation of the two surface-exposed cysteine residues [65].

Besides nitration of the heme, plasma induces the oxidation of specific amino acid residues of CYGB. Here, the three most oxidized amino acids were methionine, tryptophan, and tyrosine. In 2014, Takai et al. reported that plasma was able to chemically modify amino acids through the oxidation of their side chains, with sulfur-containing (i.e. Met and Cys) and aromatic amino acids (i.e. Trp, Tyr, and Phe) preferentially modified. Furthermore, they found that the relative reactivity towards plasma treatment was Met > Cys > Trp > Phe > Tyr. This is not entirely in agreement with our findings (Table 3.1). However, in this study, a complete protein was treated with plasma, whereas in the study of Takai *et al.*, a mixture of amino acids was treated with plasma. Therefore, it is highly likely that in CYGB, due to its 3D-structure, some amino acids, e.g., Phe, are less solvent accessible compared to when individual amino acids are studied, leading to different results. This is further highlighted in Table S3.2, where it can be seen that certain locations of preferably oxidized amino acids, such as Met and Trp were never oxidized, indicating that the access of certain amino acids is hindered due to the tertiary structure of CYGB. This observed reactivity is in agreement with an increasing body of evidence from other experimental approaches which utilize ROS to cause oxidation of the solvent-accessible surface area of proteins, such as hydroxyl radical footprinting by synchrotron radiation [51] as well as fast photochemical oxidation of proteins [67] and other oxidative labelling techniques [68].

As for cysteine, during the digestion of the protein sample prior to measuring with LC-MS/MS, the cysteines are reduced by TCEP and carbamidomethylated. This modification is introduced on purpose to prevent disulfide bridges from forming again, and was therefore not selected for the analysis of oxidative modifications [69]. Yet, from the MS data (Figure 3.2 and 3.4) it is clear that cysteines do become oxidized (i.e., formation of disulfide bridge). CYGB possesses two cysteine residues (Cys_{38} and Cys_{83}), which are known to be able to form disulfide bridges, either inter- or intramolecularly [25, 26]. Such a formation of CYGB dimers upon plasma treatment can indeed be observed in native mass spectra (Figure 3.2), and even more clearly under denaturing conditions in Figure 3.3. Moreover, the addition of the reducing agent DTT to both the untreated and treated samples led to the disappearance of the dimeric peaks in the spectrum (Figure 3.4). However, there is still a significant portion of CYGB that stays in the monomeric form (Figure 3.2). It is highly likely that the monomers that are still present after treatment have formed

intramolecular disulfide bridges. Although the dimeric form of CYGB has been suggested to be less active than the monomeric form (see paragraph below), this observed dimerization after treatment could be an artefact of the experimental setup. *In vivo,* the concentration of CYGB lies somewhere between 0.1-5 µM, at which CYGB is proposed to be a monomer [70]. Higher concentrations, like the one that was used here, could bring CYGB molecules closer together and subsequently stimulate the formation of dimers. Nonetheless, from the abovementioned, we can conclude that plasma treatment leads to the formation of intermolecular disulfide bridges, thereby stabilizing the CYGB dimers, but presumably also intramolecular disulfide bridges in the remaining monomers. This would confirm the two cysteine residues as redox-active cysteines.

The state of the two surface-exposed cysteine residues, either free, intra- or intermolecularly linked, has been proposed to be critical in determining the biochemical and redox properties of CYGB [71]. A recent study demonstrated a clear difference in the ability of CYGB to bind lipids between the monomeric and dimeric form of the protein, with the monomer, containing an intramolecular disulfide bridge, more easily able to bind lipids [25]. This difference is suggested to occur because the presence of an intramolecular disulfide bond leads to the formation of a more open heme pocket structure, thereby facilitating access for external ligands, such as lipids, whereas an intermolecular disulfide bond does not alter the environment of the heme pocket [25]. This is perfectly in line with the MD and docking simulations performed in this study on monomeric CYGB. Here, it is seen that in $CYGB_{SH...SH}$, the access to the heme group is more limited than in $CYGB_{S\text{-}S}$. We further found that the His_{117} residue plays a vital role in either limiting or increasing the access to the heme group, thereby acting like a gate function for $CYGB_{SH...SH}$ and $CYGB_{S\text{-}S}$. Thus, our investigations confirm, and further show, that the formation of an intramolecular disulfide bond affects the CYGB structure, thereby opening the access to the heme group, through gate functioning of His_{117}, which in turn could lead to a higher binding affinity. In addition the redox state of the Cys_{38} and Cys_{83} residues appears to act as a 'molecular switch', activating the protein only under the correct conditions, i.e., oxidative stress. This would support CYGB's proposed cytoprotective role in oxidative stress conditions, which is probably linked to the lipid peroxidase activity of the protein [25, 49].

3.6 CONCLUSION

In conclusion, the treatment of CYGB with CAP leads to chemical modifications of the protein, yet the overall structure of the protein remains largely intact. Short treatment times were already sufficient to induce the oxidative modification of mainly sulfur-containing and aromatic amino acids. Longer treatment times also lead to the nitration of the heme, through the binding of $^{\bullet}NO_2$ to the vinyl groups, which proposes a role for CYGB in NO homeostasis. Upon plasma treatment the two cysteine residues of CYGB were oxidized, which stabilizes the dimeric CYGB, through intermolecular disulfide bridges, but most likely also monomeric CYGB containing an intramolecular disulfide bond. The simulations performed in this study also confirm the importance of the oxidation of Cys_{38} and Cys_{83} residues in regulating the ligand-binding properties, and thus also the activity, of CYGB. Furthermore, His_{177} was found to play a vital role in regulating the access to the heme group.

As mentioned in the introduction, the aim of this study was to elucidate the effects of plasma-generated (and in general) RONS on the structure and, to some extent, the function(s) of CYGB. Although some protein denaturing occurred, our results nonetheless confirm that (plasma-generated) RONS can indeed induce chemical modifications at specific sites, which lead to different conformations of CYGB. These different conformations are mediated by the oxidation status of two redox-active cysteines. As globins (more particularly hexacoordinated globins) are increasingly hypothesized to play a role in redox biology, findings here seem to further support the idea of CYGB functioning as a redox-active protein.

This study is of great interest because it provides further support and new insights that CYGB, on a molecular basis, has the potential to play a role in the cellular response against oxidative stress. However, further research on a cellular level is needed to validate these findings and to unravel the cellular pathways in which CYGB is involved. Such research should focus on elucidating the effects of (plasma-generated) RONS on cells and the role of CYGB in the response to these RONS.

3.7 REFERENCES

1. Kubinova, S., et al., *Non-thermal air plasma promotes the healing of acute skin wounds in rats.* Scientific Reports, 2017. **7**: p. 45183.
2. Zheng, J., *Inactivation of Staphylococcus aureus in water by pulsed spark discharge.* Scientific Reports, 2017. **7**(1): p. 10311.
3. Patange, A., et al., *Controlling Brochothrix thermosphacta as a spoilage risk using in-package atmospheric cold plasma.* Food Microbiol, 2017. **66**: p. 48-54.
4. Fridman, G., et al., *Blood Coagulation and Living Tissue Sterilization by Floating-Electrode Dielectric Barrier Discharge in Air.* Plasma Chemistry and Plasma Processing, 2006. **26**(4): p. 425-442.
5. Yan, D., J.H. Sherman, and M. Keidar, *Cold atmospheric plasma, a novel promising anti-cancer treatment modality.* Oncotarget, 2017. **8**(9): p. 15977-15995.
6. Chauvin, J., et al., *Analysis of reactive oxygen and nitrogen species generated in three liquid media by low temperature helium plasma jet.* Scientific Reports, 2017. **7**(1): p. 4562.
7. Vandamme, M., et al., *ROS implication in a new antitumor strategy based on non-thermal plasma.* Int J Cancer, 2012. **130**(9): p. 2185-94.
8. Graves, D.B., *Reactive Species from Cold Atmospheric Plasma: Implications for Cancer Therapy.* Plasma Processes and Polymers, 2014. **11**(12): p. 1120-1127.
9. Kalghatgi, S., et al., *Effects of non-thermal plasma on mammalian cells.* PLoS One, 2011. **6**(1): p. e16270.
10. Vermeylen, S., et al., *Cold atmospheric plasma treatment of melanoma and glioblastoma cancer cells.* Plasma Processes and Polymers, 2016. **13**(12): p. 1195-1205.
11. Hattori, N., et al., *Effectiveness of plasma treatment on pancreatic cancer cells.* International Journal of Oncology, 2015. **47**(5): p. 1655-1662.
12. Kim, C.-H., et al., *Effects of atmospheric nonthermal plasma on invasion of colorectal cancer cells.* Applied Physics Letters, 2010. **96**(24): p. 243701.
13. Kim, S.J., et al., *Induction of apoptosis in human breast cancer cells by a pulsed atmospheric pressure plasma jet.* Applied Physics Letters, 2010. **97**(2): p. 023702.
14. Lee, S., et al., *Cold atmospheric plasma restores tamoxifen sensitivity in resistant MCF-7 breast cancer cell.* Free Radic Biol Med, 2017. **110**: p. 280-290.
15. Canal, C., et al., *Plasma-induced selectivity in bone cancer cells death.* Free Radic Biol Med, 2017. **110**: p. 72-80.
16. Julák, J., et al., *Inactivation of Prions Using Electrical DC Discharges at Atmospheric Pressure and Ambient Temperature.* Plasma Processes and Polymers, 2011. **8**(4): p. 316-323.
17. Yasuda, H., et al., *States of Biological Components in Bacteria and Bacteriophages during Inactivation by Atmospheric Dielectric Barrier Discharges.* Plasma Processes and Polymers, 2008. **5**(6): p. 615-621.
18. Takai, E., et al., *Protein Inactivation by Low-temperature Atmospheric Pressure Plasma in Aqueous Solution.* Plasma Processes and Polymers, 2012. **9**(1): p. 77-82.
19. Attri, P., et al., *Influence of reactive species on the modification of biomolecules generated from the soft plasma.* Scientific Reports, 2015. **5**: p. 8221.
20. Barford, D., *The role of cysteine residues as redox-sensitive regulatory switches.* Current Opinion in Structural Biology, 2004. **14**(6): p. 679-686.
21. Gardner, A.M., M.R. Cook, and P.R. Gardner, *Nitric-oxide Dioxygenase Function of Human Cytoglobin with Cellular Reductants and in Rat Hepatocytes.* The Journal of Biological Chemistry, 2010. **285**(31): p. 23850-23857.
22. Liu, X., et al., *Characterization of the function of cytoglobin as an oxygen-dependent regulator of nitric oxide concentration.* Biochemistry, 2012. **51**(25): p. 5072-82.
23. Fordel, E., et al., *Neuroglobin and cytoglobin expression in mice. Evidence for a correlation with reactive oxygen species scavenging.* Febs j, 2007. **274**(5): p. 1312-7.

24. Shivapurkar, N., et al., *Cytoglobin, the newest member of the globin family, functions as a tumor suppressor gene.* Cancer Res, 2008. **68**(18): p. 7448-56.
25. Beckerson, P., et al., *Cytoglobin ligand binding regulated by changing haem-co-ordination in response to intramolecular disulfide bond formation and lipid interaction.* Biochem J, 2015. **465**(1): p. 127-37.
26. Tsujino, H., et al., *Disulfide bonds regulate binding of exogenous ligand to human cytoglobin.* J Inorg Biochem, 2014. **135**: p. 20-7.
27. Zhou, D., et al., *Oxygen binding and nitric oxide dioxygenase activity of cytoglobin are altered to different extents by cysteine modification.* FEBS Open Bio, 2017. **7**(6): p. 845-853.
28. Latina, A., et al., *DeltaNp63 targets cytoglobin to inhibit oxidative stress-induced apoptosis in keratinocytes and lung cancer.* Oncogene, 2016. **35**(12): p. 1493-503.
29. Zhang, S., et al., *Cytoglobin Promotes Cardiac Progenitor Cell Survival against Oxidative Stress via the Upregulation of the NFkappaB/iNOS Signal Pathway and Nitric Oxide Production.* Sci Rep, 2017. **7**(1): p. 10754.
30. Ou, L., et al., *Recombinant Human Cytoglobin Prevents Atherosclerosis by Regulating Lipid Metabolism and Oxidative Stress.* J Cardiovasc Pharmacol Ther, 2018. **23**(2): p. 162-173.
31. Dewilde, S., et al., *Expression, purification, and crystallization of neuro- and cytoglobin.* Methods Enzymol, 2008. **436**: p. 341-57.
32. Van Der Spoel, D., et al., *GROMACS: fast, flexible, and free.* Journal of computational chemistry, 2005. **26**(16): p. 1701-1718.
33. Schuler, L.D., X. Daura, and W.F. Van Gunsteren, *An improved GROMOS96 force field for aliphatic hydrocarbons in the condensed phase.* Journal of Computational Chemistry, 2001. **22**(11): p. 1205-1218.
34. Sugimoto, H., et al., *Structural basis of human cytoglobin for ligand binding.* Journal of molecular biology, 2004. **339**(4): p. 873-885.
35. Berendsen, H.J., et al., *Interaction models for water in relation to protein hydration*, in *Intermolecular forces*. 1981, Springer. p. 331-342.
36. Hanwell, M.D., et al., *Avogadro: an advanced semantic chemical editor, visualization, and analysis platform.* Journal of cheminformatics, 2012. **4**(1): p. 17.
37. Katti, S.K., D.M. LeMaster, and H. Eklund, *Crystal structure of thioredoxin from Escherichia coli at 1.68 Å resolution.* Journal of molecular biology, 1990. **212**(1): p. 167-184.
38. Wiita, A.P., et al., *Force-dependent chemical kinetics of disulfide bond reduction observed with single-molecule techniques.* Proceedings of the National Academy of Sciences, 2006. **103**(19): p. 7222-7227.
39. Shanno, D.F., *Conditioning of quasi-Newton methods for function minimization.* Mathematics of computation, 1970. **24**(111): p. 647-656.
40. Bussi, G., D. Donadio, and M. Parrinello, *Canonical sampling through velocity rescaling.* The Journal of chemical physics, 2007. **126**(1): p. 014101.
41. Parrinello, M. and A. Rahman, *Polymorphic transitions in single crystals: A new molecular dynamics method.* Journal of Applied physics, 1981. **52**(12): p. 7182-7190.
42. Essmann, U., et al., *A smooth particle mesh Ewald method.* The Journal of chemical physics, 1995. **103**(19): p. 8577-8593.
43. Kozakov, D., et al., *The FTMap family of web servers for determining and characterizing ligand-binding hot spots of proteins.* Nature protocols, 2015. **10**(5): p. 733-755.
44. Brooks, B.R., et al., *CHARMM: a program for macromolecular energy, minimization, and dynamics calculations.* Journal of computational chemistry, 1983. **4**(2): p. 187-217.
45. Schaefer, M. and M. Karplus, *A comprehensive analytical treatment of continuum electrostatics.* The Journal of Physical Chemistry, 1996. **100**(5): p. 1578-1599.
46. Humphrey, W., A. Dalke, and K. Schulten, *VMD: visual molecular dynamics.* Journal of molecular graphics, 1996. **14**(1): p. 33-38.
47. DeLano, W.L., *The PyMOL molecular graphics system.* http://pymol. org, 2002.

48. Sawai, H., et al., *Characterization of the heme environmental structure of cytoglobin, a fourth globin in humans.* Biochemistry, 2003. **42**(17): p. 5133-42.
49. Reeder, B.J., D.A. Svistunenko, and M.T. Wilson, *Lipid binding to cytoglobin leads to a change in haem co-ordination: a role for cytoglobin in lipid signalling of oxidative stress.* Biochem J, 2011. **434**(3): p. 483-92.
50. Kelly, S.M., T.J. Jess, and N.C. Price, *How to study proteins by circular dichroism.* Biochim Biophys Acta, 2005. **1751**(2): p. 119-39.
51. Xu, G. and M.R. Chance, *Hydroxyl Radical-Mediated Modification of Proteins as Probes for Structural Proteomics.* Chemical Reviews, 2007. **107**(8): p. 3514-3543.
52. Lechauve, C., et al., *Cytoglobin conformations and disulfide bond formation.* FEBS Journal, 2010. **277**(12): p. 2696-2704.
53. Vinck, E., et al., *Structural change of the heme pocket due to disulfide bridge formation is significantly larger for neuroglobin than for cytoglobin.* Journal of the American Chemical Society, 2004. **126**(14): p. 4516-4517.
54. Lu, X., et al., *Reactive species in non-equilibrium atmospheric-pressure plasmas: Generation, transport, and biological effects.* Physics Reports, 2016. **630**(Supplement C): p. 1-84.
55. Dayer, M.R., A.A. Moosavi-Movahedi, and M.S. Dayer, *Band assignment in hemoglobin porphyrin ring spectrum: using four-orbital model of Gouterman.* Protein Pept Lett, 2010. **17**(4): p. 473-9.
56. Bondoc, L.L. and R. Timkovich, *Structural characterization of nitrimyoglobin.* J Biol Chem, 1989. **264**(11): p. 6134-45.
57. Otsuka, M., et al., *Covalent modifications of hemoglobin by nitrite anion: formation kinetics and properties of nitrihemoglobin.* Chem Res Toxicol, 2010. **23**(11): p. 1786-95.
58. Navascués, J., et al., *Leghemoglobin green derivatives with nitrated hemes evidence production of highly reactive nitrogen species during aging of legume nodules.* Proceedings of the National Academy of Sciences, 2012. **109**(7): p. 2660-2665.
59. Lin-Vien, D., et al., *CHAPTER 11 - The Nitro Group*, in *The Handbook of Infrared and Raman Characteristic Frequencies of Organic Molecules*. 1991, Academic Press: San Diego. p. 179-189.
60. Lambrou, A. and E. Pinakoulaki, *Resonance Raman detection of the myoglobin nitrito heme Fe-O-N=O/2-nitrovinyl species: implications for helix E-helix F interactions.* Phys Chem Chem Phys, 2015. **17**(5): p. 3841-9.
61. Ioannou, A., et al., *Nitrite coordination in myoglobin.* Journal of Inorganic Biochemistry, 2017. **166**: p. 49-54.
62. Van Boxem, W., et al., *Anti-cancer capacity of plasma-treated PBS: effect of chemical composition on cancer cell cytotoxicity.* Scientific Reports, 2017. **7**(1): p. 16478.
63. Girard, P.M., et al., *Synergistic Effect of H2O2 and NO2 in Cell Death Induced by Cold Atmospheric He Plasma.* Sci Rep, 2016. **6**: p. 29098.
64. Kurake, N., et al., *Cell survival of glioblastoma grown in medium containing hydrogen peroxide and/or nitrite, or in plasma-activated medium.* Arch Biochem Biophys, 2016. **605**: p. 102-8.
65. Reeder, B.J. and J. Ukeri, *Strong modulation of nitrite reductase activity of cytoglobin by disulfide bond oxidation: Implications for nitric oxide homeostasis.* Nitric Oxide, 2018. **72**(Supplement C): p. 16-23.
66. Takai, E., et al., *Chemical modification of amino acids by atmospheric-pressure cold plasma in aqueous solution.* Journal of Physics D: Applied Physics, 2014. **47**(28): p. 285403.
67. Li, K.S., L. Shi, and M.L. Gross, *Mass Spectrometry-Based Fast Photochemical Oxidation of Proteins (FPOP) for Higher Order Structure Characterization.* Accounts of Chemical Research, 2018. **51**(3): p. 736-744.
68. Roeser, J., et al., *Oxidative protein labeling in mass-spectrometry-based proteomics.* Anal Bioanal Chem, 2010. **397**(8): p. 3441-55.
69. Lippincott, J. and I. Apostol, *Carbamylation of cysteine: a potential artifact in peptide mapping of hemoglobins in the presence of urea.* Anal Biochem, 1999. **267**(1): p. 57-64.

70. Yoshizato, K., et al., *Discovery of cytoglobin and its roles in physiology and pathology of hepatic stellate cells.* Proceedings of the Japan Academy. Series B, Physical and Biological Sciences, 2016. **92**(3): p. 77-97.
71. Tsujino, H., et al., *Disulfide bonds regulate binding of exogenous ligand to human cytoglobin.* Journal of Inorganic Biochemistry, 2014. **135**(Supplement C): p. 20-27.

3.8 SUPPLEMENTARY

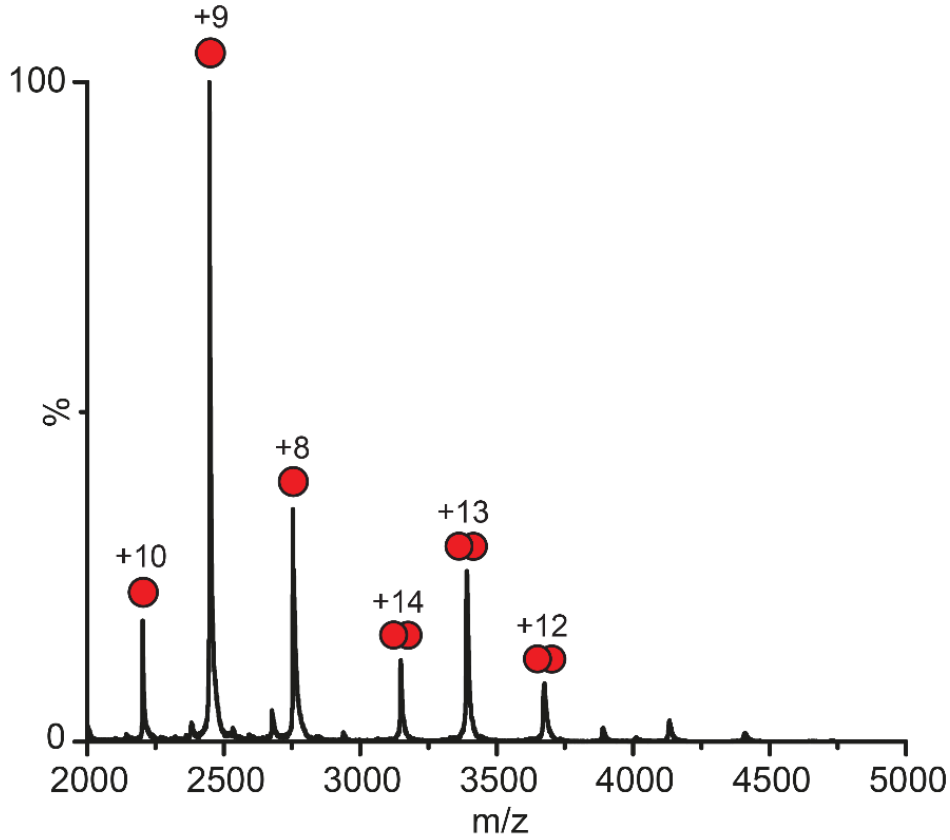

Figure S3.1. Native MS spectrum of untreated CYGB at a concentration of 10 µM dissolved in 100 mM ammonium acetate. Monomeric (+10, +9, and +8 peaks), and dimeric species (+14, +13, and +12 peaks) can be observed.

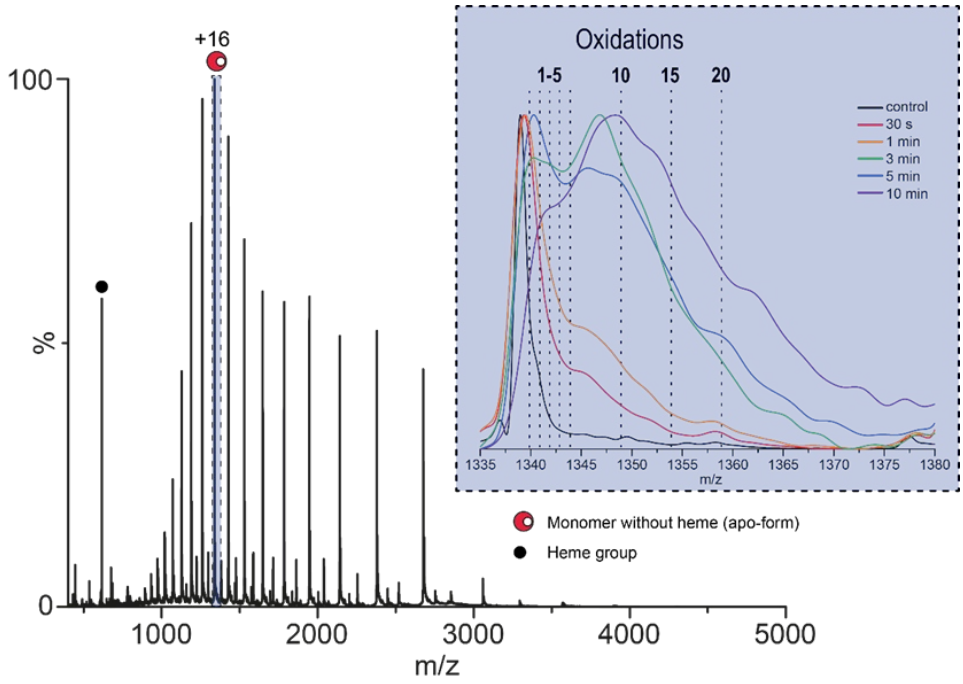

Figure S3.2. Mass spectrum of the untreated sample under denaturing conditions. The inset shows an overlay of the +16 apo peak of the untreated and plasma treated samples, with the corresponding mass shift.

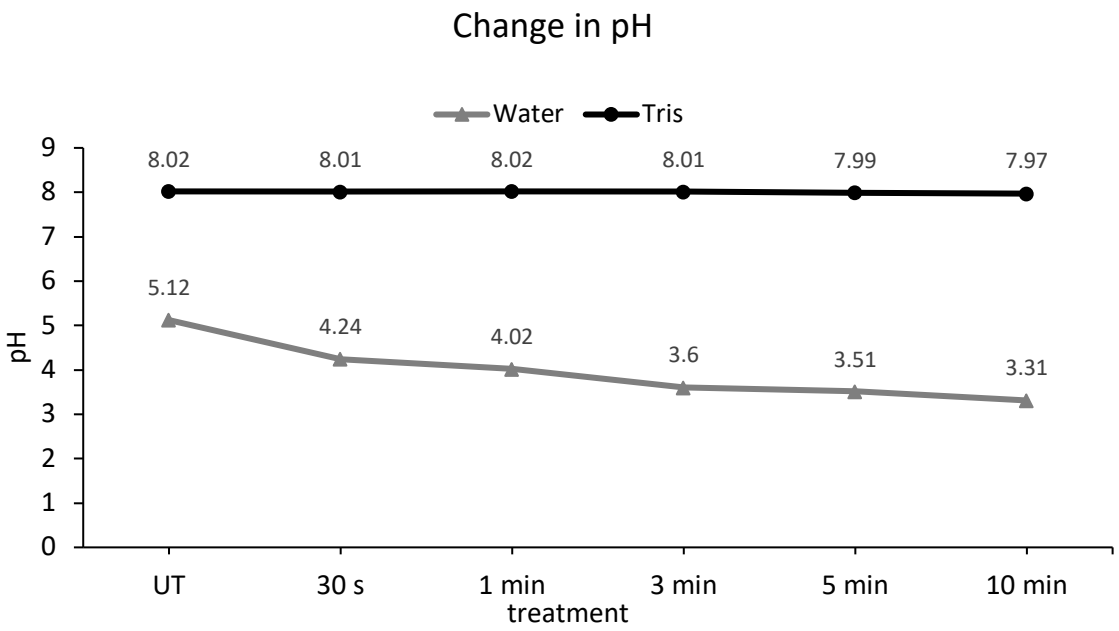

Figure S3.3. Change in solvent pH after different CAP treatment times (UT: untreated). Water becomes increasingly acidic with longer treatment times, whereas the Tris-solution remains at constant pH, illustrating the buffering capacity of the solvent.

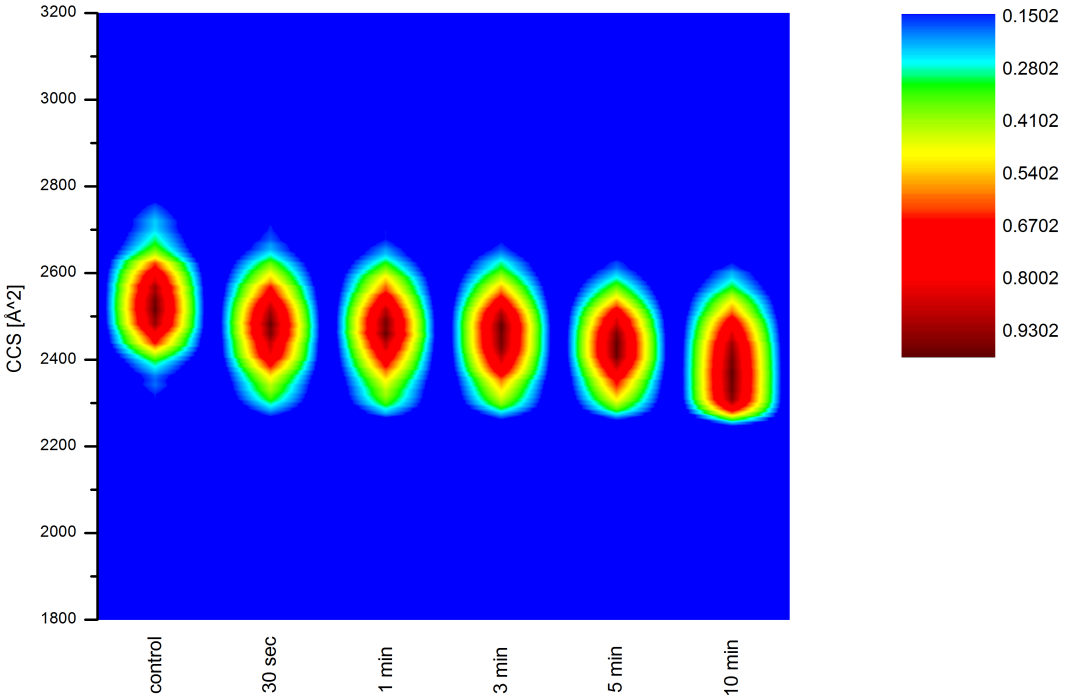

Figure S3.4. Collision cross section (CCS) of CYGB in Tris buffer. The CCS value does not significantly change upon plasma treatment, showing only minor compaction, meaning that the protein remains folded after plasma treatment.

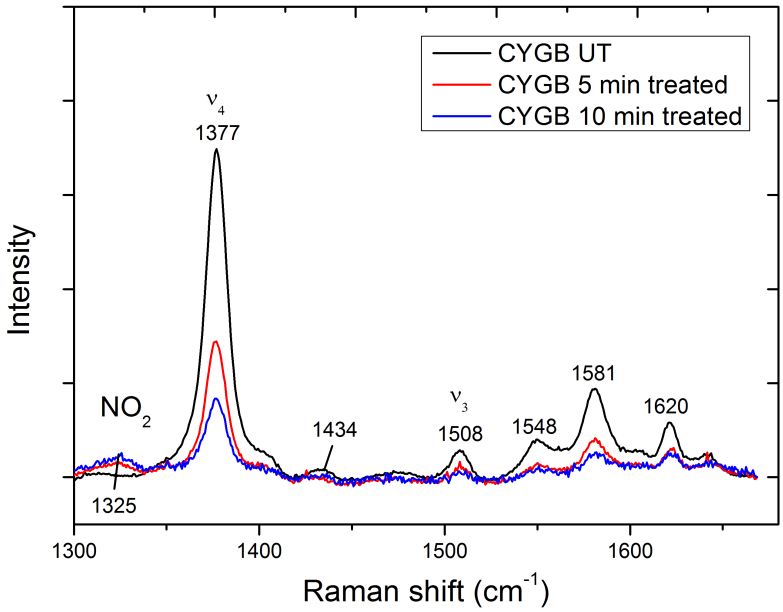

Figure S3.5. High frequency region of RR spectra of CYGB. The non-normalized high frequency region RR spectra, excited at 413.1 nm, of the untreated CYGB sample (in Tris-buffer) compared to the RR spectra of the 5 min (red) and 10 min (blue) treated sample. The major modification in the high-frequency spectra of treated CYGB is the appearance of a strong band at ± 1,325 cm^{-1}. This band corresponds to a symmetric stretching of NO_2 bound to the heme. The marker lines ν_4 and ν_3 were located at 1377 and 1508 cm^{-1}, respectively, characteristic of hemoproteins in the hexacoordinate and low-spin iron. The lowering of the peak at 1377 cm^{-1} is in accordance with the decrease of the Soret band.

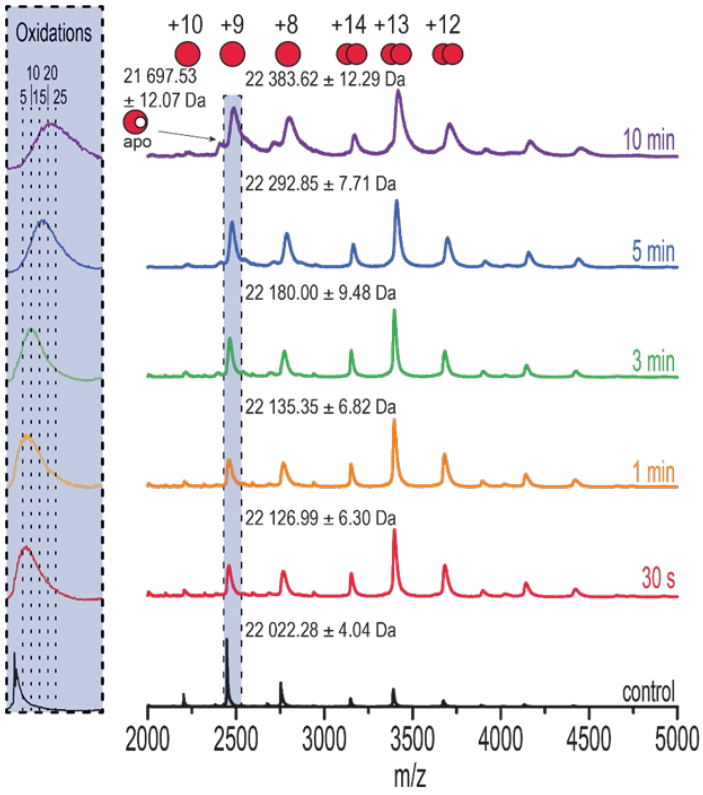

Figure S3.6. Native MS spectra of 10 µM CYGB in 100 mM ammonium acetate after different time points of plasma treatment. Plasma treatment was performed on 20 µM CYGB in water. Monomeric (+10, +9, +8) and dimeric (+14, +13, +12) species are identified. The monomeric +9 species are highlighted in blue. Inset: zoomed in spectra of the monomeric +9 species, highlighting mass shifts and peak broadening caused by plasma-induced oxidations.

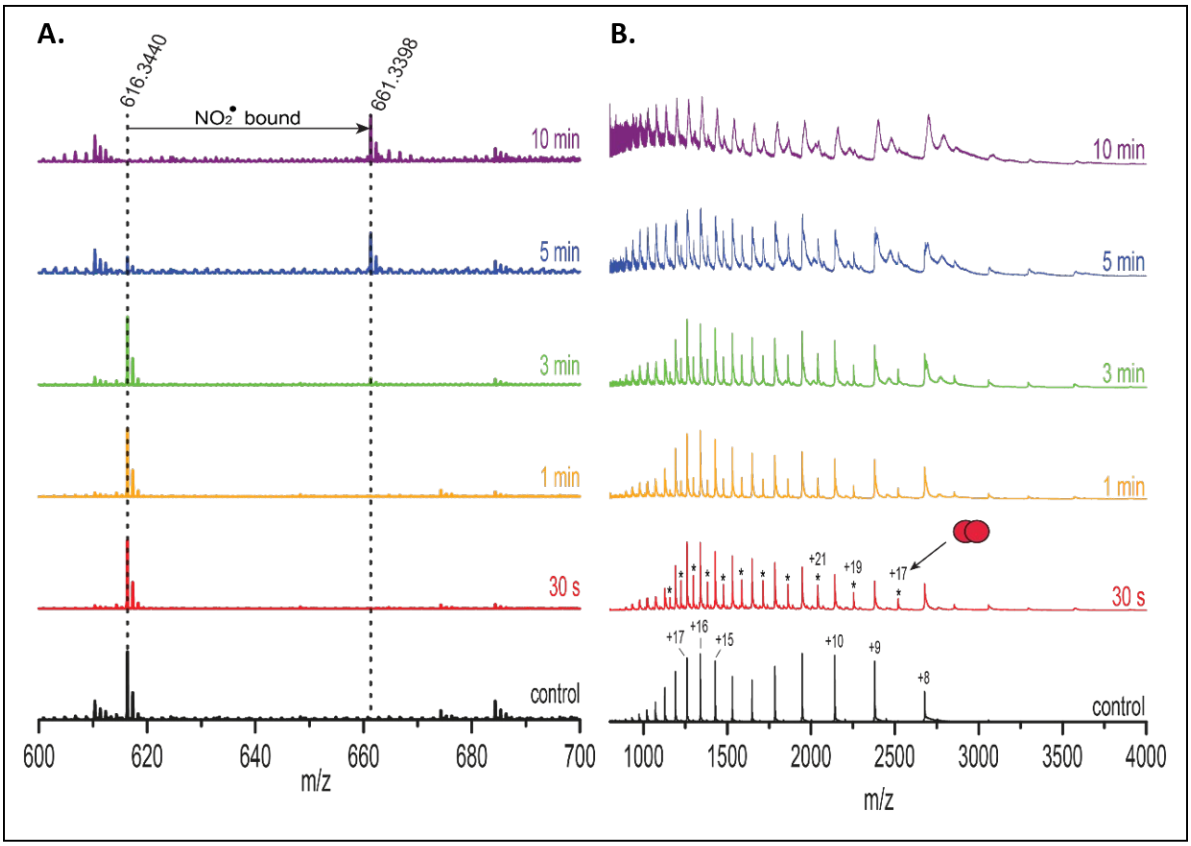

Figure S3.7. MS measurements of CYGB under denaturing conditions. Spectra of 10 µM CYGB (diluted 1:1 in acetonitrile containing 1% formic acid) after different time points of plasma treatment. Plasma treatment was performed on 20 µM CYGB in water. (A.): Zoomed in m/z region from 600 to 700. The peak at 616.3440 m/z represents the heme group. 5 min or 10 min of treatment induces the binding of a molecule, i.e. NO_2 to the heme group (661.3398 m/z). *(*B.): Full spectrum ranging from 800-4000 m/z. The appearance of smaller peaks (asterisks) in between the larger peaks highlights the presence of dimeric species in the sample.

Table S3.1. Distance between amino acids located in the F and E helices, as well as between the N atom of His_{117} and the Fe atom of the heme group of CYGB (cf. Figure 5).

amino acids	**$CYGB_{SH...SH}$ (Å)**	**$CYGB_{S-S}$ (Å)**
Ala88-Ala107	9.12 ± 0.03	9.88 ± 0.03
Ala82-Ala112	14.94 ± 0.04	15.62 ± 0.04
$His117_{NE2}$-$Heme_{Fe}$	6.63 ± 1.30	13.48 ± 0.09

Table S3.2. Full protein sequence of human CYGB consisting of 190 amino acids. Oxidized amino acids are depicted in red. Methionine (M), Tryptophan (W), Tyrosine (Y), Phenylalanine (F), Histidine (H), Proline (P), Aspartic acid (D), and Asparagine (N) were chosen for analysis. Data was analyzed with Sequest and Mascot search engines.

	Sample	10	20	30	40	50	60	70	80	90	
Tris-buffer	Control	MEKVPGEMEI	ERRERSEELS	EAERKAVQAM	WARLYANCED	VGVAILVRFF	VNFPSAKQYF	SQFKHMEDPL	EMERSPQLRK	HACRVMGALN	
		TVVENLHDPD	KVSSVLALVG	KAHALKHKVE	PVYFKILSGV	ILEVVAEEFA	SDFPPETQRA	WAKLRGLIYS	HVTAAYKEVG	WVQQVPNATT	PPATLPSSGP (190)
	30s	MEKVPGEMEI	ERRERSEELS	EAERKAVQAM	WARLYANCED	VGVAILVRFF	VNFPSAKQYF	SQFKHMEDPL	EMERSPQLRK	HACRVMGALN	
		TVVENLHDPD	KVSSVLALVG	KAHALKHKVE	PVYFKILSGV	ILEVVAEEFA	SDFPPETQRA	WAKLRGLIYS	HVTAAYKEVG	WVQQVPNATT	PPATLPSSGP (190)
	1min	MEKVPGEMEI	ERRERSEELS	EAERKAVQAM	WARLYANCED	VGVAILVRFF	VNFPSAKQYF	SQFKHMEDPL	EMERSPQLRK	HACRVMGALN	
		TVVENLHDPD	KVSSVLALVG	KAHALKHKVE	PVYFKILSGV	ILEVVAEEFA	SDFPPETQRA	WAKLRGLIYS	HVTAAYKEVG	WVQQVPNATT	PPATLPSSGP (190)
	3min	MEKVPGEMEI	ERRERSEELS	EAERKAVQAM	WARLYANCED	VGVAILVRFF	VNFPSAKQYF	SQFKHMEDPL	EMERSPQLRK	HACRVMGALN	
		TVVENLHDPD	KVSSVLALVG	KAHALKHKVE	PVYFKILSGV	ILEVVAEEFA	SDFPPETQRA	WAKLRGLIYS	HVTAAYKEVG	WVQQVPNATT	PPATLPSSGP (190)
	5min	MEKVPGEMEI	ERRERSEELS	EAERKAVQAM	WARLYANCED	VGVAILVRFF	VNFPSAKQYF	SQFKHMEDPL	EMERSPQLRK	HACRVMGALN	
		TVVENLHDPD	KVSSVLALVG	KAHALKHKVE	PVYFKILSGV	ILEVVAEEFA	SDFPPETQRA	WAKLRGLIYS	HVTAAYKEVG	WVQQVPNATT	PPATLPSSGP (190)
	10min	MEKVPGEMEI	ERRERSEELS	EAERKAVQAM	WARLYANCED	VGVAILVRFF	VNFPSAKQYF	SQFKHMEDPL	EMERSPQLRK	HACRVMGALN	
		TVVENLHDPD	KVSSVLALVG	KAHALKHKVE	PVYFKILSGV	ILEVVAEEFA	SDFPPETQRA	WAKLRGLIYS	HVTAAYKEVG	WVQQVPNATT	PPATLPSSGP (190)
	Sample	10	20	30	40	50	60	70	80	90	
Water	Control	MEKVPGEMEI	ERRERSEELS	EAERKAVQAM	WARLYANCED	VGVAILVRFF	VNFPSAKQYF	SQFKHMEDPL	EMERSPQLRK	HACRVMGALN	
		TVVENLHDPD	KVSSVLALVG	KAHALKHKVE	PVYFKILSGV	ILEVVAEEFA	SDFPPETQRA	WAKLRGLIYS	HVTAAYKEVG	WVQQVPNATT	PPATLPSSGP (190)
	30s	MEKVPGEMEI	ERRERSEELS	EAERKAVQAM	WARLYANCED	VGVAILVRFF	VNFPSAKQYF	SQFKHMEDPL	EMERSPQLRK	HACRVMGALN	
		TVVENLHDPD	KVSSVLALVG	KAHALKHKVE	PVYFKILSGV	ILEVVAEEFA	SDFPPETQRA	WAKLRGLIYS	HVTAAYKEVG	WVQQVPNATT	PPATLPSSGP (190)
	1min	MEKVPGEMEI	ERRERSEELS	EAERKAVQAM	WARLYANCED	VGVAILVRFF	VNFPSAKQYF	SQFKHMEDPL	EMERSPQLRK	HACRVMGALN	
		TVVENLHDPD	KVSSVLALVG	KAHALKHKVE	PVYFKILSGV	ILEVVAEEFA	SDFPPETQRA	WAKLRGLIYS	HVTAAYKEVG	WVQQVPNATT	PPATLPSSGP (190)
	3min	MEKVPGEMEI	ERRERSEELS	EAERKAVQAM	WARLYANCED	VGVAILVRFF	VNFPSAKQYF	SQFKHMEDPL	EMERSPQLRK	HACRVMGALN	
		TVVENLHDPD	KVSSVLALVG	KAHALKHKVE	PVYFKILSGV	ILEVVAEEFA	SDFPPETQRA	WAKLRGLIYS	HVTAAYKEVG	WVQQVPNATT	PPATLPSSGP (190)
	5min	MEKVPGEMEI	ERRERSEELS	EAERKAVQAM	WARLYANCED	VGVAILVRFF	VNFPSAKQYF	SQFKHMEDPL	EMERSPQLRK	HACRVMGALN	
		TVVENLHDPD	KVSSVLALVG	KAHALKHKVE	PVYFKILSGV	ILEVVAEEFA	SDFPPETQRA	WAKLRGLIYS	HVTAAYKEVG	WVQQVPNATT	PPATLPSSGP (190)
	10min	MEKVPGEMEI	ERRERSEELS	EAERKAVQAM	WARLYANCED	VGVAILVRFF	VNFPSAKQYF	SQFKHMEDPL	EMERSPQLRK	HACRVMGALN	
		TVVENLHDPD	KVSSVLALVG	KAHALKHKVE	PVYFKILSGV	ILEVVAEEFA	SDFPPETQRA	WAKLRGLIYS	HVTAAYKEVG	WVQQVPNATT	PPATLPSSGP (190)

CHAPTER IV

A RELIABLE SET OF REFERENCE GENES TO NORMALIZE OXYGEN-DEPENDENT CYTOGLOBIN GENE EXPRESSION LEVELS IN MELANOMA

Published as:

De Backer, J*., Maric, D.*, Bosman, M. *et al. A reliable set of reference genes to normalize oxygen-dependent cytoglobin gene expression levels in melanoma*. *Sci Rep***11,** 10879 (2021). https://doi.org/10.1038/s41598-021-90284-6

*Equal authorship

4.1 ABSTRACT

Cytoglobin (CYGB) is a ubiquitously expressed protein with a protective role against oxidative stress, fibrosis, and tumor growth, shown to be transcriptionally regulated under hypoxic conditions. Hypoxia-inducible *CYGB* expression is observed in several cancer cell lines and particularly in various melanoma-derived cell lines. However, reliable detection of hypoxia-inducible mRNA levels by qPCR depends on the critical choice of suitable reference genes for accurate normalization. Limited evidence exists to support selection of the commonly used reference genes in hypoxic models of melanoma. This study aimed to select the optimal reference genes to study *CYGB* expression levels in melanoma cell lines exposed to hypoxic conditions (0.2% O_2) and to the HIF prolyl hydroxylase inhibitor roxadustat (FG-4592). The expression levels of candidate genes were assessed by qPCR and the stability of genes was evaluated using the geNorm and NormFinder algorithms. Our results display that *B2M* and *YWHAZ* represent the most optimal reference genes to reliably quantify hypoxia-inducible *CYGB* expression in melanoma cell lines. We further validate hypoxia-inducible CYGB expression on protein level and by using *CYGB* promoter-driven luciferase reporter assays in melanoma cell lines.

4.2 INTRODUCTION

Over the last few decades, gene expression analysis has become increasingly more important, as the understanding of gene expression patterns can reveal complex regulatory networks involved in disease initiation or progression [1]. Nowadays, the method of choice for individual gene expression analysis is real-time quantitative PCR (qPCR). qPCR is characterized by a high sensitivity and sequence-specificity, and a broad dynamic range [2]. An inherent drawback associated with the sensitivity is the need for an accurate way of normalization and standardization. Variations in the amount of starting material, RNA extraction, and enzyme efficiencies are inherently associated with the multistep qPCR workflow [3]. Consequently, obtaining reliable gene expression patterns require an accurate normalization strategy.

Currently, the method of choice for (data) normalization is through the use of internal reference genes and by the analysis of relative gene expression using the $2^{-\Delta Ct}$ method [4, 5]. The most commonly used reference genes are constitutive genes that regulate basic ubiquitous cellular functions [6]. It has been shown however that the expression of these genes is not stable under various experimental conditions [6-8]. Hypoxic conditions in particular have recently been shown to pose a hurdle for gene expression studies. For example, glyceraldehyde-3-phosphate dehydrogenase (*GAPDH*), β-actin (*ACTB*), and β-tubulin (*TUBB*), three of the most commonly used reference genes, were shown to be transcriptionally modulated upon hypoxia in specific cell types [1, 7, 9, 10], possibly leading to misinterpretation of changes in target gene expression. Therefore, gene expression should always be normalized with an appropriate, i.e. neither influenced by experimental conditions nor differently regulated in the samples being studied, reference gene [11]. As identifying such a gene might be rather difficult, normalization by geometric averaging of multiple internal reference genes is currently considered the most appropriate and universally applicable approach in the evaluation of qPCR-based gene expression [3, 12, 13]. The statistical software algorithm geNorm represents a well-established tool for the identification of the most stably expressed genes from a set of candidate control genes. The method also allows the determination of the optimal number of genes required for reliable normalization of qPCR generated gene expression data.

Hypoxia is a key microenvironmental factor during the initiation, progression, and propagation of cancer [14, 15]. In solid tumors, the intensive proliferation of cancer cells combined with the

structural abnormalities of the tumor vasculature results in the delivery of suboptimal concentrations of oxygen and other nutrients to cancer cells, creating a hypoxic milieu [14, 16]. As a survival strategy, major adaptive pathways are activated in hypoxic cancer cells and cells undergo reprogramming of the transcriptional activity towards more aggressive and therapy resistant phenotypes [17]. In melanoma hypoxia also plays a crucial role and contributes to radiotherapy resistance [16]. Melanoma arises from pigment-producing melanocytes located in the basal layer of the epidermis of the skin. The skin is a mildly hypoxic environment and oxygen levels are sufficiently low enough to allow stabilization of the hypoxia-inducible factor α (HIF-α) subunit, thereby increasing the expression of established HIF target genes such as carbonic anhydrase IX (*CAIX*), glucose transporter-1 (*GLUT1*) and prolyl hydroxylase domain-2 (*PHD2*) [18-20]. Furthermore, a hypoxic microenvironment contributes to the oncogenic transformation of melanocytes to melanoma and plays a pivotal role in epithelial-to-mesenchymal transition (EMT), enabling metastasis [16]. Hence, investigating the genetic alterations that contribute to melanoma initiation and progression under hypoxic conditions is essential for a better understanding of overall cellular responses, which can form the basis for novel therapeutic targets.

Cytoglobin (CYGB) is a ubiquitously expressed hexacoordinated globin recently found to be highly enriched in melanocytes, and frequently downregulated during melanomagenesis [21]. Fujita and colleagues suggested that reduced CYGB expression is implicated into the transition from melanocytes (high CYGB content) to melanoma (low CYGB content) [21]. Although the mechanism remains enigmatic, CYGB is thought to play a role in the cellular response towards oxidative stress [22-25]. Response elements for HIF-1, AP-1, and NFAT have been located within the *CYGB* promoter, all of which are sensitive to hypoxia [26], and hypoxia-dependent regulation of CYGB mRNA levels was observed in various cell types and tissues [27-30].

In this study we selected and validated the most appropriate reference genes for analysis of *CYGB* gene expression in two melanoma cell lines (A375 and Malme-3M) under hypoxic conditions using geNorm and NormFinder algorithms. To validate the selected internal controls for the analysis of *CYGB* expression, we compared the expression of eight candidate reference genes under normoxic and hypoxic conditions as well as upon treatment with the HIF prolyl hydroxylase domain (PHD) inhibitor roxadustat (FG-4592). The presented approach can be

applied to accurately normalize expression of any hypoxia-induced gene in these and likely other melanoma cell lines.

4.3 METHODS

4.3.1 Cell Culture

Human Malme-3M (ATCC HTB-64) melanoma cells were maintained in Roswell Park Memorial Institute (RPMI) 1640 medium (Gibco, Life Technologies), containing L-glutamine, supplemented with 10% heat-inactivated fetal bovine serum (FBS) (Gibco, Life Technologies) and 1% Penicillin/Streptomycin (10'000 Units/mL P; 10'000 µg/mL S; Gibco, Life Technologies). Human A375 (ATCC CRL-1619) cells were maintained in Dulbecco's Minimum Essential Media (DMEM) (Gibco, Life Technologies), containing L-Glutamine, supplemented with 10% FBS and 1% Penicillin/Streptomycin (10'000 Units/mL P; 10'000 µg/mL S; Gibco, Life Technologies). Both cell lines were incubated in a humidified 5% CO_2 atmosphere (normoxia) at 37°C and were routinely subcultured after trypsinization. For the hypoxic experiments 3.5 x 10^5 (RNA extraction) or 2.5 x 10^6 (protein extraction) A375 and Malme-3M cells were seeded out in 6-well plates or 100 mm culture dishes. The subsequent day hypoxia experiments were carried out at 0.2% O_2 and 5% CO_2 in a gas-controlled glove box (InvivO2 400, Ruskinn Technologies). Additionally, cells were treated with 100 µM Roxadustat (FG-4592) (Sigma-Aldrich), or an equal amount of dimethyl sulfoxide (DMSO) as a vehicle control.

4.3.2 RNA extraction, purification, and cDNA conversion

RNA extraction and purification from A375 and Malme-3M cells cultured under normoxic or hypoxic conditions was performed using a RNeasy Mini Kit (QIAGEN) according to the manufacturer's instructions. RNA concentration and purity were measured with an Implen NanoPhotometer® N50 UV/Vis NanoVolume spectrophotometer (Implen). cDNA was reverse transcribed using PrimeScript™ RT Reagent Kit (Takara) according to the manufacturer's protocol.

4.3.3 Real-time quantitative PCR

Amplification of cDNA and subsequent quantification was performed on a CFX96 C1000 (BioRad) using a KAPA SYBR® FAST qPCR reagent (Sigma-Aldrich). All PCR reactions were performed in duplicate for biological replicates with an inter-run calibrator (IRC) to detect and remove inter-

run variation between the different mRNA quantification runs. The following conditions were used during PCR: 95°C for 10 minutes and 40 cycles of: 95°C for 15 seconds; 60°C for 1 minute. A list of the selected reference genes is given in Table 4.1. The following candidate reference genes were assessed: *ACTB*, *UBC*, *HMBS*, *SDHA*, *HPRT1*, *TBP*, *B2M* and *YHWAZ*. We also analysed *CAIX*, *GLUT1* and *PHD2* as established hypoxic control genes to monitor the efficacy of the hypoxia response. All primers were manufactured and provided by Eurogentec or Microsynth. Table 4.2 contains primer sequences, amplicon sizes and amplification efficiencies. Reaction efficiencies of PCR assays were derived from standard curves that were generated using serial dilutions of the corresponding cDNA. Amplification efficiency is determined using the formula $10^{-1/slope}$. For the actual calculations, the base of the exponential amplification function is used (e.g., 1.94 means 94% efficiency). Amplification efficiencies were subsequently used to transform the raw threshold cycle (C_t) values to relative quantities by qBase software (version 3.2) [31].

Table 4.1 List of candidate reference genes.

Gene symbol	Gene name	GeneID
Actb	Actin beta	60
B2m	Beta-2 microglubulin	567
Hprt1	Hypoxanthine phosphoribosyltransferase 1	3251
Sdha	Succinate dehydrogenase complex flavoprotein subunit A	6389
Ubc	Ubiquitin C	7316
Ywhaz	Tyrosine 3-monooxygenase/tryptophan 5-monooxygenase activation protein zeta	7534
Tbp	TATA-box binding protein	6908
Hmbs	Hydroxymethylbilane synthase	3145

Table 4.2 Primer sequences, amplification efficiencies and amplicon sizes for candidate normalization genes and target genes. Amplification efficiency is determined using the formula $10^{-1/slope}$. For the actual calculations, the base of the exponential amplification function is used (e.g., 1.94 means 94% amplification efficiency).

Gene symbol	Forward primer	Reverse primer	Efficiency	Amplicon size
Reference gene				
ACTB	AAAGACCTGTACGCCAACAC	GTCATACTCCTGCTTGCTGAT	1.94	219
B2M	TGCTGTCTCCATGTTTGATGTATCT	TCTCTGCTCCCCACCTCTAAGT	2.04	86
HPRT-1	TGACACTGGCAAAACAATGCA	GGTCCTTTTCACCAGCAAGCT	1.95	94
SDHA	GGAAGCATAAGAACATCGGAACTG	CTGATTTTCCCACAACCTTCTTGC	2.06	110
UBC	ATTTGGGTCGCGGTTCTTG	TGCCTTGACATTCTCGATGGT	2.03	133
YWHAZ	ACTTTTGGTACATTGTGGCTTCAA	CCGCCAGGACAAACCAGTAT	2.03	94
TBP	TGCACAGGAGCCAAGAGTGAA	CACATCACAGCTCCCCACCA	2.08	132
HMBS	AAGTGCGAGCCAAGGACCAG	TTACGAGCAGTGATGCCTACCAAC	1.93	298
Target gene				
CYGB	CTCTATGCCAACTGCGAG	AACTGGCTGAAGTACTGCTTG	2.04	89
PHD2	GAAAGCCATGGTTGCTTGTT	TTGCCTTCTGGAAAAATTCG	2.01	162
GLUT1	TCACTGTGCTCCTGGTTCTG	CCTGTGCTGAGAGATCC	1.98	230
CAIX	GGGTGTCATCTGGACTGTGTT	CTTCTGTGCTGCCTTCTCATC	1.89	309

4.3.4 Analysis of gene expression stability by RT-qPCR

The stability of the reference genes expression was evaluated by the geNorm algorithm. GeNorm analyses the stability of reference genes transcripts taking into account the expression stability value (*M*) [32]. This stability value is calculated for each gene of a panel of candidate reference genes based on pairwise variation analysis. Moreover, lower values of *M* correspond to higher gene expression stability. Furthermore, geNorm is also capable to determine the ideal number of reference genes needed for accurate normalization.

4.3.5 Protein extraction and quantification

Lysis buffer, containing 10 mM Tris HCl (pH 8), 1 mM EDTA, 400 mM NaCl, 1% NP-40 and protease inhibitors (Sigma-Aldrich) was used to lyse cells as described before [33]. Lysed cells were placed on a rotating arm at 4°C for 30 minutes to allow optimal performance of the lysis buffer. The suspension was subsequently sonicated for 1 minute at 60 Hz to degrade any potential formed DNA-aggregates. Finally, samples were centrifuged at 10'000 g for 15 minutes and the protein-containing supernatant was collected. Protein concentrations were determined using the Bradford Dye Reagent (Chemie Brunschwig).

4.3.6 Immunoblotting

Extracted proteins for immune-based western blotting were first separated, according to molecular weight, using sodium dodecyl sulphate polyacrylamide gel-electrophoresis (SDS-PAGE) gels, followed by electrotransfer to nitrocellulose membranes (Amersham Hybond-ECL, GE Healthcare) as described before [34, 35]. Equal amounts of protein and volume were loaded onto a 7.5% polyacrylamide gel for HIF-1α and HIF-2α, and 15% polyacrylamide gel for CYGB. Membranes were blocked in TBS-T (Tris-buffered Saline; 0.1% Tween-20), containing 5% non-fat dry milk, for 1 hour at room temperature. After blocking, the membranes were incubated overnight at 4 °C with primary antibodies (anti-HIF-1α, BD Transduction
Laboratories, 610958; anti-HIF-2α, Bethyl, A700-003; anti-GFP, Proteintech, 50430-2-AP-150UL; anti-β-actin, Sigma, SP124). The following day, membranes were washed with TBS-T, and incubated during 1 hour with horseradish-conjugated secondary antibodies (anti-mouse IgG HRP, Sigma, GENA931-1ML, anti-rabbit IgG HRP, Sigma, GENA934-1ML). The signal was revealed using ECL Prime (Amersham, GERPN2232) on a C-DiGit® Western blot scanner (LI-COR Biosciences) and exported and quantified using Image Studio™ program (LI-COR Biosciences).

4.3.7 Luciferase reporter assays

CYGB promoter construct generation was described before [36]. 3 x 10^5 Hep3B or 3.5 x 10^5 A375 cells were transiently transfected with 300 ng reporter plasmid and YFP-HIF-1α or YFP-HIF-2α as indicated, in a six-well format using JetOptimus (Polyplus). To control for differences in transfection efficiency and extract preparation, 25 ng pRL-SV40 *Renilla* luciferase reporter vector (Promega) was co-transfected. Cultures were evenly split onto 12-well plates 24 hours after transfection. Luciferase activities of triplicate wells were determined using the Dual Luciferase Reporter Assay System (Promega) as described before [37, 38]. Reporter activities were expressed as relative firefly/*Renilla* luciferase activities. All reporter gene assays were performed at least 3 times independently.

4.3.8 Statistical Analysis

All values in the figures are presented as mean ± standard error of the mean (SEM). Differences in means between two groups were analyzed with unpaired 2-tailed Student's t-test and those among multiple groups with one-way ANOVA followed by Tukey posthoc test. All statistics were performed with GraphPad Prism software 7.05. Values of $p \leq 0.05$ were considered statistically significant.

4.4 RESULTS

4.4.1 B2M and YWHAZ are optimal reference genes for normalization of gene expression data under hypoxia conditions by real-time qPCR

To investigate the stability of eight of the most commonly used reference genes from different functional classes as recommended by Vandesompele and colleagues [32] (*ACTB*, *UBC*, *HMBS*, *SDHA*, *HPRT1*, *TBP*, *B2M* and *YHWAZ*) within a hypoxic setting we set up an experiment containing two melanoma cell lines expressing high and moderately high endogenous CYGB levels, Malme-3M and A375, incubated under either normoxic or hypoxic conditions for 24 hours. Additionally, cells were treated with the PHD inhibitor roxadustat (FG-4592) for 24 hours. Data were collected using RNA from three replicate A375 and Malme-3M cultures and three independent real-time qPCR experiments were performed. In each experiment the expression levels of the candidate reference genes were measured in duplicate in eight different samples.

To identify the most stable reference genes we employed the geNorm algorithm. In Table 4.3, each candidate reference gene was ranked according to their stability measure value (*M*) in every biological replicate. The stepwise elimination of genes with the highest *M* value results in the ranking of the selected genes according to their expression stability with the two most stable genes ranked equally. For all three replicates, *UBC*, *TBP*, *B2M* and *YWHAZ* displayed a low degree of average expression variation in A375 and Malme-3M cells between the tested conditions, indicating that these reference genes might be optimal candidates for calculation of the normalization factor. Notably, NormFinder, an independent algorithm to assess the stability of reference genes, [39] displayed very comparable results, with *B2M* and *YWHAZ* consistently among the 3 most stable reference genes in all 3 independent replicates (Table 4.4).

Table 4.3 Ranking of candidate reference genes in order of their average expression variation, decreasing from top to bottom. Average expression stability values (M) are shown between brackets.

Replicate 1	Replicate 2	Replicate 3
B2M (0.348)	B2M (0.307)	YHWAZ (0.197)
YWHAZ (0.348)	YHWAZ (0.307)	Act-B (0.197)
TBP (0.402)	TBP (0.356)	B2M (0.306)
UBC (0.454)	UBC (0.400)	TBP (0.361)
HPRT-1 (0.618)	SDHA (0.548)	UBC (0.436)
SDHA (0.763)	HPRT-1 (0.672)	SDHA (0.520)
HMBS (2.08)	HMBS (2.03)	HMBS (0.628)
Act-B (4.56)	Act-B (4.26)	HPRT-1 (0.693)

Table 4.4 Reference gene stability. Ranking of selected reference genes based on stability. Similar to GeNorm, NormFinder is a mathematical algorithm used to identify the best normalization gene according to their expression stability (*M*) [31]. Two consistent most stable references genes are labeled in bold.

	Replicate 1		Replicate 2		Replicate 3	
Rank	GeNorm	NormFinder	GeNorm	NormFinder	GeNorm	NormFinder
1	**B2M**	**B2M**	**B2M**	**YWHAZ**	**YHWAZ**	**B2M**
2	**YHWAZ**	TBP	**YHWAZ**	HPRT-1	Act-B	TBP
3	TBP	**YWHAZ**	TBP	**B2M**	**B2M**	**YWHAZ**
4	UBC	Act-B	UBC	TBP	TBP	Act-B
5	HPRT-1	UBC	SDHA	UBC	UBC	UBC
6	SDHA	HMBS	HPRT-1	SDHA	SDHA	HMBS
7	HMBS	HPRT-1	HMBS	HMBS	HMBS	HPRT-1
8	Act-B	SDHA	Act-B	Act-B	HPRT-1	SDHA

In order to determine the number of optimal candidate reference genes that should be used in the normalization process, the pairwise variation $V_{n/n+1}$ was calculated between the two sequential normalization factors (NF_n and NF_{n+1}) for all samples, using geNorm. As recommended by Vandesompele et al. [32] a cut-off value of 0.15 was used, below which the inclusion of an additional reference gene does not result in a substantial improvement of normalization. According to this criterion, no major improvement in normalization factor calculation was visible when three (or more) genes were included, indicating that two reference genes are sufficient for the normalization process (Figure 4.1). More specifically, our results illustrated that *B2M* and *YWHAZ* are the most optimal reference genes for normalization of qPCR-based relative expression levels within a hypoxia-based experimental setup involving A375 and Malme-3M cells.

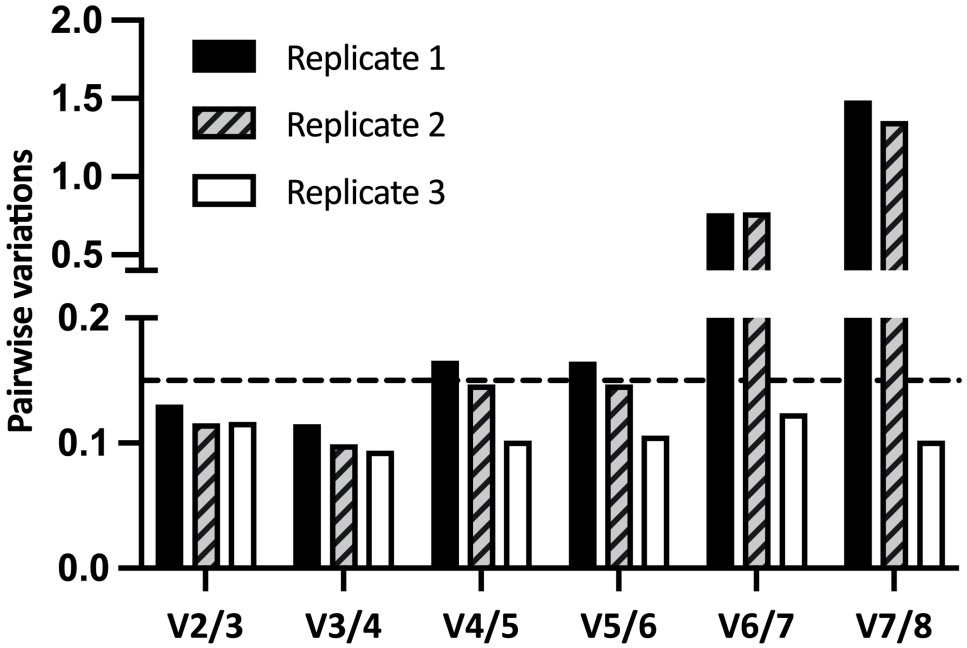

Figure 4.1. Pairwise variations ($V_{n/n+1}$) for all three replicate experiments. A large variation between two sequential normalization factors means that the added gene has a significant effect and should be preferably included for calculation of the normalization factor. Addition of a 3rd reference gene does not result in further improvement to the normalization factor in each of the three replicates.

4.4.2 CYGB mRNA expression levels are hypoxia-inducible in A375, but not in Malme-3M

We next investigated the hypoxia-inducible regulation of *CYGB* in A375 and Malme-3M cells and determined CYGB mRNA levels as well as hypoxia-responsive control gene expression levels (*CAIX*, *GLUT1* and *PHD2*) after 24 hours of hypoxia (0.2% O_2) and upon roxadustat treatment in A375 and Malme-3M cells. A normalization factor based on the geometric mean of *B2M* and *YWHAZ* expression level was employed to analyze their relative expression level.

Our results showed that in A375 expression levels of *CAIX*, *GLUT1*, *PHD2* and *CYGB* are significantly upregulated under hypoxic conditions, incubation with roxadustat (100 µM) and combined treatment of roxadustat (100 µM) and hypoxia (Figure 4.2). Both hypoxia alone and the combination with roxadustat display a very similar response in the fold change expression of *CAIX*, *GLUT1*, and *PHD2*, whereas roxadustat by itself induces a lower, yet still highly significant, increase in control gene expression. Although *CYGB* expression is clearly upregulated under every experimental condition, significant regulation is observed under hypoxic conditions and upon roxadustat treatment in the presence of hypoxic conditions.

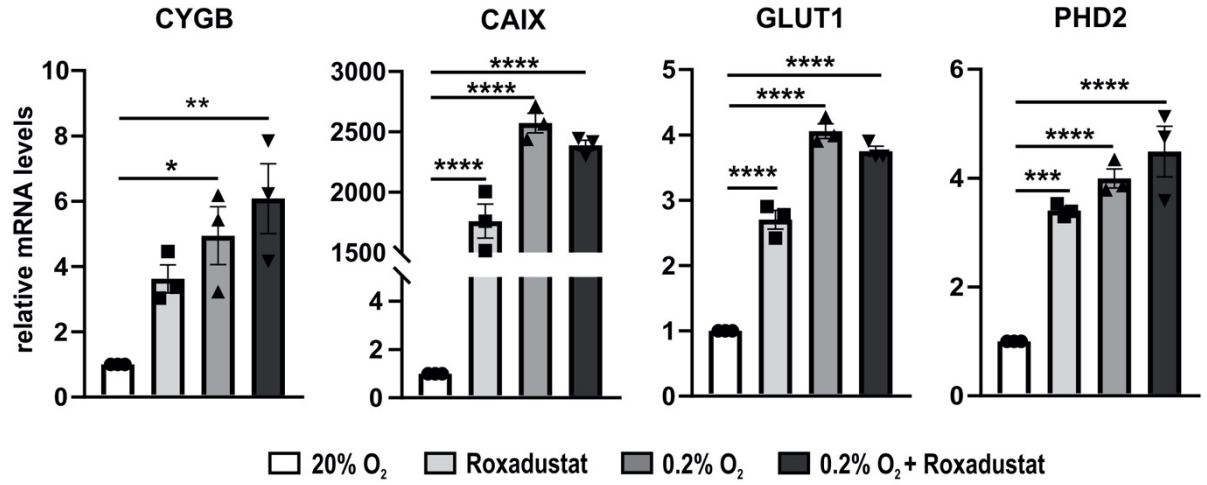

Figure 4.2. Gene expression after 24 h hypoxia or PHD inhibitor treatment in A375. Average fold change expression of three hypoxia control genes (*CAIX*, *GLUT1*, and *PHD2*) and *CYGB*, compared to the normoxic control (set as 1), after 24 h of roxadustat (100 µM), hypoxia (0.2% O_2), and combined hypoxia and roxadustat (100 µM). qPCR values were normalized to *B2M* and *YWHAZ* (mean ± S.E.M; n = 3). Individual values of replicates are depicted as black dots. One-way ANOVA (*$p \leq 0.05$; **$p \leq 0.01$; ***$p \leq 0.001$; ****$p \leq 0.0001$).

In Malme-3M similar observations could be made (Figure 4.3). *GLUT1* and *PHD2* were significantly induced upon treatment with roxadustat, hypoxic conditions, and the combination of both, whereas *CAIX* was only found to be significantly upregulated in hypoxia and the combination of hypoxia and roxadustat. Yet, a clear response in *CAIX* expression could be observed throughout all conditions. Although not statistically significant, a very slight upregulation of *CYGB* expression was detected under all conditions.

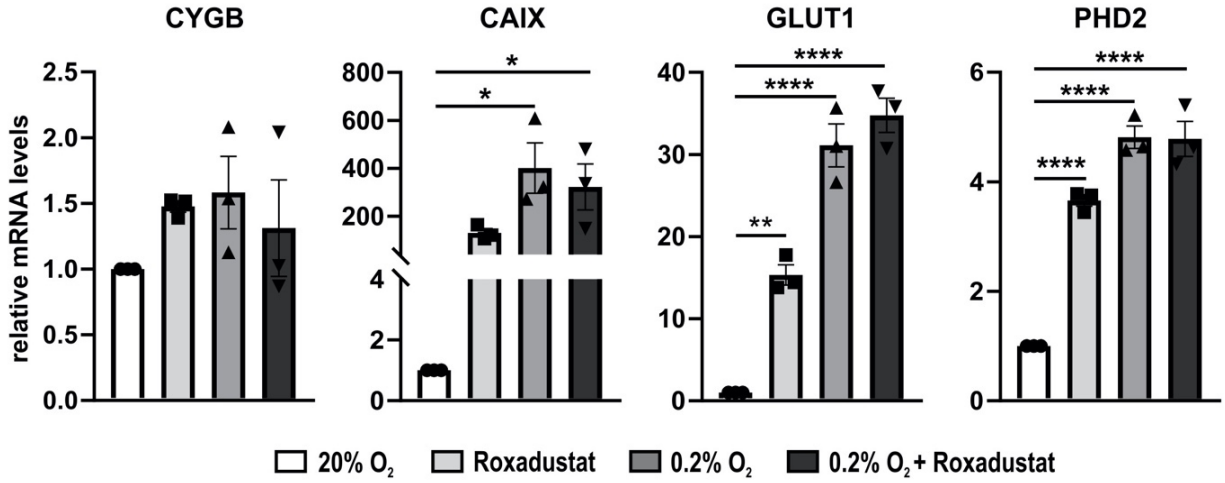

Figure 4.3. Gene expression after 24 h hypoxia or PHD inhibitor treatment in Malme-3M. Average fold change expression of three hypoxia control genes (*CAIX*, *GLUT1*, and *PHD2*) and *CYGB*, compared to the normoxic control (set as 1), after 24 h of roxadustat (100 µM), hypoxia (0.2% O_2), and combined hypoxia and roxadustat (100 µM). qPCR values were normalized to *B2M* and *YWHAZ* (mean ± S.E.M; n = 3). Individual values of replicates are depicted as black dots. One-way ANOVA (*$p \leq 0.05$; **$p \leq 0.01$; ****$p \leq 0.0001$).

Comparison of absolute *CYGB* expression values (i.e., C_t values) between the two melanoma cell lines Malme-3M and A375 (Figure 4.4), indicated that Malme-3M cells contain substantially higher endogenous *CYGB* expression than A375, with an average expression value for Malme-3M (under normoxic conditions) more than 800 times higher as compared to A375.

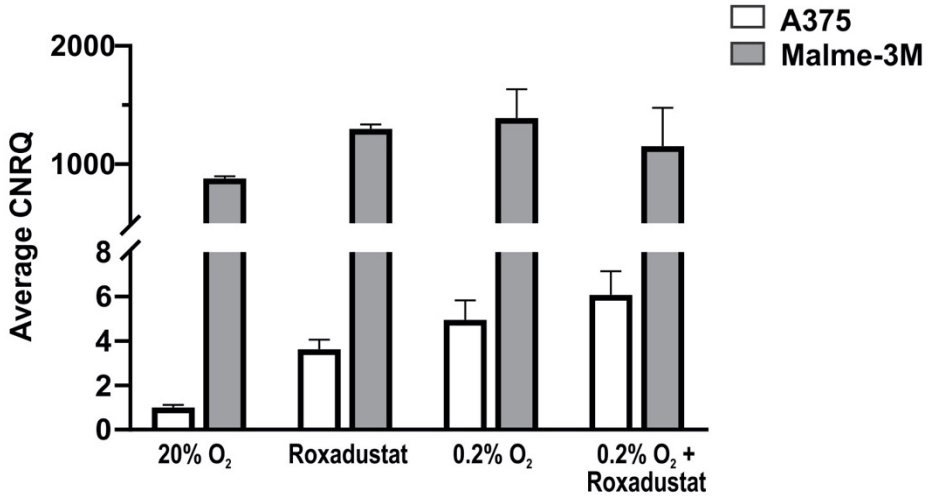

Figure 4.4. Comparison of *CYGB* expression levels in A375 and Malme-3M cells. Average *CYGB* expression, compared to the normoxic A375 control (set as 1), after 24 h of roxadustat (100 µM), hypoxia (0.2% O_2), and hypoxia and roxadustat (100 µM). qPCR values were normalized to *B2M* and *YWHAZ* (mean ± S.E.M; n = 3). Calibrated normalized relative quantities (CNRQ) represent the relative quantity between different samples for a given target gene (i.e., *CYGB*) [31].

4.4.3 Hypoxia-dependent regulation of CYGB protein levels in A375 cells

Subsequently we assessed if hypoxia-inducible regulation of *CYGB* on mRNA level, could be also observed on protein level. Immunoblotting results confirmed that CYGB is strongly upregulated under hypoxic conditions (0.1% O_2) (Figure 4.5A). Interestingly, this upregulation in A375 cells is most likely HIF-2α -dependent, as no increase was observed under HIF-1α overexpression conditions. Moreover, in presence of the PHD inhibitor, we could detect a clear upregulation both under normoxic and hypoxic conditions (Figure 4.5A; Supplemental Figure S4.1). Consistent with absolute mRNA levels Malme-3M cells exhibited higher CYGB protein levels than A375 cells, but no regulation could be observed under hypoxic conditions (Figure 4.5B).

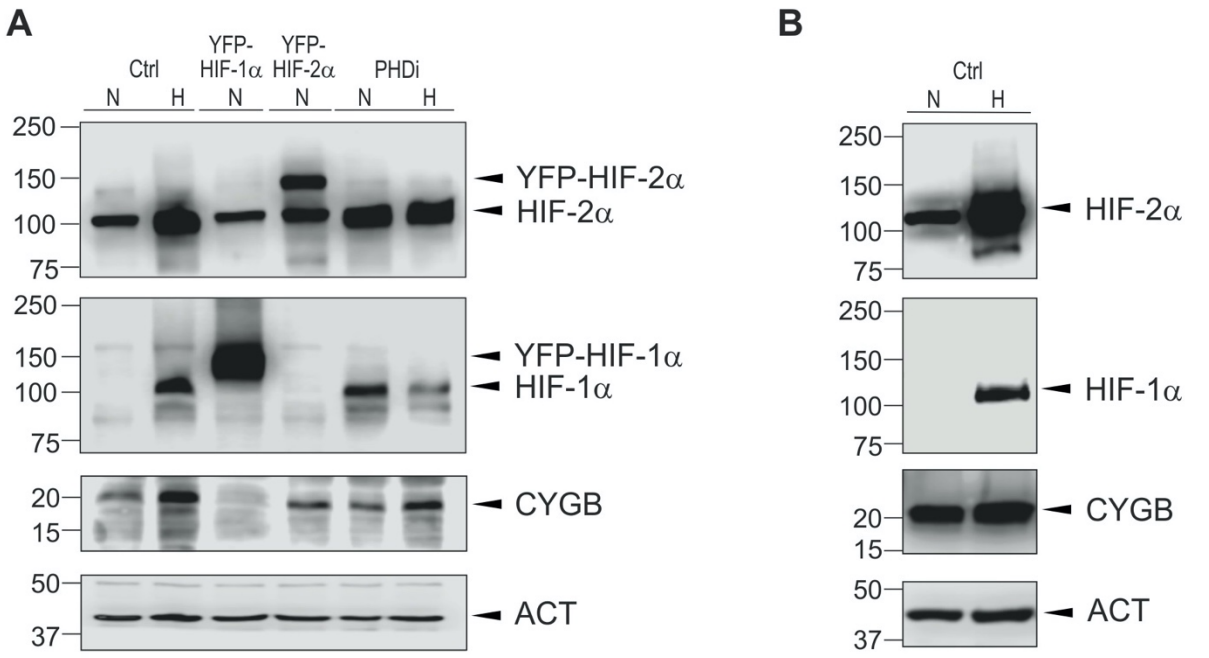

Figure 4.5. CYGB protein expression is upregulated under hypoxic conditions or in presence of PHD inhibitor. Representative immunoblots of CYGB in A375 (**A**) and Malme-3M (**B**) cells after 48 h under normoxic (N) or hypoxic (H) (0.1% O_2) conditions, in the presence of overexpressed YFP-HIF-1α or YFP-HIF-2α (24 h), and upon treatment with 4 mM PHD inhibitor (PHDi) (24 h). HIF-1α and HIF-2α were revealed using a mouse monoclonal anti-HIF-1α or a rabbit monoclonal anti-HIF-2α antibody, respectively. CYGB was detected with a rabbit polyclonal anti-CYGB antibody. β-actin (ACT) was used as a loading control and revealed using a rabbit monoclonal anti-β-actin antibody.

To obtain additional independent support of HIF-α dependent regulation of *CYGB* we employed reporter assays using a *CYGB* promoter-driven luciferase gene*. CAIX* and *PAI1* were used as HIF-1 and HIF-2 isoform target controls, respectively (Figure 4.6A). Consistent with established HIF-α isoform dependency *CAIX* promoter-driven luciferase activity was more induced upon HIF-1α overexpression whereas *PAI1* promoter-driven luciferase activity was more inducible upon HIF-2α overexpression. Immunoblotting further validated equal overexpression levels of HIF-1α and HIF-2α. Our results confirmed an 8-fold induction of *CYGB* promoter-dependent luciferase activity that was only detectable upon HIF-2α overexpression, whereas HIF-1α had no effect (Figure 4.6A). Finally, we validated these reporter gene assays in a non-melanoma cancer cell line and used Hep3B hepatocarcinomatous cells, in which *CYGB* mRNA levels were shown to be strongly induced under hypoxic conditions (Supplemental Figure S4.2). Our data in Hep3B cells display a similar trend as in A375 cells with mostly HIF-2α dependent regulation, even though a moderate induction could be observed under HIF-1α overexpression conditions as well (Figure 4.6B).

Taken together our results indicate that in A375 cells hypoxia-inducible *CYGB* mRNA regulation is also observed on protein level and by promoter-driven reporter gene assays and is HIF-2α dependent under overexpression conditions.

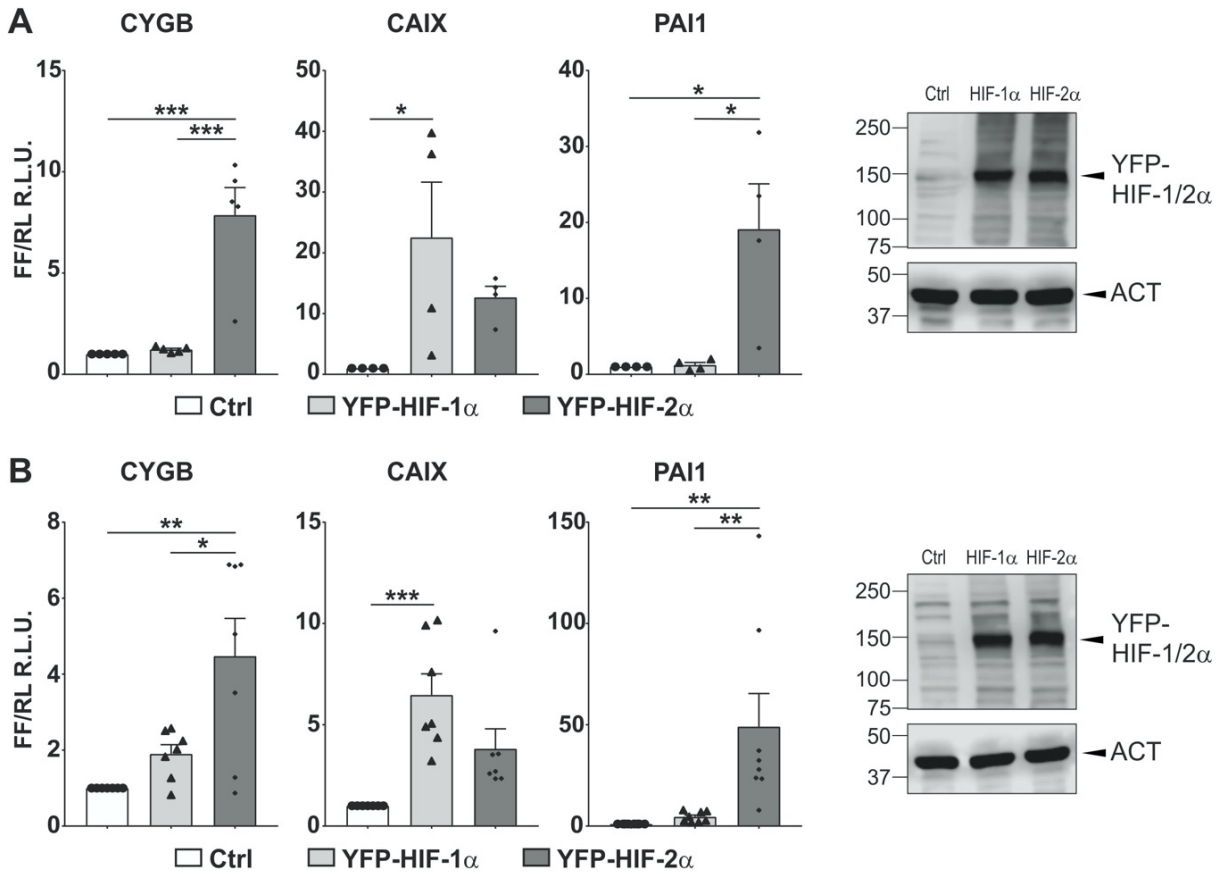

Figure 4.6. Reporter gene assays demonstrate HIF-2α-dependent induction of *CYGB* promoter-driven luciferase activity in A375 and Hep3B. A375 cells (**A**) and Hep3B cells (**B**) were transfected with *CYGB* promoter constructs and HIF-1α or HIF-2α isoform overexpression plasmids, as indicated. *CAIX* and *PAI* promoter constructs served as HIF-1α and HIF-2α control genes, respectively. For each cell line equal overexpression levels of YFP-HIF-1α and YFP-HIF-2α were detected by immunoblotting with a GFP antibody. Luciferase activity is reported as the induction compared to the control (Ctrl) and represents the ratio of firefly (FF) to *Renilla* (RL) relative light units (R.L.U.). Each column represents the mean ± SEM of four to eight different experiments performed in duplicate. One-way ANOVA (*$p \leq 0.05$; **$p \leq 0.01$; ***$p \leq 0.001$).

4.5 DISCUSSION

Reliable qPCR results require accurate normalization based on validated stably expressed reference genes. Several reports have underlined that gene expression analyses in hypoxic cancer cells have disregarded the proper validation of the used reference genes, leading to reduced reproducibility among investigations in different laboratories [40, 41]. It is now established that the stability of possible reference genes should be assessed for each cell

line/tissue and experimental condition to avoid false interpretations [1, 41, 42]. This prompted us to undertake a comprehensive analysis of a panel of potential reference genes in two melanoma cell lines cultured under various experimental hypoxia conditions. Specifically, we included the HIF prolyl hydroxylase inhibitor roxadustat (FG-4592) as a hypoxia mimetic. Roxadustat represents an oxoglutarate analogue which was shown to increase HIF-2α-regulated endogenous erythropoietin levels in patients with chronic kidney disease suffering from renal anemia [43].

GeNorm analysis revealed that *B2M* and *YWHAZ* are among the three best performing reference genes identified in each of three biological replicates (Table 4.3). When analyzing the expression stability with the NormFinder algorithm [39] both *B2M* and *YWHAZ* are consistently identified as the most stable reference genes to address the effect of hypoxia on melanoma cells (Table 4.4). B2M is part of the MHC class I molecules, which is present on almost all cells. In accordance with our results B2M was found to be stably expressed in hypoxic cultured human chondrocytes and bladder cancer cells [44, 45]. In contrast B2M expression was found to be significantly altered in hypoxic prostate cancer cells [46]. YWHAZ is a central hub protein involved in many signal transduction pathways and plays a key role in tumor progression [47]. Contrary to our results, two studies systematically evaluating stability of internal reference genes for qPCR analysis of human neural stem cells preconditioned with hypoxia, and chronically hypoxic rat heart, identified *YWHAZ* as one of the least stable reference genes, underlining the need for proper validation of reference genes in every experimental setup [32, 48, 49].

Our analysis showed that *ACTB* is the least stable reference gene in two out of three biological replicates, which is in accordance with other studies [44, 45, 50]. Hypoxic cells frequently undergo EMT, where differentiated epithelial cells are converted into poorly differentiated migratory and invasive mesenchymal cells [18, 51]. This comprehends a profound remodelling of the cytoskeleton, which includes an altered expression of ACTB. Contradictory findings also exist, with *ACTB* observed to be stably expressed in some breast and prostate cancer cell lines under hypoxic conditions [40, 46]. Despite varying *ACTB* mRNA levels following hypoxia in our study, normalization of CYGB protein levels in immunoblotting experiments was performed with stable levels of ACTB. Our data are in broad agreement with those of Staudacher and colleagues showing that low oxygen levels lead to an increase in untranslated *ACTB* levels, however only weakly impacting its protein expression which remains stable [52]. Collectively these

observations highlight that gene expression stability under hypoxic conditions is strongly dependent on the origin of cells/tissues.

Our results indicate that after 24 hours of environmentally and chemically induced hypoxia, *CYGB* mRNA levels were significantly upregulated in A375 cells, ranging from a four- to six-fold increase as compared to the normoxic condition (Figure 4.2). In Malme-3M, *CYGB* was only slightly upregulated (Figure 4.3). The lower response of Malme-3M cells to a hypoxic environment can partly be explained by the difference in intrinsic *CYGB* levels. Indeed, under normoxic conditions, we observed that *CYGB* mRNA levels were more than 800-fold higher in Malme-3M as compared to A375 cells. Moreover, when comparing the protein levels, we noticed strong differences between both cell lines with a 50-fold higher expression in Malme-3M as compared to A375 cells (data not shown). These data are consistent with previously reported results for different melanoma cell lines, G361, P22, C32TG, highly expressing *CYGB* (100- to 220-fold more than A375 cells) and only showing a slight or no induction under hypoxic conditions [53].

In line with our data, several studies reported that *CYGB* is upregulated under strong hypoxic conditions in Hep3B, renal clear cell carcinoma (RCC4), transformed human bronchial epithelial cells (BEAS-2B), human cervix carcinoma (HeLa) and murine derived hippocampal neurons (HN33) cells [54-56]. Furthermore, some of these studies suggested the involvement of HIF-1α in the hypoxic regulation of *CYGB* [54, 56]. This prompted us to further explore the molecular mechanism responsible for hypoxia-inducible *CYGB*, and specifically the contribution of HIF-1α and HIF-2α in A375 cells. Surprisingly, our results showed that only overexpression of HIF-2α induced *CYGB* promoter-driven luciferase activity, which was confirmed on protein level, whereas HIF-1α did not result in any detectable regulation. Additionally, these results were validated in the non-melanoma cell line Hep3B, even though a weak upregulation could be observed in the luciferase experiments upon HIF-1α overexpression. HIF-1α and HIF-2α have the same DNA-binding consensus sequence (5'-RCGTG-3'), however, cell type, duration, type of stimulation and culture conditions were reported to influence HIF-1α versus HIF-2α -mediated transcription [57-59]. Moreover, by overexpressing constitutively active HIF-1α and HIF-2α (i.e. with mutated proline residues) in primary endothelial cells, Downes and colleagues demonstrated that both HIF-α isoforms share more than 300 genes [57]. Furthermore, Smythies and co-workers showed that cell-specific gene induction by HIF-1α or HIF-2α arises by recruitment and association with other transcription factors that are enriched at HIF-1α or HIF-

2α binding sites [60]. Therefore, it is conceivable that in Hep3B and A375 cells, HIF-2α, rather than HIF-1α, by recruitment and binding of other transcription factors, positively regulates *CYGB* under hypoxic conditions in a cell type specific way.

Throughout our study we applied 21% incubator O_2 conditions and referred to this as normoxia. Although widely applied in physiological terms, these conditions are rather hyperoxic as not even lung alveolar cells are ever exposed to 21% O_2. Because the cellular O_2-sensing system is self-adaptive [61], the absolute pO_2 levels in the cellular microenvironment remain unknown [62]. In fact, hypoxia rather refers to a temporal than a spatial condition. Therefore, every decrease in pO_2 leading to a biological effect, like a transient increase in HIFα protein stability, can be termed hypoxia [58]. For routine experimental work, it is broadly acceptable to compare at least two O_2 concentrations that are sufficiently different from each other to cause specific biological effects while not affecting general cell viability [58].

A possible limitation of our study is the use of UV/Vis spectra-based determination of RNA concentration. Ideally a specific fluorescent dye selectively binding RNA should be employed for the sensitive and accurate quantification of RNA [63]. On the other hand, UV/Vis spectrophotometry enables the simultaneous assessment of RNA purity, a factor contributing to potential variability in reference gene expression stability [64].

4.6 CONCLUSION

In conclusion, our results underline the importance of selecting and validating an appropriate set of reference genes for gene expression analysis using real-time qPCR depending on cell type and experimental conditions. In particular, we have established that in two melanoma cell lines, Malme-3M and A375, *B2M* and *YWHAZ* are the most optimal genes to be used under experimentally-induced hypoxic conditions. Moreover, we have demonstrated that in A375 cells *CYGB* is HIF-2α -dependently regulated. The presented approach of normalizing hypoxia-inducible *CYGB* gene expression will be of major interest for further studies focussing on the importance and functional implications of hypoxic CYGB regulation and how this may impact melanoma cell survival, growth and spreading.

4.7 REFERENCES

1. Klenke, S., et al., *Easy-to-use strategy for reference gene selection in quantitative real-time PCR experiments.* Naunyn Schmiedebergs Arch Pharmacol, 2016. **389**(12): p. 1353-1366.
2. Gachon, C., A. Mingam, and B. Charrier, *Real-time PCR: what relevance to plant studies?* J. Exp. Bot, 2004. **55**(402): p. 1445-54.
3. Nolan, T., R.E. Hands, and S.A. Bustin, *Quantification of mRNA using real-time RT-PCR.* Nat. Protoc, 2006. **1**(3): p. 1559-82.
4. Schmittgen, T.D. and K.J. Livak, *Analyzing real-time PCR data by the comparative C(T) method.* Nat. Protoc, 2008. **3**(6): p. 1101-8.
5. Huggett, J., et al., *Real-time RT-PCR normalisation; strategies and considerations.* Genes Immun, 2005. **6**(4): p. 279-84.
6. Kozera, B. and M. Rapacz, *Reference genes in real-time PCR.* J. Appl. Genet, 2013. **54**(4): p. 391-406.
7. Caradec, J., et al., *'Desperate house genes': the dramatic example of hypoxia.* Br. J. Cancer, 2010. **102**(6): p. 1037-43.
8. Schmittgen, T.D. and B.A. Zakrajsek, *Effect of experimental treatment on housekeeping gene expression: validation by real-time, quantitative RT-PCR.* J Biochem Biophys Methods, 2000. **46**(1-2): p. 69-81.
9. Lima, L., et al. *Reference Genes for Addressing Gene Expression of Bladder Cancer Cell Models under Hypoxia: A Step Towards Transcriptomic Studies*. PLoS One, 2016. **11**, e0166120 DOI: 10.1371/journal.pone.0166120.
10. Bakhashab, S., et al., *Reference genes for expression studies in hypoxia and hyperglycemia models in human umbilical vein endothelial cells.* G3 (Bethesda), 2014. **4**(11): p. 2159-65.
11. Hoogewijs, D., et al. *Selection and validation of a set of reliable reference genes for quantitative sod gene expression analysis in C. elegans*. BMC Mol. Biol, 2008. **9**, 9 DOI: 10.1186/1471-2199-9-9.
12. Vandesompele, J., et al. *Accurate normalization of real-time quantitative RT-PCR data by geometric averaging of multiple internal control genes*. Genome Biol, 2002. **3**, research0034.1 DOI: 10.1186/gb-2002-3-7-research0034.
13. Derveaux, S., J. Vandesompele, and J. Hellemans, *How to do successful gene expression analysis using real-time PCR.* Methods, 2010. **50**(4): p. 227-30.
14. Bertout, J.A., S.A. Patel, and M.C. Simon, *The impact of O_2 availability on human cancer.* Nat. Rev. Cancer, 2008. **8**(12): p. 967-975.
15. Hockel, M. and P. Vaupel, *Tumor hypoxia: definitions and current clinical, biologic, and molecular aspects.* J. Natl. Cancer Inst, 2001. **93**(4): p. 266-76.
16. Bedogni, B. and M.B. Powell, *Hypoxia, melanocytes and melanoma - survival and tumor development in the permissive microenvironment of the skin.* Pigment Cell Melanoma Res, 2009. **22**(2): p. 166-74.
17. Hanahan, D. and R.A. Weinberg, *Hallmarks of cancer: the next generation.* Cell, 2011. **144**(5): p. 646-74.
18. Bedogni, B., et al., *The hypoxic microenvironment of the skin contributes to Akt-mediated melanocyte transformation.* Cancer Cell, 2005. **8**(6): p. 443-54.
19. Stewart, F.A., J. Denekamp, and V.S. Randhawa, *Skin sensitization by misonidazole: a demonstration of uniform mild hypoxia.* Br. J. Cancer, 1982. **45**(6): p. 869-77.
20. Watts, D., et al., *Hypoxia Pathway Proteins are Master Regulators of Erythropoiesis.* Int J Mol Sci, 2020. **21**(21): p. 8131.
21. Fujita, Y., et al. *Melanoma transition is frequently accompanied by a loss of cytoglobin expression in melanocytes: a novel expression site of cytoglobin*. PLoS One, 2014. **9**, e94772 DOI: 10.1371/journal.pone.0094772.
22. De Backer, J., et al., *The effect of reactive oxygen and nitrogen species on the structure of cytoglobin: A potential tumor suppressor.* Redox Biol, 2018. **19**: p. 1-10.

23. Mathai, C., et al. *Emerging perspectives on cytoglobin, beyond NO dioxygenase and peroxidase*. Redox Biol, 2020. **32**, 101468 DOI: 10.1016/j.redox.2020.101468.
24. Keppner, A., et al. *Lessons from the post-genomic era: Globin diversity beyond oxygen binding and transport*. Redox Biol, 2020. **37**, 101687 DOI: 10.1016/j.redox.2020.101687.
25. Randi, E., et al., *The Antioxidative Role of Cytoglobin in Podocytes: Implications for a Role in Chronic Kidney Disease.* Antioxid. Redox Signal, 2020. **32**: p. 1155-1171.
26. Chakraborty, S., R. John, and A. Nag, *Cytoglobin in tumor hypoxia: novel insights into cancer suppression.* Tumour Biol, 2014. **35**(7): p. 6207-19.
27. Emara, M., A.R. Turner, and J. Allalunis-Turner, *Hypoxic regulation of cytoglobin and neuroglobin expression in human normal and tumor tissues.* Cancer Cell Int, 2010. **10**: p. 33-33.
28. Fordel, E., et al., *Cytoglobin expression is upregulated in all tissues upon hypoxia: an in vitro and in vivo study by quantitative real-time PCR.* Biochem. Biophys. Res. Commun, 2004. **319**(2): p. 342-348.
29. Shaw, R.J., et al., *Cytoglobin is upregulated by tumour hypoxia and silenced by promoter hypermethylation in head and neck cancer.* Br. J. Cancer, 2009. **101**(1): p. 139-144.
30. Nishi, H., et al., *Cytoglobin, a Novel Member of the Globin Family, Protects Kidney Fibroblasts against Oxidative Stress under Ischemic Conditions.* Am. J. Pathol, 2011. **178**(1): p. 128-139.
31. Hellemans, J., et al. *qBase relative quantification framework and software for management and automated analysis of real-time quantitative PCR data*. Genome Biol, 2007. **8**, R19 DOI: 10.1186/gb-2007-8-2-r19.
32. Vandesompele, J., et al., *Accurate normalization of real-time quantitative RT-PCR data by geometric averaging of multiple internal control genes.* Genome Biology, 2002. **3**(7): p. research0034.1.
33. Schörg, A., et al., *Destruction of a distal hypoxia response element abolishes trans-activation of the PAG1 gene mediated by HIF-independent chromatin looping.* Nucleic Acids Res, 2015. **43**(12): p. 5810-5823.
34. Fuady, J.H., et al., *Hypoxia-inducible factor-mediated induction of WISP-2 contributes to attenuated progression of breast cancer.* Hypoxia (Auckl), 2014. **2**: p. 23-33.
35. Keppner, A., et al. *Deletion of the serine protease CAP2/Tmprss4 leads to dysregulated renal water handling upon dietary potassium depletion*. Sci. Rep, 2019. **9**, 19540 DOI: 10.1038/s41598-019-55995-x.
36. Randi, E., et al., *The Antioxidative Role of Cytoglobin in Podocytes: Implications for a Role in Chronic Kidney Disease.* Antioxidants & Redox Signaling, 2020. **32**.
37. Koay, T.W., et al., *Androglobin gene expression patterns and FOXJ1-dependent regulation indicate its functional association with ciliogenesis.* J Biol Chem, 2021. **296**(100291).
38. Storti, F., et al. *A novel distal upstream hypoxia response element regulating oxygen-dependent erythropoietin gene expression*. Haematologica, 2014. **99**, e45-8 DOI: 10.3324/haematol.2013.102707.
39. Andersen, C.L., J.L. Jensen, and T.F. Ørntoft, *Normalization of real-time quantitative reverse transcription-PCR data: a model-based variance estimation approach to identify genes suited for normalization, applied to bladder and colon cancer data sets.* Cancer Res, 2004. **64**(15): p. 5245-50.
40. Caradec, J., et al., *'Desperate house genes': the dramatic example of hypoxia.* Br J Cancer, 2010. **102**(6): p. 1037-43.
41. Kozera, B. and M. Rapacz, *Reference genes in real-time PCR.* J Appl Genet, 2013. **54**(4): p. 391-406.
42. Godecke, A., *qPCR-25 years old but still a matter of debate.* Cardiovasc. Res, 2018. **114**(2): p. 201-202.
43. Chen, N., et al., *Roxadustat for Anemia in Patients with Kidney Disease Not Receiving Dialysis.* N. Engl. J. Med., 2019. **381**(11): p. 1001-1010.
44. Lima, L., et al., *Reference Genes for Addressing Gene Expression of Bladder Cancer Cell Models under Hypoxia: A Step Towards Transcriptomic Studies.* PLoS One, 2016. **11**(11): p. e0166120.

45. Foldager, C.B., et al. *Validation of suitable house keeping genes for hypoxia-cultured human chondrocytes*. BMC Mol. Biol, 2009. **10**, 94 DOI: 10.1186/1471-2199-10-94.
46. Vajda, A., et al., *Gene expression analysis in prostate cancer: the importance of the endogenous control.* Prostate, 2013. **73**(4): p. 382-90.
47. Gan, Y., F. Ye, and X.-X. He, *The role of YWHAZ in cancer: A maze of opportunities and challenges.* J. Cancer, 2020. **11**(8): p. 2252-2264.
48. Benak, D., et al., *Selection of optimal reference genes for gene expression studies in chronically hypoxic rat heart.* Mol. Cell. Biochem, 2019. **461**(1): p. 15-22.
49. Kang, I.N., C.Y. Lee, and S.C. Tan *Selection of best reference genes for qRT-PCR analysis of human neural stem cells preconditioned with hypoxia or baicalein-enriched fraction extracted from Oroxylum indicum medicinal plant*. Heliyon, 2019. **5**, e02156 DOI: 10.1016/j.heliyon.2019.e02156.
50. Sun, Y., et al. *Pseudogenes as weaknesses of ACTB (Actb) and GAPDH (Gapdh) used as reference genes in reverse transcription and polymerase chain reactions*. PloS one, 2012. **7**, e41659 DOI: 10.1371/journal.pone.0041659.
51. Jiang, J., Y.L. Tang, and X.H. Liang, *EMT: a new vision of hypoxia promoting cancer progression.* Cancer Biol. Ther, 2011. **11**(8): p. 714-23.
52. Staudacher, J.J., et al., *Hypoxia-induced gene expression results from selective mRNA partitioning to the endoplasmic reticulum.* Nucleic Acids Res, 2015. **43**(6): p. 3219-36.
53. Fujita, Y., et al., *Melanoma transition is frequently accompanied by a loss of cytoglobin expression in melanocytes: a novel expression site of cytoglobin.* PLoS One, 2014. **9**(4): p. e94772.
54. Guo, X., S. Philipsen, and K.C. Tan-Un, *Study of the hypoxia-dependent regulation of human CYGB gene.* Biochem. Biophys. Res. Commun, 2007. **364**(1): p. 145-50.
55. Gorr, T.A., et al., *Old proteins - new locations: myoglobin, haemoglobin, neuroglobin and cytoglobin in solid tumours and cancer cells.* Acta Physiol. (Oxf), 2011. **202**(3): p. 563-81.
56. Fordel, E., et al., *Cytoglobin expression is upregulated in all tissues upon hypoxia: an in vitro and in vivo study by quantitative real-time PCR.* Biochemical and Biophysical Research Communications, 2004. **319**(2): p. 342-348.
57. Downes, N.L., et al., *Differential but Complementary HIF1α and HIF2α Transcriptional Regulation.* Mol Ther, 2018. **26**(7): p. 1735-1745.
58. Wenger, R.H., et al., *Frequently asked questions in hypoxia research.* Hypoxia (Auckl), 2015. **3**: p. 35-43.
59. Dengler, V.L., M. Galbraith, and J.M. Espinosa, *Transcriptional regulation by hypoxia inducible factors.* Crit. Rev. Biochem. Mol, 2014. **49**(1): p. 1-15.
60. Smythies, J.A., et al. *Inherent DNA-binding specificities of the HIF-1α and HIF-2α transcription factors in chromatin*. EMBO Rep, 2019. **20**, e46401 DOI: 10.15252/embr.201846401.
61. Wenger, R.H. and D. Hoogewijs, *Regulated oxygen sensing by protein hydroxylation in renal erythropoietin-producing cells.* Am J Physiol Renal Physiol, 2010. **298**(6): p. F1287-96.
62. Hoogewijs, D., et al., *From critters to cancers: bridging comparative and clinical research on oxygen sensing, HIF signaling, and adaptations towards hypoxia.* Integr Comp Biol, 2007. **47**(4): p. 552-77.
63. Jones, L.J., et al., *RNA quantitation by fluorescence-based solution assay: RiboGreen reagent characterization.* Anal Biochem, 1998. **265**(2): p. 368-74.
64. Vermeulen, J., et al., *Measurable impact of RNA quality on gene expression results from quantitative PCR.* Nucleic Acids Res, 2011. **39**(9): p. e63.

4.8 SUPPLEMENTARY

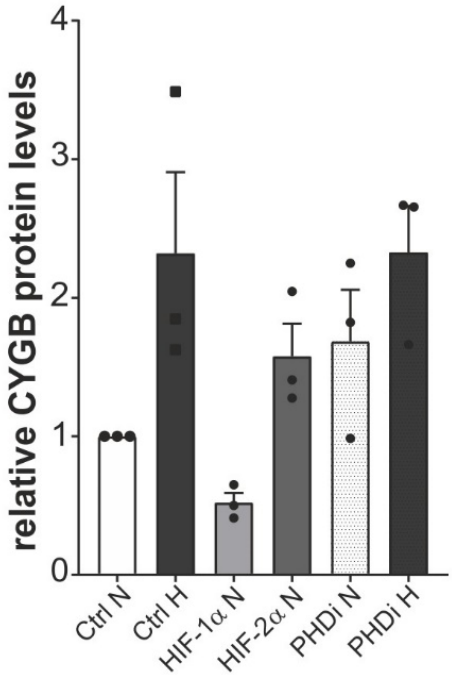

Figure S4.1. Quantification of protein levels of Figure 5A. Quantification of CYGB protein levels from 3 independent replicates (mean ± S.E.M; n = 3) of A375 cells after 48 hours cultured under normoxic (N) or hypoxic (H) (0.1% O_2) conditions, in the presence of overexpressed YFP-HIF-1α or YFP-HIF-2α, and upon treatment with 4 mM PHD inhibitor (PHDi).

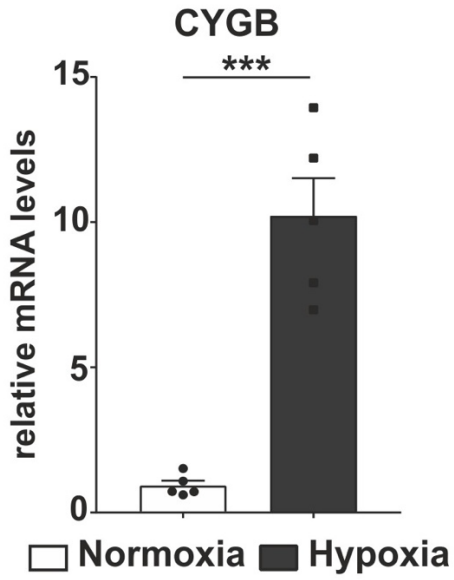

Figure S4.2. CYGB mRNA expression levels are hypoxia-inducible in Hep3B cells. CYGB expression levels measured by qPCR in Hep3B cells cultured for 24 hours under normoxic and hypoxic conditions. qPCR values were normalized to *B2M* and *YWHAZ* (mean ± S.E.M; n = 5). Individual values of replicates are depicted as black dots. Student's t-test (***p≤0.001)

CHAPTER V

CYTOGLOBIN INHIBITS NON-THERMAL PLASMA INDUCED APOPTOSIS IN MELANOMA CELLS THROUGH REGULATION OF THE NRF2-MEDIATED ANTIOXIDANT RESPONSE

Published as:

De Backer J, Lin A, Berghe WV, Bogaerts A, Hoogewijs D. *Cytoglobin inhibits non-thermal plasma-induced apoptosis in melanoma cells through regulation of the NRF2-mediated antioxidant response*. Redox Biol. 2022 Jul 14;55:102399. doi: 10.1016/j.redox.2022.102399.

5.1 ABSTRACT

Melanoma arises from pigment-producing cells called melanocytes located in the basal layers of the epidermis of the skin. Cytoglobin (CYGB) is a ubiquitously expressed hexacoordinated globin that is highly enriched in melanocytes and frequently downregulated during melanomagenesis. Previously, we showed that non-thermal plasma (NTP)-produced reactive oxygen and nitrogen species (RONS) lead to the formation of an intramolecular disulfide bridge that would allow CYGB to function as a redox-sensitive protein. Here, we investigate the cytotoxic effect of indirect NTP treatment in two melanoma cell lines with divergent endogenous CYGB expression levels, and we explore the role of CYGB in determining treatment outcome. Our findings are consistent with previous studies supporting that NTP cytotoxicity is mediated through the production of RONS and leads to apoptotic cell death in melanoma cells. Furthermore, we show that NTP-treated solutions elicit an antioxidant response through the activation of nuclear factor erythroid 2-related factor 2 (NRF2). The knockdown and overexpression of CYGB respectively sensitizes and protects melanoma cells from RONS-induced apoptotic cell death. The presence of CYGB enhances heme-oxygenase 1 (HO-1) and NRF2 protein expression levels, whereas the absence impairs their expression. Moreover, analysis of the CYGB-dependent transcriptome demonstrates the tumor suppressor long non-coding RNA maternally expressed 3 (MEG3) as a hitherto undescribed link between CYGB and NRF2. Thus, the presence of CYGB, at least in melanoma cells, seems to play a central role in determining the therapeutic outcome of RONS-inducing anticancer therapies, like NTP-treated solutions, possessing both tumor-suppressive and oncogenic features. Hence, CYGB expression could be of interest either as a biomarker or as a candidate for future targeted therapies in melanoma.

5.2 INTRODUCTION

Skin cancer is the most common cancer in the United States and the 19th most common worldwide [1]. Of all types of skin cancers, melanoma has the lowest incidence rate, with only 1% of skin cancers diagnosed being melanoma. However, melanoma (especially metastatic malignant melanoma) causes most of the skin cancer deaths with a 5-year survival of 20% [1]. Recent advancements in targeted and immunotherapy for melanoma have offered drastic improvements in survival to some patients, but most patients fail to have a sustained response.

Solar ultraviolet radiation (UVR) is considered to be the main etiological factor for melanomagenesis [2]. UVR comprises ultraviolet C (UVC; 200–290 nm), ultraviolet B (UVB; 290–320 nm), and ultraviolet A (UVA; 320–400 nm), with the latter two constituting the main effectors of skin damage [3]. UV can induce DNA damage through direct as well as mediated mechanisms [4]. UVB exposure directly leads to the generation of DNA photoproducts, DNA strand breaks, and DNA crosslinks. On the other hand, UVA is mostly responsible for oxidative stress-induced DNA damage [5].

Melanoma arises from pigment-producing cells called melanocytes located in the basal layers of the epidermis of the skin. Melanocytes play a very important role in the response to UVR via melanin synthesis [6]. Melanin produced in specialized organelles called melanosomes is transferred to keratinocytes (mediated by multiple keratinocyte-produced paracrine factors) where they protect nuclear DNA from UV irradiation, thereby preventing the generation of DNA damage [7, 8]. However, melanin synthesis involves oxidation reactions generating superoxide anion (O_2^-) and hydrogen peroxide (H_2O_2), which subjects melanocytes to increased levels of intracellular reactive oxygen species (ROS) [9, 10]. The balance between the pro-oxidant and antioxidant properties of melanin are dependent on the redox state of the melanocytes, the relative eumelanin and pheomelanin contents, the levels of melanin intermediates, and the presence of reactive metals within the melanosome microenvironment [11, 12]. There is increasing evidence concerning the significance of oxidative stress in the initiation and progression of melanoma, supported by findings that mutations in several melanoma-associated genes result from, or exacerbate, oxidative stress [10, 13-15].

To maintain redox homeostasis melanocytes possess a highly efficient antioxidant network comprising of both enzymatic (e.g. superoxide dismutase (SOD), catalase, glutathione peroxidase

(GPx), glutathione reductase (GR), and thioredoxin reductase (TR)) and non-enzymatic (e.g. ascorbic acid, glutathione) antioxidants, along with various antioxidant genes, including heme-oxygenase 1 (HO-1), ferritin, and master regulator of the antioxidant response–nuclear factor erythroid 2–related factor 2 (NRF2) [16-19].

Cytoglobin (CYGB) is a ubiquitously expressed hexacoordinated globin recently found to be highly enriched in melanocytes, and frequently downregulated during melanomagenesis [20]. Although the mechanism remains enigmatic, CYGB is thought to play a role in the cellular response towards oxidative stress [21-25]. In melanocytes, highly enriched CYGB may act as a ROS scavenger, protecting the cell from oxidative damage [20]. In melanoma, the transition from melanocytes is frequently, but not always, accompanied by a loss of CYGB expression. Modulation of CYGB expression levels during melanocyte-to-melanoma transition may influence tumor malignancy and the efficacy of cancer treatments.

Non-thermal plasma (NTP) and its biomedical applications have recently become a major focus of research [26-28]. One of the most exciting and extensively studied application is the treatment of cancer [29, 30]. NTP consists of a mixture of various components, including charged particles (ions, electrons), reactive neutral species (reactive oxygen and nitrogen species; RONS), UV radiation, and electromagnetic fields [31, 32]. Of those, RONS are hypothesized to mediate the effects observed in biological systems as they are known to be involved in rapid reactions with important biomolecules such as proteins, lipids, and nucleic acids [21, 33, 34]. In recent years, multiple studies have shown that plasma is able to effectively kill many types of cancer cells via different cell death mechanisms, including melanoma [35-39]. NTP can exert its biomedical effects either by direct treatment of cancer cells or by indirect treatment, i.e., by applying NTP-treated solutions, rich in long-lived reactive species [39, 40].

Previously, our group has shown that NTP-generated RONS induced an altered conformation of recombinant CYGB, supporting the role of redox-sensitive protein [21]. Although many studies have demonstrated the efficacy of NTP treatment for melanoma, the potential influence of the presence or absence of CYGB in melanoma cells on NTP treatment outcome remains unknown. In this study, different melanoma cell lines, containing abundant or low endogenous CYGB expression levels, were treated indirectly through incubation with phosphate buffered saline (PBS), treated with a non-thermal plasma jet (kINPen IND) for several treatment times. After

treatment, cell viability was assessed by flow cytometry, and intracellular ROS concentration was determined using fluorescent probes. CYGB mRNA and protein expression was assessed by real-time quantitative PCR (qPCR) and immunoblotting, respectively. Additionally, CYGB-overexpressing and CYGB-knockdown cells were generated to investigate the influence of CYGB on sensitivity to NTP-treatment. Finally, the CYGB-dependent transcriptome was analyzed.

5.3 EXPERIMENTAL

5.3.1 Cell culture

Human A375 (ATCC CRL-1619) and G361 (ATCC CRL-1424) melanoma cells were maintained in Dulbecco's Minimum Essential Media (DMEM) (Gibco, Life Technologies), containing L-Glutamine, supplemented with 10% heat-inactivated fetal bovine serum (FBS, Gibco, Fisher Scientific), and 1% Penicillin/Streptomycin (10,000 Units/mL P; 10,000 µg/mL S; Gibco, Life Technologies). Both cell lines were incubated in a humidified 5% CO_2 atmosphere at 37 °C and were routinely subcultured after trypsinization.

5.3.2 Generation of stable knock-down and overexpression cell lines

Expression vectors encoding short hairpin RNA (shRNA) sequences targeting human CYGB in a pLKO.1-puro plasmid were purchased from Sigma-Aldrich (shCYGB: order number TRCN0000059378). Control cells (shCTR) were transfected with a non-targeting control shRNA under the control of a U6 promoter in a pKLO.1 puromycin resistance vector (Sigma-Aldrich) as described previously [41]. Viral particles were produced in HEK293T cells by co-transfection of the respective transfer vector (3 µg) with the packaging plasmids pLP1 (4.2 µg), pLP2 (2µg) and pVSV-G (2.8 µg, all from Invitrogen) using $CaCl_2$ transfection as described before [42]. Malme-3M cells were transduced with lentiviral-pseudotyped particles and cell pools were cultured in DMEM supplemented with 10% FBS and 1% Penicillin/Streptomycin with the appropriate antibiotic for selection. For stable overexpression in A375 cells full-length human *CYGB* gene and control gene β-glucuronidase *(GUS)* were cloned into a pLENTI6 plasmid. Viral particles were produced as described above.

5.3.3 Plasma setup and treatment

Plasma was generated by using the kINPen IND plasma jet (Neoplas GmbH) [43]. Plasma was sustained at an operating frequency of 1 MHz, using argon as a feed gas. The applied gas flow rate and gap distance (nozzle end to surface of solution) were set at 1 L/min, and 10 mm, respectively. For the generation of an NTP-treated solution, 1x PBS was used. In a 12-well plate, 2 mL 1x PBS was treated for 5, 7, or 9 min. Depending on the experiment, plasma-treated PBS (pPBS) was added to cells cultured in complete DMEM in a 1:3 ratio (sections 5.3.3, 5.3.5, 5.3.8, 5.3.10) or 1:5 ratio (sections 5.3.6, 5.3.7, 5.3.13). In NTP-treated solutions, long-lived RONS H_2O_2, NO_2^- and NO_3^- have already been extensively described as the three main effectors of the cytotoxic and genotoxic effects observed in cancer cells, as other short-lived species are quenched very rapidly [35, 44, 45]. Fluorometric quantification of the concentration of H_2O_2 in pPBS with different treatment times demonstrated the linear treatment time-dependent generation of H_2O_2 in pPBS (Figure S5.4).

5.3.4 Fluorometric hydrogen peroxide assay

The concentration of H_2O_2 was quantified using the fluorometric hydrogen peroxide assay (Sigma-Aldrich) according to the manufacturer's protocol. This kit utilizes a peroxidase substrate that generates an infra-red fluorescent product (λex = 640/ λem = 680 nm) after reaction with hydrogen peroxide that can be analyzed by a fluorescent microplate reader. Immediately after NTP treatment, 50 µL pPBS was added to a black clear bottom 96 well plate (Corning). An equal amount of the assay's Master Mix was added to each pPBS containing well. After 30 min incubation in the dark the fluorescence intensity was measured on the Spark Cyto (Tecan). Concentrations were calculated using a H_2O_2 standard.

5.3.5 Viability and apoptotic cell death

Cell viability and the presence of apoptosis was determined using the fluorescein isothiocyanate (FITC)-Annexin V (BD Pharmingen) dye in conjunction with the vital dye propidium iodide (PI, Invitrogen) to allow the detection of early apoptotic cells (PI negative, FITC Annexin V positive). The day before treatment 4 x 10^4 cells were seeded in a 24-well plate, containing complete DMEM. The next day, cells were treated (described in section 2.2) and incubated for 24h in a humidified 5% CO_2 atmosphere at 37 °C. Cells were collected in round-bottom polystyrene tubes (Falcon), washed (FACS buffer; 1x PBS, 3% FBS, 1mM ethylenediaminetetraacetic acid (EDTA))

and centrifuged for 5 min at 1500 rpm before being resuspended in ice-cold 1x Annexin V binding buffer (BD Pharmingen). Finally, 1x FITC annexin V was added to the suspension. PI (500 ng) was added right before measuring on the CytoFLEX flow cytometer (Beckman Coulter). Data was analyzed using FlowJo software (FlowJo, BD).

5.3.6 Caspase activity

The IncuCyte Caspase 3/7 green dye (Sartorius) was used to determine the activation of essential mediators of apoptosis caspases 3 and 7. The IncuCyte Caspase 3/7 Dye is specially formulated for use in the IncuCyte Live-Cell Analysis System (Sartorius). Cells (3×10^3) were seeded in a 96-well plate containing complete DMEM the day before treatment. 30 min before adding pPBS, 5 μM Caspase 3/7 green dye was added to each well. In addition, 1h prior to treatment, 1 mM of N-acetyl cysteine (NAC) was added to some cells. After treatment the plate was incubated in the IncuCyte and images were taken every 2h over a period of 24h. Data were analyzed with the IncuCyte ZOOM version 2016B (Essen BioScience) to collect the total green object count per well, defined as the number of apoptotic cells per well.

5.3.7 Intracellular ROS

To determine the intracellular ROS, CellROX Green Reagent (Invitrogen) was used. The cell-permeant dye is weakly fluorescent while in a reduced state and exhibits bright green photostable fluorescence upon oxidation and subsequent binding to DNA. Cells (3×10^3) were seeded in a 96-well plate containing complete DMEM the day before treatment. 30 min before adding pPBS, 2.5 μM CellROX Green Reagent was added to each well. In addition, 1h prior to treatment, 1 mM of NAC was added to some cells. After treatment the plate was incubated in an IncuCyte device and images were taken every 2h over a period of 24h. Data were analyzed with the IncuCyte ZOOM version 2016B (Essen BioScience) to collect the average green object mean intensity of each well.

5.3.8 RNA extraction, purification, and cDNA conversion

RNA extraction and purification was performed using a PureLink RNA Mini Kit (Invitrogen), according to the manufacturer's instructions. RNA concentration and purity was measured with an Epoch spectrophotometer (BioTek) by measuring absorbance at 260/280 nm ratio. cDNA was

reverse transcribed using Superscript II reverse transcriptase (Invitrogen) according to the manufacturer's protocol.

5.3.9 Real-time quantitative PCR

Amplification of cDNA and subsequent quantification was performed using the StepOne Real-Time PCR system (Applied Biosystems) using a Power SYBR Green Master Mix (Applied Biosystems). The following conditions were used during PCR: 95 °C for 10 min and 40 cycles of: 95 °C for 15 s; 60 °C for 1 min. All PCR-reactions were performed in duplicate for three biological replicates. Where needed, an inter-run calibrator (IRC) to detect and remove inter-run variation between the different mRNA quantification runs was used. Results were subsequently analyzed using qbase+ software (version 3.2, Biogazelle) as described before [46]. A list of used reference and target genes, together with their primer sequences, amplification efficiency, and amplicon size is given in Table S1. All primers were manufactured and provided by Eurogentec or Microsynth.

5.3.10 Protein extraction and quantification

Lysis buffer, containing 10 mM Tris-HCl (pH 8), 1 mM EDTA, 400 mM NaCl, 1% NP-40 and protease inhibitors (Sigma-Aldrich) was used to lyse cells as described before [41]. Lysed cells were placed on a rotating arm at 4 °C for 30 min to allow optimal performance of the lysis buffer. The suspension was subsequently sonicated for 1 min at 60 Hz to degrade any potential formed DNA-aggregates. Finally, samples were centrifuged at 10,000 g for 15 min and the protein-containing supernatant was collected. Protein concentrations were determined using the BCA Protein Assay Kit (ThermoFisher Scientific).

5.3.11 Immunoblotting

Extracted proteins for immune-based western blotting were first separated, according to molecular weight, using sodium dodecyl sulphate polyacrylamide gel-electrophoresis (SDS-PAGE) gels, followed by electrotransfer to nitrocellulose membranes (Amersham Hybond-ECL, GE Healthcare) as described before [47, 48]. Equal amounts of protein and volume were loaded onto a 12.5% polyacrylamide gel for CYGB, heme oxygenase 1 (HO-1), and NF E2 related factor 2 (NRF2). Membranes were blocked in TBS-T (Tris-buffered Saline; 0.1% Tween-20), containing 5% non-fat dry milk, for 1 h at room temperature. After blocking, membranes were incubated

overnight at 4 °C with primary antibodies (anti-CYGB, Proteintech, 13317-1-AP; anti-β-2-Microglobulin (B2M), Proteintech, 13511-1-AP; anti-HO-1, Proteintech, 10701-1-AP; anti-NRF2, Proteintech, 16396-1-AP). The following day, membranes were washed with TBST-T, and incubated during 1 h with horseradish-conjugated secondary antibodies (anti-rabbit IgG HRP, Sigma, GENA934-1ML). The signal was revealed using ECL Prime (Amersham, GERPN2232) on a C-DiGit® Western blot scanner (LI-COR Biosciences) and exported and quantified using Image Studio™ program (LI-COR Biosciences).

5.3.12 RNA sequencing

Total RNA sample quality was assessed with TapeStation (Agilent Technologies, Santa Clara, CA, USA) and Qubit assay (Invitrogen). Total RNA samples with an RNA integrity number (RIN) > 7.0 and purity (OD_{260}/OD_{280}) ratio 1.8-2.2 were used for subsequent experiments. Sequence libraries were generated using the poly(A) RNA selection method and sequenced by GENEWIZ (Azenta Life Sciences). An independent library was constructed for each of the triplicate samples. High throughput RNA sequencing (RNA-seq) was performed with pair end 150 bp reading length on an Illumina NovaSeq 6000 (Illumina, San Diego, CA) sequencer. The DESeq2 analysis was used to estimate variance-mean dependence and test for differential expression [49]. Genes with a p-adjusted value ≤ 0.05 were considered differentially expressed. Genes with a p-adjusted value ≤ 0.05 and an absolute $\log_2$ fold change ≥ 1 were recognized as significantly differentially expressed genes (DEGs). Volcano plots were generated using the EnhancedVolcano R package to usefully visualize the results of the differential expression analyses.

5.3.13 Glutathione assay

Total cellular glutathione (GSH) levels were detected using the luminescence-based GSH-Glo Glutathione Assay (Promega), according to the manufacturers protocol. The assay is based on the conversion of a luciferin derivative into luciferin in the presence of glutathione, catalyzed by glutathione S-transferase (GST). Briefly, 5000 A375-GUS, A375-hCYGB, G361-shCTR, and G361-shCYGB cells were seeded out in a white opaque 96-well microplate (PerkinElmer). The next day, cells were either untreated, treated with 1 mM NAC only, or pre-treated with 1 mM NAC 1h before pPBS treatment. After 6h, luminescence was measured using the Spark Cyto (Tecan). GSH concentrations were calculated using a GSH standard curve.

5.3.14 Statistical analysis

The data are presented as the mean ± standard error of the mean (SEM). The statistical tests were performed with Prism GraphPad software. Flow cytometric viability data was assessed for statistical significance using one-way ANOVA followed by Tukey's multiple comparison test. Statistically significant differences compared to the untreated control were visually represented in the figures. The time-dependent measurement of apoptotic cell death and intracellular ROS using the Incucyte were analyzed using two-way ANOVA and Tukey's multiple comparisons test. Significance was compared to the untreated control for the untransduced A375 and G361 cells. For the transduced cell lines A375-hCYGB and G361-shCYGB statistically significant differences were assessed compared to their respective isogenic control. Unless otherwise noted, qPCR and immunoblotting data were analyzed for statistical significance using one-way ANOVA, followed by Tukey's multiple comparison.

5.4 RESULTS

5.4.1 pPBS induces apoptotic cell death in melanoma

The first aim of this study was to assess the anti-tumoral effect of plasma-treated PBS (pPBS) in A375 and G361 melanoma cells. We therefore treated PBS with the kINPen IND for different times and incubated the cells for 24 hours before assessing the cell viability and type of cell death. pPBS incubation was able to induce a significant decrease in cell viability in both cell lines, reflecting a pPBS-dependent cytotoxic effect (Figure 5.1A & B). Furthermore, longer treatment times of PBS and subsequent incubation resulted in a lower cell viability, indicating a correlation between treatment time and cytotoxicity. Interestingly, A375 cells seemed more sensitive than G361 cells, with responses of both 5 min and 7 min pPBS being significantly different from one another (Figure S5.1). Where incubation with 7 min pPBS was able to kill almost all A375 cells after 24 hours, cell viability in G361 cells remained 55%.

In addition to overall cell viability, the type of cell death was assessed. Flow cytometric analysis with annexin-V-FITC and PI showed that after 24 hours, almost all dead cells were double ($FITC^+/PI^+$) positive, indicative of late-apoptotic cells (Figure S5.1). Apoptotic cell death was further validated by an independent assay, where the activation of caspases 3 and 7 was determined (Figure 5.1C & D). Caspase 3/7 was clearly activated upon incubation with pPBS.

Apoptotic cell death was initiated eight hours after treatment in both cell lines. In the A375, cell death reached a plateau 18 hours post treatment, whereas in the G361 cells, no significant increase in (apoptotic) cell death was noticeable after twelve hours. Remarkably, incubation with 1mM NAC before treatment dramatically inhibited caspase 3/7 activity and cell death in both cell lines.

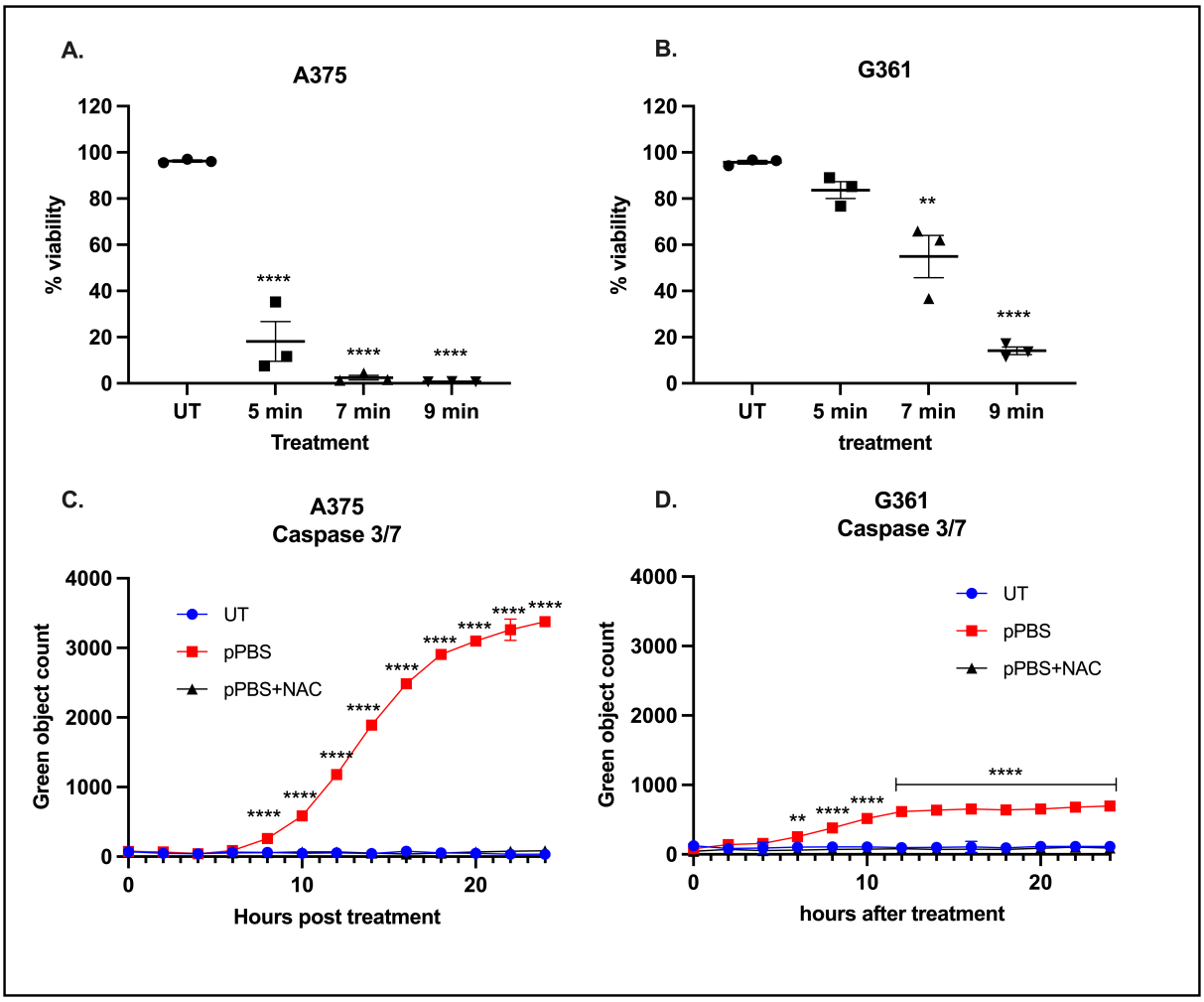

Figure 5.1. pPBS induces apoptotic cell death. A375 (A) and G361 (B) cells were treated with 5, 7, or 9 minutes pPBS, and cell viability was measured 24 hours post treatment using flow cytometry. In (C) and (D) apoptotic cell death in respectively A375 and G361 was determined by measuring the activation of caspases 3 and 7 in two-hour intervals for 24 hours, using an Incucyte device. A375 and G361 cells were either treated with pPBS only or a combination of 1 mM NAC and pPBS. Results are depicted as the mean with S.E.M of three independent experiments (n=3). One-way ANOVA (A & B), Two-way ANOVA (C & D) (**$p \leq 0.01$; ****$p \leq 0.0001$). UT, untreated; pPBS, plasma-treated PBS; NAC, N-acetyl cysteine.

5.4.2 Intracellular ROS levels are elevated upon pPBS treatment

In a subsequent step, the intracellular ROS levels were measured before and after treatment to verify the mechanism through which pPBS induces its effect. The treatment with pPBS induced a strongly significant and immediate increase in the measured average green fluorescent intensity,

both in A375 and G361 cells (Figure 5.2C & D). In A375 cells, the measured intensity dropped six hours after treatment, after which no difference in intracellular ROS between the untreated and pPBS-treated cells was observed. The treatment with 1 mM NAC before pPBS treatment significantly reduced the green fluorescent signal compared to the untreated group, indicating that NAC was able to very efficiently scavenge ROS produced by pPBS.

In G361 cells, the same trend can be observed as that of the A375 (Figure 5.2C). However, the maximum measured fluorescent signal suggests a higher accumulation of ROS after pPBS treatment compared to A375 cells. Additionally, intracellular ROS levels were still significantly augmented twelve hours after treatment. The incubation with NAC prior to pPBS treatment significantly reduced the intracellular ROS content indicating here also that NAC eliminated all pPBS produced ROS. As can be seen in Figure 5.2A, no difference in basal ROS levels between A375 and G361 could be observed.

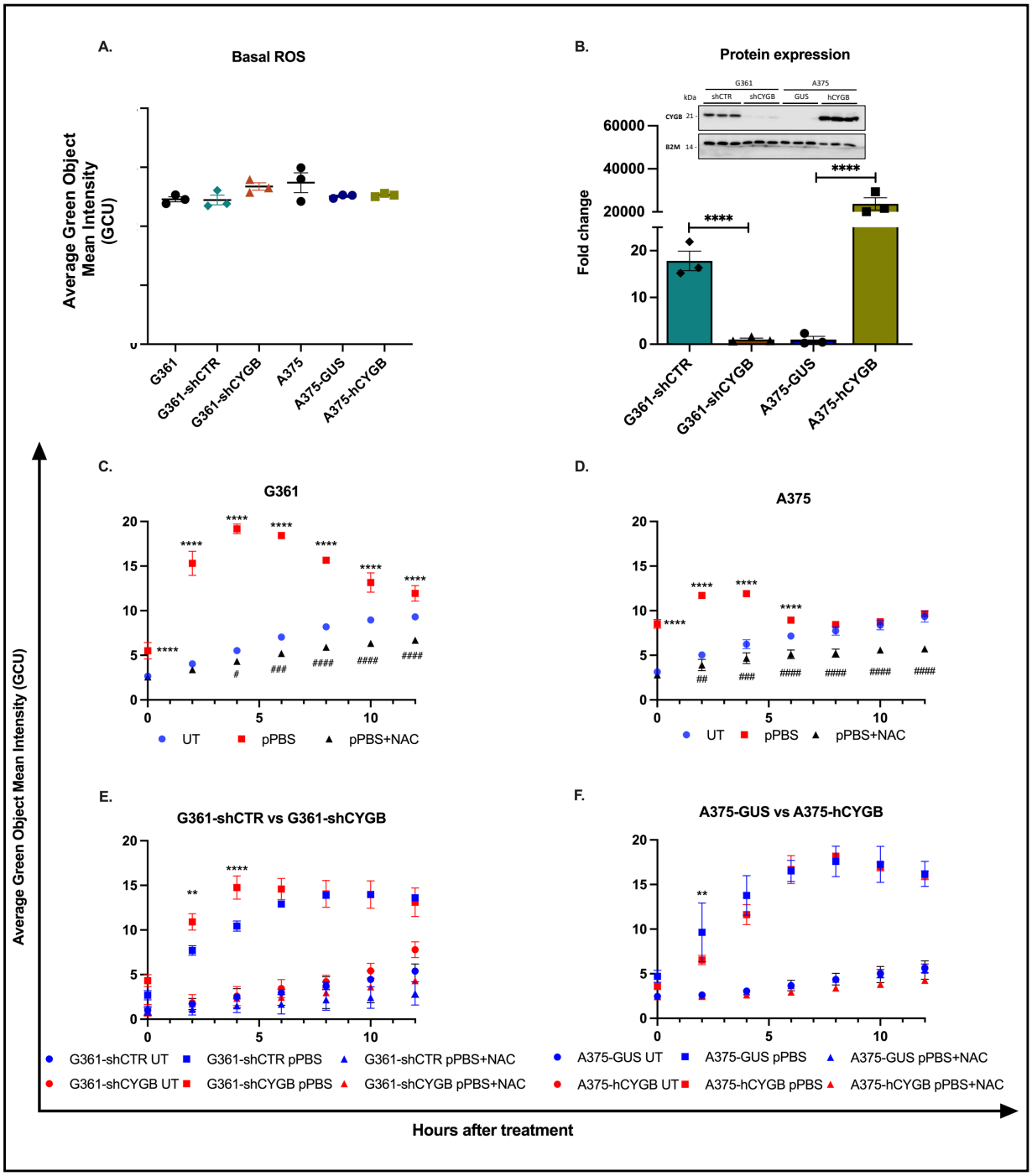

Figure 5.2. Intracellular ROS levels are elevated. Intracellular ROS levels were determined with the Incucyte, using the CellROX Green reagent. (A) The basal ROS level of all used cell lines is shown as the average green object mean intensity. (B) Average CYGB protein expression in transduced G361 and A375 cells. G361-shCYGB and A375-hCYGB protein levels were normalized to their respective transgenic controls. B2M was used as loading control. (C) 5min pPBS treatment of A375 cells and (D) 7 min pPBS treatment of G361 cells induced a significant increase in green fluorescent signal compared to the untreated control. (E & F) Intracellular ROS levels of CYGB overexpressing (A375-hCYGB) and CYGB knockdown (G361-shCYGB) cells compared to control cell lines A375-GUS and G361-shCTR. Pre-treatment with 1 mM NAC (pPBS+NAC) significantly reduced intracellular ROS levels compared to the control (mean ± S.E.M; n=3). Asterisks represent significant difference compared to the respective control cell lines. Two-way ANOVA (**$p \leq 0.01$; ****$p \leq 0.0001$; ## $p \leq 0.01$; ### $p \leq 0.001$; #### $p \leq 0.0001$). UT, untreated; pPBS, plasma-treated PBS; NAC, N-acetyl cysteine.

5.4.3 CYGB overexpression protects, and CYGB knockdown sensitizes cells to pPBS effects

To study the importance of CYGB in determining cell fate after pPBS treatment a CYGB overexpressing A375 cell line (A375-hCYGB) and CYGB knockdown G361 cell line (G361-shCYGB) was established. To account for the possible effect of transduction an A375 cell line overexpressing plant β-glucoronidase (A375-GUS) and a mock-knockdown G361 cell line was also established (G361-shCTR). Immunoblotting illustrated the efficient knockdown of CYGB protein levels. (Figure 5.2B).

The knockdown of CYGB in G361 led to a strongly significant decrease in cell viability in all three pPBS treatments compared to the G361-shCTR control cell line (Figure 5.3A). In fact, G361-shCTR cell viability 24 hours after 9 min pPBS treatment was comparable to the amount of viable G361-shCYGB cells present that were treated with 5 min pPBS. Furthermore, in A375, the overexpression of CYGB greatly protected cells from 5 and 7 min pPBS-induced cell death (Figure 5.3B). No significant increase in viable cells could be observed with 9 min pPBS treatment. This data clearly indicates the involvement of CYGB in determining pPBS treatment outcome.

The activation of caspase 3/7 was assessed in a time-dependent manner. Similarly, an increase and decrease in apoptotic cell death can be observed in the CYGB-knockdown G361-shCYGB and CYGB-overexpressing A375-hCYGB, respectively. In G361-shCYGB, a significant increase in caspase 3/7 activation is noticeable from six hours post treatment onwards (Figure 5.3C). In contrast, significantly less caspase 3/7 was activated in A375-hCYGB (Figure 5.3D). Incubation with 1mM NAC before treatment inhibited caspase 3/7 activity and cell death in all cell lines.

Additionally, the intracellular ROS levels were compared between A375-GUS and A375-hCYGB and G361-shCTR and G361-shCYGB (Figure 5.2E & F). Initially, significantly higher ROS levels were measured in both A375-GUS and G361-shCYGB compared to their corresponding isogenic control. Although no significant differences were observed in basal ROS levels between cells, a slightly higher signal was measured in the CYGB-knockdown cell line compared to G361-shCTR. In the CYGB-overexpressing cell line a difference is visible between A375 wild-type cells, but not with A375-GUS cells.

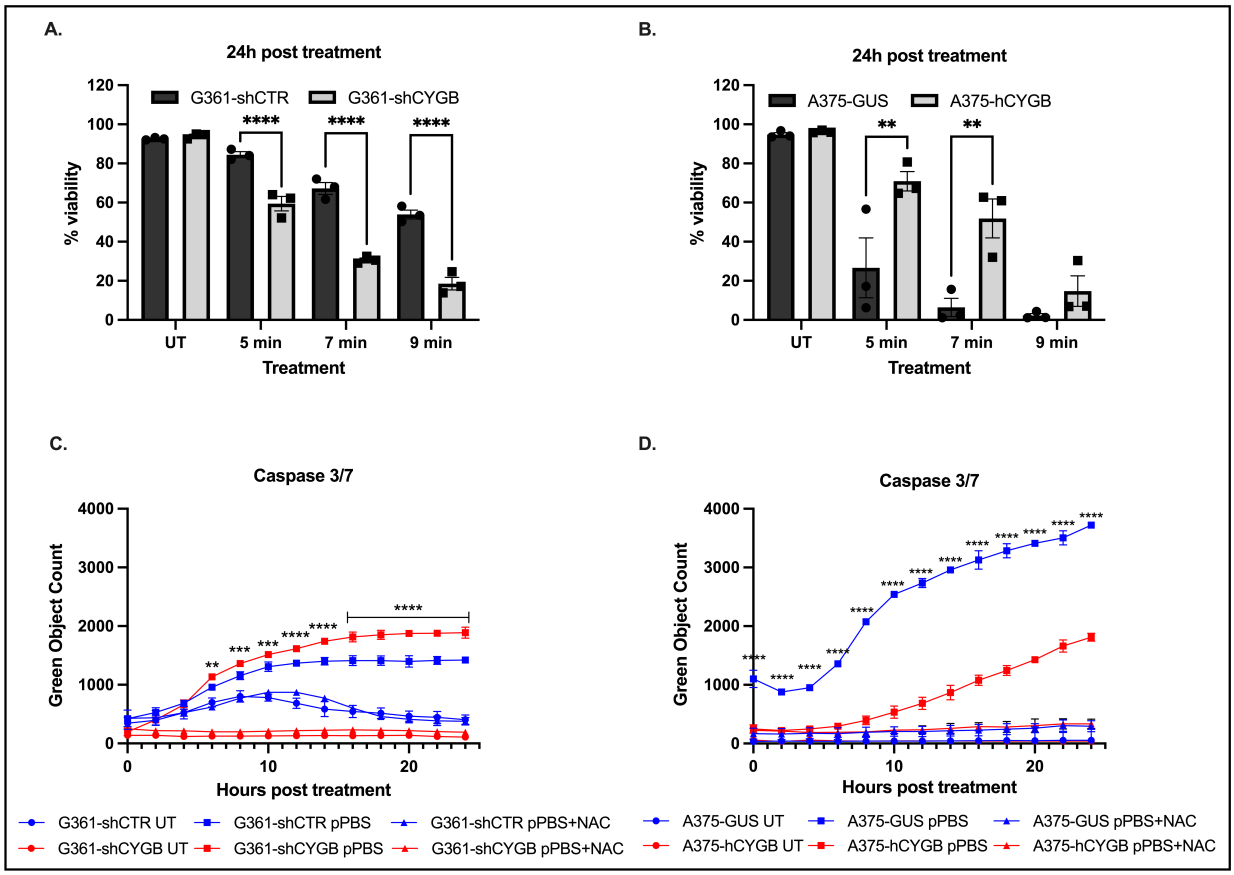

Figure 5.3. CYGB protects cells from pPBS treatment. (A) Percentage viable G361-shCTR and G361-shCYGB cells 24 hours post treatment. The knockdown of CYGB sensitized G361 cells towards pPBS treatment. (B) Percentage viable A375-GUS and A375-hCYGB cells 24 hours after pPBS treatment. CYGB overexpressing A375-hCYGB were more resistant to pPBS treatment. (C) The activation of apoptosis mediators caspase 3/7 in G361-shCTR (blue) was compared to G361-shCYGB (red) during 24 hours using an Incucyte device. (D) The amount of apoptotic cell death was determined in A375-GUS (blue) and A375-hCYGB cells (red) (mean ± S.E.M; n=3). Asterisks represent statistical significance compared to the isogenic control (G361-shCTR or A375-GUS) of the corresponding treatment. Two-way ANOVA (**$p \leq 0.01$; ****$p \leq 0.0001$). UT, untreated; pPBS, plasma-treated PBS; NAC, N-acetyl cysteine.

5.4.4 pPBS treatment elicits an antioxidant response on both mRNA and protein level

To investigate the cellular response to pPBS treatment, expression levels of CYGB and two other oxidative stress related genes (HO-1 and NRF2) were measured by qPCR, 6 and 24 hours after treatment in the A375-GUS and G361-shCTR cells. In A375-GUS cells, CYGB mRNA levels were significantly downregulated at both 6 and 24 hours post treatment (Figure 5.4A). Incubation with NAC prior to pPBS treatment also downregulated CYGB mRNA after 6h but stabilized CYGB expression to baseline after 24 hours. Interestingly, in A375-hCYGB cells, CYGB is upregulated more than 2-fold 6 hours after treatment, and even 6-fold when pre-incubated with 1 mM NAC (Figure 5.4A). The treatment of A375-GUS and hCYGB-overexpressing A375 cells with pPBS induced a steep increase in HO-1 mRNA levels after 6 hours, which decreased back to almost baseline after 24 hours, or by prior incubation with NAC. There was however a prolonged

upregulation noticeable in the CYGB-overexpressing A375 cells, with HO-1 expression levels significantly upregulated in all conditions and timepoints tested (Figure 5.4B). Although NRF2 (protein) expression is regulated post-translationally [50], NRF2 mRNA levels were found to be significantly upregulated 6 hours after treatment in both A375-GUS and A375-hCYGB and after 24 hours in A375-hCYGB only (Figure 5.4C).

In G361 control (G361-shCTR) cells CYGB expression remained stable throughout all tested conditions. Remarkably, in the CYGB-knockdown cell line G361-shCYGB, CYGB levels were significantly upregulated 24 hours post treatment, even in the presence of 1mM NAC. The expression pattern of HO-1 in G361-shCTR and G361-shCYGB 6 hours after treatment was similar to their respective A375 counterparts (Figure 5.4E). Six hours after treatment, HO-1 mRNA levels increased more than 8-fold and 6-fold in G361-shCTR and G361-shCYGB respectively. Although pre-incubation with NAC decreased the effect of pPBS on HO-1 expression after 6 hours, HO-1 mRNA was still significantly upregulated. In G361-shCTR, HO-1 levels decreased further to 2-fold the expression of the untreated condition after 24 hours. In CYGB-knockdown G361 cells however, HO-1 expression was still significantly upregulated after 24 hours. In the NAC pre-treated group, HO-1 expression was not upregulated in both G361 cell lines. Overall, NRF2 expression levels were found to be relatively stable throughout all conditions, with only a statistically significant upregulation found six hours after pPBS treatment in G361-shCYGB.

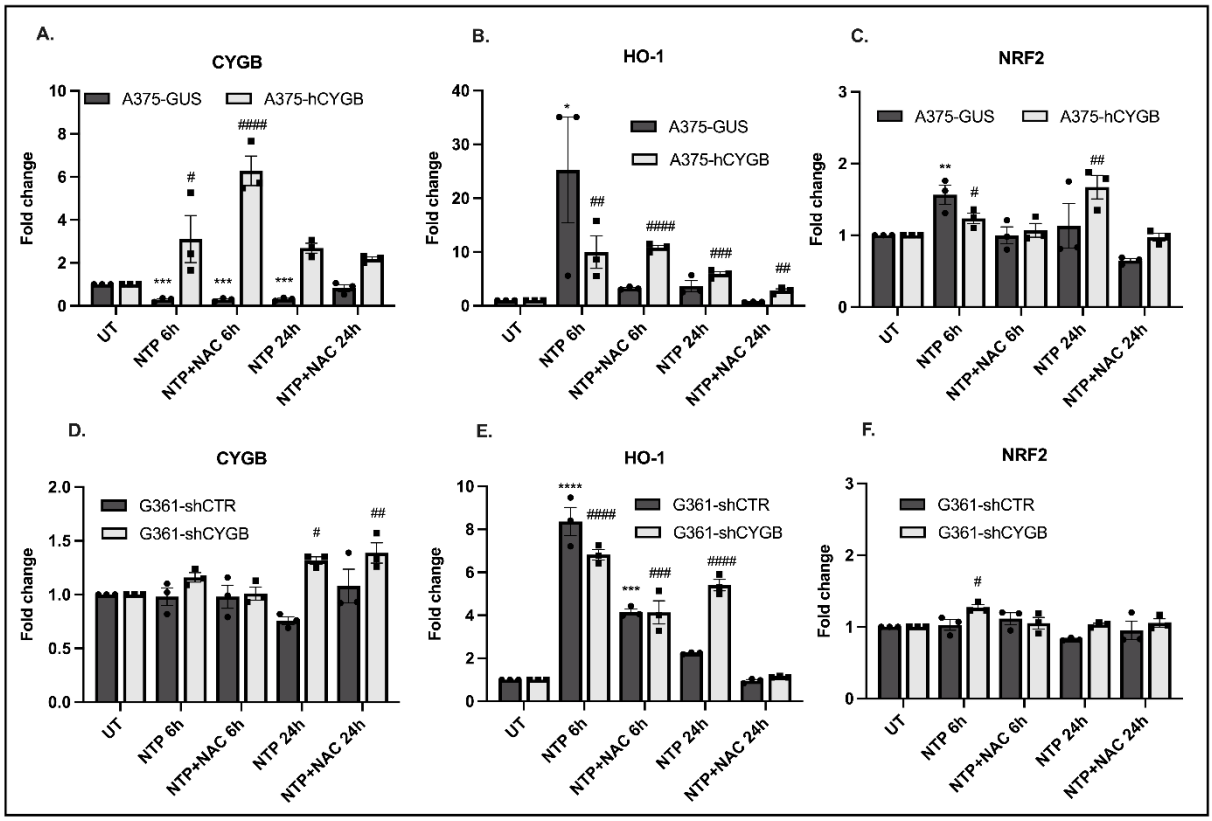

Figure 5.4. pPBS treatment induces an antioxidant response at mRNA level. (A-C) Gene expression levels of CYGB, HO-1, and NRF2 in A375-GUS and A375-hCYGB cells. The average fold change mRNA expression of two antioxidant response genes (HO-1 and NRF2) and CYGB, compared to the untreated control (set as 1) was determined 6 and 24 hours after pPBS treatment alone, or a combination of 1 mM NAC and pPBS, using qPCR. (D-F) The average fold change gene expression in G361-shCTR and G361-shCYGB cells of two antioxidant response genes (HO-1 and NRF2) and CYGB, compared to the untreated control 6 and 24 hours after pPBS treatment alone, or a combination of 1 mM NAC and pPBS. qPCR values were normalized to B2M and YWHAZ (mean ± S.E.M; n = 3). Individual values of replicates are depicted as black dots or squares. One-way ANOVA (**$p \leq 0.01$; ***$p \leq 0.001$; ****$p \leq 0.0001$), ($^{\#}p \leq 0.05$; ($^{\#\#}p \leq 0.01$ $^{\#\#\#}p \leq 0.001$; $^{\#\#\#\#}p \leq 0.0001$). UT, untreated; pPBS, plasma-treated PBS; NAC, N-acetyl cysteine.

Subsequently, the protein expression of CYGB, HO-1, and NRF2 was investigated six hours after pPBS treatment (Figure 5.5A). Immunoblotting analysis showed that pPBS treatment inhibited NRF2 protein degradation, leading to a significant increase in NRF2 protein expression in all tested cell lines except A375-hCYGB, though the latter presented also a non-significant increase in signal (Figure 5.5A-E). Interestingly, the pre-incubation of cells with 1 mM NAC induced the same response. This suggests that pPBS exerts the same intracellular effects in these cells, but with different outcomes.

Besides NRF2, HO-1 protein levels were also found to be upregulated six hours post-treatment. Although the quantification of the immunoblotting signal showed a two-fold upregulation of HO-1 in G361-shCTR, this was not deemed significant. In G361-shCYGB, HO-1 expression was upregulated ~3-fold in both tested conditions (Figure 5.5B & C). pPBS treatment of A375-GUS

and A375-hCYGB cells significantly induced HO-1 protein after six hours. However, incubation with NAC prior to treatment, slightly reduced the induction of HO-1 protein after treatment (Figure 5.5D & E).

Finally, the quantification of the CYGB immunoblotting signal showed a slight increase in CYGB expression in G361-shCTR cells in pPBS treated cells and a ~2-fold increase in NAC pre-treated cells (Figure 5.5B). Interestingly, the CYGB-knockdown cell line G361-shCYGB also displayed a significant upregulation of CYGB expression in both tested conditions (Figure 5.5C). Although in A375-GUS cells CYGB expression appeared to be significantly upregulated, the measured signal was acquired after extensive exposure, as A375-GUS expresses almost no endogenous CYGB (Figure 5.6A). In the CYGB-overexpressing cell line A375-hCYGB, no significant upregulation was found six hours after pPBS treatment. However, a slight, yet significant increase in CYGB expression could be observed in the NAC pre-treated group (Figure 5.5E).

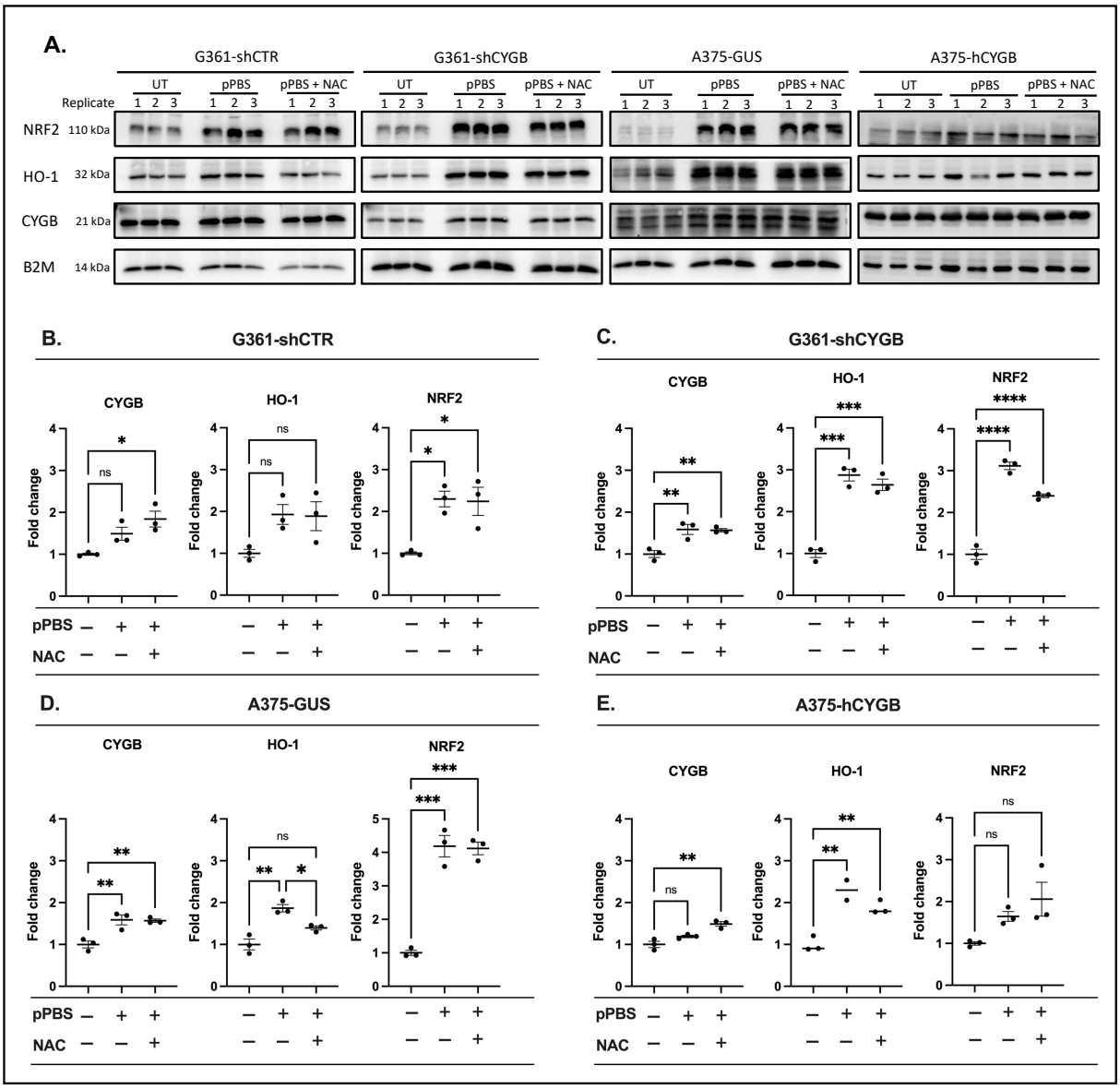

Figure 5.5. Protein expression of HO-1, NRF2 and CYGB is upregulated. (A) Immunoblots of G361-shCTR, G361-shCYGB, A375-GUS, and A375-hCYGB showing 3 biological replicates of untreated, pPBS only (pPBS), or pre-treated with 1 mM NAC (NAC) cells, 6 hours post treatment. HO-1, NRF2, and CYGB were revealed using their respective rabbit polyclonal antibodies. B2M was used as loading control. (B-E) The average fold change protein expression of HO-1, NRF2, and CYGB in G361-shCTR (B), G361-shCYGB (C), A375-GUS (D), A375-hCYGB (E), compared to the untreated control (set as 1). Quantified immunoblot signals were normalized to the loading control B2M (mean ± S.E.M; n = 3). Individual values of replicates are depicted as black dots. One-way ANOVA (**p ≤ 0.01; ***p ≤ 0.001; ****p ≤ 0.0001). pPBS, plasma-treated PBS; NAC, N-acetyl cysteine.

5.4.5 The presence of CYGB affects HO-1 and NRF2 expression.

As the overexpression and/or knockdown of CYGB could potentially affect the basal cellular state, we compared the basal protein (and mRNA; see Figure S5.3) levels of NRF2, HO-1 and CYGB between cells. Immunoblotting showed that the used overexpressing and knockdown systems of CYGB were very efficient (Figure 5.6A, C, & D). Although CYGB mRNA expression was very similar in G361-shCTR and A375-hCYGB (Figure S5.2), CYGB protein levels were clearly superior in A375-

hCYGB. A substantial difference in basal expression levels of NRF2, CYGB and HO-1 was observed between G361-shCTR and A375-GUS (Figure 5.6B). When comparing the protein levels of CYGB, HO-1, and NRF2 between G361-shCTR and G361-shCYGB, a significantly higher expression of all three proteins can be observed in G361-shCTR. Furthermore, the knockdown of CYGB resulted in a 2-fold decrease in HO-1 and NRF2 (Figure 5.6A & D). In contrast, A375-hCYGB exhibited a strongly significant increase (besides CYGB) in HO-1 and NRF2 (Figure 5.6C). Thus, it seems that the presence of CYGB enhances HO-1 and NRF2 expression levels, whereas the absence impairs their expression.

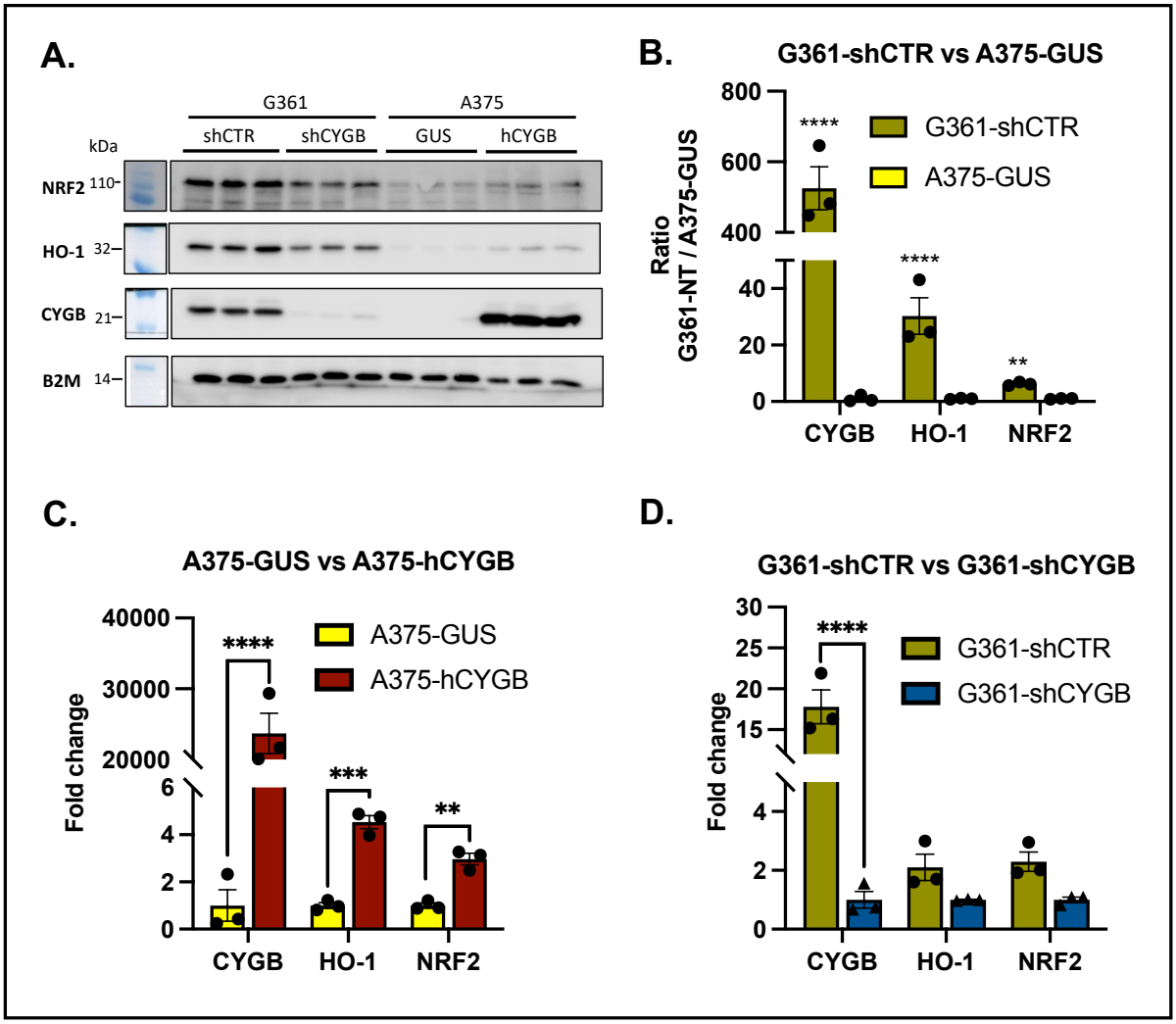

Figure 5.6. CYGB affects HO-1 and NRF2 expression. (A) Immunoblots of untreated G361-shCTR, G361-shCYGB, A375-GUS, and A375-hCYGB showing 3 biological replicates. HO-1, NRF2, and CYGB were revealed using their respective rabbit polyclonal antibodies. B2M was used as loading control. (B) The ratio of the average protein expression of G361-shCTR versus A375-GUS (set as 1) to compare differences in basal expression of HO-1, NRF2, and CYGB. (C) The average fold change difference in expression between A375-hCYGB (CYGB-overexpressing) and A375-GUS (set as 1) of each probed protein. (D) The average fold change difference in protein expression of G361-shCTR compared to the CYGB-knockdown cell line G361-shCYGB). Quantified immunoblot signals were normalized to the loading control B2M (mean ± S.E.M; n = 3). Individual values of replicates are depicted as black dots. Two-way ANOVA (**p ≤ 0.01; ***p ≤ 0.001; ****p ≤ 0.0001).

5.4.6 Transcriptomics reveal differentially expressed genes in G361-shCYGB

To explore the CYGB-dependent transcriptome we performed RNA-seq on G361-shCTR and G361-shCYGB cells under basal conditions. Three independent samples for each genotype were analyzed and the knockdown efficiency of shCYGB was confirmed to be > 90%. Differential analysis of normalized counts using DESeq2 identified 316 genes that were differentially expressed. Of those 316 genes, 111 genes (26 up- and 85 downregulated) were differentially expressed above an absolute $\log_2$ fold change of 1 (DEGs; Figure 5.7A). One of the top DEGs identified was the long non-coding RNA (lncRNA) maternally expressed gene 3 (MEG3). MEG3 expression was dramatically downregulated in CYGB knockdown G361-shCYGB compared to G361-shCTR cells. Additionally, the observed downregulation of MEG3 in G361-shCYGB cells was validated in an independent qPCR experiment (Figure 5.7B). Hence, the presence or absence of CYGB seems to influence the expression of lncRNA MEG3.

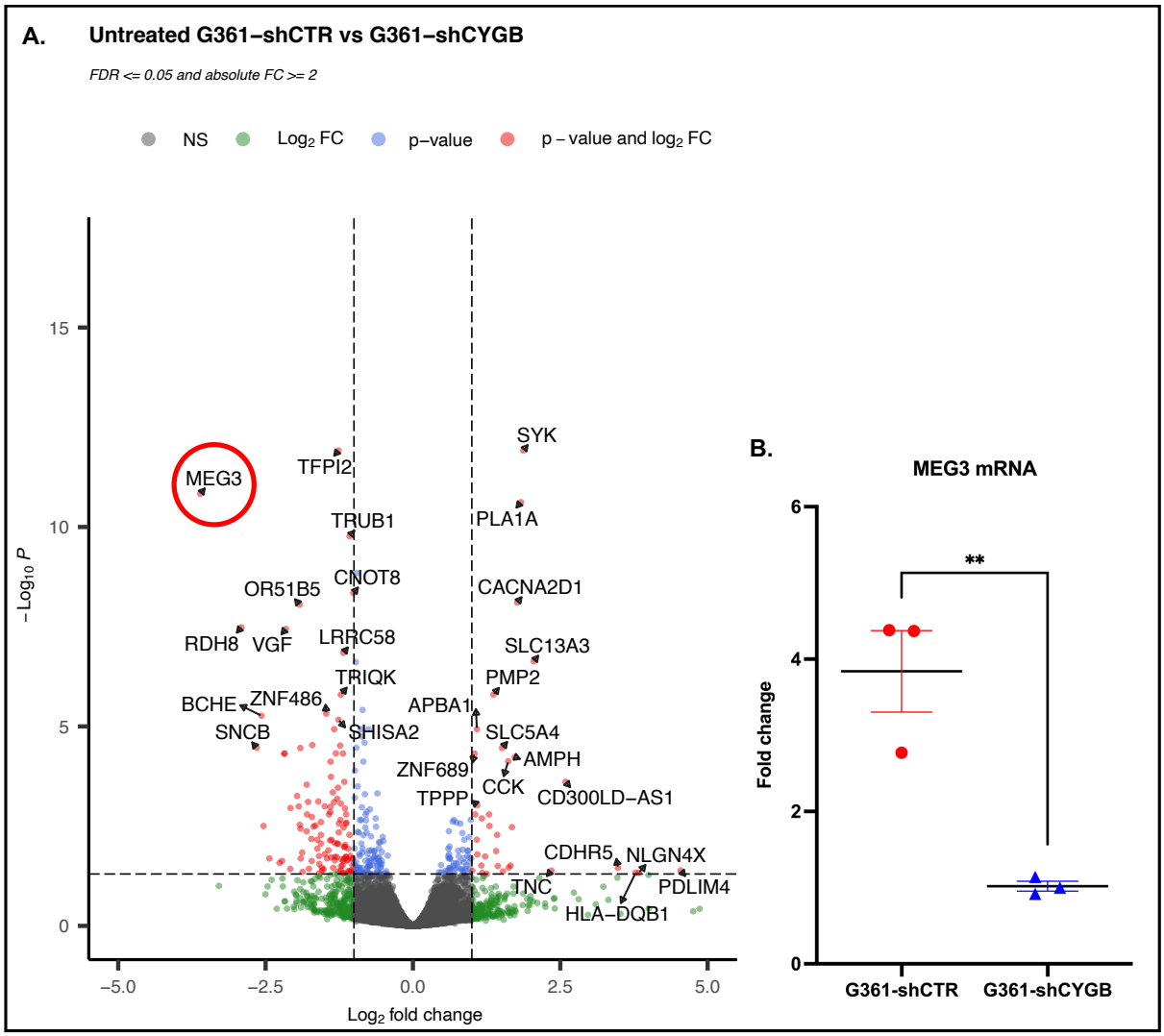

Figure 5.7. Basal CYGB-dependent transcriptome. Comparison of the G361-shCTR and G361-shCYGB transcriptomes under basal conditions. (A) Enhanced volcano plot plots the differentially expressed genes based on their Log_2 fold change (Log_2FC) and -Log_{10} p-adjusted value (-Log_{10} *P*). CYGB was excluded from plotting. Individual genes were color coded depending on the set Log_2FC and (-Log_{10} *P*) thresholds. (B) Fold change mRNA expression compared to G361-shCYGB cell line (set as 1). Relative quantities were normalized to B2M and YWHAZ (mean ± S.E.M; n = 3). Individual values of replicates are depicted as red dots or blue triangles. Student's t-test (**p ≤ 0.01).

5.5 DISCUSSION

In this study, the sensitivity of two different melanoma cell lines, expressing different levels of endogenous CYGB, towards pPBS treatment was investigated. The NTP treatment of PBS induced an exposure time-dependent reduction in cell viability in both A375 and G361 cell lines, demonstrating the cytotoxicity of NTP-treated liquids (Figure 5.1A & B). Additionally, pPBS treatment mainly induced cell death through apoptosis, as shown by the activation of caspases 3 and 7 (Figure 5.1C & D) and annexin V-FITC/PI staining (Figure S5.1). The mediators of the cytotoxicity of NTP have previously been shown to be attributed to the production of multiple

short-lived and long-lived RONS [51, 52]. In NTP-treated solutions, however, long-lived RONS like H_2O_2, NO_2^- and NO_3^- are considered the main effectors of the cytotoxic and genotoxic effects observed in cancer cells [44, 45].

Indeed, here we found that incubation with pPBS induced a rapid elevation of intracellular ROS levels and that the pre-incubation with NAC could abrogate this response (Figure 5.2B & C). NAC is a synthetic precursor of intracellular cysteine and glutathione, and its antioxidant activity results from its free radical scavenging properties, either directly via the redox potential of thiols or secondarily via increasing glutathione (GSH) levels in the cells [53]. The treatment with NAC increased GSH levels consistently in all employed cell models (Figure S5.5). Therefore, the incubation with NAC prior to pPBS treatment boosts the cellular antioxidant defense systems, thereby dramatically reducing the accumulation of ROS and ROS-induced apoptosis (Figures 5.1 & 5.2). Collectively our findings are consistent with previous studies supporting that pPBS cytotoxicity is mediated through the production of RO(N)S and leads to apoptotic cell death [45].

As the pre-incubation with NAC showed, cellular antioxidant mechanisms are in place to protect cells from the detrimental effects of increased levels of RONS, also known as oxidative stress. NRF2 is a transcription factor responsible for the regulation of cellular redox balance and protective antioxidant and phase II detoxification responses in mammals [54]. NRF2 controls the expression of key components of the glutathione and thioredoxin antioxidant system, as well as enzymes involved in NADPH regeneration, ROS and xenobiotic detoxification, and heme metabolism, thus playing a fundamental role in maintaining the redox homeostasis of the cell [55]. Here, we showed that pPBS treatment induced NRF2 protein expression in A375 and G361 cells (Figure 5.5), but mRNA expression remained largely unchanged (Figure 5.4C & F), with only a significant upregulation in NRF2 mRNA found in A375 cells 6 hours after treatment. Previous studies have shown that NRF2 activity and abundance are tightly regulated at the transcriptional, post-transcriptional, and post-translational level [50, 56, 57]. Therefore, the observed upregulation in A375 cells is most likely of no biological importance. One of the genes regulated through NRF2 is HO-1 [58]. Besides NRF2, HO-1 is strongly upregulated by several stimuli, including heme, nitric oxide, heavy metals, growth factor, cytokines, and modified lipids. Here, we demonstrated that HO-1 mRNA and protein expression was highly upregulated in A375 and G361 cells after pPBS treatment (Figure 5.4B & D).

Interestingly, cells that were pre-treated with NAC also showed an increase in NRF2 (and to a lesser extent, HO-1) protein levels. This would imply that NRF2 is activated by pPBS-induced ROS but that NAC aids in the protection of the cell. However, no increase in intracellular ROS upon pPBS administration was observed in cells pre-treated with NAC. Yet, pPBS treatment caused a drop in GSH levels in cells pre-treated with NAC (Figure S5.5). This suggests that ROS were present in NAC pre-treated cells upon pPBS treatment but were efficiently neutralized by the increased levels of GSH. Considering that GSH also serves as a substrate or cofactor of many NRF2-regulated detoxifying cellular enzymes [59], and NRF2 is critical for maintaining the GSH redox state via transcriptional regulation of glutathione reductase [60], it is likely that NAC (through increasing the total GSH content) contributed to the induction of NRF2 (and HO-1) protein levels.

The aforementioned findings on the molecular and cellular responses to pPBS treatment were very similar in both A375 and G361 cells. However, A375 cells were much more sensitive to pPBS treatment compared to G361. This suggests possible cell type specific differences in the ability to eliminate the RONS produced by pPBS treatment. As A375 cells display low endogenous CYGB levels, while G361 cells display rather high levels, we investigated the potential involvement of CYGB in determining the sensitivity to pPBS by establishing a CYGB-overexpressing A375 cell line (A375-hCYGB) and a CYGB-knockdown G361 cell line (G361-shCYGB) together with their corresponding isogenic controls (i.e., A375-GUS and G361-shCTR). Overexpression of CYGB in A375-hCYGB and knockdown in G361-shCYGB respectively rescued and sensitized cells to pPBS treatment. Furthermore, significantly less cells underwent programmed cell death through apoptosis (Figure 5.3). Although no significant difference in basal intracellular ROS was found between A375-hCYGB, G361-shCYGB, and their respective controls (Figure 5.2A), the overexpression of CYGB slightly (but significantly) reduced the intracellular ROS content after pPBS treatment, and increased ROS levels in CYGB knockdown cells. Thus, it seems that CYGB expression protects melanoma cells from ROS-induced apoptosis by the scavenging of ROS. However, a direct ROS scavenging function is unlikely, as previous biochemical studies have shown the reaction rate of CYGB with H_2O_2 to be several orders of magnitude slower than specialized metal- and thiol-based peroxidases [22]. In contrast, a nitric oxide dioxygenase and nitrite reductase activity has received experimental support [61-63]. As NTP-treated solutions like pPBS also contain nitrogen species, CYGB could aid cell survival after pPBS treatment by detoxifying RNS.

We cannot exclude that the cytoprotective effect of CYGB occurs independent from direct antioxidant properties. In fact, here we found the protein expression of NRF2 and HO-1 to be dysregulated upon CYGB knockdown and overexpression (Figure 5.6). This was especially noticeable in CYGB-overexpressing A375-hCYGB. The reason why this effect was greater in A375-hCYGB might be explained by the much larger (relative) change in CYGB expression. Yet, in G361-shCYGB cells, NRF2 and HO-1 levels were reduced by half, which could potentially have a large biological impact. This is in accordance with other studies that showed a downregulation of antioxidant enzymes or a dysregulation of the NRF2 pathway upon loss of CYGB [24, 64-66].

NRF2s involvement in heme biosynthesis could possibly explain these findings [67]. Several genes involved in the heme biosynthetic pathway are transcriptional targets of NRF2. Thus, it is possible that the high levels of endogenous CYGB in G361-shCTR demand a higher level of basal NRF2 to maintain adequate levels of heme biosynthesis. At the same time, the excessive production of heme could either directly itself induce HO-1 protein levels, or indirectly through NRF2 activation [68].

Interestingly, a possible mechanism through which CYGB can regulate NRF2 and HO-1 expression is represented by the lncRNA MEG3. MEG3 was one of the DEGs identified to be dramatically downregulated in G361-shCYGB cells (Figure 5.7). Strong evidence exists that MEG3 is a lncRNA tumor suppressor [69]. One way MEG3 can exert its tumor-suppressive function is by acting as a competing endogenous RNA (ceRNA) for shared microRNAs (miRNAs) [70]. miRNAs involvement in the post-transcriptional regulation of NRF2 has been demonstrated in multiple studies [71-73]. MEG3 has been shown to regulate NRF2 expression in hepatocytes and retinal pigment endothelial cells by acting as a ceRNA for miRNAs targeting NRF2. Moreover, RNA immunoprecipitation analysis revealed MEG3-NRF2 protein formation in fibroblasts, which positively affected NRF2 protein levels [74]. In melanoma, MEG3 expression suppressed melanoma development, growth, and metastasis through modulation of several cancer-associated pathways [75-77]. It is therefore conceivable that CYGB can regulate NRF2 and its downstream target HO-1 through the regulation of MEG3 lncRNA levels. Additionally, the correlation between CYGB and MEG3 expression sheds a new light on the tumor-suppressive function of CYGB. Notably, the expression levels of MEG3 are nearly undetectable in the

endogenously low CYGB expressing A375 cell line [76], which was also found in this study (data not shown). However, CYGB overexpression did not increase MEG3 expression.

Furthermore, CYGB mRNA expression was found to be upregulated upon pPBS treatment in A375-hCYGB and G361-shCYGB, and CYGB protein levels in all cells. Recently, chromatin immunoprecipitation analysis of the human regulatory region of CYGB identified the transcription factor p63 as an important transcriptional regulator of cytoglobin expression in keratinocytes via direct binding to the *CYGB* promoter [78]. The ΔNp63 isoform targets multiple genes involved in the oxidative stress response [79, 80]. Hence, the pPBS treatment-dependent regulation of CYGB was possibly mediated by ΔNp63. In addition, NRF2 was shown to bind to the promiscuous activator protein 1 (AP-1) binding site of β-globin [81]. As an AP-1 response element has been located within the upstream region of the CYGB gene [82], the observed induction of CYGB mRNA and protein could, at least partly, be explained by NRF2-mediated activation of the CYGB promoter. We should note however that CYGB expression in A375-hCYGB is under the control of a cytomegalovirus (CMV) promoter. Thus, CYGB mRNA and protein induction upon pPBS treatment in CYGB overexpressing A375-hCYGB cells is likely of no biological importance. The CMV promoter has been shown to be induced upon cellular stresses, including oxidative stress [83, 84].

Previously, we showed that NTP-produced RONS lead to the formation of an intramolecular disulfide bridge that would allow CYGB to function as a redox-sensitive protein [21]. Therefore, we believe it is plausible that CYGB protects cells from pPBS cytotoxicity first by maintaining a higher basal antioxidant defense via upregulating the master regulator NRF2 (and downstream targets), and second by aiding in the detoxification of RONS via acting as a redox-sensitive switch in an antioxidant response signaling cascade.

Thus, the presence of CYGB, at least in melanoma cells, seems to play a central role in determining the therapeutic outcome of ROS-inducing anticancer therapies, like NTP-treated solutions. Furthermore, the presence of CYGB influenced MEG3 expression (and subsequently NRF2) in G361 cells, which warrants further investigation into the interplay between CYGB and MEG3. CYGB expression is frequently downregulated (through hypermethylation) in melanocyte-to-melanoma transition, which would suit a tumor-suppressive role. However, in melanoma cells that still abundantly express CYGB, its function could also be seen as rather oncogenic, especially

under stress conditions. Hence, CYGB expression could be of interest either as a biomarker or as a candidate for future targeted therapies in melanoma.

5.6 CONCLUSION

Taken together, our data showed that pPBS treatment leads to apoptotic cell death in melanoma cells through the production of ROS, and that the presence of CYGB plays a key role in determining the outcome of ROS-based anticancer therapies. Furthermore, pPBS treatment elicited an NRF2-mediated antioxidant response. The expression of CYGB was upregulated upon pPBS treatment and CYGB expression itself positively regulated NRF2 and HO-1 protein levels. CYGB possibly exerts its cytoprotective effect indirectly by serving as a redox-sensitive protein. Moreover, transcriptomics revealed aberrant expression of the tumor suppressor MEG3 upon CYGB knockdown, which proposes a novel mechanism for CYGBs role as a tumor suppressor and cytoprotective protein. As CYGB expression is frequently downregulated (through hypermethylation) in melanocyte-to-melanoma transition, CYGB expression could be of interest either as a biomarker or as a candidate for future targeted therapies in melanoma.

5.7 REFERENCES

1. Siegel, R.L., K.D. Miller, and A. Jemal, *Cancer statistics, 2020.* CA Cancer J Clin, 2020. **70**(1): p. 7-30.
2. Sun, X., et al., *Ultraviolet Radiation and Melanomagenesis: From Mechanism to Immunotherapy.* Frontiers in oncology, 2020. **10**: p. 951-951.
3. Anna, B., et al., *Mechanism of UV-related carcinogenesis and its contribution to nevi/melanoma.* (1746-9872 (Print)).
4. Kim, Y. and Y.-Y. He, *Ultraviolet radiation-induced non-melanoma skin cancer: Regulation of DNA damage repair and inflammation.* Genes & diseases, 2014. **1**(2): p. 188-198.
5. Kvam, E. and R.M. Tyrrell, *Induction of oxidative DNA base damage in human skin cells by UV and near visible radiation.* Carcinogenesis, 1997. **18**(12): p. 2379-84.
6. Cichorek, M., et al., *Skin melanocytes: biology and development.* Postepy Dermatol Alergol, 2013. **30**(1): p. 30-41.
7. Kobayashi, N., et al., *Supranuclear melanin caps reduce ultraviolet induced DNA photoproducts in human epidermis.* J Invest Dermatol, 1998. **110**(5): p. 806-10.
8. Kadekaro, A.L., et al., *alpha-Melanocortin and endothelin-1 activate antiapoptotic pathways and reduce DNA damage in human melanocytes.* Cancer Res, 2005. **65**(10): p. 4292-9.
9. Simon, J.D., et al., *Current challenges in understanding melanogenesis: bridging chemistry, biological control, morphology, and function.* Pigment Cell Melanoma Res, 2009. **22**(5): p. 563-79.
10. Denat, L., et al., *Melanocytes as instigators and victims of oxidative stress.* J Invest Dermatol, 2014. **134**(6): p. 1512-1518.
11. Liu, Y., et al., *Comparison of structural and chemical properties of black and red human hair melanosomes.* Photochem Photobiol, 2005. **81**(1): p. 135-44.
12. Di Donato, P., A. Napolitano, and G. Prota, *Metal ions as potential regulatory factors in the biosynthesis of red hair pigments: a new benzothiazole intermediate in the iron or copper assisted oxidation of 5-S-cysteinyldopa.* Biochim Biophys Acta, 2002. **1571**(2): p. 157-66.
13. Jenkins, N.C., et al., *The p16(INK4A) tumor suppressor regulates cellular oxidative stress.* Oncogene, 2011. **30**(3): p. 265-74.
14. Cassidy, P.B., et al., *Selenium for the prevention of cutaneous melanoma.* Nutrients, 2013. **5**(3): p. 725-49.
15. Govindarajan, B., et al., *Overexpression of Akt converts radial growth melanoma to vertical growth melanoma.* J Clin Invest, 2007. **117**(3): p. 719-29.
16. Pinnell, S.R., *Cutaneous photodamage, oxidative stress, and topical antioxidant protection.* J Am Acad Dermatol, 2003. **48**(1): p. 1-19; quiz 20-2.
17. Kokot, A., et al., *Alpha-melanocyte-stimulating hormone counteracts the suppressive effect of UVB on Nrf2 and Nrf-dependent gene expression in human skin.* Endocrinology, 2009. **150**(7): p. 3197-206.
18. Kadekaro, A.L., et al., *Melanocortin 1 receptor genotype: an important determinant of the damage response of melanocytes to ultraviolet radiation.* FASEB J, 2010. **24**(10): p. 3850-60.
19. Diehl, C., *Melanocytes and Oxidative Stress.* Journal of Pigmentary Disorders, 2014. **1**.
20. Fujita, Y., et al., *Melanoma Transition Is Frequently Accompanied by a Loss of Cytoglobin Expression in Melanocytes: A Novel Expression Site of Cytoglobin.* PLOS ONE, 2014. **9**(4): p. e94772.
21. De Backer, J., et al., *The effect of reactive oxygen and nitrogen species on the structure of cytoglobin: A potential tumor suppressor.* Redox Biol, 2018. **19**: p. 1-10.
22. Mathai, C., et al., *Emerging perspectives on cytoglobin, beyond NO dioxygenase and peroxidase.* Redox Biol, 2020. **32**: p. 101468.
23. Keppner, A., et al., *Lessons from the post-genomic era: Globin diversity beyond oxygen binding and transport.* Redox Biol, 2020. **37**: p. 101687.
24. Randi, E.B., et al., *The Antioxidative Role of Cytoglobin in Podocytes: Implications for a Role in Chronic Kidney Disease.* Antioxid Redox Signal, 2020. **32**(16): p. 1155-1171.

25. Zweier, J.L., et al., *Cytoglobin has potent superoxide dismutase function.* Proceedings of the National Academy of Sciences, 2021. **118**(52): p. e2105053118.
26. Stoffels, E., et al., *Plasma needle forin vivomedical treatment: recent developments and perspectives.* Plasma Sources Science and Technology, 2006. **15**(4): p. S169-S180.
27. Kim, G.J., et al., *DNA damage and mitochondria dysfunction in cell apoptosis induced by nonthermal air plasma.* Applied Physics Letters, 2010. **96**(2): p. 021502.
28. Stoffels, E., Y. Sakiyama, and D.B. Graves, *Cold Atmospheric Plasma: Charged Species and Their Interactions With Cells and Tissues.* IEEE Transactions on Plasma Science, 2008. **36**(4): p. 1441-1457.
29. Yan, D., J.H. Sherman, and M. Keidar, *Cold atmospheric plasma, a novel promising anti-cancer treatment modality.* Oncotarget, 2017. **8**(9): p. 15977-15995.
30. Weltmann, K.D. and T. von Woedtke, *Plasma medicine—current state of research and medical application.* Plasma Physics and Controlled Fusion, 2016. **59**(1): p. 014031.
31. Lu, X., et al., *Reactive species in non-equilibrium atmospheric-pressure plasmas: Generation, transport, and biological effects.* Physics Reports, 2016. **630**: p. 1-84.
32. Graves, D.B., *Reactive Species from Cold Atmospheric Plasma: Implications for Cancer Therapy.* Plasma Processes and Polymers, 2014. **11**(12): p. 1120-1127.
33. Furuta, R., et al., *Intracellular responses to reactive oxygen and nitrogen species, and lipid peroxidation in apoptotic cells cultivated in plasma-activated medium.* Plasma Processes and Polymers, 2017. **14**(11): p. 1700123.
34. Hirst, A.M., et al., *Low-temperature plasma treatment induces DNA damage leading to necrotic cell death in primary prostate epithelial cells.* Br J Cancer, 2015. **112**(9): p. 1536-45.
35. Privat-Maldonado, A., et al., *Reduction of Human Glioblastoma Spheroids Using Cold Atmospheric Plasma: The Combined Effect of Short- and Long-Lived Reactive Species.* Cancers (Basel), 2018. **10**(11).
36. Hou, J., et al., *Non-thermal plasma treatment altered gene expression profiling in non-small-cell lung cancer A549 cells.* BMC Genomics, 2015. **16**(1): p. 435.
37. Lin, A., et al., *Non-Thermal Plasma as a Unique Delivery System of Short-Lived Reactive Oxygen and Nitrogen Species for Immunogenic Cell Death in Melanoma Cells.* Advanced Science, 2019. **6**(6): p. 1802062.
38. Bekeschus, S., *Combined Toxicity of Gas Plasma Treatment and Nanoparticles Exposure in Melanoma Cells In Vitro.* Nanomaterials (Basel), 2021. **11**(3).
39. Liedtke, K.R., et al., *Non-thermal plasma-treated solution demonstrates antitumor activity against pancreatic cancer cells in vitro and in vivo.* Scientific Reports, 2017. **7**(1): p. 8319.
40. Tanaka, H., et al., *Similarities And Differences In The Cellular Resposnses Between Plasma-Activated Medium-Treated Glioblastomas And Plasma-Activated Ringer's Lactate Solution-Treated Glioblastomas.* Clinical Plasma Medicine, 2018. **9**: p. 42-43.
41. Schörg, A., et al., *Destruction of a distal hypoxia response element abolishes trans-activation of the PAG1 gene mediated by HIF-independent chromatin looping.* Nucleic Acids Research, 2015. **43**(12): p. 5810-5823.
42. Koay, T.W., et al., *Androglobin gene expression patterns and FOXJ1-dependent regulation indicate its functional association with ciliogenesis.* J Biol Chem, 2021. **296**: p. 100291.
43. Reuter, S., T. von Woedtke, and K.-D. Weltmann, *The kINPen—a review on physics and chemistry of the atmospheric pressure plasma jet and its applications.* Journal of Physics D: Applied Physics, 2018. **51**(23): p. 233001.
44. Griseti, E., N. Merbahi, and M. Golzio, *Anti-Cancer Potential of Two Plasma-Activated Liquids: Implication of Long-Lived Reactive Oxygen and Nitrogen Species.* Cancers (Basel), 2020. **12**(3).
45. Tanaka, H., et al., *Plasma-Treated Solutions (PTS) in Cancer Therapy.* Cancers, 2021. **13**(7): p. 1737.
46. De Backer, J., et al., *A reliable set of reference genes to normalize oxygen-dependent cytoglobin gene expression levels in melanoma.* Scientific Reports, 2021. **11**(1): p. 10879.
47. Fuady, J.H., et al., *Hypoxia-inducible factor-mediated induction of WISP-2 contributes to attenuated progression of breast cancer.* Hypoxia (Auckl), 2014. **2**: p. 23-33.

48. Keppner, A., et al., *Deletion of the serine protease CAP2/Tmprss4 leads to dysregulated renal water handling upon dietary potassium depletion.* Scientific Reports, 2019. **9**(1): p. 19540.
49. Love, M.I., W. Huber, and S. Anders, *Moderated estimation of fold change and dispersion for RNA-seq data with DESeq2.* Genome Biology, 2014. **15**(12): p. 550.
50. Hayes, J.D. and A.T. Dinkova-Kostova, *The Nrf2 regulatory network provides an interface between redox and intermediary metabolism.* Trends Biochem Sci, 2014. **39**(4): p. 199-218.
51. Lin, A., et al., *Oxidation of Innate Immune Checkpoint CD47 on Cancer Cells with Non-Thermal Plasma.* Cancers, 2021. **13**(3): p. 579.
52. Lin, A., et al., *Nanosecond-Pulsed DBD Plasma-Generated Reactive Oxygen Species Trigger Immunogenic Cell Death in A549 Lung Carcinoma Cells through Intracellular Oxidative Stress.* International Journal of Molecular Sciences, 2017. **18**(5): p. 966.
53. Sun, S.-Y., *N-acetylcysteine, reactive oxygen species and beyond.* Cancer biology & therapy, 2010. **9**(2): p. 109-110.
54. Loboda, A., et al., *Role of Nrf2/HO-1 system in development, oxidative stress response and diseases: an evolutionarily conserved mechanism.* Cell Mol Life Sci, 2016. **73**(17): p. 3221-47.
55. Gorrini, C., I.S. Harris, and T.W. Mak, *Modulation of oxidative stress as an anticancer strategy.* Nat Rev Drug Discov, 2013. **12**(12): p. 931-47.
56. Stewart, D., et al., *Degradation of transcription factor Nrf2 via the ubiquitin-proteasome pathway and stabilization by cadmium.* J Biol Chem, 2003. **278**(4): p. 2396-402.
57. Nguyen, T., et al., *Increased protein stability as a mechanism that enhances Nrf2-mediated transcriptional activation of the antioxidant response element. Degradation of Nrf2 by the 26 S proteasome.* J Biol Chem, 2003. **278**(7): p. 4536-41.
58. Alam, J., et al., *Nrf2, a Cap'n'Collar transcription factor, regulates induction of the heme oxygenase-1 gene.* J Biol Chem, 1999. **274**(37): p. 26071-8.
59. Lushchak, V.I., *Glutathione homeostasis and functions: potential targets for medical interventions.* J Amino Acids, 2012. **2012**: p. 736837.
60. Harvey, C.J., et al., *Nrf2-regulated glutathione recycling independent of biosynthesis is critical for cell survival during oxidative stress.* Free Radic Biol Med, 2009. **46**(4): p. 443-53.
61. Liu, X., et al., *Characterization of the function of cytoglobin as an oxygen-dependent regulator of nitric oxide concentration.* Biochemistry, 2012. **51**(25): p. 5072-82.
62. Zweier, J.L. and G. Ilangovan, *Regulation of Nitric Oxide Metabolism and Vascular Tone by Cytoglobin.* Antioxid Redox Signal, 2020. **32**(16): p. 1172-1187.
63. Reeder, B.J. and J. Ukeri, *Strong modulation of nitrite reductase activity of cytoglobin by disulfide bond oxidation: Implications for nitric oxide homeostasis.* Nitric Oxide, 2018. **72**: p. 16-23.
64. Zhang, S., et al., *Cytoglobin Promotes Cardiac Progenitor Cell Survival against Oxidative Stress via the Upregulation of the NFκB/iNOS Signal Pathway and Nitric Oxide Production.* Sci Rep, 2017. **7**(1): p. 10754.
65. Singh, S., et al., *Cytoglobin modulates myogenic progenitor cell viability and muscle regeneration.* Proc Natl Acad Sci U S A, 2014. **111**(1): p. E129-38.
66. Thorne, L.S., et al., *Cytoglobin protects cancer cells from apoptosis by regulation of mitochondrial cardiolipin.* Scientific Reports, 2021. **11**(1): p. 985.
67. Kerins, M.J. and A. Ooi, *The Roles of NRF2 in Modulating Cellular Iron Homeostasis.* Antioxid Redox Signal, 2018. **29**(17): p. 1756-1773.
68. Chiang, S.K., S.E. Chen, and L.C. Chang, *A Dual Role of Heme Oxygenase-1 in Cancer Cells.* Int J Mol Sci, 2018. **20**(1).
69. Zhou, Y., X. Zhang, and A. Klibanski, *MEG3 noncoding RNA: a tumor suppressor.* Journal of molecular endocrinology, 2012. **48**(3): p. R45-R53.
70. Bhattacharjee, S., J. Li, and R.H. Dashwood, *Emerging crosstalk between long non-coding RNAs and Nrf2 signaling.* Cancer Letters, 2020. **490**: p. 154-164.
71. Kurinna, S. and S. Werner, *NRF2 and microRNAs: new but awaited relations.* (1470-8752 (Electronic)).

72. Cheng, X., C.H. Ku, and R.C. Siow, *Regulation of the Nrf2 antioxidant pathway by microRNAs: New players in micromanaging redox homeostasis.* Free Radic Biol Med, 2013. **64**: p. 4-11.
73. Ashrafizadeh, M., et al., *MicroRNA-mediated regulation of Nrf2 signaling pathway: Implications in disease therapy and protection against oxidative stress.* Life Sci, 2020. **244**: p. 117329.
74. Wang, Y., et al., *Biological function and mechanism of lncRNA-MEG3 in Tenon's capsule fibroblasts proliferation: By MEG3-Nrf2 protein interaction.* Biomed Pharmacother, 2017. **87**: p. 548-554.
75. Wu, L., et al., *LncRNA MEG3 promotes melanoma growth, metastasis and formation through modulating miR-21/E-cadherin axis.* Cancer Cell International, 2020. **20**(1): p. 12.
76. Li, P., et al., *LncRNA MEG3 repressed malignant melanoma progression via inactivating Wnt signaling pathway.* J Cell Biochem, 2018. **119**(9): p. 7498-7505.
77. Long, J. and X. Pi, *lncRNA-MEG3 Suppresses the Proliferation and Invasion of Melanoma by Regulating CYLD Expression Mediated by Sponging miR-499-5p.* Biomed Res Int, 2018. **2018**: p. 2086564.
78. Latina, A., et al., *ΔNp63 targets cytoglobin to inhibit oxidative stress-induced apoptosis in keratinocytes and lung cancer.* Oncogene, 2016. **35**(12): p. 1493-1503.
79. Wang, G.X., et al., *ΔNp63 Inhibits Oxidative Stress-Induced Cell Death, Including Ferroptosis, and Cooperates with the BCL-2 Family to Promote Clonogenic Survival.* Cell reports, 2017. **21**(10): p. 2926-2939.
80. Yan, W. and X. Chen, *GPX2, a direct target of p63, inhibits oxidative stress-induced apoptosis in a p53-dependent manner.* J Biol Chem, 2006. **281**(12): p. 7856-62.
81. Moi, P., et al., *Isolation of NF-E2-related factor 2 (Nrf2), a NF-E2-like basic leucine zipper transcriptional activator that binds to the tandem NF-E2/AP1 repeat of the beta-globin locus control region.* Proc Natl Acad Sci U S A, 1994. **91**(21): p. 9926-30.
82. Singh, S., et al., *Calcineurin Activates Cytoglobin Transcription in Hypoxic Myocytes*.* Journal of Biological Chemistry, 2009. **284**(16): p. 10409-10421.
83. Jaganjac, M., et al., *Induction of CMV-1 promoter by 4-hydroxy-2-nonenal in human embryonic kidney cells.* Acta Biochim Pol, 2010. **57**(2): p. 179-83.
84. Bruening, W., et al., *Activation of stress-activated MAP protein kinases up-regulates expression of transgenes driven by the cytomegalovirus immediate/early promoter.* Nucleic Acids Res, 1998. **26**(2): p. 486-9.

5.8 SUPPLEMENTARY

Table S5.1. Primer sequences of reference and target genes used in this study, including amplification efficiency and amplicon size.

Gene symbol	Forward primer (5' → 3')	Reverse primer (5' → 3')	Efficiency	Amplicon size
Reference gene				
B2M	TGCTGTCTCCATGTTTGATGTATCT	TCTCTGCTCCCCACCTCTAAGT	2.04	86
YWHAZ	ACTTTTGGTACATTGTGGCTTCAA	CCGCCAGGACAAACCAGTAT	2.03	94
Target gene				
CYGB	CTCTATGCCAACTGCGAG	AACTGGCTGAAGTACTGCTTG	2.04	89
HO-1	ATGACACCAAGGACCAGAGC	GTGTAAGGACCCATCGGAGA	2.01	153
NRF2	TCCAGTCAGAAACCAGTGGAT	GAATGTCTGCGCCAAAAGCTG	1.98	230
MEG3	GCATTAAGCCCTGACCTTTG	TCCAGTTTGCTAGCAGGTGA	1.91	119

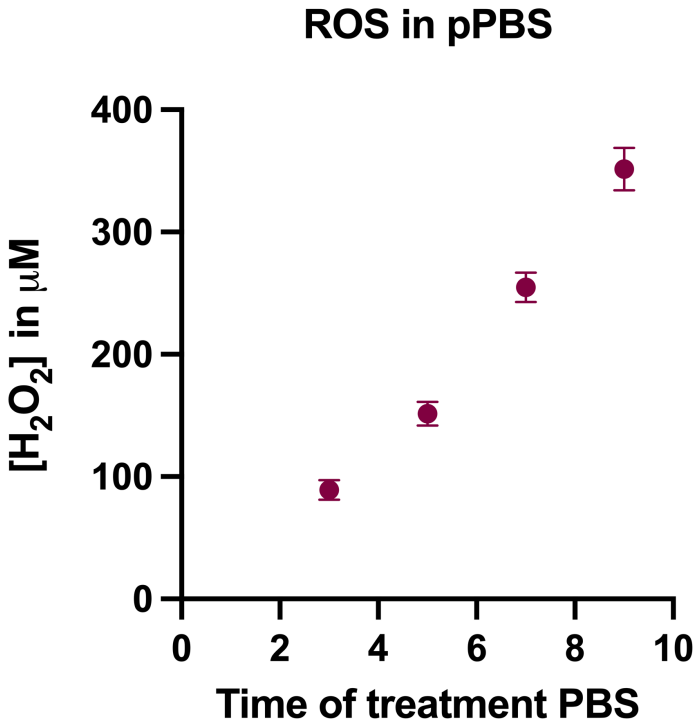

Figure S5.1. ROS production. The fluorometric measurement of H_2O_2 upon different NTP treatment times of pPBS. A linear increase in H_2O_2 concentration was observed demonstrating the effectiveness of NTP in generating ROS (mean ± S.E.M; n = 3).

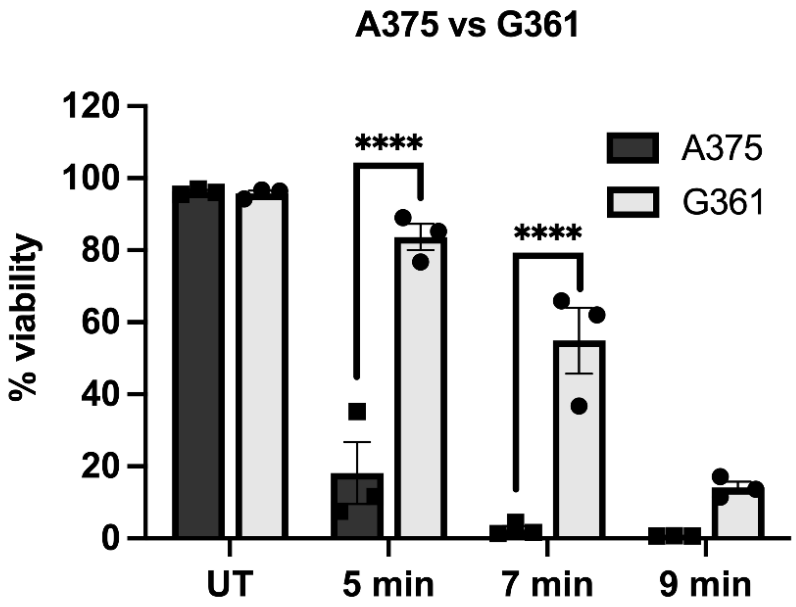

Figure S5.2. Comparison viability A375 and G361. Comparison of the average cell viability of A375 and G361 24 hours after treatment, for each of the investigated treatment times (5, 7, and 9 min) of pPBS. (mean ± S.E.M; n = 3) Individual values of replicates are depicted as black squares (A375) or dots (G361). One-way ANOVA (****p ≤ 0.0001).

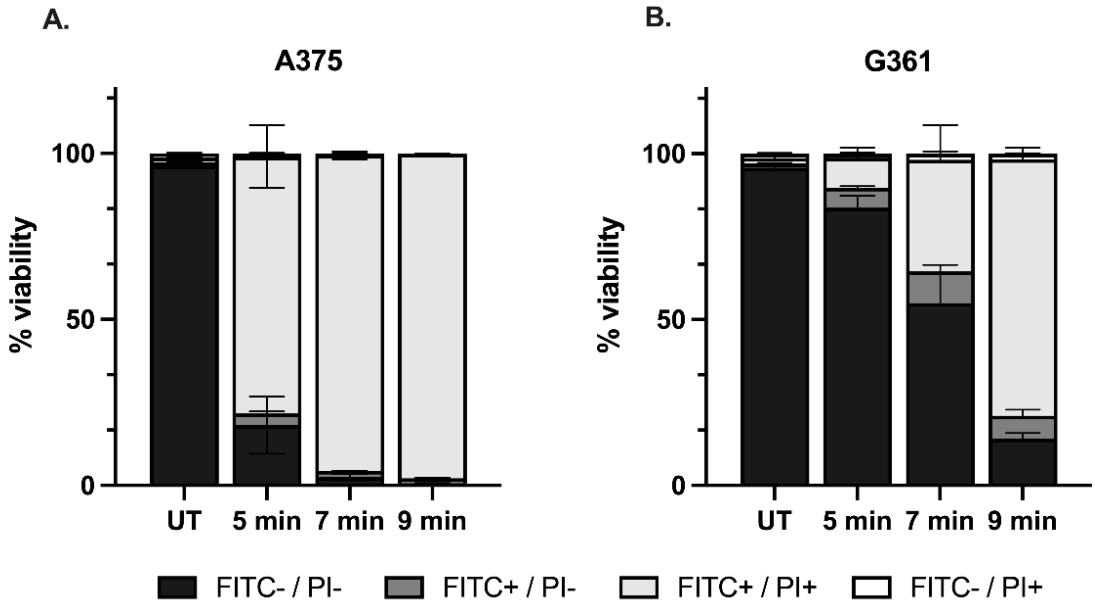

Figure S5.3. Cell death after pPBS treatment. (A & B) Flow cytometric analysis of cell death 24 hours after treatment by Annexin-V FITC and PI staining. After 24 hours, almost all dead cells were double positive ($FITC^+/PI^+$). Doubles positive cells indicate the presence of late-apoptotic and/or cells that died through necrosis. Only a small percentage early apoptotic cells ($FITC^+/PI^-$) were measured in A375. With G361 cells, a relatively larger fraction of early-apoptotic cells were present 24 hours post treatment. (mean ± S.E.M; n = 3)

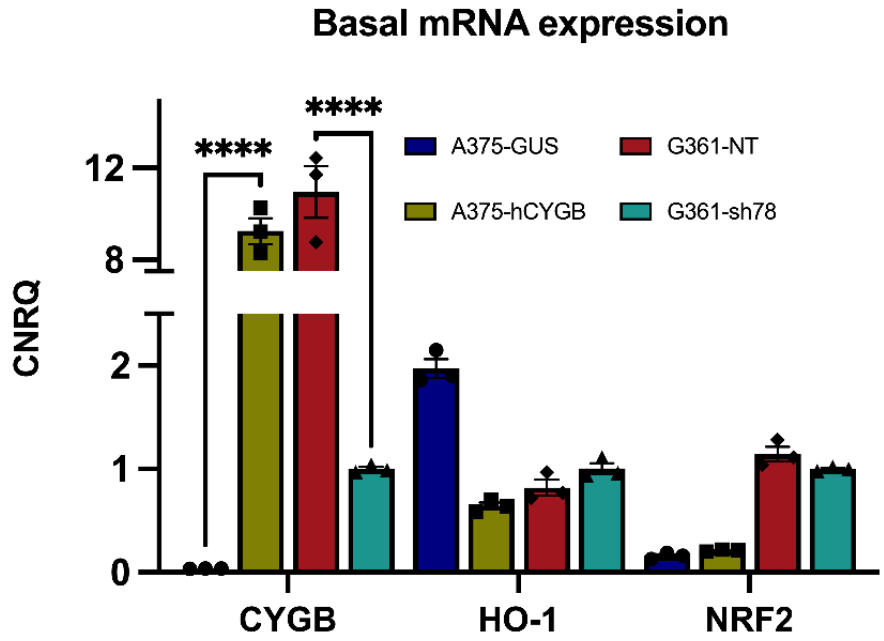

Figure S5.4. Basal mRNA expression levels. Average mRNA expression levels of CYGB, HO-1, and NRF2 in A375-GUS, A375-hCYGB cells, G361-shCTR, and G361-shCYGB. Calibrated normalized relative quantities were normalized to B2M and YWHAZ (mean ± S.E.M; n = 3). Individual values of replicates are depicted as black dots, squares, clubs, or triangles. One-way ANOVA (****p ≤ 0.0001).

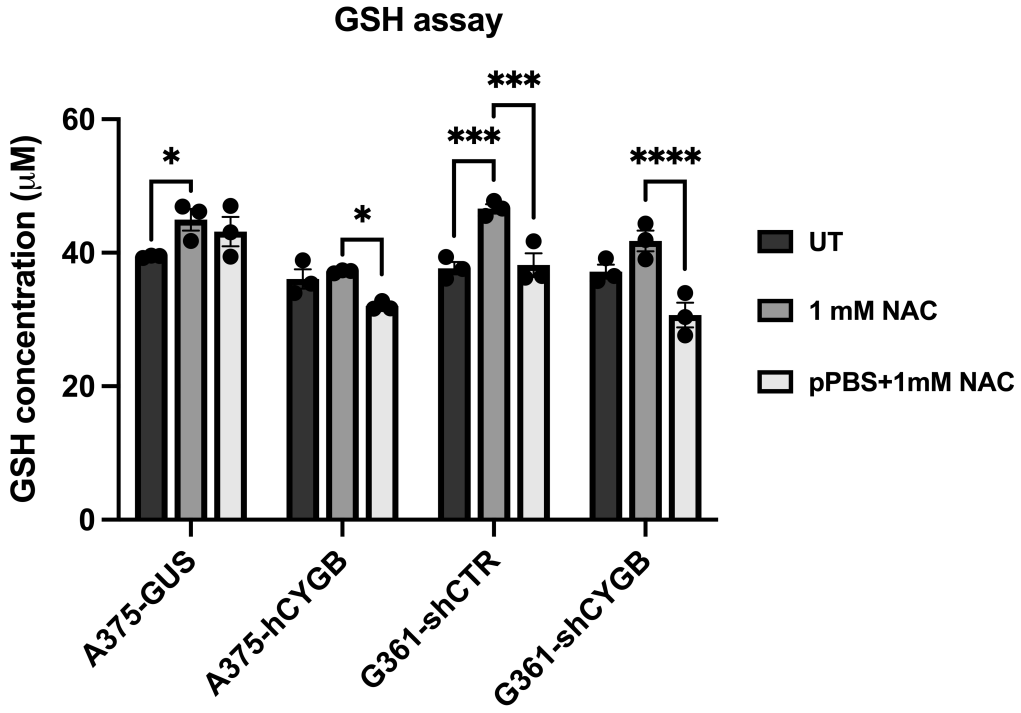

Figure S5.5. Total cellular glutathione levels. Detection of glutathione (GSH) using the luminscence-based GSH-Glo Glutathione Assay. GSH activity was measured in untreated (UT), 1mM N-acetyl cysteine (NAC), or NAC and pPBS co-treated A375-GUS, A375-hCYGB, G361-shCTR, and G361-shCYGB cells. A GSH standard curve was used to calculate the GSH concentration. Results are depicted as the mean of three independent experiments ± S.E.M. Two-way ANOVA (*p ≤ 0.05, **p ≤ 0.01, ***p ≤ 0.001, ****p ≤ 0.0001).

CHAPTER VI

CYTOGLOBIN SILENCING PROMOTES MELANOMA MALIGNANCY BUT SENSITIZES FOR FERROPTOSIS AND PYROPTOSIS THERAPY RESPONSE

Published as:

De Backer J, Maric D, Zuhra K, Bogaerts A, Szabo C, Vanden Berghe W, Hoogewijs D. *Cytoglobin Silencing Promotes Melanoma Malignancy but Sensitizes for Ferroptosis and Pyroptosis* Therapy Response. *Antioxidants*. 2022; 11(8):1548. https://doi.org/10.3390/antiox11081548

6.1 ABSTRACT

Despite recent advances in melanoma treatment, there are still patients that either do not respond or develop resistance. This unresponsiveness and/or acquired resistance to therapy could be explained by the fact that some melanoma cells reside in a dedifferentiated state. Interestingly, this dedifferentiated state is associated with greater sensitivity to ferroptosis, a lipid peroxidation-reliant, iron-dependent form of cell death. Cytoglobin (CYGB) is an iron hexacoordinated globin that is highly enriched in melanocytes and frequently downregulated during melanomagenesis. In this study, we investigated the potential effect of CYGB on the cellular sensitivity towards (1S, 3R)-RAS-selective lethal small molecule (RSL3)-mediated ferroptosis in the G361 melanoma cells with abundant endogenous expression. Our findings show that an increased basal ROS level and higher degree of lipid peroxidation upon RSL3 treatment contribute to the increased sensitivity of CYGB knockdown G361 cells to ferroptosis. Furthermore, transcriptome analysis demonstrates the enrichment of multiple cancer malignancy pathways upon CYGB knockdown, supporting a tumor-suppressive role for CYGB. Remarkably, CYGB knockdown also triggers activation of the NOD-, LRR- and pyrin domain-containing protein 3 (NLRP3) inflammasome and subsequent induction of pyroptosis target genes. Altogether, we show that silencing of CYGB expression modulates cancer therapy sensitivity via regulation of ferroptosis and pyroptosis cell death signaling pathways.

6.2 INTRODUCTION

Cutaneous melanoma is the most aggressive form of skin cancer and incidence has risen consistently over the last few decades [1], mainly through increased exposure to ultraviolet radiation [2]. When melanoma is diagnosed in the early stages, surgical resection of the lesion leads to a 5-year survival of 99%. However, metastatic melanoma has a much less favorable prognosis, with a recorded 5-year survival of 20% [1].

In 2004, no systemic therapy available for melanoma had shown any survival benefit [3]. Since then, several immune-based therapies that mediate checkpoint inhibition have been approved for the treatment of advanced melanoma, including antibodies designed to block cytotoxic T-lymphocyte-associated protein 4 (CTLA4; ipilimumab) and programmed cell death protein 1 (PD-1; nivolumab and pembrolizumab) [4]. Melanoma has one of the highest mutational burdens among solid tumors [3]. Approximately half of all melanomas have v-Raf murine sarcoma viral oncogene homolog B (*BRAF)* mutations, and 80–90% of these mutations are a missense V600E mutation, where the wild-type amino acid 600 (a valine) is replaced by a glutamic acid residue, resulting in the constitutive activation of mitogen-activated protein kinase kinase (MEK) and extracellular signal regulated kinase (ERK) signaling [5]. Dual inhibition of this pathway using a combination of BRAF and MEK inhibitors (dabrafenib and trametinib; vemurafenib and cobimetinib; encorafenib and binimetinib) has demonstrated improved overall survival [6]. However, despite all these advances in immunotherapy and targeted therapy, there are still patients that either do not respond or develop resistance.

Recently, Tsoi et al. suggested that this unresponsiveness and/or acquired resistance to therapy could be explained by the fact that melanoma cells can exist in at least four different differentiation states [7]. Some melanoma cells predominantly reside in a dedifferentiated state, while others acquire this state in response to treatment. Interestingly, this dedifferentiated state is associated with greater sensitivity to ferroptosis. Originally, ferroptosis was identified as a unique form of cell death in mammalian cancer cells by studying the effects of the small molecule eradicator of RAS and ST (erastin), (1S, 3R)-RAS-selective lethal small molecule RSL3 and related compounds [8]. Ferroptotic cell death distinguishes itself biochemically from other types of cell death through the requirement of phospholipid peroxidation, a process reliant on iron accumulation, reactive oxygen species (ROS) and polyunsaturated fatty acid-containing phospholipids (PUFA-PLs) [9].

Cytoglobin (CYGB) is a ubiquitously expressed, hexacoordinated globin believed to be involved in the regulation of redox homeostasis. Many antioxidative functions have been assigned to CYGB, including nitric oxide dioxygenase [10], nitrite reductase [11], superoxide dismutase [12] and peroxidase activity [13]. Furthermore, CYGB expression has been found to be regulated by oxidative stress and hypoxia [14, 15]. Although CYGB is expressed in many different cell types and tissues, CYGB is particularly highly enriched in pigment-producing melanocytes and frequently downregulated during melanocyte-to-melanoma transition [16]. Reduced CYGB expression through hypermethylation has also been reported in other cancer cell types, indicating that CYGB potentially serves a tumor-suppressive function [17-22].

In this study, we investigated the potential effect of CYGB on the cellular sensitivity towards RSL3-mediated ferroptosis in G361 melanoma cells that express highly abundant endogenous levels of CYGB [16]. We applied lentiviral shRNA approaches to generate G361 cells with stable knockdown of CYGB expression to measure the effects of CYGB silencing on cellular bioenergetics, redox signaling and viability via redox-sensitive fluorescent DCF and ARE-dependent luciferase assays. We further employed RNA sequencing to study the CYGB-dependent gene clusters and enriched pathways under RSL3-induced ferroptosis conditions. Collectively, our results suggest a cytoprotective role of CYGB in the cellular response to ferroptosis in melanoma via the interplay of ferroptosis and pyroptosis cell death pathways.

6.3 EXPERIMENTAL

6.3.1 Cell Culture

G361 (ATCC CRL-1424; Manassas, VA, USA) melanoma cells were maintained in Dulbecco's Minimum Essential Media (DMEM) (Gibco, Life Technologies; Waltham MA, USA), containing L-glutamine, supplemented with 10% heat-inactivated fetal bovine serum (FBS, Gibco, Fisher Scientific, Waltham, MA, USA) and 1% Penicillin/Streptomycin (10,000 Units/mL P; 10,000 µg/mL S; Gibco, Life Technologies; Waltham, MA, USA). Cells were incubated in a humidified 5% CO_2 atmosphere at 37 °C and were routinely subcultured after trypsinization.

6.3.2 Generation of Stable Knockdown and Overexpressed Cell Lines

Expression vectors encoding short hairpin RNA (shRNA) sequences targeting human CYGB in a pLKO.1-puro plasmid were purchased from Sigma-Aldrich (Burlington, MA, USA) (shCYGB: order number TRCN0000059378). Control cells (shCTR) were transfected with a non-targeting control shRNA under the control of a U6 promoter in a pLKO.1 puromycin resistance vector (Sigma-Aldrich), as described previously [23]. Viral particles were produced in HEK293T cells by co-transfection of the respective transfer vector (3 μg) with the packaging plasmids pLP1 (4.2 μg), pLP2 (2 μg) and pVSV-G (2.8 μg, all from Invitrogen) using $CaCl_2$ transfection, as described before [24]. G361 cells were transduced with lentiviral-pseudotyped particles and cell pools were cultured in DMEM supplemented with 10% FBS and 1% Penicillin/Streptomycin with the appropriate antibiotic for selection.

6.3.3 Determination of Cellular Bioenergetics

Cellular bioenergetics was measured by the Extracellular Flux Analysis method. Briefly, G361, G361-shCYGB and G361-shCTR cells were seeded on XFe24-well microplates (Agilent technologies, Santa Clara, CA, USA) at 2×10^4 cells per well and incubated at 37 °C and 5% CO_2 for 24 h. The day after, cells were washed twice with DMEM at pH 7.4 supplemented with L-glutamine (2 mM, Gibco), sodium pyruvate (1 mM, Sigma-Aldrich, Burlington, MA, USA) and glucose (10 mM, Sigma-Aldrich). The plate was then incubated in a CO_2-free incubator at 37 °C for 1 h to allow temperature and pH equilibration. The assay protocol consisted of 3 min mix, 3 min wait and 3 min measurement cycles, with measurement of basal values of oxygen consumption rate (OCR) (2 cycles), followed by injection of 1 μM oligomycin, used to evaluate the ATP generation rate (2 cycles). Afterward, 0.2 μM carbonyl cyanide-4-trifluoromethoxy phenylhydrazone (FCCP) was employed to evaluate the maximal mitochondrial respiratory capacity (2 cycles). Finally, 0.5 μM of rotenone and antimycin A was injected to inhibit the electron transport through complex I and III, respectively, aiming to detect the extra-mitochondrial OCR (2 cycles). At the end of the assay, total protein per well was measured using the Bradford reagent (BioRad, Hercules, CA, USA) and OCR values were normalized to the protein amount. Data were analyzed with Wave (v. 2.6; Agilent Technologies, Santa Clara, California, USA) and graphed with GraphPad Prism 8 (GraphPad Software Inc.; San Diego, California, USA).

6.3.4 H_2DCF-DA Assay

G361-shCTR and G361-shCYGB were seeded in black, clear-bottom 24-well plates at 6×10^5 cells per well and incubated with 10 µM H_2DCF-DA for 30 min in the dark. Fluorescence was measured using a 96-well fluorometer (Infinite 200Pro, Tecan, Männedorf, Switzerland).

6.3.5 Cell Viability

Cell viability was determined using the vital dye propidium iodide (PI, Invitrogen, Waltham, MA, USA) to allow the detection of dead cells. The day before treatment, 5×10^4 cells were seeded in a 24-well plate, containing complete DMEM. The next day, cells were treated with 7.5 µM RSL3 (for dose kinetics, see Figure S1) and incubated for 24 h in a humidified 5% CO_2 atmosphere at 37 °C. Cells were collected in round-bottom polystyrene tubes (Falcon, Corning, NY, USA), washed (FACS buffer; 1x phosphate-buffered saline (PBS), 3% FBS, 1mM ethylenediaminetetraacetic acid (EDTA)) and centrifuged for 5 min at 1500 rpm before being resuspended in ice-cold PBS. PI (500 ng) was added immediately before measurement on the CytoFLEX flow cytometer (Beckman Coulter, Brea, CA, USA). Data were analyzed using FlowJo software (FlowJo, BD, Franklin Lakes, NJ, USA).

6.3.6 Lipid Peroxidation Assay

The Image-iT Lipid Peroxidation Kit (Thermo Scientific, Waltham, MA, USA) was used for the detection of lipid peroxidation in live cells through oxidation of BODIPY™ 581/591 C11 reagent, according to the manufacturer's protocol. Briefly, 5×10^4 cells were seeded in a 24-well plate, containing complete DMEM. The next day, cells were treated with 7.5 µM RSL3 and incubated for 4 h in a humidified 5% CO_2 atmosphere at 37 °C. Thirty minutes before collection, 10 µM reagent was added. Upon oxidation by lipid hydroperoxides, the reagent displays a shift in peak fluorescence emission from ~590 nm to ~510 nm. Fluorescence from live cells shifts from red to green, providing a ratiometric (red over green signal) indication of lipid peroxidation. The more lipid peroxidation, the lower the red over green ratio will be. Fluorescence was measured using the CytoFLEX flow cytometer (Beckman Coulter, Brea, CA, USA). Cumene hydroperoxide was used as a positive control.

6.3.7 Luciferase Reporter Assays

First, 1×10^5 G361 cells were transiently transfected with 250 ng ARE-driven reporter plasmid and 50 ng NRF2-expressing plasmid, in a twelve-well format, using JetOptimus (Polyplus, Illkirch-graffenstaden, Alsace, France). To control for differences in transfection efficiency and extract preparation, 25 ng pRL-SV40 *Renilla* luciferase reporter vector (Promega, Madison, WI, USA) was co-transfected. Luciferase activities of triplicate wells were determined using the Dual Luciferase Reporter Assay System (Promega, Madison, WI, USA), as described before [25]. Reporter activities were expressed as relative firefly/*Renilla* luciferase activities (R.L.U.). All reporter gene assays were performed at least 3 times independently.

6.3.8 2.8. RNA Extraction, Purification and cDNA Conversion

RNA extraction and purification was performed using a PureLink RNA Mini Kit (Invitrogen, Waltham, MA, USA), according to the manufacturer's instructions. RNA concentration and purity was measured with an Epoch spectrophotometer (BioTek, Winooski, VM, USA) by measuring absorbance at a 260/280 nm ratio. cDNA (1 µg) was reverse transcribed using Superscript II reverse transcriptase (Invitrogen, Waltham, MA, USA), according to the manufacturer's protocol.

6.3.9 Real-Time Quantitative PCR

Amplification of cDNA and subsequent quantification was performed using the StepOne Real-Time PCR system (Applied Biosystems, Waltham, MA, USA) using a Power SYBR Green Master Mix (Applied Biosystems, Waltham, MA, USA). The following conditions were used during PCR: 95 °C for 10 min and 40 cycles of 95 °C for 15 s; 60 °C for 1 min. All PCR reactions were performed in duplicate for three biological replicates. Results were subsequently analyzed using qbase+ software (v3.2, Biogazelle, Zwijnaarde, Ghent, Belgium), as described before [15]. A list of used reference and target genes, together with their primer sequences, amplification efficiency and amplicon size, is given in Table S6.1. All primers were manufactured and provided by Eurogentec (Seraing, Liège, Belgium).

6.3.10 Protein Extraction and Quantification

Lysis buffer, containing 10 mM Tris HCl (pH 8), 1 mM EDTA, 400 mM NaCl, 1% NP-40 and protease inhibitors (Sigma-Aldrich, Burlington, MA, USA), was used to lyse cells, as described before [23]. Lysed cells were placed on a rotating arm at 4 °C for 30 min to allow optimal performance of the

lysis buffer. The suspension was subsequently sonicated for 1 min at 60 Hz to degrade any potential formed DNA aggregates. Finally, samples were centrifuged at 10,000× *g* for 15 min and the protein-containing supernatant was collected. Protein concentrations were determined using the BCA Protein Assay Kit (ThermoFisher Scientific, Waltham, MA, USA).

6.3.11 Immunoblotting

Extracted proteins for immune-based Western blotting were first separated, according to molecular weight, using sodium dodecyl sulphate polyacrylamide gel electrophoresis (SDS-PAGE) gels, followed by electrotransfer to nitrocellulose membranes (Amersham Hybond-ECL, GE Healthcare, Chicago, IL, USA), as described before [26]. Equal amounts of protein and volume were loaded onto a 12.5% polyacrylamide gel for CYGB, heme oxygenase 1 (HO-1) and NF E2-related factor 2 (NRF2). Membranes were blocked in TBS-T (Tris-buffered saline; 0.1% Tween-20), containing 5% non-fat dry milk, for 1 h at room temperature. After blocking, membranes were incubated overnight at 4 °C with primary antibodies (anti-CYGB, Proteintech, Rosemont, IL, USA; 13317-1-AP; anti-β-2-Microglobulin (B2M), Proteintech, 13511-1-AP; anti-β-Actin (ACTB), Santa Cruz, sc-47778; anti-HO-1, Proteintech, 10701-1-AP; anti-NRF2, Proteintech, 16396-1-AP). The following day, membranes were washed with TBST-T and incubated for 1 h with horseradish-conjugated secondary antibodies (anti-rabbit IgG HRP, Sigma, GENA934-1ML; anti-mouse IgG HRP, Invitrogen, 31430). The signal was revealed using ECL Prime (Amersham, GERPN2232) on an Amersham Imager 680 (GE Life Sciences; Piscataway, NJ, USA) and exported and quantified using the Image Studio™ program (LI-COR Biosciences, Lincoln, NE, USA).

6.3.12 RNA sequencing

Total RNA sample quality was assessed with TapeStation (Agilent Technologies, Santa Clara, CA, USA) and Qubit assay (Invitrogen, Waltham, MA, USA). Total RNA samples with an RNA integrity number (RIN) > 7.0 and purity (OD_{260}/OD_{280}) ratio 1.8–2.2 were used for subsequent experiments. Sequence libraries were generated using the poly(A) RNA selection method and sequenced by GENEWIZ (Azenta Life Sciences, Chelmsford, MA, USA). An independent library was constructed for each of the triplicate samples. High-throughput RNA sequencing was performed with pair end 150 bp reading length on an Illumina NovaSeq 6000 (Illumina, San Diego, CA, USA) sequencer. The DESeq2 analysis was used to estimate variance–mean dependence and test for differential expression [27]. Genes with a *p*-adjusted value ≤ 0.05 were considered differentially expressed.

Genes with a *p*-adjusted value ≤ 0.05 and an absolute $\log_2$ fold change ≥ 1 were recognized as significantly differentially expressed genes (DEGs). Fast gene set enrichment analysis (fGSEA) was performed on the complete (normalized) count data [28] using the hallmark gene sets [29]. A gene ontology (GO) enrichment analysis was performed on the DEGs by implementing the software GeneSCF (v1.1-p2). The Gene Ontology Analysis (GOA) human GO list was used to cluster the set of genes based on their biological processes and determine their statistical significance [30]. A list of genes clustered based on their gene ontologies was generated. Volcano plots were generated using the EnhancedVolcano R package to visualize the results of the differential expression analyses.

6.4 RESULTS

6.4.1 CYGB Knockdown Influences Cellular Bioenergetics

To investigate the role of CYGB in melanoma cells, we first established an shRNA-mediated CYGB knockdown cell line (G361-shCYGB) as well as a knockdown control line (G361-shCTR). RT-PCR and immunoblotting experiments illustrated efficient knockdown of CYGB at the mRNA and protein level, respectively (Figure 6.1A & B).

Next, the mitochondrial oxidative phosphorylation was analyzed in G361, G361-shCTR and G361-shCYGB cells through quantification of the oxygen consumption rate (OCR) using the Seahorse Extracellular Flux Analyzer (Figure 6.1C–G). Knockdown of CYGB resulted in an overall decrease in OCR (Figure 6.1C). Besides the OCR, additional respiratory parameters were measured by using different pharmacological compounds of the mitochondrial function. Initially, the baseline cellular OCR was measured. After subtraction of the non-mitochondrial respiration, a significant reduction in basal respiration was observed in G361-shCYGB cells compared to both G361 and G361-shCTR cells (Figure 6.1D). To determine ATP-linked respiration, the complex V inhibitor oligomycin was used. ATP production was significantly decreased in the CYGB knockdown cell line (Figure 6.1E). Subsequently, the maximal respiration was measured after addition of the protonophore FCCP. Similarly, a significant reduction in the maximal respiratory rate in G361-shCYGB was observed compared to both G361 and G361-shCTR (Figure 6.1F). Lastly, by inhibiting complex III and I, the non-mitochondrial respiration was measured. Rotenone and antimycin A inhibition showed a significant decrease in the spare respiratory capacity (Figure 6.1G).

Collectively, these data suggest that CYGB deficiency in G361 cells negatively affects mitochondrial oxidative phosphorylation.

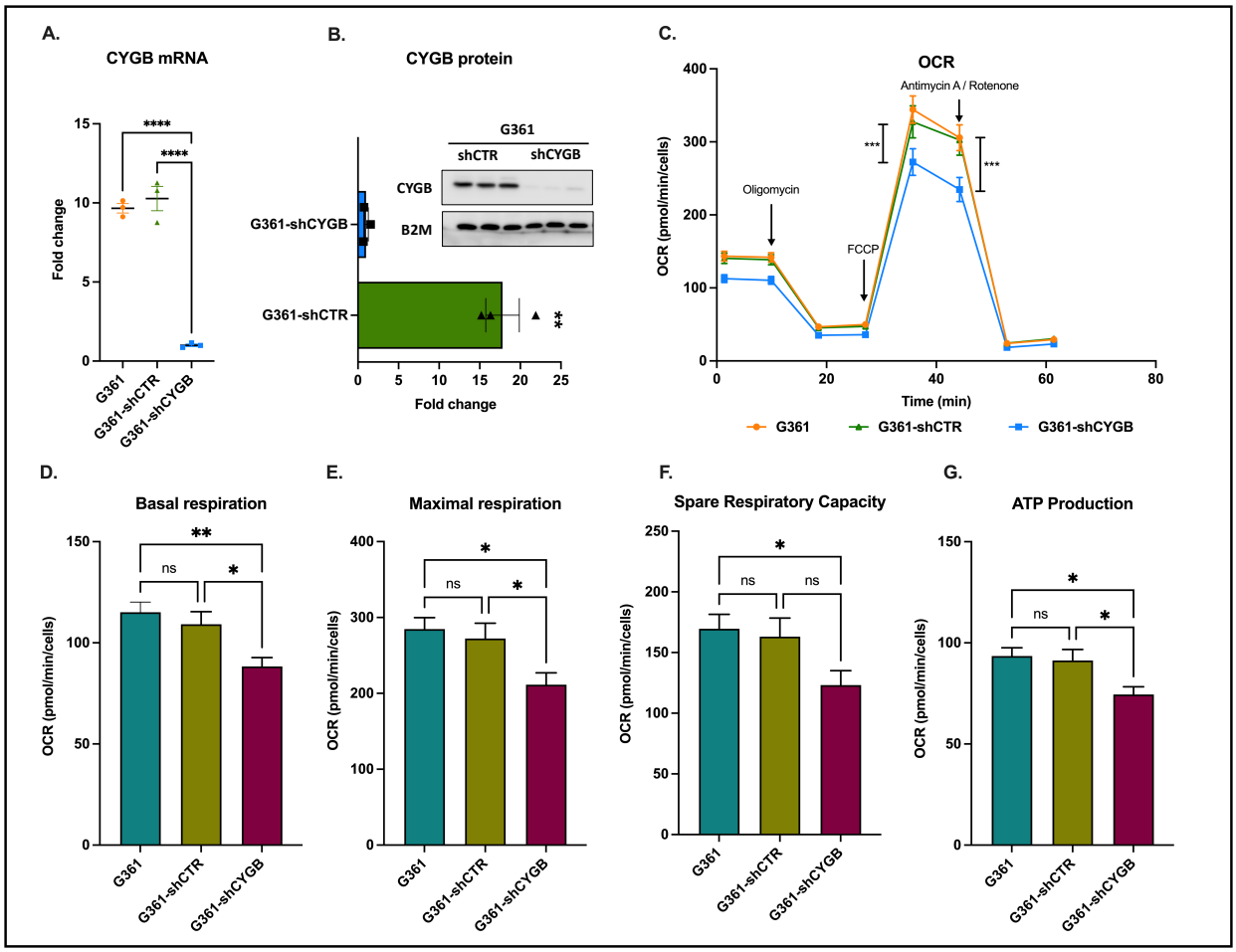

Figure 6.1 CYGB knockdown reduces mitochondrial respiration. Knockdown of CYGB in G361 cells was validated at mRNA (**A**) and protein (**B**) level. (**C**) The average oxygen consumption rate (OCR) was measured between G361 (untransduced), G361-shCTR (transduction control) and G361-shCYGB (CYGB knockdown). (**D**) Initially, the basal respiration rate was measured. (**E**) After oligomycin injection, ATP production was measured. (**F**) Subsequently, the maximal respiration was measured, after FCCP injection. (**G**) The spare respiratory capacity was measured upon addition of antimycin A and rotenone. Results are depicted as the mean with S.E.M. of three independent experiments (n = 3). One-way ANOVA (**A**), Student *t*-test (**B**), two-way ANOVA (**C**–**G**) (* $p \leq 0.05$; ** $p \leq 0.01$; *** $p \leq 0.001$; **** $p \leq 0.0001$). FCCP: Carbonyl cyanide-4 (trifluoromethoxy) phenylhydrazone.

6.4.2 CYGB Expression Affects ROS Homeostasis and Ferroptosis Sensitivity

A potential effect of CYGB knockdown in G361 melanoma cells on the intracellular ROS levels was assessed using the fluorescent dye H_2DCF-DA (Figure 6.2A). The measured fluorescent intensity was significantly higher in the G361-shCYGB cell line, which implies that CYGB knockdown leads to augmented levels of intracellular ROS. Following these findings, the sensitivity to RSL3 was assessed. RSL3 treatment resulted in a decrease in cell viability in both cell lines (Figure 6.2B). However, cell viability in G361-shCYGB was significantly lower compared to the control.

Furthermore, the level of lipid peroxidation occurring 4h after RSL3 treatment was measured. Although RSL3 induced lipid peroxidation in both G361-shCTR and G361-shCYGB, lipid peroxidation was noticeably higher in CYGB knockdown cells (Figure 6.2F; see also Figure S6.2).

As ferroptosis is regulated by the transcription factor nuclear factor erythroid 2-related factor 2 (NRF2) and its downstream targets, expression levels of NRF2 and HO-1 were measured. RSL3 treatment greatly induced HO-1 mRNA expression but only slightly increased NRF2 levels (Figure 6.2C). No significant differences in mRNA levels between G361-shCTR and G361-shCYGB were observed. Immunoblotting experiments showed, however, that both NRF2 and HO-1 protein levels were dramatically increased in both cell lines after RSL3 treatment (Figure 6.2D & E). Additionally, CYGB protein expression was slightly elevated in both G361-shCTR and G361-shCYGB.

Of special note, a clear difference in the basal expression of NRF2 and HO-1 was observed, with protein levels being significantly decreased in CYGB knockdown G361-shCYGB cells (Figure 6.2E; see also Figure S6.3). However, RSL3 treatment led to a significantly higher fold change in HO-1 protein levels in G361-shCYGB cells compared to G361-shCTR. No difference was observed in NRF2 protein induction between G361-shCTR and G361-shCYGB cells.

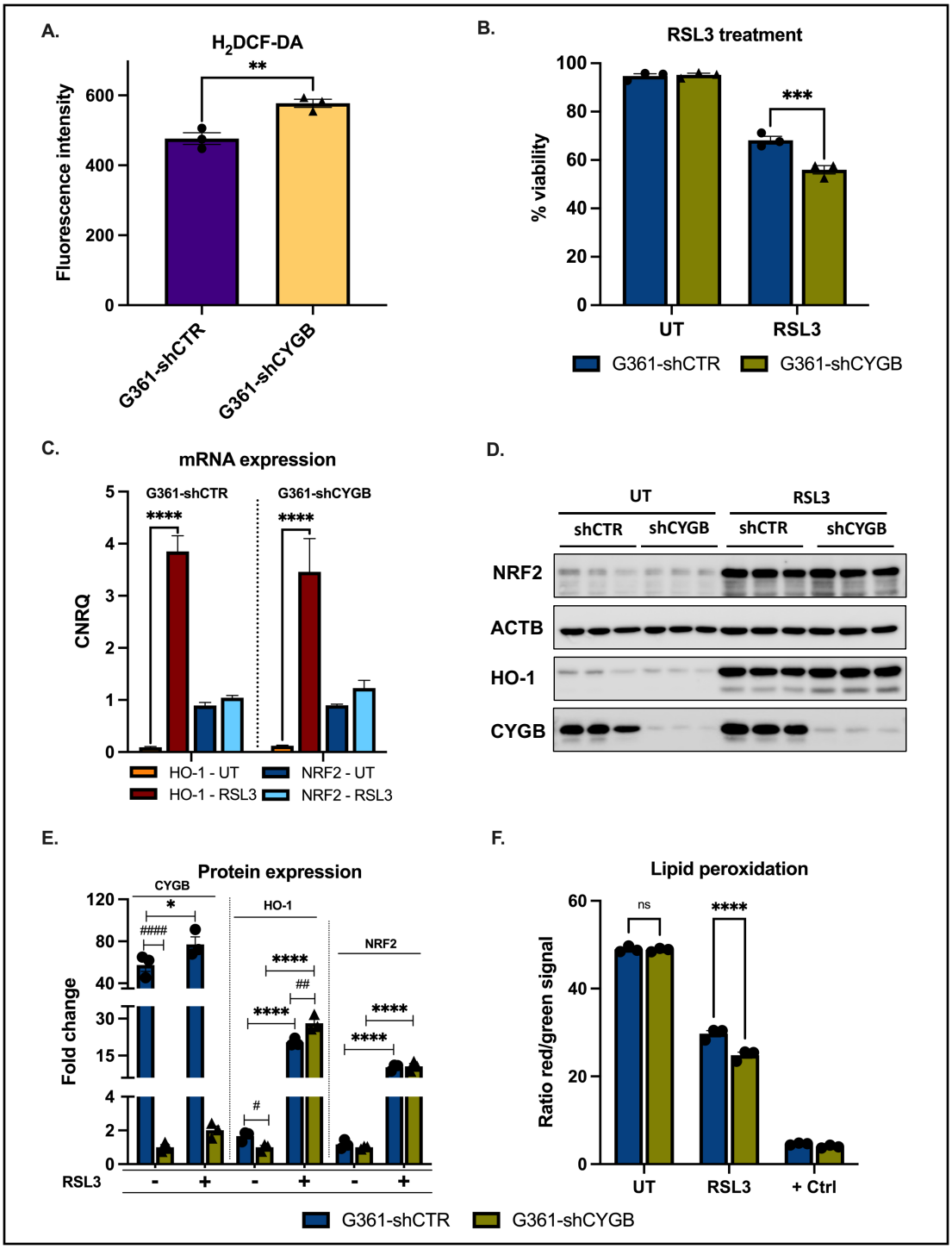

Figure 6.2. Cytoprotective effect of CYGB. (**A**) Knockdown of CYGB increased basal intracellular ROS levels. (**B**) G361-shCTR and G361-shCYGB cells were treated with 7.5 µM RSL3 and cell viability was measured after 24 h using propidium iodide (PI) staining. (**C**) The average calibrated normalized relative quantities (CNRQ) of HO-1 and NRF2 mRNA under basal conditions (UT) or upon RSL3 treatment. CNRQ values were normalized to B2M and YWHAZ. (**D**) Immunoblotting results of NRF2, HO-1 and CYGB 6h after RSL3 treatment. ACTB was used as loading control. (**E**) The average fold change in protein expression of HO-1, NRF2 and CYGB in G361-shCTR and G361-shCYGB cells, compared to the untreated G361-shCYGB samples (set as 1). Measured immunoblot signals were normalized to the loading control ACTB. (**F**) Average ratio of the measured red (reduced) over green (oxidized) signal of the BODIPY 581/591 C11 reagent in G361-shCTR and G361-shCYGB cells. Cells were either untreated or treated with 7.5 µM RSL3 or 100 µM cumene hydroperoxide (positive control). All results are depicted as the mean with S.E.M. of three independent experiments (n = 3). (**A**) Student's *t*-test (** $p \leq 0.01$), (**B**–**F**) two-way ANOVA (*/# $p \leq 0.05$; **/## $p \leq 0.01$; *** $p \leq 0.001$; **** $p \leq 0.0001$).

6.4.3 CYGB-Dependent Antioxidant Response Element-Driven Luciferase Activity Is Increased upon RSL3 Treatment and NRF2 Overexpression

To obtain additional independent support of the NRF2-dependent regulation of the antioxidant response through binding to the antioxidant response element (ARE), a reporter assay using an ARE-driven luciferase gene was employed. Induction of ARE-driven luciferase activity was assessed under RSL3-treated conditions (Figure 6.3). RSL3 treatment clearly increased luciferase activity in both G361 control and CYGB knockdown cells compared to the untreated control. A small tendency towards increased activity was also seen under RSL3-treated conditions in CYGB-deficient cells versus control cells. Overexpression of NRF2 profoundly increased luciferase activity even further in both RSL3-treated and untreated cells. Moreover, the measured luciferase activity was mostly increased in RSL3-treated NRF2-overexpressing G361-shCTR and G361-shCYGB cells. Interestingly, ARE-driven luciferase activity was significantly higher in CYGB knockdown cells compared to G361-shCTR NRF2 overexpression cells, and substantially elevated in RSL3-treated cells (Figure 6.3). However, under basal conditions, luciferase activity was significantly lower in G361-shCYGB compared to G361-shCTR cells.

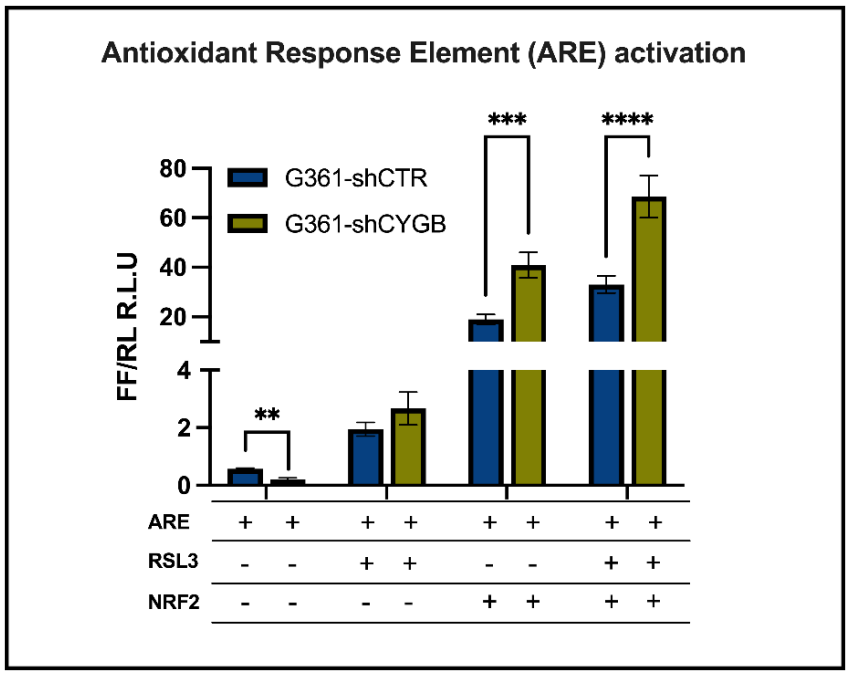

Figure 6.3. CYGB-dependent changes in antioxidant response element-driven luciferase activity. Binding of NRF2 to the antioxidant response element (ARE) in G361-shCTR and G361-shCYGB cells was assessed using an ARE-driven luciferase gene reporter assay. Cells were co-transfected with *Renilla* luciferase reporter vector to control for differences in transfection efficiency and extract preparation. Reporter activities were expressed as relative firefly/*Renilla* luciferase activities (R.L.U.). Luciferase reporter activity was measured after 6 h under basal conditions or upon 10 µM RSL3 treatment in the presence or absence of NRF2 overexpression in G361-shCTR and G361-shCYGB cells. Results are depicted as the mean with S.E.M. of six independent experiments (n = 6). Two-way ANOVA (** $p \leq 0.01$; *** $p \leq 0.001$; **** $p \leq 0.0001$).

6.4.4 RNA Sequencing Analysis of RSL3-Treated G361-shCTR and G361-shCYGB versus Control

As the treatment of G361-shCTR and G361-shCYGB cells with RSL3 resulted in a different degree of lipid peroxidation and cell viability (Figure 6.2), we explored the CYGB-dependent transcriptome in G361-shCTR and G361-shCYGB cells under basal versus RSL3-treated conditions. Differential analysis of normalized counts using DESeq2 identified 316 genes that were differentially expressed under basal conditions. Of those 316 genes, 111 genes were differentially expressed above an absolute $\log_2$ fold change of 1 (DEGs) (see [31] for more details).

Moreover, to identify enriched sets of genes between the G361-shCTR and G361-shCYGB datasets, fGSEA was next performed (Figure 6.4A). fGSEA analysis showed that multiple hallmarks were positively enriched in G361-shCYGB, including cell cycle-related hallmarks mitotic spindle, G2M checkpoint and E2F targets, as well as cancer-associated hallmarks hedgehog signaling, IL2-STAT5 signaling, inflammatory response, estrogen response early, PI3K-AKT-mTOR, KRAS signaling, TNFα signaling via NF-κB and epithelial–mesenchymal transition. The hallmark-representing genes that are downregulated in response to ultraviolet (UV) radiation were also positively enriched. Additionally, several pathways were found to be negatively enriched in G361-shCYGB. Of those hallmark pathways, oxidative phosphorylation, fatty acid metabolism and cholesterol homeostasis are related to metabolism. The remaining pathways MYC targets, angiogenesis, Wnt/β-catenin signaling and KRAS signaling are associated with cancer.

To further gain insight into biological processes, the 111 significantly DEGs were clustered by their gene ontology (GO) and the 40 most differentially expressed ontology terms were plotted (Figure 6.4B). Some of the top GO terms enriched are involved in response to drugs, cell division, proliferation, migration and differentiation, but also calcium and sodium ion transport and the immune response to other organisms.

Upon RSL3 treatment, 8939 genes were found to be differentially expressed in G361-shCTR. Compared to the untreated control, a total of 2980 significantly DEGs, of which 2034 were upregulated and 946 downregulated, were identified (Figure 6.5A). fGSEA analysis showed that 25 hallmark pathways were significantly enriched in the RSL3-treated group (Figure 6.6A). RSL3 treatment seemed to induce multiple signaling pathways, including TNFα signaling via NF-κB, IL6-JAK-STAT, IL2-STAT, MTORC1 and KRAS signaling. Furthermore, treatment enriched several stress-related pathways, i.e., hypoxia, apoptosis, the P53 pathway, the UV response (up and

down), the reactive oxygen species pathway and the unfolded protein response. Hallmark pathways E2F targets, oxidative phosphorylation, G2M checkpoint, MYC targets, fatty acid metabolism and DNA repair were negatively correlated with RSL3 treatment. GO enrichment analysis of the DEGs assigned these genes to be involved in processes related to the regulation of transcription, apoptosis, proliferation, and the inflammatory response (Figure 6.6C). Furthermore, GO terms encompassing signaling, e.g., MAPK cascade, phosphatidyl-inositol-3 kinase (PI3K) and circadian rhythm, were also found to be over-represented among others.

DESeq2 analysis of RSL3-treated G361-shCYGB identified 9574 differentially expressed genes (Figure 6.5B). In total, 3597 matched the criteria of DEGs, of which 2451 and 1146 were up- and downregulated, respectively. fGSEA analysis of the G361-shCYGB datasets showed a very similar pattern of significantly enriched hallmark pathways to that of G361-shCTR treated cells (Figure 6.6B). Of the pathways that were positively enriched in the RSL3-treated group, only the hallmark reactive oxygen species pathway was not significantly enriched compared to the fGSEA analysis of G361-shCTR. Hallmark pathways G2M checkpoint, mitotic spindle-related, oxidative phosphorylation and E2F targets were negatively enriched in RSL3-treated G361-shCYGB cells. In concordance with the fGSEA analysis, GO enrichment analysis of the DEGs showed very similar enrichment of GO terms compared to G361-shCTR cells (Figure 6.6D).

A ferroptosis gene signature was clearly present in both G361-shCTR and G361-shCYGB upon RSL3 treatment (Figure S6.4).

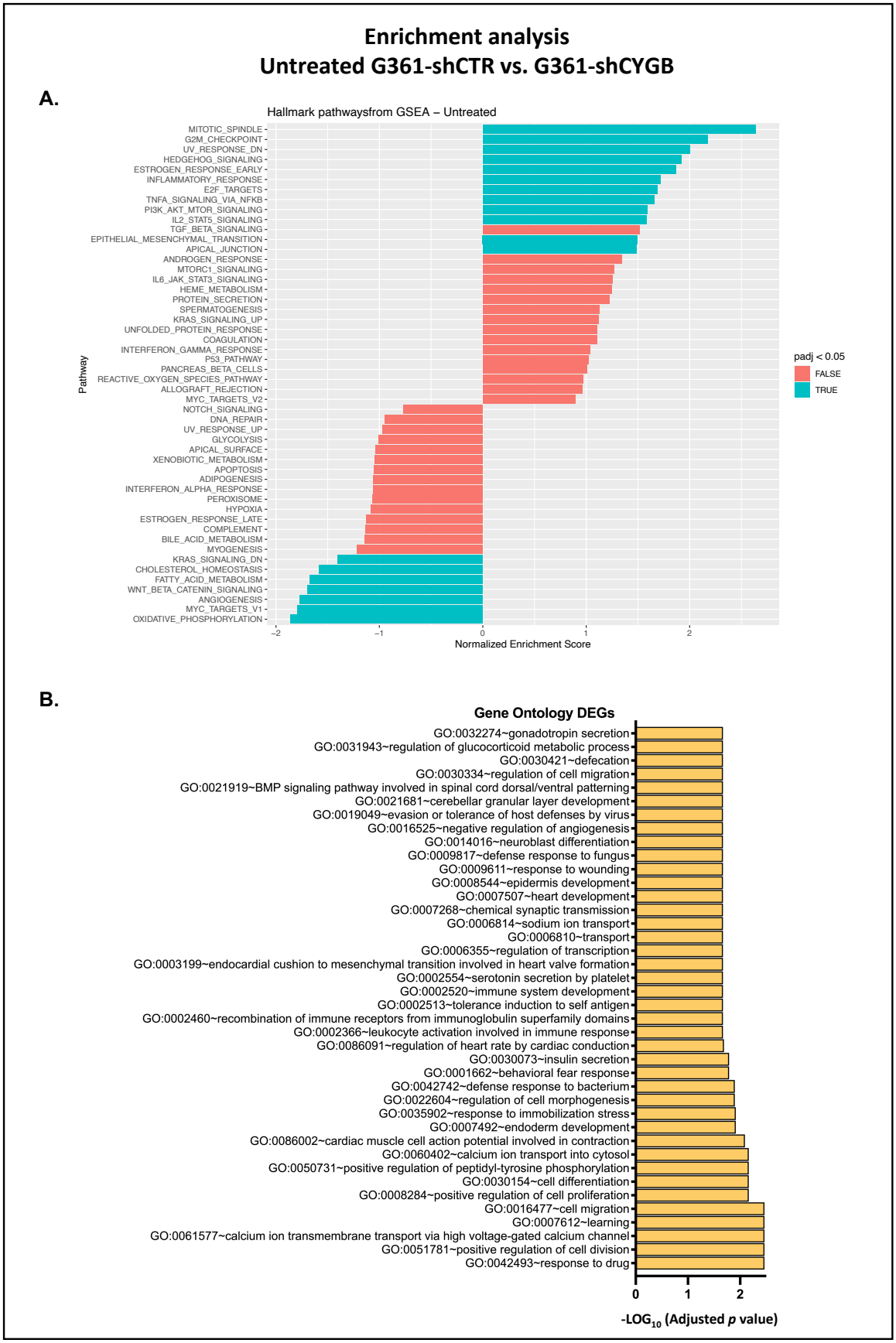

Figure 6.4. Basal CYGB-dependent transcriptome. Comparison of the G361-shCTR and G361-shCYGB transcriptomes under basal conditions using (**A**) fast Gene Set Enrichment Analysis (fGSEA), using the hallmark pathway gene sets and (**B**) gene ontology (GO) enrichment analysis.

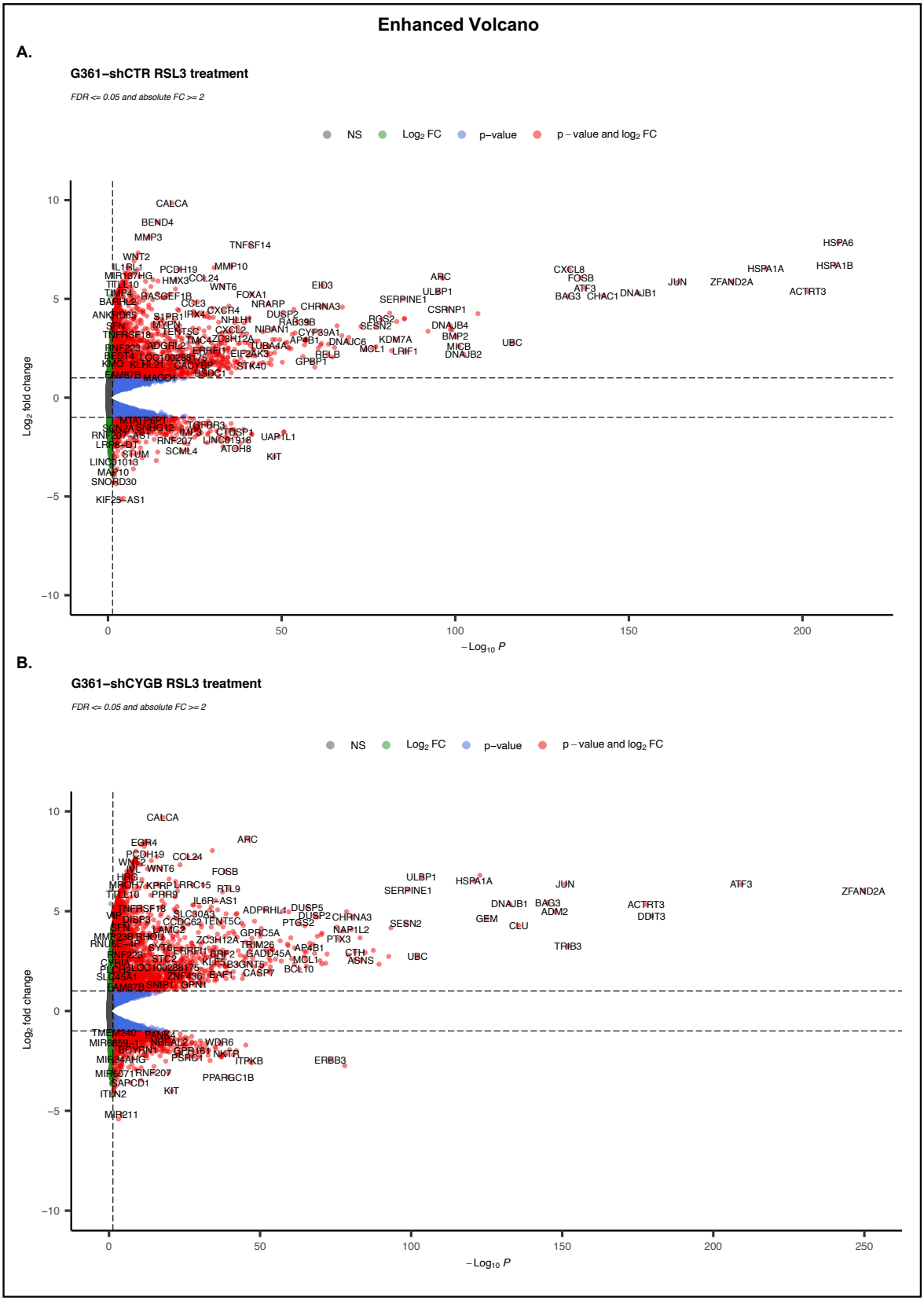

Figure 6.5. Enhanced volcano RSL3 treatment. Volcano representation of the differential expression analysis (DESeq2) of RSL3-treated G361-shCTR (**A**) and G361-shCYGB cells (**B**). Differentially expressed genes were represented based on their Log_2 fold change (Log_2FC) and $-Log_{10}$ *p*-adjusted value ($-Log_{10}$ *P*).

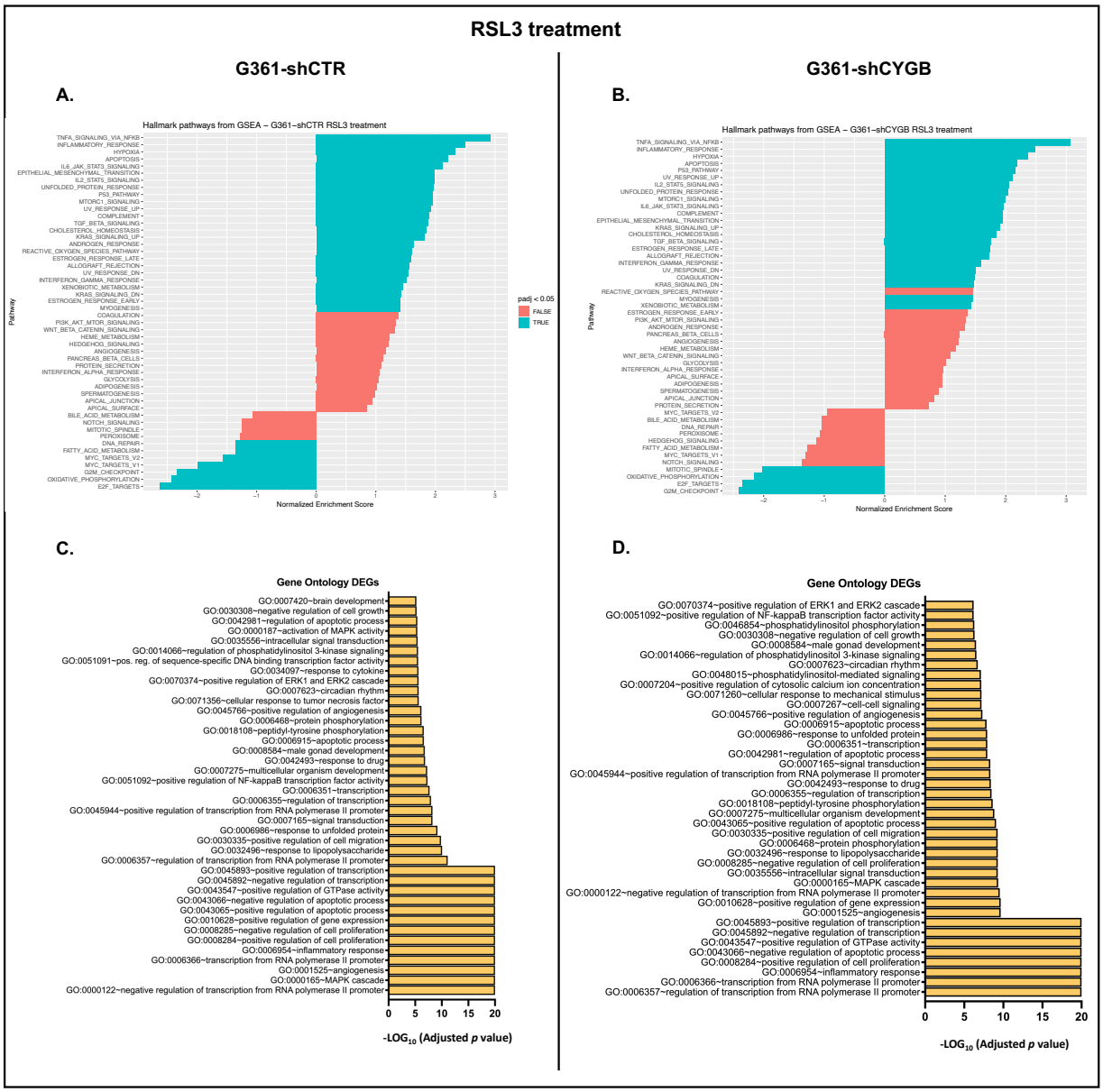

Figure 6.6 RSL3-mediated transcriptomic changes. Analysis of the transcriptomic changes induced by RSL3 treatment in G361-shCTR and G361-shCYGB cells compared to the untreated control. (**A**,**B**) fast Gene Set Enrichment Analysis (fGSEA) using the hallmark pathway gene sets was performed on G361-shCTR (**A**) and G361-shCYGB (**B**) melanoma cells. Gene ontology (GO) enrichment analysis was performed on the significantly differentially expressed genes (DEGs) in G361-shCTR (**C**) and G361-shCYGB (**D**) cells.

6.4.5 Differences between RSL3-treated G361-shCTR and G361-shCYGB Cells

Finally, we investigated whether the knockdown of CYGB resulted in differences in the response to RSL3 treatment. Therefore, we compared the RSL3-treated G361-shCTR and G361-shCYGB datasets. DESeq2 analysis identified 1461 genes with altered gene expression, of which 354 (240 up- and 114 downregulated) were significant DEGs (Figure 6.7A). fGSEA analysis showed that hallmark pathways TNFα signaling via NF-κB, inflammatory response, hypoxia, P53 pathway, UV

response (up), IL2-STAT5 signaling, coagulation, KRAS signaling (up), allograft rejection, IFNγ response, epithelial–mesenchymal transition, myogenesis, estrogen response, MTORC1 signaling, and oxidative phosphorylation were all enriched in RSL3-treated G361-shCYGB cells compared to G361-shCTR. In contrast, hallmarks G2M checkpoint, mitotic spindle and Wnt/β-catenin signaling were rather enriched in RSL3-treated G361-shCTR cells (Figure S6.5). GO enrichment analysis of the 354 DEGs showed (among others) an overrepresentation of GO terms related to signal transduction, transcription, the inflammatory response, the extracellular matrix and IL1β production (Figure 6.7B).

Interestingly, multiple pyroptosis-associated DEGs were found to be upregulated in G361-shCYGB cells compared to G361-shCTR upon RSL3 treatment (Figure 6.7B; see also supplementary Figure S6.6). We therefore validated the differential expression of 5 py-roptosis related genes (CASP1, CD74, CXCR4, NLRP3, SYK) by RT-qPCR (Figure 6.7C).

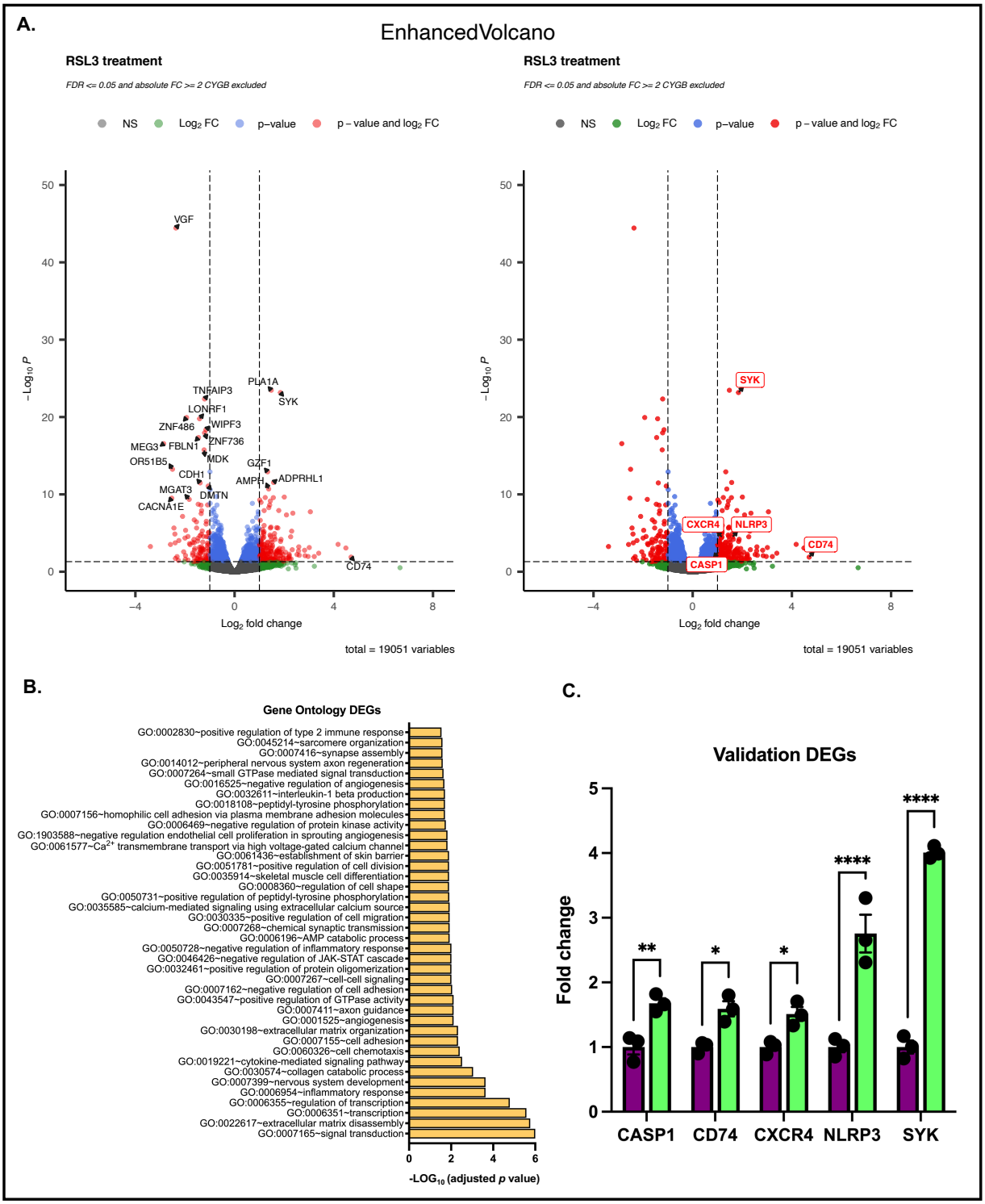

Figure 6.7. CYGB-dependent differences in response to RSL3 treatment. Comparison of RSL3-treated G361-shCTR and G361-shCYGB cells. (**A**) Enhanced volcano plots of the differential expression analysis (DESeq2) of RSL3-treated G361-shCTR versus G361-shCYGB cells. Differentially expressed genes were represented based on their Log_2 fold change (Log_2FC) and $-Log_{10}$ *p*-adjusted value ($-Log_{10}$ *P*). (**B**) The top-ranked gene ontology (GO) terms of the differentially expressed genes (DEGs) identified upon GO enrichment analysis. (**C**) Validation of selected DEGs by RT-PCR. Fold change represents the average fold change expression in G361-shCYGB cells compared to G361-shCTR cells (set as 1). Results are depicted as the mean with S.E.M. of three independent experiments ($n = 3$). One-way ANOVA (* $p \leq 0.05$; ** $p \leq 0.01$; **** $p \leq 0.0001$).

6.5 DISCUSSION

CYGB displays substantial sequence similarities with other globins and even has ~40% homology with myoglobin (Mb) [32]. It is now well established that mitochondria and Mb are intimately linked through their functional regulation of one another [33, 34]. Considering the homology to Mb and their very similar oxygen affinity, we sought to investigate a potential effect of CYGB knockdown in G361 melanoma cells on mitochondrial respiration. Mitochondrial oxidative phosphorylation was significantly diminished in CYGB-depleted G361-shCYGB cells (Figure 6.1B–F), consistent with the RNA-seq data, where G361-shCTR cells were compared to G361-shCYGB cells under basal conditions. Moreover, fGSEA analysis identified three metabolism-related pathways that were significantly enriched in the G361-shCTR cells, of which the hallmark pathway oxidative phosphorylation was most enriched (Figure 6.4A).

CYGBs tumor-suppressive role has previously been investigated [17, 35]. Several studies have shown that CYGB can function as a cytoprotective protein through the scavenging of ROS [12,14,36]. Recently, Zweier et al. demonstrated the potent superoxide dismutase activity of CYGB. In the current study, increased levels of ROS were found in G361-shCYGB cells under basal conditions, which would support a ROS-scavenging function (Figure 6.2A). Additionally, G361-shCYGB cells treated with the ferroptosis inducer RSL3 were significantly more sensitive and displayed increased levels of lipid peroxidation compared to treated G361-shCTR cells (Figure 6.2B & F). The increase in basal ROS levels in G361-shCYGB would facilitate the initiation of phospholipid peroxidation and subsequently lead to more ferroptotic cell death. Furthermore, CYGB has been shown to reduce anionic phospholipids through innate peroxidase activity [13]. Therefore, the knockdown of CYGB would result in a diminished ability to clear phospholipid hydroperoxides (PLOOHs), and thus increase lipid peroxidation. However, the lack of increased lipid peroxidation observed under basal conditions in G361-shCYGB cells would argue against peroxidase activity.

The small molecule RSL3 induces ferroptosis by directly inhibiting glutathione peroxidase 4 (GPX4) [36]. GPX4, a selenoprotein, is the major enzyme catalyzing the reduction, and thus toxification, of PLOOHs in mammalian cells, which makes it an essential regulator of ferroptotic cell death. GPX4 is a downstream target of the master regulator of the antioxidant response NRF2. Furthermore, NRF2 target genes have been shown to regulate the activity of proteins and enzymes responsible for preventing lipid peroxidation, including the enzyme HO-1. Whereas only NRF2 protein expression

was stabilized upon RSL3 treatment in both cell lines, HO-1 was clearly induced both on the mRNA and protein level (Figure 63C–E). NRF2's activity and abundance are tightly regulated at the transcriptional, post-transcriptional and post-translational level [37, 38]. On the other hand, NRF2 itself, as a redox-sensitive transcription factor, regulates the expression of antioxidant and detoxifying genes, including HO-1, through binding to the cis-acting enhancer sequence ARE. Consistently, ARE-driven reporter assays demonstrated increased luciferase activity upon RSL3 treatment under basal and NRF2 overexpression conditions in CYGB-deficient G361 cells (Figure 6.4).

Intriguingly, the knockdown of CYGB also affected NRF2 and HO-1 protein expression under basal conditions (Figure S6.3). This is in accordance with previous studies [14, 39-41] and is consistent with results obtained recently by our group [31]. Considering NRF2's central role in heme biosynthesis and taking into account CYGB as a heme-containing protein, cells possessing abundant endogenous CYGB levels constitutively induce NRF2 protein, and subsequently HO-1 [42, 43]. Furthermore, CYGB, as a hemeprotein, could potentially be involved in the regulation of the labile iron pool, and thus ameliorate RSL3-mediated ferroptosis.

Notably, HO-1 protein levels were significantly higher in G361-shCYGB cells upon RSL3 treatment. There is conflicting evidence concerning the role of HO-1 in ferroptosis, suggesting HO-1 to either promote or suppress ferroptosis [44, 45]. However, it seems that the pro- or anti-ferroptotic effect of HO-1 is dependent on the intracellular ROS levels and degree of HO-1 induction [46]. HO-1 breaks down heme into biliverdin/bilirubin, carbon monoxide and ferrous iron. Although biliverdin and bilirubin are antioxidants, ferrous iron is highly reactive and can lead to the accumulation of ROS. Therefore, labile free iron is sequestered by ferritin. Under moderate levels of HO-1 induction, the labile free iron is adequately buffered by ferritin and therefore HO-1 can exert its cytoprotective effect. However, higher levels of HO-1 expression could exceed the labile free iron buffering capacity of the cell, thereby facilitating lipid peroxidation and subsequent ferroptotic cell death [43]. Thus, the increased induction of HO-1 in CYGB knockdown G361-shCYGB cells, together with the increased basal ROS levels, could potentially have contributed to the increased sensitivity towards RSL3 treatment.

Another regulator of ferroptosis that recently was discovered, ferroptosis-suppressor protein 1 (FSP1; also known as AIFM2), plays a prominent role in the suppression of ferroptosis [47, 48]. FSP1 suppresses lipid peroxidation through the reduction of ubiquinone to ubiquinol, which in

turn either directly reduces lipid radicals to terminate lipid autoxidation, or indirectly via regenerating vitamin E. In T cell lymphoblastic lymphoma cells, FSP1 was shown to be upregulated by the long non-coding RNA maternally expressed 3 (MEG3), a regulatory RNA involved in tumor development [49].

Interestingly, MEG3 was one of the DEGs identified to be dramatically downregulated in G361-shCYGB cells upon RSL3 treatment (Figure 6.7A) and was recently found to also be downregulated under basal conditions [31]. Furthermore, MEG3 was shown to inhibit tumor formation, growth and metastasis in melanoma [50]. Thus, whilst the knockdown of CYGB in G361 melanoma cells gives rise to a more malignant cancer phenotype, it also makes cells more susceptible to ferroptosis. Additionally, multiple cancer-associated pathways were enriched in the CYGB-deficient G361-shCYGB cell line compared to G361-shCTR. Overactivation of the PI3K/AKT/mTOR pathway is known to promote proliferation and survival [51]. Oncogenic KRAS promotes cell survival, proliferation and cytokine secretion [52]. One of the cytokines secreted is TNFα, which in turn activates NF-κB, which promotes tumor metastasis and invasiveness [53]. Hedgehog signaling has been shown to promote metastasis through its involvement in the epithelial–mesenchymal transition (EMT) [54]. EMT transforms polarized epithelial cells into motile mesenchymal cells, thereby facilitating invasiveness and metastasis [55]. Thus, the knockdown of CYGB seems to induce cellular changes that lead to a more malignant cancer phenotype, further supporting a tumor-suppressive role for CYGB.

Remarkably, multiple DEGs found to be upregulated in G361-shCYGB cells compared to G361-shCTR upon RSL3 ferroptosis treatment are associated with pyroptosis (Figure 6.7B). More specifically, NOD-, LRR- and pyrin domain-containing protein 3 (NLRP3) and caspase 1 (CASP1) were significantly upregulated, as confirmed by RT-PCR (Figure 6.7C). Pyroptosis is driven by inflammatory caspases that are activated upon the formation of a multiprotein complex called the inflammasome [56, 57]. The NLRP3 inflammasome consists of a sensor (NLRP3), an adaptor (ASC; also known as PYCARD) and an effector (caspase 1). NLRP3 and CASP1 transcription is upregulated by the activation of pathogen-associated molecular patterns (PAMPS), toll-like receptors (TLRs) or cytokines such as TNFα and IL-1β that lead to NF-κB activation and gene transcription [58, 59], which is perfectly in line with the findings here, showing the enrichment of hallmark pathway TNFα via NF-κB signaling and GO term IL-1β production (Figures 6.7B and S6.5). Additionally, cluster of differentiation (CD74) together with C-X-C chemokine receptor type

4 (CXCR4) were also upregulated. CD74 is involved in cell signaling by acting as a receptor for the pro-inflammatory cytokine macrophage migration inhibitory factor (MIF) [60]. However, to trigger the intracellular signal transduction, the presence of co-receptor protein CXCR4 is needed [61]. MIF can initiate several cellular signaling pathways in a CD74-dependent manner, including signaling cascades involving spleen tyrosine kinase (Syk) and NF-κB [62-64], and promotes the expression of TLR4 [65]. Moreover, accumulating evidence suggests that MIF plays a central role in NLRP3 inflammasome activation [66, 67].

Collectively, our results revealed a cytoprotective role for CYGB in suppressing ferroptosis and pyroptosis cell death hallmarks. Moreover, transcriptome analysis revealed the enrichment of multiple cancer-associated pathways in CYGB knockdown G361 cells, demonstrating the tumor-suppressive function of CYGB. This could potentially have important therapeutic implications. Meta-analysis of the whole-genome bead array dataset (GSE29359) comparing human primary melanocyte cell lines and 82 patient-derived metastatic melanoma samples demonstrated that although CYGB is mostly lost during melanocyte-to-melanoma transition, some melanoma cells retain their high endogenous CYGB levels [16]. Therefore, modulated CYGB expression during melanomagenesis can determine the sensitivity towards treatments focused on inducing ferroptosis. CYGB expression in (metastatic) melanoma tissues could be used as a biomarker for determining the best therapeutic approach and treatment outcome.

Remarkably, RSL3 treatment in G361-shCYGB led to the activation of the NLRP3 inflammasome and subsequent induction of pyroptosis. Several studies already proposed an anti-inflammatory role for CYGB through the regulation of the cytokine TNFα [68, 69] via inhibition of the NF-κB pathway [70], which is in accordance with our RNA-seq data (Figure 6.2). CYGB was also shown to inhibit LPS-induced NADPH oxidase activity and ROS, NO and $O_2^{\bullet -}$ generation [71]. CYGB could possibly regulate inflammasome activation by attenuating inflammation through its polyvalent RONS-scavenging functions. However, cardiolipin (CL) was shown to be necessary for NLRP3 inflammasome activation [72]. As CYGB can interact with and regulate the redox status of CL [41, 73], CYGB could indirectly regulate pyroptotic cell death.

Conflicting evidence exists regarding the tumor-promoting or -inhibiting role of pyroptosis [74]. However, inducing pyroptosis in tumor cells holds great promise as a novel cancer treatment strategy. Here, pyroptosis likely contributed to the increased overall cell death in CYGB knockdown G361 cells. Studies focused on pyroptosis signaling pathways would provide

opportunities for finding tumor biomarkers and novel chemotherapeutic drug development [75]. In this light, CYGB could be of great interest for further research.

Of special note, changes in mitochondrial aldehyde dehydrogenase metabolism have been demonstrated at the crossroad of ferroptosis and pyroptosis signaling pathways [76]. Along the same line, Kang et al. recently reported that the key ferroptosis regulator GPX4 also acts as a negative regulator of the pyroptotic cell death pathway [77]. Furthermore, pyroptosis was also shown to be induced by increased intracellular iron and ROS in melanoma [78]. Hence, RSL3, as a GPX4 inhibitor, can lead to pyroptosis.

6.6 CONCLUSION

In this study, we explored the role of CYGB in determining the cellular sensitivity towards RSL3-mediated ferroptosis. The presence of the cytoprotective protein CYGB determined the outcome of RSL3 treatment through the regulation of lipid peroxidation and ROS levels, supporting a redox-regulatory role. RSL3 treatment strongly increased the expression of the master regulator of the antioxidant response NRF2 and downstream target HO-1, whereas CYGB protein levels determined the basal expression of NRF2 and HO-1, likely mediated through MEG3. Moreover, transcriptome analysis following CYGB knockdown further revealed the enrichment of multiple cancer malignancy pathways, supporting a tumor-suppressive function of CYGB. Remarkably, RSL3 treatment of G361-shCYGB cells also led to the activation of the NLRP3 inflammasome and pyroptosis pathways, which identified CYGB expression regulation as a critical determinant of the ferroptosis–pyroptosis therapy response. CYGB could be an exciting new predictive biomarker candidate.

6.7 REFERENCES

1. Siegel, R.L., K.D. Miller, and A. Jemal, *Cancer statistics, 2018.* CA Cancer J Clin, 2018. **68**(1): p. 7-30.
2. Sample, A. and Y.Y. He, *Mechanisms and prevention of UV-induced melanoma.* Photodermatol Photoimmunol Photomed, 2018. **34**(1): p. 13-24.
3. Curti, B.D. and M.B. Faries, *Recent Advances in the Treatment of Melanoma.* New England Journal of Medicine, 2021. **384**(23): p. 2229-2240.
4. Yu, C., et al., *Combination of Immunotherapy With Targeted Therapy: Theory and Practice in Metastatic Melanoma.* Frontiers in Immunology, 2019. **10**(990).
5. Davies, H., et al., *Mutations of the BRAF gene in human cancer.* Nature, 2002. **417**(6892): p. 949-954.
6. Moreira, A., et al., *Current Melanoma Treatments: Where Do We Stand?* Cancers (Basel), 2021. **13**(2).
7. Tsoi, J., et al., *Multi-stage Differentiation Defines Melanoma Subtypes with Differential Vulnerability to Drug-Induced Iron-Dependent Oxidative Stress.* Cancer Cell, 2018. **33**(5): p. 890-904 e5.
8. Yang, W.S. and B.R. Stockwell, *Synthetic lethal screening identifies compounds activating iron-dependent, nonapoptotic cell death in oncogenic-RAS-harboring cancer cells.* Chem Biol, 2008. **15**(3): p. 234-45.
9. Jiang, X., B.R. Stockwell, and M. Conrad, *Ferroptosis: mechanisms, biology and role in disease.* Nature Reviews Molecular Cell Biology, 2021. **22**(4): p. 266-282.
10. Zweier, J.L. and G. Ilangovan, *Regulation of Nitric Oxide Metabolism and Vascular Tone by Cytoglobin.* Antioxid Redox Signal, 2020. **32**(16): p. 1172-1187.
11. Reeder, B.J. and J. Ukeri, *Strong modulation of nitrite reductase activity of cytoglobin by disulfide bond oxidation: Implications for nitric oxide homeostasis.* Nitric Oxide, 2018. **72**: p. 16-23.
12. Zweier, J.L., et al., *Cytoglobin has potent superoxide dismutase function.* Proceedings of the National Academy of Sciences, 2021. **118**(52): p. e2105053118.
13. Tejero, J., et al., *Peroxidase activation of cytoglobin by anionic phospholipids: Mechanisms and consequences.* Biochimica et Biophysica Acta (BBA) - Molecular and Cell Biology of Lipids, 2016. **1861**(5): p. 391-401.
14. Randi, E.B., et al., *The Antioxidative Role of Cytoglobin in Podocytes: Implications for a Role in Chronic Kidney Disease.* Antioxid Redox Signal, 2020. **32**(16): p. 1155-1171.
15. De Backer, J., et al., *A reliable set of reference genes to normalize oxygen-dependent cytoglobin gene expression levels in melanoma.* Scientific Reports, 2021. **11**(1): p. 10879.
16. Fujita, Y., et al., *Melanoma transition is frequently accompanied by a loss of cytoglobin expression in melanocytes: a novel expression site of cytoglobin.* PLoS One, 2014. **9**(4): p. e94772.
17. Shivapurkar, N., et al., *Cytoglobin, the newest member of the globin family, functions as a tumor suppressor gene.* Cancer research, 2008. **68**(18): p. 7448-7456.
18. McRonald, F.E., et al., *Down-regulation of the cytoglobin gene, located on 17q25, in tylosis with oesophageal cancer (TOC): evidence for trans-allele repression.* Hum Mol Genet, 2006. **15**(8): p. 1271-7.
19. Shaw, R.J., et al., *Cytoglobin is upregulated by tumour hypoxia and silenced by promoter hypermethylation in head and neck cancer.* Br J Cancer, 2009. **101**(1): p. 139-44.
20. Presneau, N., et al., *Loss of heterozygosity and transcriptome analyses of a 1.2 Mb candidate ovarian cancer tumor suppressor locus region at 17q25.1-q25.2.* Mol Carcinog, 2005. **43**(3): p. 141-54.
21. Wojnarowicz, P.M., et al., *Chromosome 17q25 genes, RHBDF2 and CYGB, in ovarian cancer.* Int J Oncol, 2012. **40**(6): p. 1865-80.
22. Hubers, A.J., et al., *DNA hypermethylation analysis in sputum for the diagnosis of lung cancer: training validation set approach.* Br J Cancer, 2015. **112**(6): p. 1105-13.

23. Schörg, A., et al., *Destruction of a distal hypoxia response element abolishes trans-activation of the PAG1 gene mediated by HIF-independent chromatin looping.* Nucleic Acids Research, 2015. **43**(12): p. 5810-5823.
24. Koay, T.W., et al., *Androglobin gene expression patterns and FOXJ1-dependent regulation indicate its functional association with ciliogenesis.* J Biol Chem, 2021. **296**: p. 100291.
25. Storti, F., et al., *A novel distal upstream hypoxia response element regulating oxygen-dependent erythropoietin gene expression.* Haematologica, 2014. **99**(4): p. e45-8.
26. Keppner, A., et al., *Androglobin, a chimeric mammalian globin, is required for male fertility.* eLife, 2022. **11**: p. e72374.
27. Love, M.I., W. Huber, and S. Anders, *Moderated estimation of fold change and dispersion for RNA-seq data with DESeq2.* Genome Biology, 2014. **15**(12): p. 550.
28. Korotkevich, G., et al., *Fast gene set enrichment analysis.* bioRxiv, 2021: p. 060012.
29. Liberzon, A., et al., *The Molecular Signatures Database (MSigDB) hallmark gene set collection.* Cell systems, 2015. **1**(6): p. 417-425.
30. Huntley, R.P., et al., *The GOA database: gene Ontology annotation updates for 2015.* Nucleic Acids Res, 2015. **43**(Database issue): p. D1057-63.
31. De Backer, J., et al., *Cytoglobin inhibits non-thermal plasma-induced apoptosis in melanoma cells through regulation of the NRF2-mediated antioxidant response.* Redox Biology, 2022. **55**: p. 102399.
32. Yoshizato, K., et al., *Discovery of cytoglobin and its roles in physiology and pathology of hepatic stellate cells.* Proceedings of the Japan Academy. Series B, Physical and biological sciences, 2016. **92**(3): p. 77-97.
33. Keppner, A., et al., *Lessons from the post-genomic era: Globin diversity beyond oxygen binding and transport.* Redox Biology, 2020. **37**: p. 101687.
34. Kamga, C., S. Krishnamurthy, and S. Shiva, *Myoglobin and mitochondria: a relationship bound by oxygen and nitric oxide.* Nitric oxide : biology and chemistry, 2012. **26**(4): p. 251-258.
35. Rowland, L.K., et al., *Putative tumor suppressor cytoglobin promotes aryl hydrocarbon receptor ligand-mediated triple negative breast cancer cell death.* J Cell Biochem, 2019. **120**(4): p. 6004-6014.
36. Yang, W.S., et al., *Regulation of ferroptotic cancer cell death by GPX4.* Cell, 2014. **156**(1-2): p. 317-331.
37. Hayes, J.D. and A.T. Dinkova-Kostova, *The Nrf2 regulatory network provides an interface between redox and intermediary metabolism.* Trends Biochem Sci, 2014. **39**(4): p. 199-218.
38. Stewart, D., et al., *Degradation of transcription factor Nrf2 via the ubiquitin-proteasome pathway and stabilization by cadmium.* J Biol Chem, 2003. **278**(4): p. 2396-402.
39. Singh, S., et al., *Cytoglobin modulates myogenic progenitor cell viability and muscle regeneration.* Proc Natl Acad Sci U S A, 2014. **111**(1): p. E129-38.
40. Zhang, S., et al., *Cytoglobin Promotes Cardiac Progenitor Cell Survival against Oxidative Stress via the Upregulation of the NFκB/iNOS Signal Pathway and Nitric Oxide Production.* Sci Rep, 2017. **7**(1): p. 10754.
41. Thorne, L.S., et al., *Cytoglobin protects cancer cells from apoptosis by regulation of mitochondrial cardiolipin.* Scientific Reports, 2021. **11**(1): p. 985.
42. Kerins, M.J. and A. Ooi, *The Roles of NRF2 in Modulating Cellular Iron Homeostasis.* Antioxid Redox Signal, 2018. **29**(17): p. 1756-1773.
43. Chiang, S.K., S.E. Chen, and L.C. Chang, *A Dual Role of Heme Oxygenase-1 in Cancer Cells.* Int J Mol Sci, 2018. **20**(1).
44. Kwon, M.Y., et al., *Heme oxygenase-1 accelerates erastin-induced ferroptotic cell death.* Oncotarget, 2015. **6**(27): p. 24393-403.
45. Nitti, M., et al., *Heme Oxygenase 1 in the Nervous System: Does It Favor Neuronal Cell Survival or Induce Neurodegeneration?* Int J Mol Sci, 2018. **19**(8).
46. Hassannia, B., et al., *Nano-targeted induction of dual ferroptotic mechanisms eradicates high-risk neuroblastoma.* J Clin Invest, 2018. **128**(8): p. 3341-3355.

47. Bersuker, K., et al., *The CoQ oxidoreductase FSP1 acts parallel to GPX4 to inhibit ferroptosis.* Nature, 2019. **575**(7784): p. 688-692.
48. Doll, S., et al., *FSP1 is a glutathione-independent ferroptosis suppressor.* Nature, 2019. **575**(7784): p. 693-698.
49. Fan, F.Y., et al., *The inhibitory effect of MEG3/miR-214/AIFM2 axis on the growth of T-cell lymphoblastic lymphoma.* Int J Oncol, 2017. **51**(1): p. 316-326.
50. Wu, L., et al., *LncRNA MEG3 promotes melanoma growth, metastasis and formation through modulating miR-21/E-cadherin axis.* Cancer Cell International, 2020. **20**(1): p. 12.
51. Alzahrani, A.S., *PI3K/Akt/mTOR inhibitors in cancer: At the bench and bedside.* Semin Cancer Biol, 2019. **59**: p. 125-132.
52. Drosten, M. and M. Barbacid, *Targeting the MAPK Pathway in KRAS-Driven Tumors.* Cancer Cell, 2020. **37**(4): p. 543-550.
53. Ueda, Y. and A. Richmond, *NF-kappaB activation in melanoma.* Pigment Cell Res, 2006. **19**(2): p. 112-24.
54. Gupta, S., N. Takebe, and P. Lorusso, *Targeting the Hedgehog pathway in cancer.* Ther Adv Med Oncol, 2010. **2**(4): p. 237-50.
55. Rubin, L.L. and F.J. de Sauvage, *Targeting the Hedgehog pathway in cancer.* Nat Rev Drug Discov, 2006. **5**(12): p. 1026-33.
56. Swanson, K.V., M. Deng, and J.P. Ting, *The NLRP3 inflammasome: molecular activation and regulation to therapeutics.* Nat Rev Immunol, 2019. **19**(8): p. 477-489.
57. Shi, J., et al., *Cleavage of GSDMD by inflammatory caspases determines pyroptotic cell death.* Nature, 2015. **526**(7575): p. 660-665.
58. Bauernfeind, F.G., et al., *Cutting edge: NF-kappaB activating pattern recognition and cytokine receptors license NLRP3 inflammasome activation by regulating NLRP3 expression.* J Immunol, 2009. **183**(2): p. 787-91.
59. Franchi, L., T. Eigenbrod, and G. Núñez, *Cutting edge: TNF-alpha mediates sensitization to ATP and silica via the NLRP3 inflammasome in the absence of microbial stimulation.* J Immunol, 2009. **183**(2): p. 792-6.
60. Leng, L., et al., *MIF signal transduction initiated by binding to CD74.* J Exp Med, 2003. **197**(11): p. 1467-76.
61. Schwartz, V., et al., *A functional heteromeric MIF receptor formed by CD74 and CXCR4.* FEBS Letters, 2009. **583**(17): p. 2749-2757.
62. Starlets, D., et al., *Cell-surface CD74 initiates a signaling cascade leading to cell proliferation and survival.* Blood, 2006. **107**(12): p. 4807-4816.
63. Lantner, F., et al., *CD74 induces TAp63 expression leading to B-cell survival.* Blood, 2007. **110**(13): p. 4303-4311.
64. Gore, Y., et al., *Macrophage Migration Inhibitory Factor Induces B Cell Survival by Activation of a CD74-CD44 Receptor Complex*.* Journal of Biological Chemistry, 2008. **283**(5): p. 2784-2792.
65. Jankauskas, S.S., et al., *Evolving complexity of MIF signaling.* Cellular Signalling, 2019. **57**: p. 76-88.
66. Li, T., et al., *Downregulation of macrophage migration inhibitory factor attenuates NLRP3 inflammasome mediated pyroptosis in sepsis-induced AKI.* Cell Death Discovery, 2022. **8**(1): p. 61.
67. Lang, T., et al., *Macrophage migration inhibitory factor is required for NLRP3 inflammasome activation.* Nature Communications, 2018. **9**(1): p. 2223.
68. Wen, J., et al., *Protective effects of recombinant human cytoglobin against chronic alcohol-induced liver disease in vivo and in vitro.* Scientific Reports, 2017. **7**(1): p. 41647.
69. Yassin, M., et al., *Cytoglobin affects tumorigenesis and the expression of ulcerative colitis-associated genes under chemically induced colitis in mice.* Sci Rep, 2018. **8**(1): p. 6905.
70. Gomes, B.R.B., et al., *Cytoglobin Attenuates Neuroinflammation in Lipopolysaccharide-Activated Primary Preoptic Area Cells via NF-κB Pathway Inhibition.* Front Mol Neurosci, 2019. **12**: p. 307.
71. Ou, L., et al., *Recombinant Human Cytoglobin Prevents Atherosclerosis by Regulating Lipid Metabolism and Oxidative Stress.* J Cardiovasc Pharmacol Ther, 2018. **23**(2): p. 162-173.

72. Iyer, S.S., et al., *Mitochondrial cardiolipin is required for Nlrp3 inflammasome activation.* Immunity, 2013. **39**(2): p. 311-323.
73. Reeder, B.J., D.A. Svistunenko, and M.T. Wilson, *Lipid binding to cytoglobin leads to a change in haem co-ordination: a role for cytoglobin in lipid signalling of oxidative stress.* Biochem J, 2011. **434**(3): p. 483-92.
74. Lu, X., T. Guo, and X. Zhang, *Pyroptosis in Cancer: Friend or Foe?* Cancers (Basel), 2021. **13**(14).
75. Wang, L., et al., *Induction of Pyroptosis: A Promising Strategy for Cancer Treatment.* Front Oncol, 2021. **11**: p. 635774.
76. Cao, Z., et al., *Crosstalk of pyroptosis, ferroptosis, and mitochondrial aldehyde dehydrogenase 2-related mechanisms in sepsis-induced lung injury in a mouse model.* Bioengineered, 2022. **13**(3): p. 4810-4820.
77. Kang, R., et al., *Lipid Peroxidation Drives Gasdermin D-Mediated Pyroptosis in Lethal Polymicrobial Sepsis.* Cell Host Microbe, 2018. **24**(1): p. 97-108 e4.
78. Zhou, B., et al., *Tom20 senses iron-activated ROS signaling to promote melanoma cell pyroptosis* Cell Research, 2018. **28**(12): p. 1171-1185.

6.8 SUPPLEMENTARY

Table S6.1. Primer sequences of the used reference and target genes.

Gene symbol	Forward primer (5' to 3')	Reverse primer (5' to 3')
Reference gene		
B2M	TGCTGTCTCCATGTTTGATGTATCT	TCTCTGCTCCCCACCTCTAAGT
YWHAZ	ACTTTTGGTACATTGTGGCTTCAA	CCGCCAGGACAAACCAGTAT
Target gene		
CXCR4	ACTACACCGAGGAAATGGGCT	CCCACAATGCCAGTTAAGAAGA
CD74	GACGAGAACGGCAACTATCTG	GTTGGGGAAGACACACCAGC
CASP1	TTTCCGCAAGGTTCGATTTTCA	GGCATCTGCGCTCTACCATC
SYK	TGCACTATCGCATCGACAAAG	CATTTCCCTGTGTGCCGATTT
NLRP3	GATCTTCGCTGCGATCAACAG	CGTGCATTATCTGAACCCCAC

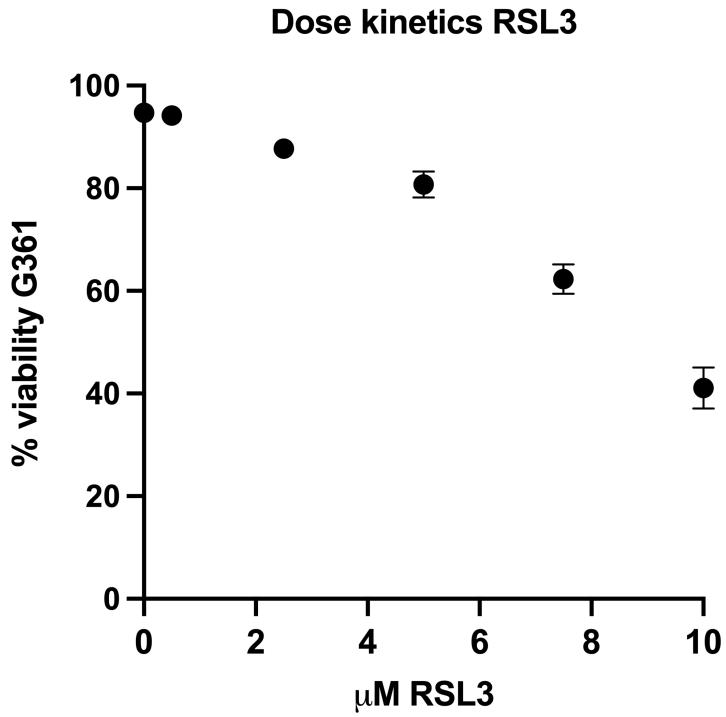

Figure S6.1. Dose titration RSL3. G361 cells were treated with different concentrations (0, 0.5, 2.5, 5, 7.5, 10 μM) of RSL3. Following propidium iodide (PI) staining, viability was measured 24 hours after treatment on the CytoFLEX flow cytometer.

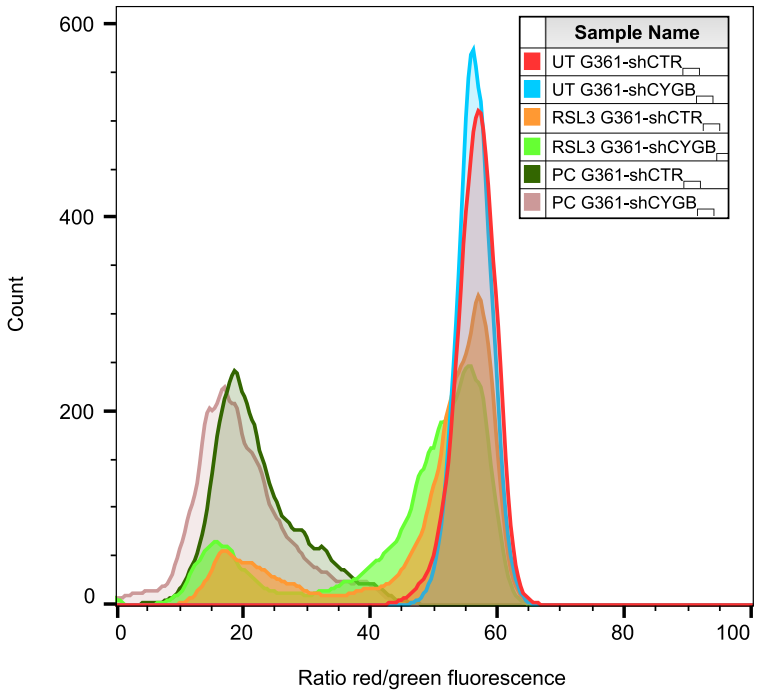

Figure S6.2. **Lipid peroxidation in G361 cells.** Lipid peroxidation measurements with Image-iT Lipid Peroxidation kit using flow cytometry. Lipid peroxidation Reagent is a ratiometric probe and the signal is detected on a flow cytometer with 488 nm laser excitation and fluorescence emission measured at 530/30 nm, and 532 nm laser excitation and fluorescence emission measured at 585/42 nm. The data are represented as the ratio of red/green fluorescence intensities. Ratios are higher in untreated (UT) cell populations and upon treatment with 7.5 µM RSL3 and cumene hydroperoxide (positive control; PC). A decrease in red/green fluorescence intensity ratios is visible because of the increase in green signal as a result of cumene hydroperoxide and RSL3 induced lipid peroxidation in G361-shCTR and G361-shCYGB cells.

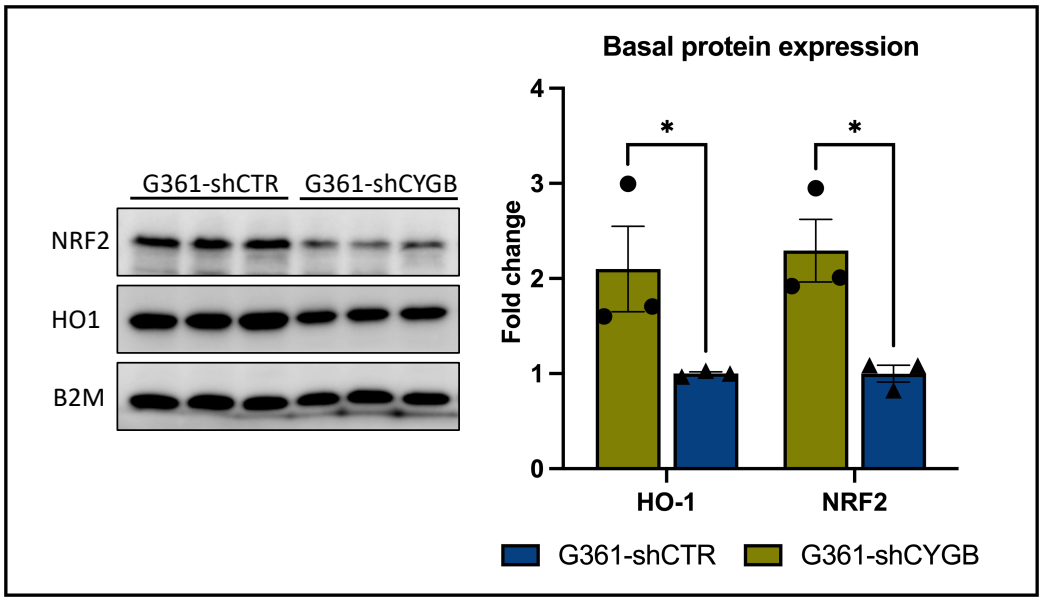

Figure S6.3. Basal protein expression. The protein expression of NRF2 and HO-1 was measured in G361-shCTR cells and G361-shCYGB melanoma cells. Quantification of the immunoblot signal showed that the knockdown of CYGB resulted in the decreased expression of NRF2 and HO-1. B2M was used as a loading control. Quantification is depicted as fold change compared to G361-shCYGB.Results are depicted as the mean with S.E.M of three independent experiments (n=3). Student's t-test (*$p \leq 0.05$).

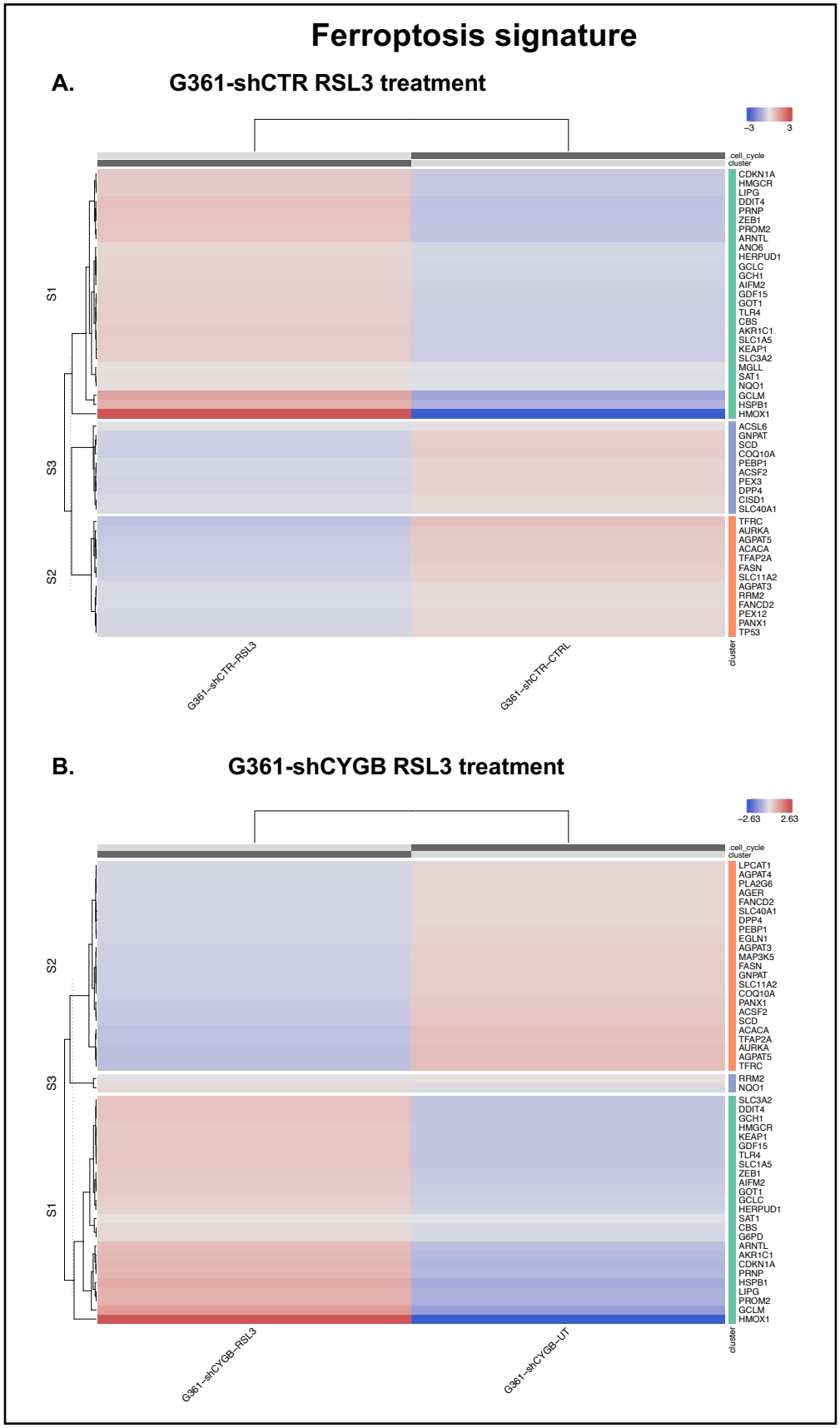

Figure S6.4. Ferroptosis signature heatmap. Hierarchical clustering of ferroptosis-related gene expression in (A) G361-shCTR and (B) G361-shCYGB upon RSL3 treatment. The top 50 ranked genes are represented.

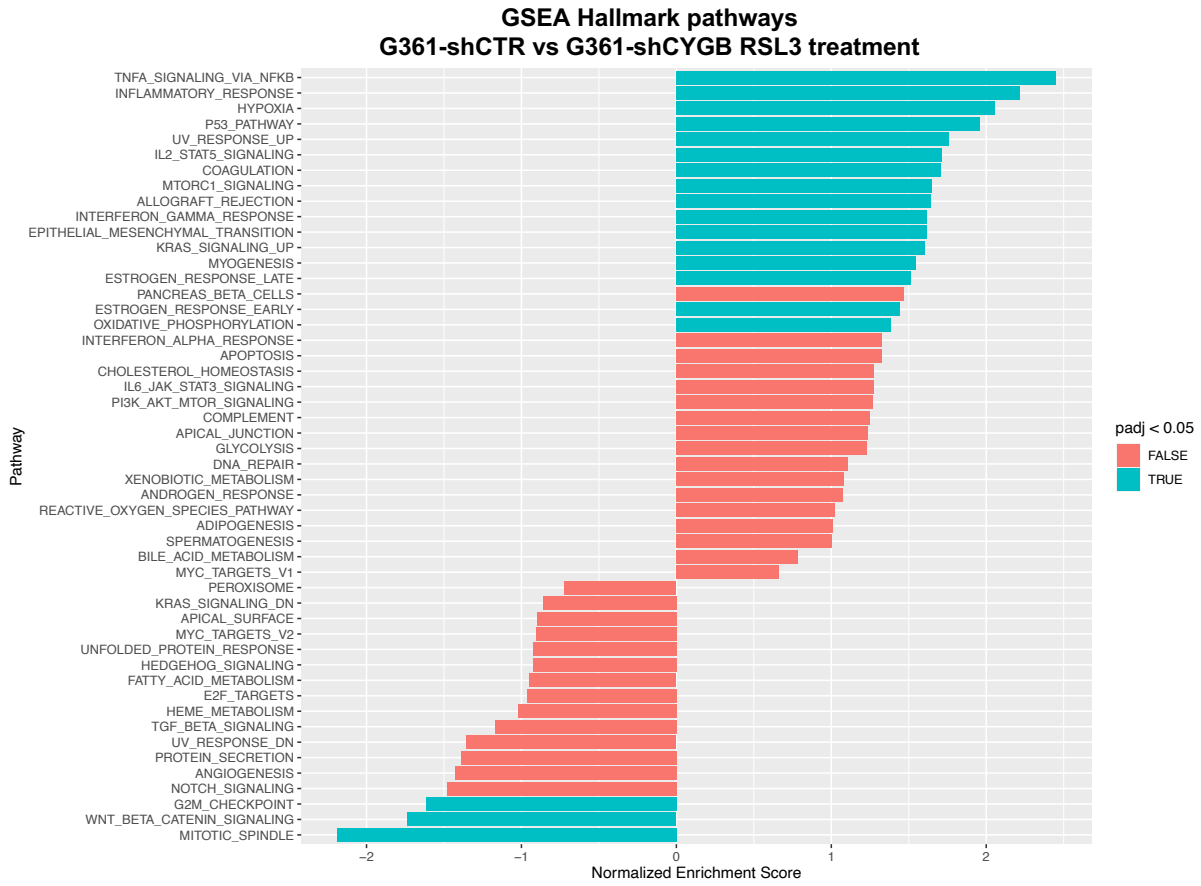

Figure S6.5. Gene Set Enrichment Analysis. Fast Gene Set Enrichment Analysis (fGSEA) using the hallmark pathway gene sets was performed on RSL3 treated G361-shCTR and G361-shCYGB melanoma cells.

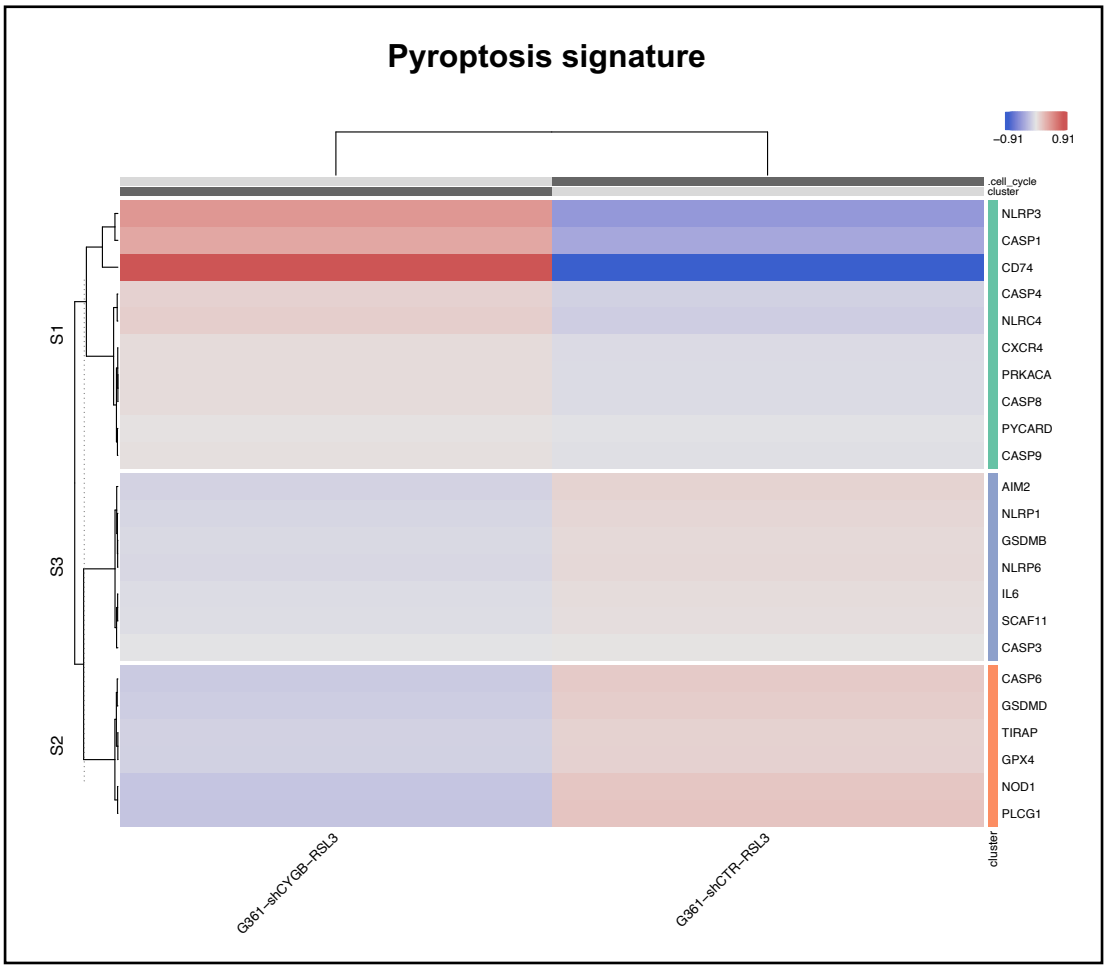

Figure S6.6. Pyroptosis signature heatmap. Hierarchical clustering of pyroptosis-related gene expression differences between RSL3 treated G361-shCTR and G361-shCYGB.

CHAPTER VII

NON-THERMAL PLASMA AS A UNIQUE DELIVERY SYSTEM OF SHORT-LIVED REACTIVE OXYGEN AND NITROGEN SPECIES FOR IMMUNOGENIC CELL DEATH IN MELANOMA

Published as:

Lin A, Gorbanev Y, **De Backer J***, Van Loenhout J, Van Boxem W, Lemière F, Cos P, Dewilde S, Smits E, Bogaerts A. *Non-Thermal Plasma as a Unique Delivery System of Short-Lived Reactive Oxygen and Nitrogen Species for Immunogenic Cell Death in Melanoma Cells*. Adv Sci (Weinh). 2019 Jan 28;6(6):1802062. doi: 10.1002/advs.201802062.

**Own contribution: in vivo vaccination assay*

7.1 ABSTRACT

Breakthroughs in cancer immunotherapies have demonstrated considerable success, though not without limitations. Non-thermal plasma (NTP) for cancer therapy has been emerging as a potential adjuvant treatment via induction of immunogenic cell death (ICD). Cancer cells undergoing ICD stimulates a patient's immune system to mount an anti-cancer response. While promising, the underlying mechanisms of NTP-induced ICD must be closely examined. Here we study the interaction between non-thermal plasma and cancerous cells. We report that the short-lived reactive oxygen and nitrogen species (e.g., hydroxyl radicals, atomic oxygen, nitric oxide) produced by plasma are the main effectors that elicit ICD in melanoma while surprisingly, persistent species do not. This was demonstrated *in vitro* using a dielectric barrier discharge plasma system and was validated in a vaccination assay *in vivo*. Plasma generation of reactive species appears to be dictated by the total energy. Collectively, our work provides fundamental insight into plasma interactions with biological material. Furthermore, our work lays the foundation for future development of NTP systems for clinical translation. The addition of plasma systems into the existing arsenal of cancer therapies opens the possibility for new combination strategies for safer and more robust control of cancer.

7.2 INTRODUCTION

Recent advances in cancer immunotherapy have led to significant positive impacts on patient survival, especially in patients with cancers previously limited to first-line treatments [1, 2]. Cancer immunotherapy intends to assist a patient's natural cancer-immunity cycle to fight cancer [3], and major success has been achieved with checkpoint inhibitors such as anti-PD-1/PDL-1 and anti-CTLA-4 therapies [1, 2]. However, the benefits of these treatments have been met with challenges including severe side-effects and efficacy in only a subset of patients [4, 5]. Therefore, there is a considerable need to develop new treatment modalities which, in combination with current therapies, may help improve clinical outcomes by supporting different steps of the cancer-immunity cycle. The goal of treatments should be to enable an effective, self-sustaining anti-cancer response in the patient.

One approach to enhance the initial step of the cycle is to induce immunogenic cell death (ICD) in the tumour. ICD is a form of regulated cell death, characterized by the timely release of 'danger signals' known as damage-associated molecular patterns (DAMPs) [6, 7]. Several DAMPs have been linked to ICD (e.g. high-mobility group box 1 (HMGB1), adenosine triphosphate), the most critical and well-studied being surface-exposed calreticulin (CRT) [8]. CRT on the outer leaflet of the cell functions as an 'eat-me" signal for uptake by dendritic cells DCs [9-11]. ICD inducers have been identified, and novel modalities continue to be explored [10, 11]. One such treatment is plasma generated at room temperature and atmospheric pressure, also known as non-thermal plasma (NTP).

NTP treatment of mice has been shown to reduce tumour burden and extend survival in different cancer types [12, 13]. The majority of these studies have used NTP for direct tumour cell killing or to induce cell senescence via reactive oxygen and nitrogen species (RONS) -mediated pathways [13, 14]. Small clinical studies with NTP have only recently commenced for palliative and curative treatment of dermatological diseases, and to date, plasma has been effective with mild to no side-effects [15-17].

Beginning in 2015, NTP has been investigated for its potential to induce ICD, and it has been reported to stimulate DAMP emission in multiple cancer cell lines *in vitro* [18-20]. The first *in vivo* demonstration of NTP-induced ICD was performed on Balb/c mice bearing subcutaneous, syngeneic CT26 colorectal tumours [21]. Tumours treated with a dielectric barrier discharge

(DBD) plasma resulted in higher expression of DAMPs (CRT and HMGB1) and increased recruitment of CD11c+ and CD45+ immune cells into the tumour environment. In combination with a therapeutic vaccine, DBD plasma treatment also enhanced cancer-specific, T-cell responses [21]. However, the underlying mechanisms by which NTP elicits ICD are still not fully understood.

When plasma is generated, a complex environment of reactive species, charged particles, neutral molecules, ultraviolet radiation, and electric fields is present and can interact with the biological target. Reactive species produced by the DBD plasma in the presence of oxygen were reported as the major contributors for ICD induction; not the physical components [20]. However, the exact chemical species that are responsible remain unclear. These include RONS with lifetimes ranging from fractions of a second (e.g., atomic species, radicals) to days and weeks (e.g., hydrogen peroxide, nitrite anion). Knowing which short-lived and persistent species are required for ICD-induction will be critical to the understanding and development of NTP technology for cancer immunotherapy.

To address the above challenges in oncology and the underlying questions in plasma chemistry and biological interactions, we sought to delineate the RONS generated by DBD plasma which are responsible for plasma-induced ICD. Knowing the species in plasma that are critical to ICD induction will lead to the development of an optimized clinical device. We have chosen to work with melanoma, a deadly disease when it reaches a regional or distant stage with 5-year survival dropping to 63% and 17%, respectively [22]. This disease has also been shown to respond to checkpoint inhibitors in the clinic [1, 2], making it a relevant model for future translational studies to potentially combine NTP with current immunotherapies to help broaden and amplify anti-tumor immunity.

In this study, a thorough examination of the RONS generated by DBD plasma operated at ICD-inducing regimes was performed. The emission of surface CRT on two melanoma cell lines was used as a surrogate marker of ICD *in vitro*. Plasma-generated RONS were measured using electron paramagnetic resonance (EPR) spectroscopy, UV-Vis spectrophotometry, and liquid chromatography-mass spectrometry (LC-MS). To further delineate the role of these species on ICD, solutions of RONS were prepared from commercially available sources, used to treat both cell lines, and assessed for their capacity to stimulate CRT. A vaccination assay was performed to

validate our findings *in vivo*. Our results show that alone, persistent RONS are not sufficient for DBD plasma-induced ICD and highlight the importance of the short-lived species. Furthermore, we observed that generating the desired RONS with the plasma system is dependent on the plasma treatment energy and not on an individual treatment parameter (e.g., pulse frequency or application time). This study provides crucial information towards our fundamental knowledge of plasma-cell interactions which, through strategic optimization of DBD plasma parameters, would allow us to develop a clinical device for controlled delivery of RONS necessary for ICD (**Figure 7.1**).

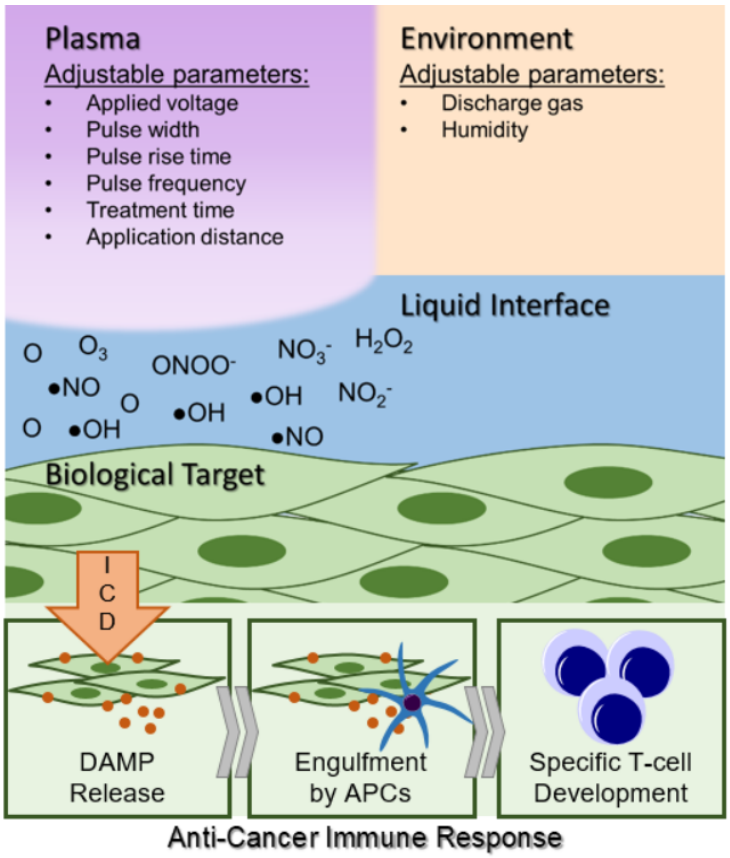

Figure 7.1. Understanding how non-thermal plasma interacts with cancerous targets would allow strategic development of a biomedical device for the controlled delivery of RONS to elicit immunogenic cell death. This could assist the initial steps of a patient's cancer-immunity cycle and lead to a robust anti-cancer immune response.

7.3 EXPERIMENTAL

The overall objective of the study was to uncover the mechanism by which non-thermal plasma elicits immunogenic cancer cell death by evaluating the role of RONS generated. This was accomplished by: 1) determining an ICD-inducing regime of plasma, 2) identifying the RONS generated in that regime, and 3) delineating their effect by comparing direct DBD plasma

treatment and treatment with exogenously prepared RONS solutions. Our initial screenings of RONS effect on ICD were performed *in vitro* on two melanoma cell lines and validated in an *in vivo* vaccination assay using syngeneic mice.

7.3.1 Cell lines

The B16F10 murine melanoma cell line and the A375 human melanoma cell line were purchased from the American Type Culture Collection (ATCC). Both cell lines were cultured in complete DMEM medium containing 10% FBS, 100 U/mL penicillin, 100 µL streptomycin, and 4 mM L-glutamine. Cells were cultured in a humidified environment at 37 ^{o}C with 5% CO_2.

7.3.2 Microsecond-pulsed DBD plasma parameters for direct treatment

A µs-pulsed power supply was purchased from Advanced Plasma Solutions, and a 1.25 cm diameter copper DBD electrode was used for treatment in 24-well plates. The copper electrode was covered with a 0.5 mm fused-silica dielectric (Technical Glass) to prevent current arching. The microsecond-pulsed power supply generates 17 kV pulses with ~5 µs rise times and 10 µs pulse widths. The duty cycle was fixed at 100%.

Both cell lines were seeded into 24-well plates at 3×10^5 cells/mL (0.5 mL/well) one day prior to plasma treatment. On the day of plasma treatment, medium was removed, and cells were washed twice with PBS to remove serum and other organics from cell culture medium. PBS from the second wash was left in the well until right before plasma treatment. For DBD plasma treatment, PBS was removed and the DBD electrode was lowered into the well and positioned 1 mm above the cells with a z-positioner (**Figure 7.2A** and **B**). Plasma was then discharged directly on the cells for 10 s at various pulse frequencies (50, 100, 250, and 500 Hz). Following plasma treatment, 500 µL of fresh cell culture medium was immediately added back into the well. Cells were incubated at 37^{o}C with 5% CO_2 for 24 h until further analysis. Mitoxantrone dihydro-chloride (Sigma-Aldrich, ≥97%, M6545), a chemotherapeutic used as a positive control, was diluted to a 5 mg/mL stock solution, and prepared into a working solution of 2 µg/mL in complete media. Cells were incubated with Mitoxantrone for 24 h before collection and analysis.

7.3.3 Treatment with pulsed-electric fields

On the day of treatment, cells were washed with PBS and 1 mL of PBS or RONS solution (700 µM of H_2O_2, 1770 µM of NO_2^-, and 35 µM of $ONOO^-$) was added to each well immediately before treatment. The DBD electrode was then submerged into the liquid and operated at 17 kV and 500 Hz for 10 s, 1 mm above the cells. This method was to subject the cells to PEF generated from the µs-pulsed power supply and DBD electrode without the production of plasma (**Figure 7.2C**). Following 10 s treatment, all the liquid was removed from the well and fresh cell culture medium was added. Cells were then incubated at 37°C with 5% CO_2 for 24 h until further analysis.

7.3.4 DBD plasma treatment of liquid

For liquid analysis, 50 µL of liquid (PBS or deionized water) was added into a 24-well plate and distributed evenly across the bottom. The DBD electrode was positioned 1 mm above the surface of the liquid using the z-positioner **(Figure 7.2D**). DBD plasma was generated at fixed voltage (17 kV) while the pulse frequency and treatment time was varied.

For preparation of plasma-treated PBS for treatment of cells, PBS was treated for 100 s at 500 Hz. Prior to finishing the 100 s treatment, PBS was removed from the wells containing cells. All 50 µL of plasma-treated PBS was then collected and added onto cells and 45 µL was removed. After 10 s treatment with 5 µL of remaining plasma-treated PBS, 500 µL of complete medium was added back into the well and the cells were incubated for 24 h until further analysis.

7.3.5 Preparation of RONS solutions and treatment

The solutions of H_2O_2, NO_2^-, and NO_3^- were prepared from commercially available H_2O_2 (Sigma-Aldrich, ≥30%, 95321), sodium nitrite ($NaNO_2$) (Sigma-Aldrich, ≥97%, 237213), and potassium nitrate (KNO_3) (Signa-Aldrich, ≥99%, P8394) dissolved in PBS (without iron, calcium, and magnesium). $ONOO^-$ was prepared from NaOONO (Cayman Chemicals, ≥90% solution in 0.3M sodium hydroxide, 14042-01-4) dissolved in PBS. Four different RONS solutions were prepared:

1) **$H_2O_2/NO_2^-/NO_3$** – H_2O_2: 700 µM, NO_3^-: 410 µM, NO_2^-:1360 µM
2) **H_2O_2/NO_2^-** – H_2O_2: 700 µM, NO_2^-:1770 µM
3) **$ONOO^-$** – 35 µM
4) **$H_2O_2/NO_2^-/ONOO^-$** – H_2O_2: 700 µM, NO_2^-:1770 µM, $ONOO^-$: 35 µM

On the day of treatment, the cells were washed twice with PBS, to follow identical handling procedures with plasma treatment. PBS from the second wash was removed immediately before treatment and 50 µL of RONS solution was added into the well and rocked to ensure even distribution on cells. 45 µL was removed and the remaining 5 µL was left on the cells for 10 s. Following treatment, 500 µL of fresh, complete media was added to the well and cells were incubated at 37^{o}C with 5% CO_2 for 24 h until further analysis. This procedure most closely mimics the process of direct DBD plasma treatment and is most realistic to the concentration of RONS generated by plasma and experienced by the cells.

7.3.6 Cell survival assay

Cell survival was quantified with a trypan blue exclusion test. Following 24 h incubation, cell supernatant was collected. Cells were then washed with 0.5 mL of PBS and detached with 200 µL of accutase. PBS from the wash was also collected with the cell supernatant. The cell suspension was collected, pooled with their supernatant and PBS wash, and homogenized by pipetting. A 50 µL sample was acquired and equal parts 0.4% trypan blue (Gibco, 15250-061) was added to the sample. Cell counts were performed using a TC20 Automated Cell Counter (Bio-Rad). The live cell concentration was recorded, and data are represented as a normalization to control.

7.3.7 CRT expression from cell lines

CRT was measured using dual staining of propidium iodide (PI) and a monoclonal CRT antibody. Following 24 h after incubation, cells were washed with PBS, detached with 200 µL of accutase and washed twice with 2 mL of FACs buffer (500 mL Sheath fluid (BD Biosciences, 342003) + 2 g Bovine Serum Albumin (Sigma, A9418) + 1 g NaN_3 (Merck, 1.06688.0100) in 100 mL H_2O). Each sample was split into two vials, and one was stained with monoclonal primary rabbit anti-CRT antibody (Abcam, ab196158) while the other was stained with rabbit IgG, monoclonal isotype control (Abcam, ab199091) for 40 min at 4^{o}C. Cells were then washed once with FACs buffer. 0.5 µL of PI was added to each sample immediately before being quantified with a flow cytometer. Fifteen thousand events were collected and only the PI- cells were analyzed for CRT emission. Data are expressed as percent CRT positive after accounting for non-specific binding with their corresponding isotype.

7.3.8 Mice and anti-tumor vaccination assay

Thirty-two 8-week-old female C57BL/6J mice were purchased from Charles River and housed in a pathogen-free room at the Animal Center of the University of Antwerp. The sample size of this study (8 mice per group) was chosen using information in literature [7] and running an a priori power analysis using G*Power software (Version 3.0.10). Input parameters include effect size (large, 0.8), α error probability (0.05), power (0.8), and number of group (4). A total sample size of 24 was calculated to give an actual power of 0.859. Eight mice were randomly assigned to one of four groups and housed during the whole of the experiment in 4 separate cages. Two mice from each group were housed in each cage. Investigators were not blind to the groups.

The vaccines for this assay were prepared from B16F10 melanoma cells exposed to: 1) DBD plasma (500 Hz), 2) PEF+RONS (RONS: 700 µM of H_2O_2, 1770 µM of NO_2^-, and 35 µM of $ONOO^-$), or 3) Mitoxantrone (2 µg/mL) *in vitro*, while untreated cells were used as a negative control. After treatment, cells were collected, washed twice with PBS, and resuspended in PBS at 10^6 cells per mL. Cell suspension was incubated for 24 h at 37°C with 5% CO_2 to reduce the viability of the cells and prevent subsequent tumor growth at the vaccination site.

On the day of vaccination, mice were shaved with electric clippers (to help visualize tumors) and injected with vaccine (10^5 cells in approximately 100 µL) on the right dorsal side. After 7 days, each mouse was injected with 10^4 live B16F10 cells (in approximately 100 µL) on the left dorsal side. Tumor size and growth was followed up to day 50 as defined prior to the start of the experiment. Three orthogonal diameters were measured using a digital caliper, and volumes were calculated using $4/3\pi\ r_1 \times r_2 \times r_3$. The humane study endpoint was set to when the total tumour volume exceeded 1500 mm^3 or if tumours began to ulcerate. For graphical representation of tumor development, the total number of days for the challenge tumor to reach humane endpoints were graphed. The exact day the tumour reached 1500 mm^3 was extrapolated from tumor measurements on the day it exceeded the defined volume and from tumour measurements on the previously recorded day. Mice that did not develop tumors at the challenge site and mice that developed tumors at the vaccination site were excluded in this graph. All animal experiments were approved by the University of Antwerp Animal Research Ethical Committee (ECD-dossier 2017-53).

7.3.9 Detection of H_2O_2

The H_2O_2 concentration was detected using potassium oxotitanate dehydrate (Alfa Aesar, 89620) solution in H_2O and H_2SO_4 (Sigma-Aldrich, 95-98%, 258105M). Concentration of H_2O_2 in plasma-treated samples was determined by UV-Vis measurements performed on a Genesys 6 (ThermoFischer) spectrophotometer with quartz cuvettes (10 mm light path, 2mm internal width). Titanium(IV) reagent (0.1 M Ti, 5 M H_2SO_4) was prepared by dissolving 0.354 g of potassium bis(oxalato)oxotitanate(IV) dihydrate in a mixture of 2.72 mL of sulphuric acid and diluted to 10 mL with milli-Q water. 50 µL of plasma-treated sample was added to the cuvette and diluted with 150 µL of PBS. 50 µL of sodium azide (NaN_3) (Sigma-Aldrich, ≥99.5%, S2002) was added to the cuvette and thoroughly mixed. Afterwards, 50 µL of Ti-Sulphate solution was added and homogenized. Air bubbles in the cuvette were eliminated with a sonicator (Branson 3200 ultrasonic bath) and water droplets were wiped from the cuvette before reading at 400 nm.

7.3.10 Detection of NO_2^- and NO_3^-

A Nitrate/Nitrite Colorimetric Assay Kit (Cayman Chemical, 780001) was used according to the provided protocol. To detect NO_2^- only, 50 µL of Griess Reagent 1 (Sulfanilamide) was added to each sample in a 96-well plate, and 50 µL of Griess Reagent 2 (N-(1-Naphthyl) ethylenediamine) was immediately added afterwards. The absorbance wavelength was read with a microplate reader Infinite 200 Pro (Tecan) at 540 nm. To detect NO_3^- and NO_2^-, a nitrate reductase mixture (Cayman Chemical, 780010) and an enzyme cofactor mixture (Cayman Chemical, 780012) was added to each sample prior to the addition of Griess Reagents. This allowed for the conversion of nitrate into nitrite. The absorbance was measured in duplicates and the samples were prepared in triplicates. The concentrations were calculated based on the obtained calibration curve.

7.3.11 EPR spectroscopy analysis

50 µL capillaries (Ringcaps) were used to collect plasma-treated samples, and a MiniScope MS200 spectrometer (Magnettech) was used to perform the analysis. After each plasma exposure experiment, the samples were immediately placed into a capillary tube. The overall time between exposure and analysis was 1 min. The general EPR parameters were as follows: frequency 9.4 GHz, power 3.16 mW (31.6 mW in case of (MGD)2Fe2+-NO), modulation frequency 100 kHz, modulation amplitude 0.1 mT, sweep time 30 s, time constant 0.1, sweep width 15 mT.

The simulated spectrum was double integrated to determine the concentrations reported here. Simulations were performed using hyperfine values obtained from literature in the Spin Trab Database (National Institute of Environmental Health Sciences, 2018). EPR calibration was performed using solutions of 4-hydroxy-TEMPO (Sigma-Aldrich, 97%, 176141) as reported elsewhere [23]. Specific spin traps and other molecules were used to detect RONS in the liquid (**Table S7.2**). All recorded experimental EPR spectra and simulations are shown in **Figure S7.2** and **S7.3**, along with the corresponding hyperfine values used.

7.3.12 Detection of $O/^1O_2/O_3$

2,2,6,6-tet-ramethylpiperidine (TEMP) spin trap was dissolved in PBS (50 mM) to detect $O/^1O_2/O_3$ following DBD plasma treatment (Sigma-Aldrich, ≥99%, 115754). TEMP reacts with these oxygen species to form the spin adduct TEMPO, which can be detected by means of EPR spectrometry. To determine the contribution of O/O_3, 100 mM of sodium azide (NaN_3) (Sigma-Aldrich, ≥99.5%, S2002) was added to the TEMP solution before plasma treatment to quench $^1O_2$. Therefore, the collected spectrum of TEMPO was a result of the remaining oxygen species.

7.3.13 Detection of •OH and $O_2•^-$ with EPR spectroscopy

5-(diethoxyphosphoryl)-5-methyl-1-pyrroline *N*-oxide (DEPMPO) spin trap (Enzo Life Sciences, ≥99%, ALX-430-093) was dissolved in PBS (100 mM) to detect •OH and $O_2•^-$. DEPMPO reacts with $O_2•^-$ to produce DEPMPO-OOH while it reacts with •OH to produce DEPMPO-OH.

7.3.14 Detection of •NO with EPR spectroscopy

The spin probe 2-phenyl-4,4,5,5-tetramethylimidazoline-1-oxyl 3-oxide (PTIO) (Enzo Life Sciences, ≥98%, ALX-430-007) was dissolved in PBS (200 µM) to detect •NO from DBD plasma treatment. •NO reacts with PTIO to form PTI which can be detected through EPR spectroscopy. When pulse frequency was varied from 50 to 500 Hz, treatment time was fixed at 50 s in order to generate detectable levels •NO.

The MGD spin trap (Enzo Life Sciences, ≥98%, ALX-400-014) was also used to detect •NO. MGD was dissolved in deionized water (20 mM) and combined with $Fe(II)SO_4×7H_2O$ (4mM) (Sigma-Aldrich, ≥99%, 215422). This solution was treated with DBD plasma and $Na_2S_2O_3$ (100 mM in deionized water degassed with argon) (Sigma-Aldrich, ≥98%, 72049) was immediately added to

the sample and collected for EPR analysis. When pulse frequency was varied from 50 to 500 Hz, treatment time was fixed at 120 s in order to generate detectable levels of •NO.

7.3.15 Detection of $ONOO^-$ with LC-MS

Solutions of 100 µM L-tyrosine (Sigma-Aldrich, ≥98%, T-3754) and 100 µM diethylenetriaminepentaacetic acid (Sigma-Aldrich, ≥98%, D1133) in 2x PBS were exposed to plasma for a given period of time, as described by Wende et al. [24] The solutions were collected and flash-frozen immediately after exposure.

The separation and detection of 3-nitrotyrosine was done by a Waters ACQUITY ultraperformance liquid chromatograph (UPLC) coupled to a Waters triple quadrupole mass spectrometer (Xevo TQ MS). The used column is a Waters ACQUITY UPLC HSS T3 2.1 x 100 mm column (1.8 µm particles), heated to 40°C. The 9 minute gradient used for separation with (A): water containing 0.1% formic acid and (B): acetonitrile containing 01% formic acid, at a flow rate of 0.6 mL/min: 0-1.0 min 2% B, 1.0-4.0 min 2% to 18% B, 4.0-5.0 min 18% to 97% B, 5.0-6.0 min 97% B, 6.0-7.0 min 97% to 2% B, 7.0-9.0 min 2% B. The parameters used in electrospray ionization tandem mass spectrometry (ESI-MS/MS) in positive mode were: capillary, 0.5kV; cone, 22V; extractor, 3V; source temperature, 150°C; desolvation temperature, 600°C; desolvation gas flow, 1000 L/h; cone gas flow, 0L/h; collision gas flow, 0.15 mL/min; collision energy 2V.

A multiple reaction monitoring (MRM) method application was optimized for the detection of tyrosine (transition m/z 182-136) and 3-nitrotyrosine (transition m/z 227-181). For calibration of 3-nitrotyrosine, 8 standard solutions were made ranging from 0-10 µM and analyzed using the MRM method. The samples were diluted to a starting concentration of 10 µM tyrosine in 95% water and 5% acetonitrile containing 0.1% formic acid.

7.3.16 Statistical Analysis

Statistical differences for cell survival and CRT expression were analyzed using the linear mixed model with JMP Pro 13 (SAS software). The fixed effect was the treatment, and the random effects included are the different dates the experiment was performed, and the flasks the cells used were split from. The interactions between the treatment and the date as well as interactions between the treatment and the flasks were tested. The random slope model was used when the interactions were significant ($p<0.05$) and the random intercept model was used in all other

cases. The fixed effect tests determines whether there was a significant difference between treatments ($p<0.05$). When the difference is significant, the Dunnett's test for statistical significance was used to calculate adjusted *P* value compared to the control. A *P* value of <0.05 was considered statistically significant. For all *in vitro* experiments, treatment conditions were performed in duplicates on the same day and repeated on 3 separate days as a minimum. The total number of observations for each treatment group is defined in the figure or figure legend. The survival curve of the vaccination study was prepared in Graphpad Prism and compared using the log-rank (Mantel-Cox) test. A *P* value of <0.05 was considered statistically significant. All figures were prepared in Graphpad Prism (Graphpad Software). For all chemical species, a non-linear regression was used to determine the best fit line and R^2 value with a y-intercept constraint at zero. Analysis was performed and figures were prepared in Graphpad Prism (Graphpad Software). No data were excluded.

7.4 RESULTS

7.4.1 DBD plasma induces cell death and CRT emission in melanoma cells

To determine whether plasma can induce ICD, we first performed a screening for cell survival and emission of CRT in mouse (B16F10) and human (A375) melanoma cell lines. CRT exposure is one of several DAMPs associated with ICD, and has been identified as a critical determinant for anti-cancer immune responses [9]. A microsecond-pulsed DBD plasma treatment system (Figure 7.2**A**) was used to generate plasma directly onto the cells after media was removed and cells were washed with phosphate buffered saline (PBS) (**Figure 7.2B**). Immediately following DBD plasma treatment, fresh media was added back into the well.

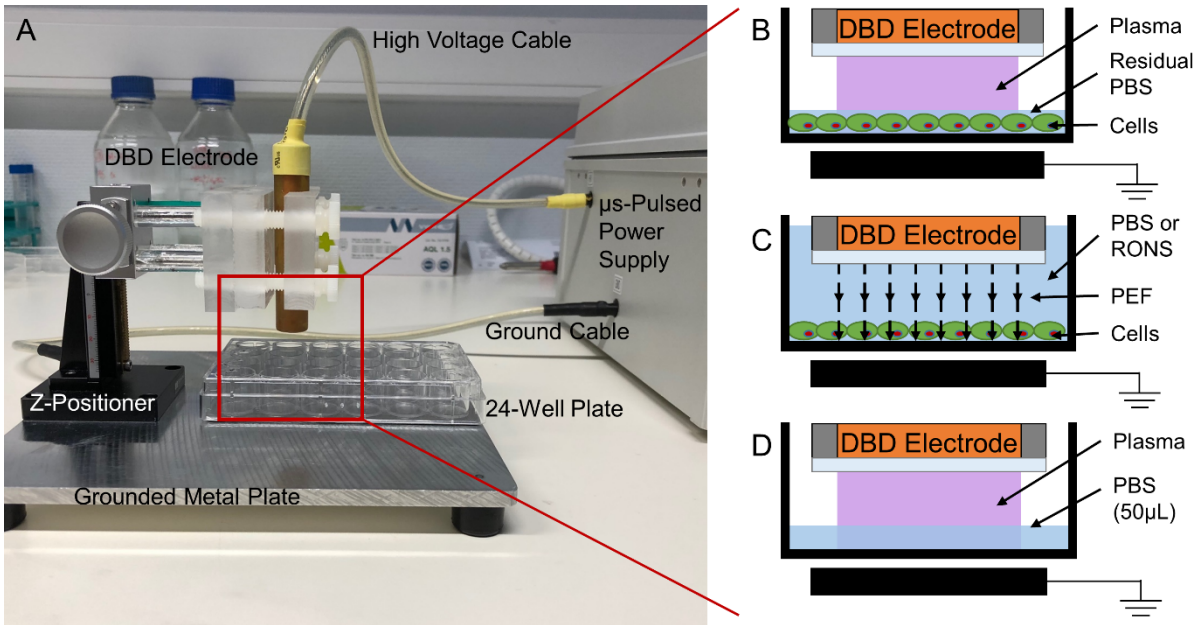

Figure 7.2. Treatments were performed using a DBD electrode supplied with 17 kV from a microsecond-pulsed power supply. (**A**) Cells were treated in a 24-well plate. PBS was used to wash the cells before treatment and was aspirated from the well immediately before exposure to plasma. The following schematics (**B-D**) are a representation of the zoomed-in area highlighted in red when the z-positioner was used to fix the DBD electrode 1 mm above the cells for treatment. (**B**) Plasma was generated in this gap directly onto the cells covered by a thin layer of residual PBS (≤ 2 µL). (**C**) For pulsed electric field (PEF) treatment, the DBD electrode was submerged in liquid, with or without added RONS, positioned 1 mm above the cells, and operated as before. In this case, while the cells still experience microsecond-pulses, no plasma was generated due to the high dielectric strength of the liquid. (**D**) For liquid analysis following plasma treatment, the DBD electrode was used to treat 50 µL of PBS, 1 mm above the liquid surface, in 24-well plates.

Cells were treated for 10 s with increasing pulse frequency to deliver higher energy treatments. Cells incubated for 24 h with 2 µg/mL Mitoxantrone (MTX), a known chemotherapeutic ICD inducer, were used as a positive control [9]. Evaluation of cell survival with a trypan blue exclusion assay and an automated cell counter revealed that with increasing plasma pulse frequency, cell survival decreased and plateaus at 250 Hz (**Figure 7.3A**). Cells were also double stained with propidium iodide (PI) and a monoclonal CRT antibody. Flow cytometry analysis showed that with higher intensity plasma treatment, the percentage of live CRT positive cells (% CRT+/PI-) increased compared to untreated (UT) (**Figure 7.3B**). Histograms of cells from each treatment group showed a rightward shift in peak CRT fluorescence (**Figure 7.3C, D**). The data indicate that there is a general increase in CRT expression, which is not limited to a subpopulation. Altogether, this suggests that plasma is able to elicit cell death and increase immunogenicity of tumor cells in an energy dependent manner.

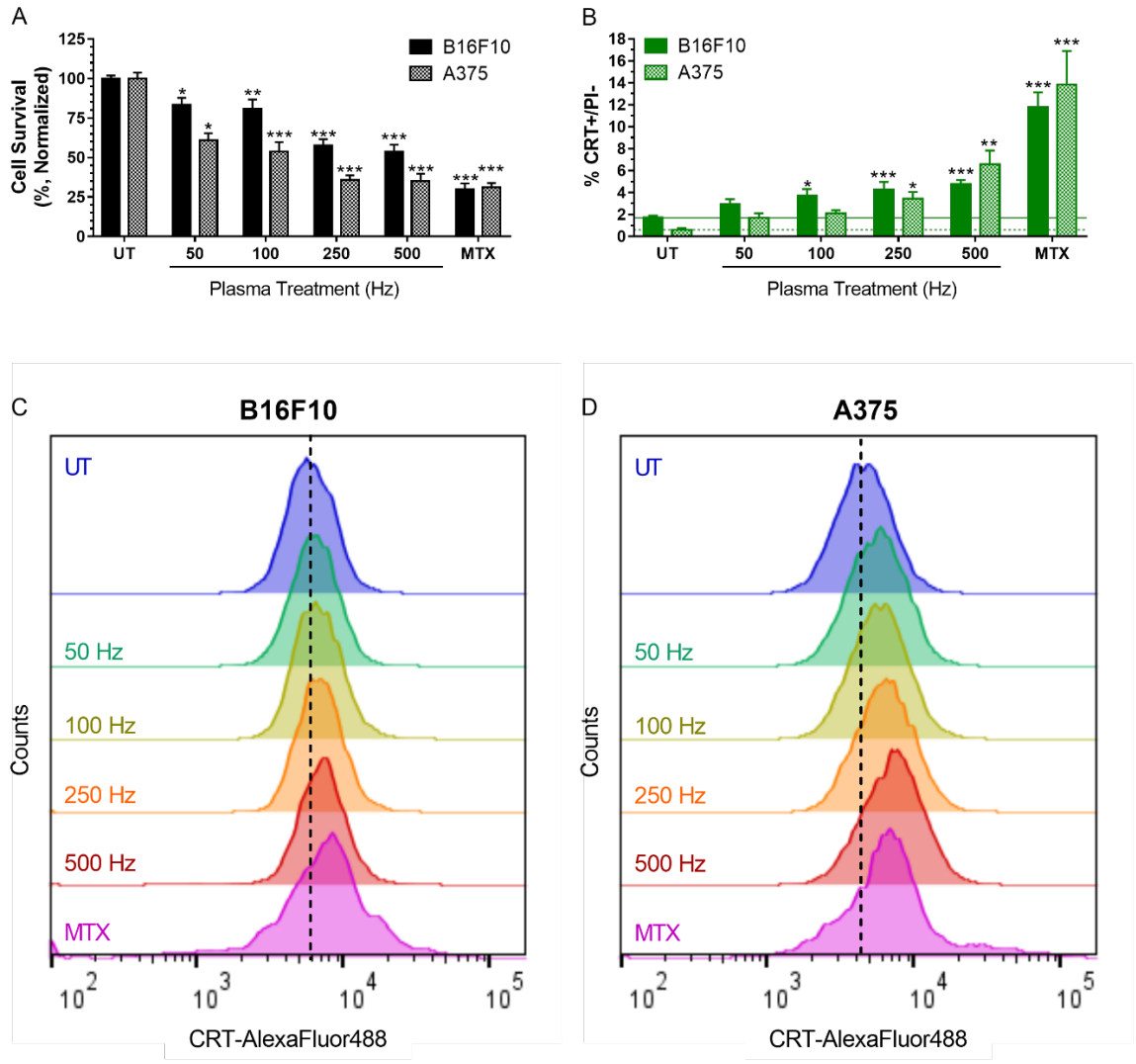

Figure 7.3. DBD plasma induces cell death and CRT exposure, which increases with higher plasma treatment frequency. Mitoxantrone (MTX) (2 µg/mL), a chemotherapeutic ICD inducer, was used as positive control. 24 h after plasma treatment of melanoma cells, cells were collected and analysed for (A) cell survival with a trypan blue exclusion assay and surface-exposed CRT with immunohistochemistry. (B) The percentage of cells that were CRT+ and PI- was quantified with flow cytometry. Histograms of CRT+/PI- cells showed a rightward shift in peak fluorescence. Representative histograms of the (C) B16F10 and (D) A375 cells are shown here. Data here are represented as mean±SEM of 3-4 independent experiments with at least 2 replicates. Statistical significance of all treatment conditions was compared to untreated (UT). *p<0.05; **p<0.01; ***p<0.001 (Generalized Linear Mixed Model).

7.4.2 DBD plasma generates short-lived and persistent RONS in PBS

During DBD plasma treatment of cells, PBS was removed from the well and plasma was generated directly onto melanoma cells. However, since the wells were not dried, there remains a residual layer of PBS (**Figure 7.2B**), which either interacts with plasma-generated RONS or creates

additional RONS (e.g. via direct electron impact). Due to the close proximity of the liquid to the biological target, RONS generated (including short-lived species) may influence subsequent biological effect. Therefore, we assessed RONS generated in PBS by DBD plasma at CRT-emitting parameters. PBS (50 µL) was treated in 24-well plates (**Figure 7.2D**) at the same operating parameters used to treat the melanoma cells. PBS was then immediately collected and analyzed using EPR, LC-MS, or UV-Vis spectrophotometry.

7.4.2.1 Short-lived RONS generated by DBD plasma (•OH, •NO, O/O_3)

The concentration of hydroxyl radicals (•OH) and superoxide radical anions ($O_2•^-$) in PBS was assessed with the spin trap 5-diethoxyphosphoryl-5-methyl-1-pyrroline *N*-oxide (DEPMPO). A solution of DEPMPO (100 mM) was prepared in PBS (without calcium, magnesium, or iron) and treated with DBD plasma. •OH react with DEPMPO to form the DEPMPO-OH radical adduct, while $O_2•^-$ would form DEPMPO-OOH [25]. The EPR spectrum following 10 s plasma treatment at all frequencies showed no DEPMPO-OOH radical adduct. However, DEPMPO-OH was detected (**Figure S7.1A**) and decreased with increasing plasma treatment frequency (**Figure 7.4A**). When plasma treatment frequency was fixed at 500 Hz and treatment time was changed, DEPMPO-OH increased up to 5 s after treatment, followed by a sharp decrease (**Figure 7.4B**). At 50 Hz treatment, DEPMPO-OH decreased with increasing plasma treatment time from 10 to 50 s. Taken together, this strongly suggests that the DEPMPO-OH spin adduct was decaying with increased treatment intensity (higher frequency or longer time). This decay was due to either degradation reactions of the nitroxide group in plasma-treated aqueous solutions upon which the radical nature is lost [26] or generation of other RONS (NO_x compounds) which decrease the stability of the adducts [27]. Therefore, we conclude that while $O_2•^-$ is not produced and/or not delivered to the liquid following DBD plasma treatment, •OH radical is present, but its dependence on pulse frequency and time cannot be determined.

Nitric oxide radical (•NO) was monitored in liquid solutions exposed to plasma by two methods. First, we used 200 µM solution of 2-phenyl-4,4,5,5-tetramethylimidazoline-1-oxyl 3-oxide (PTIO) in PBS. Nitronyl nitroxides such as PTIO react with •NO, forming imino nitroxides, in our case 2-phenyl-4,4,5,5-tetramethylimidazoline 1-oxyl (PTI) [28]. Both PTIO and PTI were monitored simultaneously, from the same EPR spectra (**Figure 7.4C**). The detected concentration of PTI increased with increasing DBD frequency, similarly to other RONS, though seemingly in non-

linear fashion (**Figure 7.4D**). PTI also increased with longer treatment times at 500 Hz until a decrease at 180 s (**Figure S7.2A** and **B**). This was most likely due to the decay of the nitroxide moiety of PTI and/or re-oxidation of PTI back to PTIO at longer exposure times, as we have shown previously [26]. Thus, these experiments confirmed the presence of •NO in the liquid after DBD plasma treatment but could only partially be used to assess the degree of frequency/time dependency of •NO production. Subsequently, we used a solution of a *N*-methyl-D-glucamine dithiocarbamate (MGD) – iron(II) complex to detect •NO [28]. Since the $(MGD)_2Fe^{2+}$-NO adduct can be formed from interaction of $(MGD)_2Fe^{2+}$ with NO_2^- [29, 30], we tested its formation by adding $NaNO_2$ in concentrations corresponding to that created during plasma treatment. No signal was detected in this case, confirming that all radical adduct formed was due to the reaction with •NO. Large amounts of reducing agent must be added after plasma treatment due to the oxidation of Fe^{2+} to Fe^{3+}, resulting in loss of paramagnetic nature of the adduct [26]. We found that 10 s treatment still allowed detection of the formed radicals under reasonable experimental conditions (volume of added reducing agent, etc.) (**Figure S7.1B**). Although too low to be quantified at 50 and 100 Hz treatment, $(MGD)_2Fe^{2+}$-NO concentration at 500 Hz was approximately twice that at 250 Hz, suggesting the near-linear frequency dependency, as was observed with all other RONS (**Figure 7.4D**).

The spin trap 2,2,6,6-tetramethylpiperidine (TEMP) was prepared in PBS at 50 mM and used to detect atomic oxygen (O), singlet oxygen ($^1O_2$), and ozone (O_3) [25, 30, 31] following DBD plasma treatment. The amine moiety of TEMP was oxidized by these species, leading to the formation of a stable nitroxide 2,2,6,6-tetramethylpiperidine *N*-oxyl (TEMPO). The trends of their generation were observed from the intensity of the TEMPO EPR signal (**Figure S7.1C**), though exact concentrations cannot be computed due to the semi-quantitative nature of spin trapping [31]. The relative amount of $^1O_2$ can be estimated by using a selective scavenger, NaN_3 [25, 30]. At fixed treatment times (10 s), TEMPO concentration increased near-linearly (R^2=0.900) with plasma treatment frequency (**Figure 7.4E**). Generation of the spin adduct also scales near-linearly with treatment time at fixed frequencies (**Figure S7.3A**). TEMPO was not reduced with the addition of NaN_3 (**Figure 7.4E**), which strongly suggests that $^1O_2$ is not present in the liquid during treatment. The measured TEMPO is then formed mainly through O and O_3. Elg et al. has proposed that this reaction in plasma-liquid systems occurs mostly with O, not O_3, though this would depend on the relative amounts of O and O_3 produced in each case [31].

7.4.2.2 Persistent RONS generated by DBD plasma ($ONOO^-$, H_2O_2, NO_2^-, NO_3^-)

Peroxynitrite ($ONOO^-$) was detected using solutions of L-tyrosine in PBS as described in past reports: 100 µM solutions of L-tyrosine in 2x PBS were treated by DBD plasma, leading to formation of 3-nitrotyrosine [24]. The concentrations of 3-nitrotyrosine were measured using LC-MS with electrospray ionization. We tentatively attribute the formation of 3-nitrotyrosine to $ONOO^-$, though other species which can yield the nitrated product may be present in our system (e.g. $\bullet NO_2$ and other nitrogen species). Therefore, the concentrations of $ONOO^-$ stated here are possibly an overestimation of the actual amount present. $ONOO^-$ increased near-linearly as well with increasing plasma pulse frequency (R^2=0.947) up to 3.4±0.4 µM for 500 Hz (**Figure 7.4F**).

The generation of hydrogen peroxide (H_2O_2) by plasma has been considered a key component of its anti-cancer properties [13, 32]. Concentration of H_2O_2 was measured with UV-Vis spectrophotometry (400 nm) from the reaction with potassium titanium (IV) oxalate solution, and the addition of sodium azide (NaN_3) (details in Materials and Methods) [23, 33]. Due to the detection limit of the instrument, the treatment time was increased to 120 s as H_2O_2 was undetected at 10 s treatments. H_2O_2 concentration increased near-linearly with plasma treatment frequency at fixed treatment time (R^2=0.965) (**Figure 7.4G**). There was no measurable evaporation within the time frames of our treatment conditions. Since H_2O_2 generation also scaled near-linearly with treatment time (**Figure S7.3B**) it confirmed that H_2O_2 did not saturate the liquid, and thus the increased exposure time can be used to assess concentrations at various frequencies. H_2O_2 concentration after 10 s treatment was extrapolated as 11.4, 31.2, and 67.8 µM for 100, 250, and 500 Hz treatment, respectively. At 50 Hz, H_2O_2 concentration was still below the detection limit even after 120 s, but is calculated to be 6.7 µM at 10 s.

The concentration of nitrite (NO_2^-) and nitrate (NO_3^-) in PBS was determined using the Griess method [33]. To delineate the amount of NO_2^- from NO_3^-, a nitrate reductase enzyme and cofactor was used to reduce NO_3^- to NO_2^- as described in Materials and Methods [33]. Both species were generated near-linearly with increasing plasma pulse frequency when treatment time was fixed (**Figure 7.4H**), and when pulse frequency was fixed and treatment time was extended (**Figure S7.3C and D**). Several possible reactions could lead to the formation of NO_3^-: (1) NO_3^- is formed in the gas and enters the liquid (in ionic or HNO_3 form), (2) NO_3^- is formed in the liquid from N_2O_5 that enters the liquid, and (3) NO_2^- enters the liquid and undergoes oxidation

to NO_3^-. Therefore, although more NO_3^- was detected in the liquid following direct DBD plasma treatment, it is possible that the initial NO_2^- concentration was higher. This was taken into account in our cellular experiments with RONS solutions, where NO_2^- was used in amounts corresponding to total NO_2^-+NO_3^- concentrations measured here.

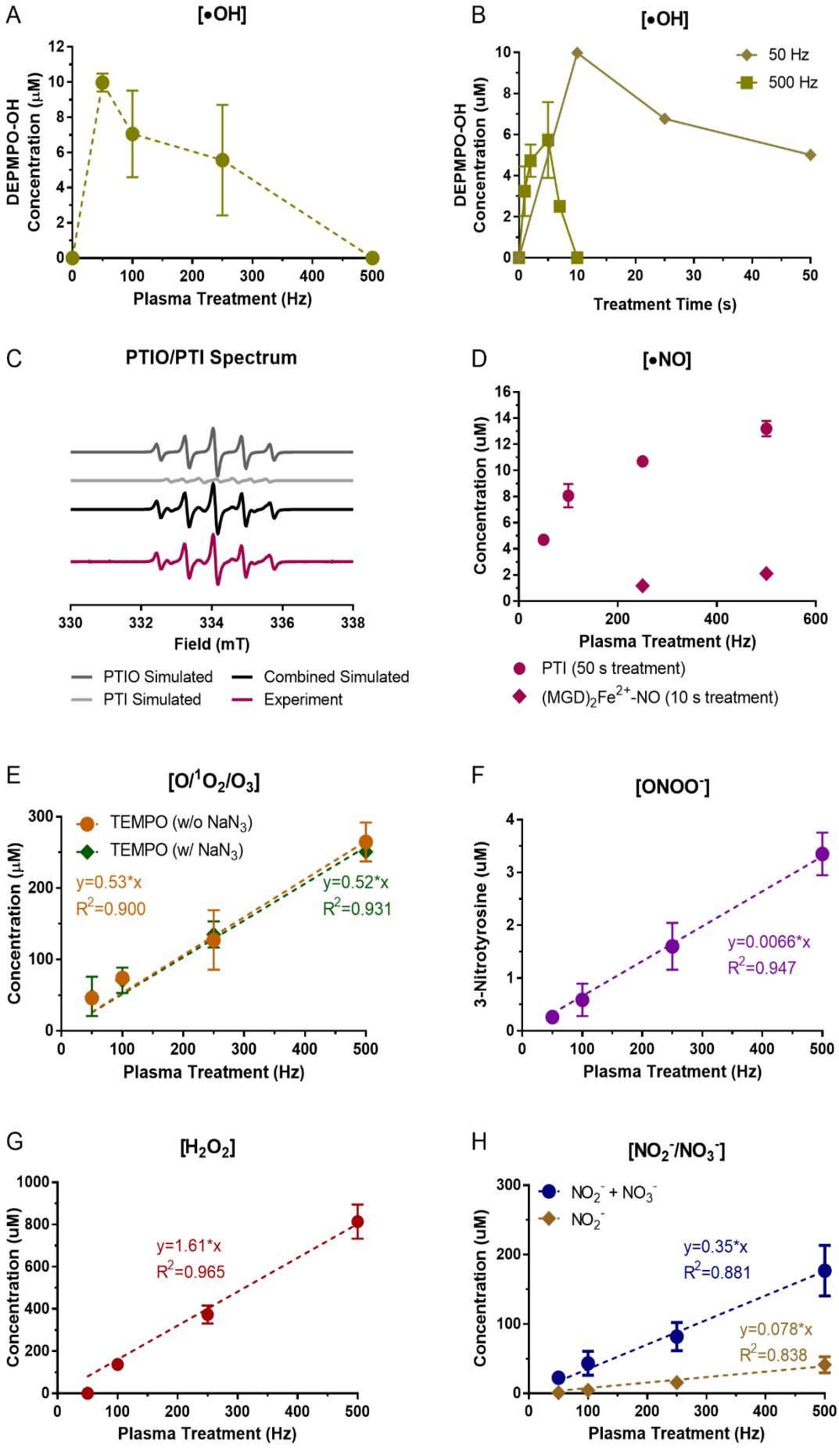
A
[•OH]
DEPMPO-OH Concentration (μM)
Plasma Treatment (Hz)
B
[•OH]
50 Hz
500 Hz
DEPMPO-OH Concentration (uM)
Treatment Time (s)
C
PTIO/PTI Spectrum
Field (mT)
PTIO Simulated
PTI Simulated
Combined Simulated
Experiment
D
[•NO]
Concentration (uM)
Plasma Treatment (Hz)
PTI (50 s treatment)
(MGD)2Fe2+-NO (10 s treatment)
E
[O/1O2/O3]
TEMPO (w/o NaN3)
TEMPO (w/ NaN3)
y=0.53*x
R2=0.900
y=0.52*x
R2=0.931
Concentration (μM)
Plasma Treatment (Hz)
F
[ONOO-]
3-Nitrotyrosine (uM)
y=0.0066*x
R2=0.947
Plasma Treatment (Hz)
G
[H2O2]
y=1.61*x
R2=0.965
Concentration (uM)
Plasma Treatment (Hz)
H
[NO2-/NO3-]
NO2- + NO3-
NO2-
y=0.35*x
R2=0.881
y=0.078*x
R2=0.838
Concentration (uM)
Plasma Treatment (Hz)

Figure 7.4. DBD plasma operated at cell treatment-parameters generates short-lived and persistent RONS in liquid. PBS (50 µL) treated by DBD plasma was immediately collected for analysis. Short-lived species were analysed with EPR spectroscopy. (A) While $O_2•^-$ was not detected with the DEPMPO spin trap, •OH formed the spin adduct DEPMPO-OH which decreased with increasing plasma treatment frequency at fixed treatment time. (B) When plasma treatment frequency was fixed and treatment time was changed, DEPMPO-OH initially increased, followed by a decrease, suggesting that DEPMPO-OH is decaying. (C). Both the probe (PTIO) and the product (PTI) was monitored simultaneously from the same EPR spectra to measure •NO. The hyperfine values of PTI and PTIO are $a_{N1}=a_{N2}=0.8$ mT and $a_{N1}=0.96$ mT and $a_{N2}=0.44$ mT, respectively. (D) The formation of $(MGD)_2Fe^{2+}$-NO from (MGD) – iron(II) complex was also used to detect •NO. (E) $O/^1O_2/O_3$ was detected using the TEMP spin trip both with and without sodium azide (NaN_3), an $^1O_2$ scavenger. Persistent RONS (F) $ONOO^-$, (G) H_2O_2, and (H), NO_2^- and NO_3^- increased near-linearly with higher plasma treatment intensity. Measurements were performed with a minimum of 3 repeats for each condition and data presented here are mean±SD (small error bars are not visible).

7.4.2.3 Summary of RONS generated by DBD plasma in liquid

In total, 10 short-lived and persistent RONS generated by DBD plasma were analyzed in liquid and their concentrations appear to increase when either plasma pulse frequency or treatment time was fixed and the other was increased (**Table 7.1**). This indicates that RONS generation may be most dependent on the total plasma treatment energy and suggests that fine-tuning the delivered energy can lead to generation of specific RONS for desired biological outcome.

Table 1. List of RONS in liquid evaluated after DBD plasma treatment

	Short-Lived RONS (lifetimes < s)					***Persistent RONS (lifetimes ≥ s)***			
Plasma Treatment (Hz)	*O/O_3*	*$^1O_2$*	*$O_2•^-$*	*•OH*	*•NO*	*$ONOO^-$ (µM)*	*NO_3^- (µM)*	*NO_2^- (µM)*	*H_2O_2 (µM)*
0	-	-	-	-	-	-	-	-	-
50	+	-	-	*	*	0.3±0.1	21.6±17.2	1.1±0.4	6.7
100	++	-	-	*	*	0.6±0.3	38.6±7.7	4.7±1.9	11.4
250	+++	-	-	*	+	1.6±0.4	66.1±1.7	15.7±1.9	31.2
500	++++	-	-	*	++	3.4±0.4	135.61.8	41.3±11.7	67.8

-, Undetectable; +, Detectable with quantifiable trends; *, Detectable without quantifiable trends

7.4.3 Persistent RONS generated by DBD plasma alone do not elicit cell death without PEF

To test whether persistent RONS generated by DBD plasma (H_2O_2, NO_2^-, NO_3^-, and $ONOO^-$) are the main effectors of cell death, exogenous RONS solutions were prepared and added to both melanoma cell lines. Since RONS concentrations reported above were measured in 50 µL of PBS, while PBS is almost entirely removed from the wells prior to direct DBD plasma treatment of cells (**Figure 7.2B**), this volume difference must be reconciled. We observed that treatment of cells with 50 µL of PBS in the well diluted the plasma effect, but treatment of cells with 5 µL of PBS remaining did not (**Figure S7.4A**). This is in line with previous studies that reported ≤20 µL of PBS

did not dilute the plasma effect on cell viability [32]. Therefore, we prepared RONS at 10x's the concentration and treated the cells with 5 µL for 10 s, as described in the Materials and Methods. This most closely replicates the process of direct DBD plasma treatment and is most realistic to the concentration of RONS generated by plasma and experienced by the cells.

As reported above, NO_3^- in the liquid could result from secondary reactions of NO_2^-, so two RONS solutions were made based on our measurements: 1) H_2O_2 + NO_3^-/NO_2^- which accounts for the concentration of all three species and 2) H_2O + NO_2^- which assumes all NO_3^- originated from NO_2^-. Concentrations of RONS in solution can be found in the Materials and Methods section. We clearly see that both conditions did not significantly affect cell survival for the melanoma cell lines, as compared to direct DBD plasma treatment (**Figure 7.5A** and **B**). A solution of $ONOO^-$ was also prepared in the same way. The stability of $ONOO^-$ in PBS was reported to be low, leading to rapid degradation [24, 34]. We tested the stability of commercial peroxynitrite in PBS using a redox probe 3,3',5,5'-tetramethylbenzidine (TMB) (Sigma-Aldrich, ≥98%, T2885), whose oxidized product can be detected with UV-Vis spectrophotometry (**Figure S7.5**) [35]. The results showed that $ONOO^-$ was stable in PBS within timeframes used here (≤ 15s). The solution of $ONOO^-$ in PBS was prepared right before treatment and added to the cells immediately to prevent decay. Treatment of cells with exogenous $ONOO^-$ also did not affect cell survival (**Figure 7.5A** and **B**).

To further validate whether persistent RONS generated by plasma can elicit cell death, PBS was treated with DBD plasma and then transferred onto cells. 50 µL of PBS was treated for 100 s. Immediately after exposure to plasma, the PBS was added to the cells in the same manner as the RONS solutions described above. Cell survival was also not affected with this treatment group (Plasma-Treated PBS), which further highlights that persistent RONS generated here by plasma are not the major effectors of cell death (**Figure 7.5A** and **B**).

When plasma is created with the DBD system, the cells will also experience pulsed-electric fields (PEF) from the high voltage DBD electrode. Although electric fields associated with DBD plasma alone do not affect cell death (**Figure 7.5A** and **B**), which is consistent with previous reports [20], they may have synergistic effects with the RONS produced by plasma. Therefore, we tested the combination of DBD produced PEF and exogenously added RONS. The RONS solution (700 µM of H_2O_2, 1770 µM of NO_2^-, and 35 µM of $ONOO^-$) was prepared immediately before treatment and 1 mL was added to the cells. The DBD electrode was then dipped into the solution and operated

as before with the same parameters (**Figure 7.2C**). Since the dielectric strength of liquid is much higher than the applied voltage from the electrode, cells in this condition are subjected to PEF without the creation of plasma.

To delineate the effect of PEF alone, the DBD electrode was dipped into PBS instead of the RONS solution. PEF treatment alone did not elicit significant cell death, but when combined with exogenous RONS, cell survival was reduced to that of direct DBD plasma treatment in both the B16F10 (58±11 % vs 54±4 %; $p>0.05$) and the A375 (46±6 % vs 35±5 %; $p>0.05$ melanoma cell lines (**Figure 7.5A** and **B**). We recognize that applying high voltage pulses to the DBD electrode while it is submerged in liquid only produces global electric fields associated with plasma and electric fields from plasma streamers and filaments are not taken into account [36]. However, our data strongly indicates a synergistic effect between pulsed-electric field and plasma-generated RONS on cell death.

7.4.4 PEF and persistent RONS do not elicit CRT emission

Since PEF and RONS had synergistic effects on cell death, we tested whether the immunogenicity of the melanoma cells was also increased by measuring CRT. The effect of PBS volume was first tested in the B16F10 cell line to ensure that 5 µL of PBS did not dilute the DBD plasma effect on CRT emission (**Figure S7.4B**). Again, there was no significant difference between the two conditions. The RONS solutions used for treatment were prepared as described above.

Interestingly, while a combination of PEF and RONS treatment reduced cell survival, it did not elicit equivalent levels of CRT emission compared to direct DBD plasma treatment for either melanoma cell lines (B16F10: 2.3±0.8 % vs 5.1±0.3 %; $p<0.001$, A375: 2.0±0.8 % vs 6.4±1.1 %; $p<0.001$) (**Figure 7.5C** and **D**). Unsurprisingly, PEF alone also did not induce significant CRT emission above the untreated, which is in-line with previous reports [20].

Neither of the RONS solutions used to treat the melanoma cells elicited significant CRT (**Figure 7.5C** and **D**). However, conditions containing equivalent amounts of H_2O_2 (H_2O_2+NO_3^-/ NO_2-, H_2O_2+NO_2^-, Plasma-Treated PBS, and PEF+RONS) appeared to increase CRT emission slightly above untreated in both cell lines at nearly the same amount. Although this change was not statistically significant, it suggests that H_2O_2 may affect the immunogenicity of cell death, perhaps

at higher concentrations. However, we note that it is not the major contributor to ICD in our DBD plasma treatment regime.

Taken together, our data underline the essential role of short-lived RONS for affecting ICD. While synergistic effects of PEF and RONS reduce cell survival, they do not elicit CRT emission required for ICD.

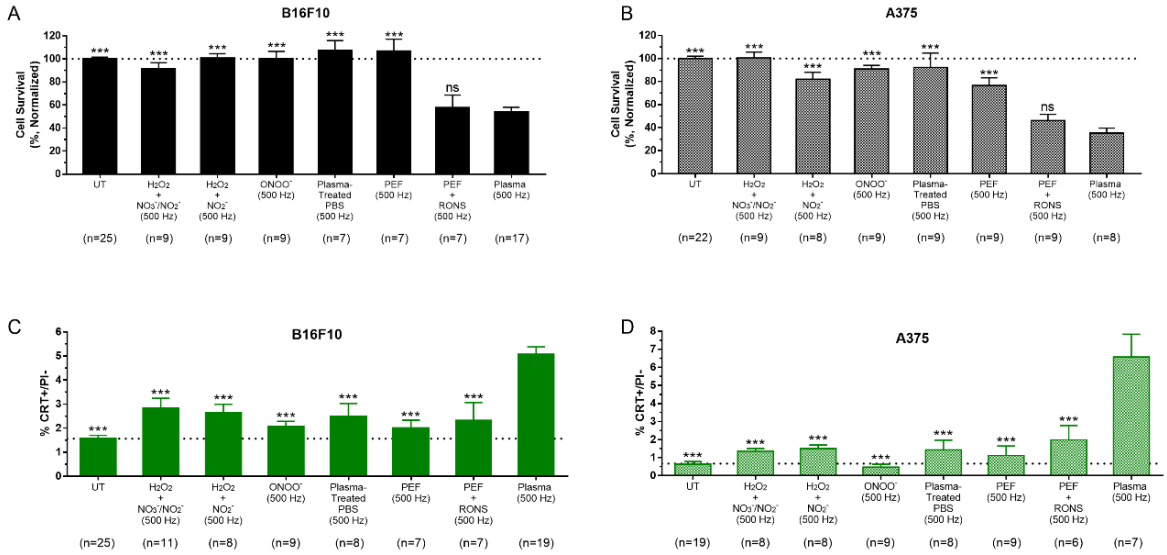

Figure 7.5. Pulsed-electric field (PEF) treatment in combination with RONS solution induced cell death but did not elicit CRT emission. Persistent RONS solutions were prepared from commercially available sources at the concentrations determined from 500 Hz DBD plasma treatment. RONS solutions and PEF alone did not elicit cell death in either (A) B16F10 or (B) A375 melanoma cells similar to that of direct DBD plasma treatment at 500 Hz. PEF treatment in the presence of RONS (PEF + RONS) reduced cell survival but did not increase the DAMP signal associated with ICD, surface CRT, to the same level as DBD plasma treatment at 500 Hz in (C) B16F10 or (D) A375 melanoma cells. In all graphs, a dotted line is placed at the mean value of the untreated control. Data represented here are mean±SEM of 3 to 4 independent experiments. The total number of observations for each group is shown at the bottom of each column. Statistical significance of all treatment conditions was compared to Plasma (500 Hz). ns, $p>0.05$; ***$p<0.001$ (Generalized Linear Mixed Model).

7.4.5 Plasma-generated short-lived RONS are the major effectors of ICD

The gold standard for confirming ICD induction with a particular stimulus is with a vaccination assay. The vaccine was prepared from B16F10 melanoma cells exposed to DBD plasma (500 Hz), PEF+RONS (RONS: 700 µM of H_2O_2, 1770 µM of NO_2^-, and 35 µM of $ONOO^-$), or MTX (2 µg/mL) *in vitro* following the same treatment procedures as before. Untreated cells were used as a negative control. After treatment, cells were collected, resuspended in PBS, and incubated for 24 h at 37°C with 5% CO_2 to reduce the viability of cells in the suspension (~12% viable, **Figure S7.6**) and prevent subsequent tumor growth at the vaccination site. This procedure was selected after trying several different methods and optimization processes (**Figure S7.6**). Thirty-two syngeneic C57BL/6J mice were vaccinated subcutaneously in the right flank (8 mice per group) and

challenged with live B16F10 melanoma cells, 7 days later in the contralateral flank (**Figure 7.6A**). Tumor development (on both the vaccination and challenge site), mouse survival, and tumor protection at the end of the study was recorded.

Only 2 of the 32 mice (both from the untreated group) developed tumors at the vaccination site, indicating that the method of preparing the vaccine is relatively safe (**Figure 7.6B**). This is important as tumors that develop on the vaccination site contribute to the total tumor volume, thus shortening the duration of the study. Tumors were measured with digital calipers to determine the volume, and mice were sacrificed when tumor burden became too large (total tumor volume >1500 mm^3) or when tumors began to ulcerate. Of the 2 mice that developed tumors at the vaccination site, 1 also developed a tumor at the challenge site, though it was small (**Figure S7.7**).

Tumor volumes at the challenge site were monitored and recorded (**Figure 7.6C**). Mouse survival was analyzed at the end of 50 days from the day of vaccination as predefined in our experimental protocol. Only 1 mouse survived in the untreated group and 3 mice survived in the PEF+RONS group (**Figure 7.6D**). The mice in the plasma group performed much better than those in the untreated control group (p=0.055), and also outperformed the positive control group (MTX) with 6 surviving mice compared to 5, respectively. It is important to note that in the plasma group, there was still one mouse with a tumor that did not reach humane endpoints on day 50. All mice were sacrificed together when the final mouse with a tumor reached humane endpoints, and necropsies were performed to confirm complete tumor protection on the challenge site of the remaining mice (**Figure S7.8**). When mice were vaccinated with untreated cells, only 25% of the population was protected against tumor challenge (**Figure 7.6E**). Mice vaccinated with cells treated with PEF+RONS did not improve protection compared to untreated. However, mice inoculated with the plasma-created vaccine had equivalent protection from tumor challenge to that of our positive control group (MTX) (**Figure 7.6E**).

This data strongly suggests that not only is DBD plasma treatment a *bona fide* ICD-inducer, but that the short-lived RONS are crucial for stimulating ICD. Here we see that DBD plasma in this treatment regime is more than the sum of the persistent RONS and PEF.

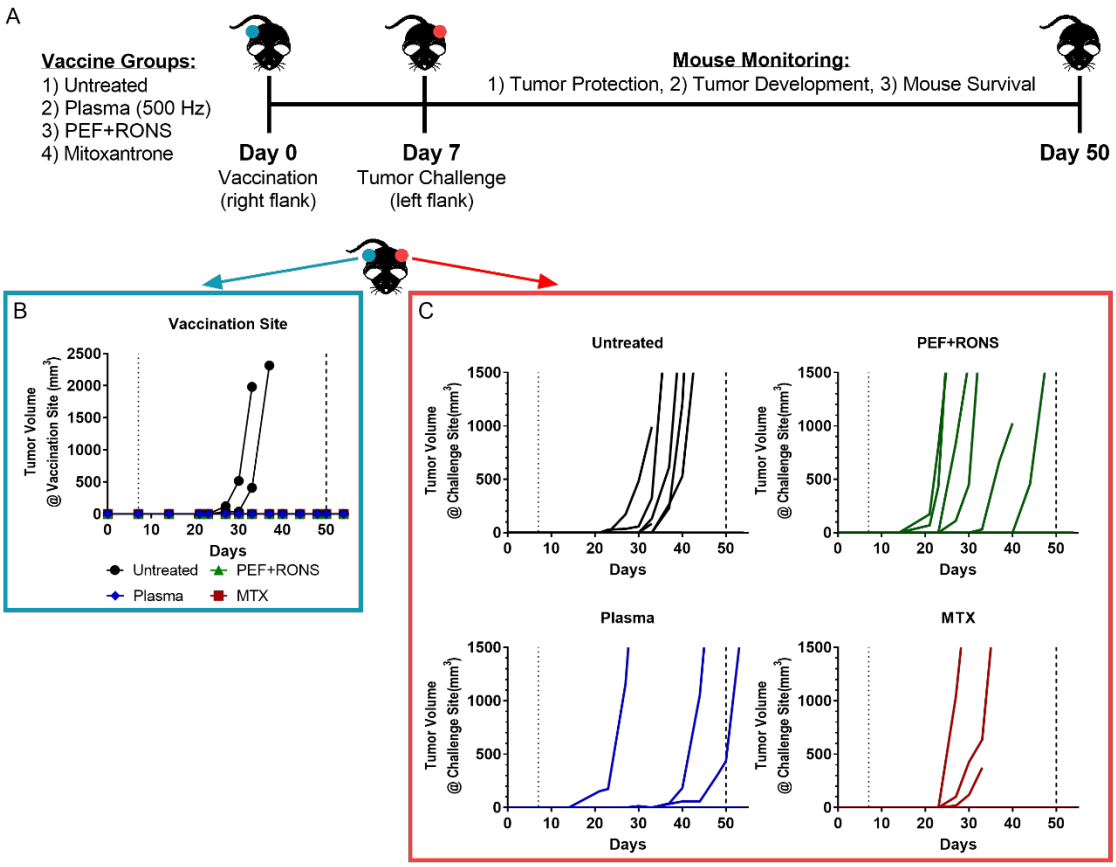

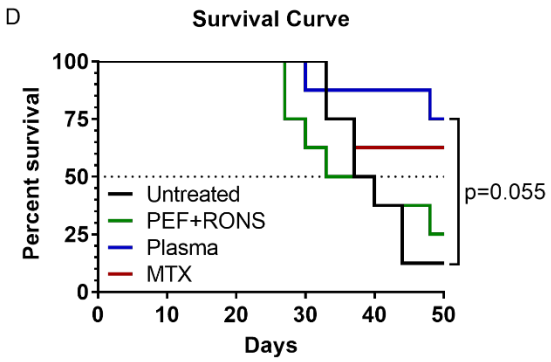

E

Vaccine Group	Tumors on Vaccination Site	Tumors on Challenge Site	Percent Protected
Untreated	2	6	25 %
PEF+RONS	0	5	37.5 %
Plasma (500 Hz)	0	3	62.5 %
MTX	0	3	62.5 %

Figure 7.6. The immunogenic potential of DBD plasma is not due to pulsed-electric field and RONS alone, as evaluated using the vaccination assay. (A) Syngeneic C57BL/6J mice were vaccinated once and challenged with 10^4 live B16F10 melanoma cells on the following week (n=8 per group). Tumor volumes were monitored for both the (B) vaccination and the (C) challenge site. A dotted line was placed in the graphs on day 7, representing the day of live tumor challenge, while a dashed line was placed on day 50 to represent the predefined end of the study when survival was assessed. All remaining mice were sacrificed together when the final mouse with a tumor reached humane endpoints. (D) Mouse survival was plotted for the entire predefined duration of the study (50 days) and the curves were compared with the log-rank (Mantel-Cox) test. (E) Tumor development on both flanks of the mice and percent protection against challenge tumors are listed here.

7.5 DISCUSSION

Immunotherapy, whereby the immune system is activated to attack cancer cells, is a major breakthrough in today's cancer treatment. It is generally believed that the cancer-immunity cycle can be initiated with cancer cells that die in a way that activates the immune system, called immunogenic cell death [3, 8]. Very recently, non-thermal plasma (NTP) has been identified to be an ICD inducer [21]. However, before this technology can be further developed for clinical use, an in-depth understanding of how NTP elicits ICD is required.

In this study, we determined the operating parameters of a microsecond-pulsed DBD plasma to induce ICD in melanoma cells and examined the RONS produced in this regime. These include short-lived (lifetimes < s) and persistent RONS (lifetimes ≥ s). Solutions composed of H_2O_2, NO_2^-, NO_3^-, and $ONOO^-$ at concentrations equivalent to those generated by DBD plasma, were prepared and used to treat melanoma cells to further delineate their role. We observed that neither of these 4 species were able to elicit significant cell death or CRT emission, a hallmark of ICD (**Figure 7.5**). Interestingly, the persistent RONS in combination with pulsed electric fields have synergistic effects on cell death (**Figure 7.5A** and **B**), but this did not elicit CRT expression (**Figure 7.5C** and **D**). It is well known that not all modalities of cell death (e.g. apoptosis, necroptosis, ferroptosis, etc.) are immunogenic [37], and therefore, NTP may be a valuable and unique tool to study fundamental cell death mechanisms.

Determining the importance of short-lived species for desired biological effect is also critical for the development of clinical NTP devices. In addition to DBDs, another subset of NTP devices for medical applications are atmospheric pressure plasma jets (APPJs). In APPJs, the majority of the plasma is generated remotely, and plasma products are delivered to the biological target via a carrier gas or ionization waves [38]. Creation of short-lived RONS with NTP devices can be fine-tuned by careful manipulation of plasma parameters (e.g., applied voltage, pulse width, pulse rise time, pulse frequency), treatment parameters (e.g., treatment time, application distance), and environmental parameters (e.g., discharge gas, humidity) (**Figure 7.1**). In this study, we also investigated the dependence of RONS generation on 2 parameters in our DBD system. Our data suggests that DBD-generation of RONS is not dependent on pulse frequency or treatment time alone. Rather, the RONS are likely generated based on the total number of pulses delivered, which is related to the total delivered plasma energy. Therefore, by controlling the physical

properties of plasma generation, we can optimize the cocktail of chemical species required for subsequent biological effects, in this case, immunogenic cancer cell death.

Another modality of NTP use for cancer applications currently being explored is with plasma-treated liquids (PTL). Liquid (often buffered saline, cell culture media, or water) is treated with NTP (typically on the order of minutes) to be enriched with RONS [39]. The solution is then injected locally in the tumor or perfused through body cavities with tumors. Studies with mouse models have shown that injection of PTL into tumor-bearing mice delayed tumor growth [39]. It is important to note that only the persistent species (e.g., H_2O_2, NO_2^-, NO_3^-, potentially $ONOO^-$) are present in PTL. Therefore, its anti-cancer effect may be through a different mechanism than what we observed here. As stated above, we observed that RONS solution treatments containing equivalent amounts of H_2O_2 (H_2O_2+NO_3^-/NO_2^-, H_2O_2+NO_2^-, Plasma-Treated PBS, and PEF+RONS) increased CRT emission slightly above untreated, though this change was not statistically significant (**Figure 7.5**). Perhaps with longer treatment times (on the order of those used to create PTL), higher CRT emission could be achieved. While there are still many ongoing studies to work out the fundamental questions and practical issues of generating and using PTL, for now, the use of PTL addresses another important challenge with clinical application of NTP: treatment of non-superficial tumors.

Treatment of superficial cancers, such as melanoma studied here, is relatively straightforward, as NTP can be applied directly. However, tumors inside the body may become problematic and limit the use of NTP. One suggested approach is to use NTP in combination with intraoperative procedures. Following surgical tumor excision, NTP could be used to treat the tumor bed or surgical margins to eliminate remaining cancer cells. These studies still need to be performed, and for that, an ergonomic NTP device should be engineered for clinicians. Engineers and physicists are also designing different plasma source geometries for focused and minimally invasive treatment inside the body. This includes an endoscopic device (μm diameters) that can propagate plasma up to several meters in length [40]. With these devices, it again becomes important to determine which plasma-generated RONS will exit the aperture and reach the intended target, as some short-lived species may be lost along the path of the tube.

Although the vaccination assay has been performed previously on a CT26 colorectal cancer model [21], this is the first report demonstrating that NTP-created vaccine is safely prepared and offers

complete protection. This could be leveraged for plasma-mediated control of non-superficial tumors. Extensive effort was made to ensure that preparation of the whole-cell vaccine limited/eliminated tumor development at the injection site (**Figure S7.6**). Not only did 0 out of 8 mice in the plasma group develop tumors from the vaccine, 6 mice survived to the end of the study and 5 were completely tumor-free (**Figure 7.6E**). Additional studies with other cancer types should be performed to assess the efficacy of this potential strategy and broaden its application.

It is clear that several hurdles must be addressed before NTP becomes mature for clinical use and understanding how NTP interacts with cancer cells will provide valuable insight into potential solutions. Ultimately, it is unlikely that NTP alone will be the solution to cancer therapy, but a combination of different therapies may be required. In the past NTP has been combined with chemotherapy and even a therapeutic cancer vaccine [12, 21]. We also suggest combining DBD plasma with other immunotherapeutic agents, particularly checkpoint inhibitors like PD-1/PDL-1 inhibitors, as ICD induction with DBD plasma may have a niche to further improve specific anti-cancer immune responses. For this to be effective, treatment schedules and combination orders should be tested. Strategies should be based on assisting different steps of the cancer-immunity cycle or attacking multiple hallmarks of tumor immune evasion [3, 41].

7.6 CONCLUSION

In summary, we demonstrate that DBD plasma is able to induce *bona fide* immunogenic cell death of melanoma cells and the observed effect is not solely due to the persistent RONS generated (H_2O_2, NO_2^-, NO_3^-, and $ONOO^-$). The short-lived RONS produced by DBD plasma are required. As DBD plasma is highly tunable and treatment is localized, it may have unique advantages over current ICD-inducers (e.g., chemotherapeutics, radiation, high hydrostatic pressure, etc.), and should be investigated further with other cancer types.

7.7 REFERENCES

1. Hamid, O., et al., *Safety and tumor responses with lambrolizumab (anti–PD-1) in melanoma.* New England Journal of Medicine, 2013. **369**(2): p. 134-144.
2. Hodi, F.S., et al., *Improved survival with ipilimumab in patients with metastatic melanoma.* N Engl j Med, 2010. **2010**(363): p. 711-723.
3. Chen, D.S. and I. Mellman, *Oncology meets immunology: the cancer-immunity cycle.* Immunity, 2013. **39**(1): p. 1-10.
4. Larkin, J., et al., *Combined nivolumab and ipilimumab or monotherapy in untreated melanoma.* N Engl J Med, 2015. **2015**(373): p. 23-34.
5. Weber, J.S., et al., *Nivolumab versus chemotherapy in patients with advanced melanoma who progressed after anti-CTLA-4 treatment (CheckMate 037): a randomised, controlled, open-label, phase 3 trial.* The lancet oncology, 2015. **16**(4): p. 375-384.
6. Galluzzi, L., et al., *Molecular mechanisms of cell death: Recommendations of the Nomenclature Committee on Cell Death 2018.* Cell Death & Differentiation, 2018. **25**: p. 486–541.
7. Kepp, O., et al., *Consensus guidelines for the detection of immunogenic cell death.* Oncoimmunology, 2014. **3**(9): p. e955691.
8. Adkins, I., et al., *Physical modalities inducing immunogenic tumor cell death for cancer immunotherapy.* Oncoimmunology, 2014. **3**(12): p. e968434.
9. Obeid, M., et al., *Calreticulin exposure dictates the immunogenicity of cancer cell death.* Nature medicine, 2007. **13**(1): p. 54-61.
10. Panaretakis, T., et al., *Mechanisms of pre-apoptotic calreticulin exposure in immunogenic cell death.* The EMBO journal, 2009. **28**(5): p. 578-590.
11. Fucikova, J., et al., *High hydrostatic pressure induces immunogenic cell death in human tumor cells.* International Journal of Cancer, 2014. **135**(5): p. 1165-1177.
12. Brullé, L., et al., *Effects of a non thermal plasma treatment alone or in combination with gemcitabine in a MIA PaCa2-luc orthotopic pancreatic carcinoma model.* PLoS One, 2012. **7**(12): p. e52653.
13. Brullé, L., et al., *Effects of a non thermal plasma treatment alone or in combination with gemcitabine in a MIA PaCa2-luc orthotopic pancreatic carcinoma model.* PLoS One, 2012. **7**(12): p. e52653.
14. Volotskova, O., et al., *Targeting the cancer cell cycle by cold atmospheric plasma.* Sci Rep, 2012. **2**.
15. Friedman, P., et al., *Successful Treatment of Actinic Keratosis Using Non-Thermal Atmospheric Pressure Plasma- A Case Series.* Journal of American Academy of Dermatology, 2017. **76**(2): p. 352-353.
16. Schuster, M., et al., *Visible tumor surface response to physical plasma and apoptotic cell kill in head and neck cancer.* Journal of Cranio-Maxillofacial Surgery, 2016. **44**(9): p. 1445-1452.
17. Metelmann, H.-R., et al., *Clinical experience with cold plasma in the treatment of locally advanced head and neck cancer.* Clinical Plasma Medicine, 2018. **9**: p. 6-13.
18. Lin, A., et al., *Uniform Nanosecond Pulsed Dielectric Barrier Discharge Plasma Enhances Anti-Tumor Effects by Induction of Immunogenic Cell Death in Tumors and Stimulation of Macrophages.* Plasma Processes and Polymers, 2015. **12**(12): p. 1392-1399.
19. Bekeschus, S., et al., *Toxicity and Immunogenicity in Murine Melanoma following Exposure to Physical Plasma-Derived Oxidants.* Oxidative medicine and cellular longevity, 2017. **2017**: p. 12.
20. Lin, A., et al., *Nanosecond-Pulsed DBD Plasma-Generated Reactive Oxygen Species Trigger Immunogenic Cell Death in A549 Lung Carcinoma Cells through Intracellular Oxidative Stress.* International Journal of Molecular Sciences, 2017. **18**(5): p. 966.
21. Lin, A.G., et al., *Non-thermal plasma induces immunogenic cell death in vivo in murine CT26 colorectal tumors.* OncoImmunology, 2018: p. 1-13.
22. Siegel, R.L., K.D. Miller, and A. Jemal, *Cancer statistics, 2016.* CA: a cancer journal for clinicians, 2016. **66**(1): p. 7-30.

23. Gorbanev, Y., et al., *Combining experimental and modelling approach to study the sources of reactive species induced in water by the COST RF plasma jet.* Physical Chemistry Chemical Physics, 2018. **20**(4): p. 2797-2808.
24. Wende, K., et al., *Identification of the biologically active liquid chemistry induced by a nonthermal atmospheric pressure plasma jet.* Biointerphases, 2015. **10**(2): p. 029518.
25. Gorbanev, Y., D. O'Connell, and V. Chechik, *Non-Thermal Plasma in Contact with Water: The Origin of Species.* Chemistry–A European Journal, 2016. **22**(10): p. 3496-3505.
26. Gorbanev, Y., et al., *Reactions of nitroxide radicals in aqueous solutions exposed to non-thermal plasma: limitations of spin trapping of the plasma induced species.* Plasma Sources Science and Technology, 2016. **25**(5): p. 055017.
27. Reszka, K.J., et al., *Nitric oxide decreases the stability of DMPO spin adducts.* Nitric Oxide, 2006. **15**(2): p. 133-141.
28. Hogg, N., *Detection of nitric oxide by electron paramagnetic resonance spectroscopy.* Free Radical Biology and Medicine, 2010. **49**(2): p. 122-129.
29. Tsuchiya, K., et al., *Nitric oxide-forming reaction between the iron-N-methyl-D-glucamine dithiocarbamate complex and nitrite.* Journal of Biological Chemistry, 2000. **275**(3): p. 1551-1556.
30. Takamatsu, T., et al., *Investigation of reactive species using various gas plasmas.* RSC Advances, 2014. **4**(75): p. 39901-39905.
31. Elg, D.T., I.-W. Yang, and D.B. Graves, *Production of TEMPO by O atoms in atmospheric pressure non-thermal plasma–liquid interactions.* Journal of Physics D: Applied Physics, 2017. **50**(47): p. 475201.
32. Bekeschus, S., et al., *A Comparison of Floating-Electrode DBD and kINPen Jet: Plasma Parameters to Achieve Similar Growth Reduction in Colon Cancer Cells Under Standardized Conditions.* Plasma Chemistry and Plasma Processing, 2018. **38**(1): p. 1-12.
33. Van Boxem, W., et al., *Anti-cancer capacity of plasma-treated PBS: effect of chemical composition on cancer cell cytotoxicity.* Scientific reports, 2017. **7**(1): p. 16478.
34. Girard, F., et al., *Formation of reactive nitrogen species including peroxynitrite in physiological buffer exposed to cold atmospheric plasma.* Rsc Advances, 2016. **6**(82): p. 78457-78467.
35. Guo, Y., et al., *Colorimetric detection of hypochlorite in tap water based on the oxidation of 3, 3', 5, 5'-tetramethyl benzidine.* Analytical Methods, 2015. **7**(10): p. 4055-4058.
36. Babaeva, N.Y. and M.J. Kushner, *Reactive fluxes delivered by dielectric barrier discharge filaments to slightly wounded skin.* Journal of Physics D: Applied Physics, 2013. **46**(2): p. 025401.
37. Garg, A.D., et al., *Immunogenic versus tolerogenic phagocytosis during anticancer therapy: mechanisms and clinical translation.* Cell death and differentiation, 2016. **23**(6): p. 938.
38. Lu, X., M. Laroussi, and V. Puech, *On atmospheric-pressure non-equilibrium plasma jets and plasma bullets.* Plasma Sources Science and Technology, 2012. **21**(3): p. 034005.
39. Utsumi, F., et al., *Effect of indirect nonequilibrium atmospheric pressure plasma on anti-proliferative activity against chronic chemo-resistant ovarian cancer cells in vitro and in vivo.* PLoS One, 2013. **8**(12): p. e81576.
40. Robert, E., et al., *Perspectives of endoscopic plasma applications.* Clinical Plasma Medicine, 2013. **1**(2): p. 8-16.
41. Hanahan, D. and R.A. Weinberg, *Hallmarks of cancer: the next generation.* Cell, 2011. **144**(5): p. 646-74.

7.8 SUPPLEMENTARY

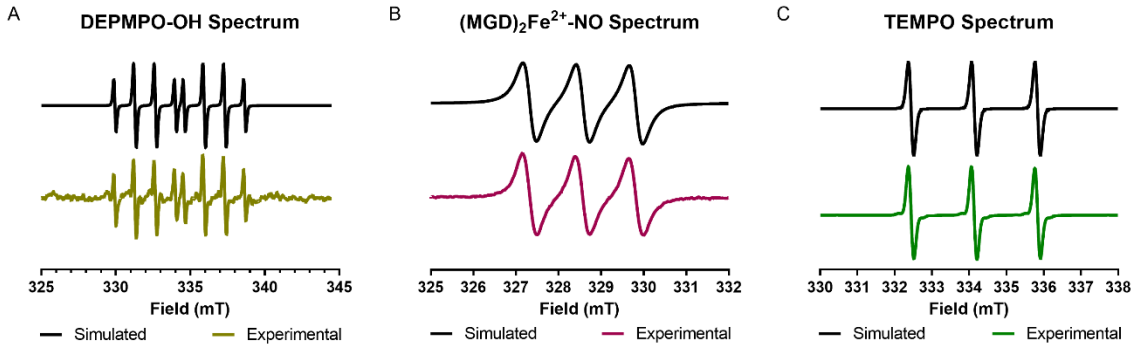

Figure S7.1. Simulated EPR spectrum of spin adducts were compared to experimental spectrum. (**A**) DEPMPO-OOH was not detected while DEPMPO-OH was. The hyperfine values used were a_N=1.38 mT, a_H=1.30 mT, and a_p=4.65 mT. (**B**) The $(MGD)_2Fe^{2+}$-NO hyperfine value was a_N=1.25 mT. C) TEMPO was simulated with hyperfine values of a_N=1.7 mT

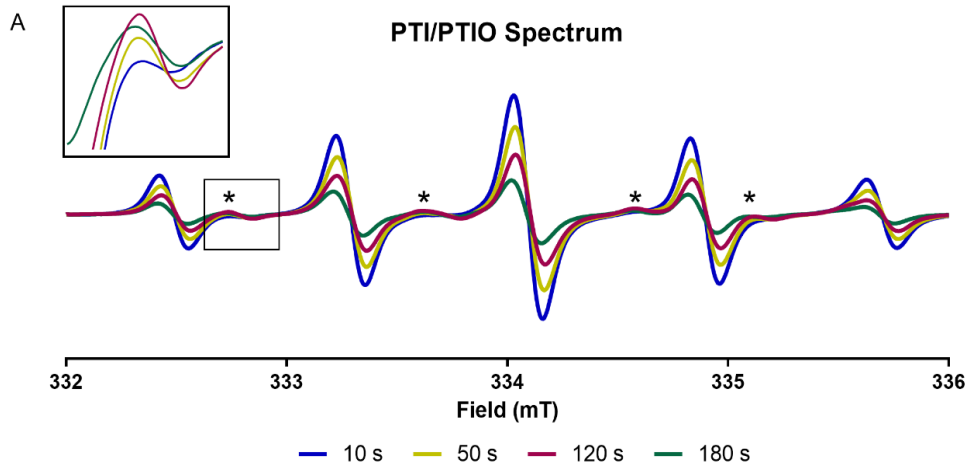

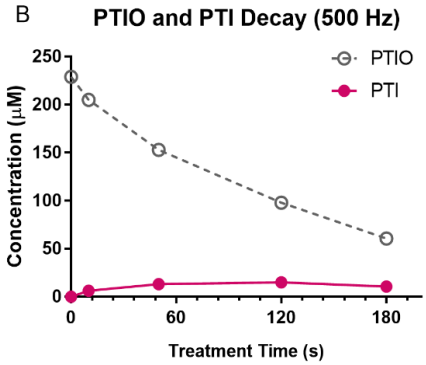

Figure S7.2. Both PTIO and PTI decay with increased plasma treatment time. (**A**) The asterisks (*) on the spectrum represent the peaks of PTI. The hyperfine values of PTI are a_{N1}=a_{N2}=0.8 mT and the hyperfine values of PTIO are a_{N1}=0.96 mT and a_{N2}=0.44 mT. (**B**) The concentration of both PTIO and PTI decay over time.

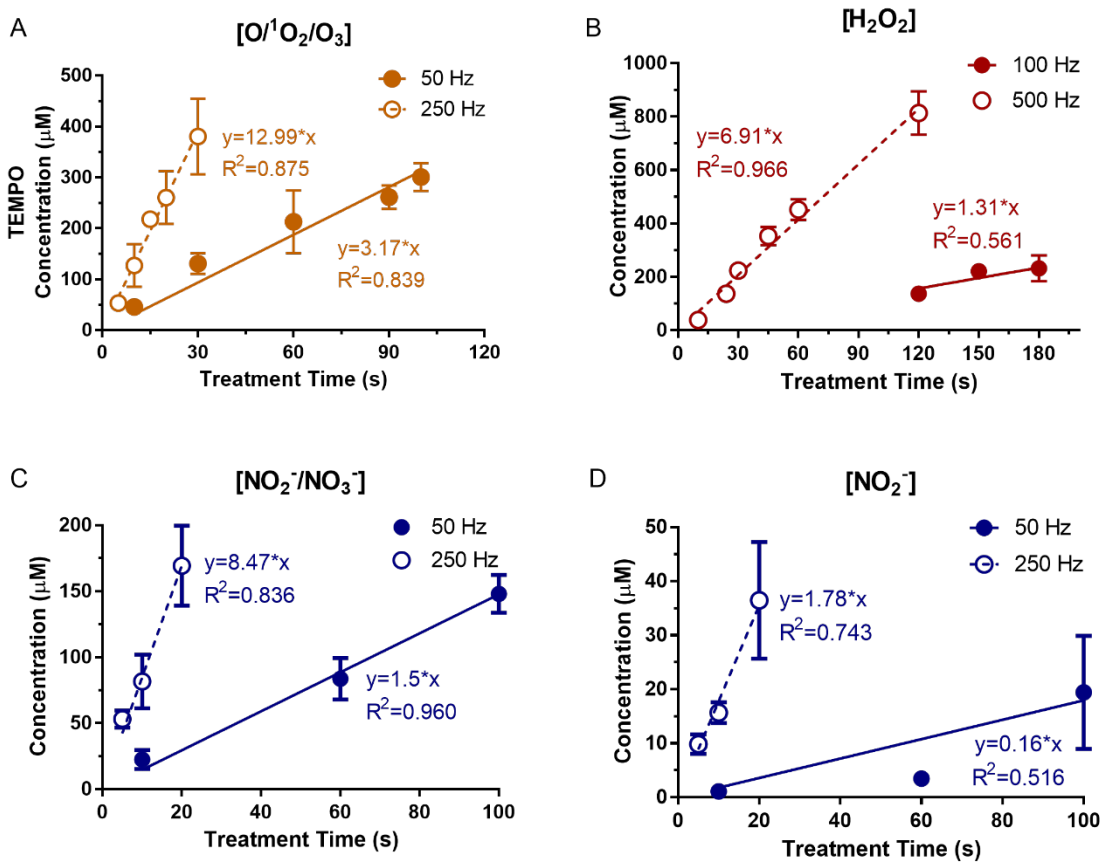

Figure S7.3. DBD plasma at fixed pulse frequencies generates RONS in PBS near-linearly with treatment time. At both low and high frequency treatments, concentrations of (A) H_2O_2, (B) TEMPO (indicative of $O/^1O_2/O_3$), (C) NO_2^-, and (D) both NO_2^- and NO_3^- did not saturate at higher treatment times but increased near-linearly.

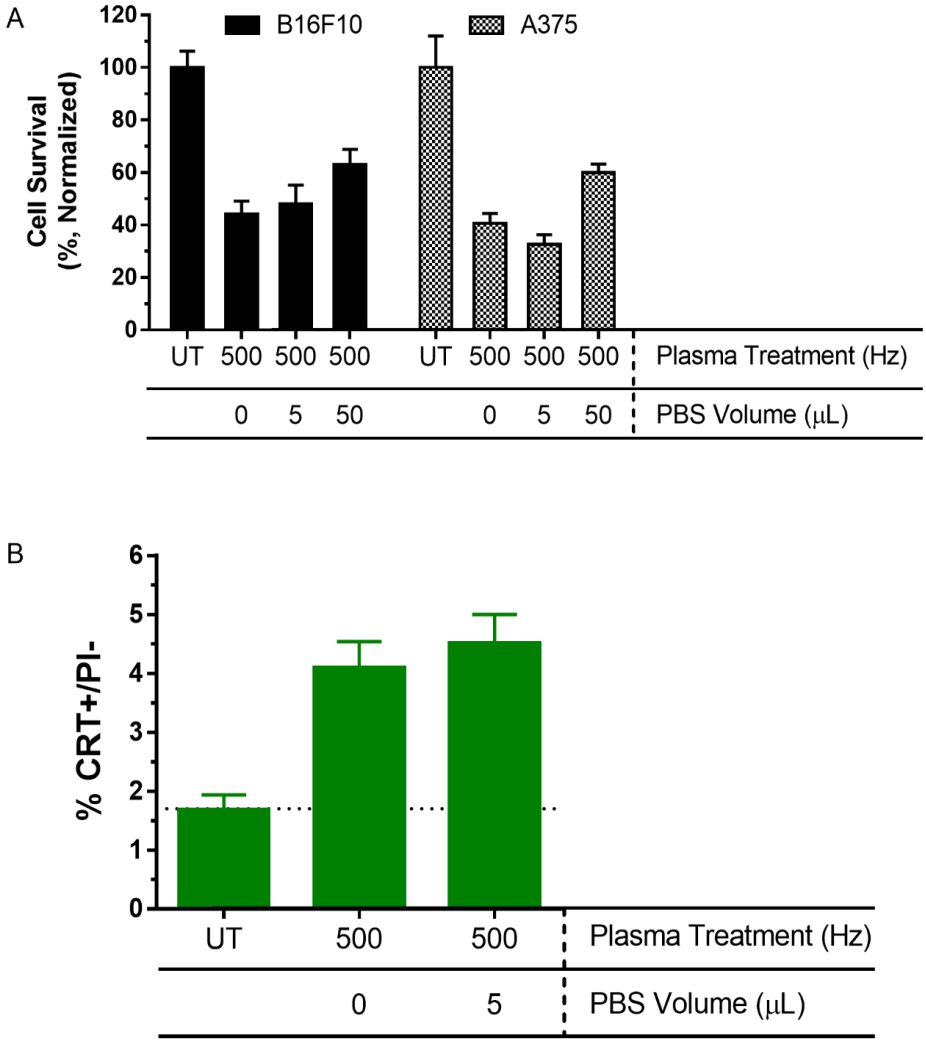

Figure S7.4. PBS (5 µL) present during DBD plasma treatment of cells did not dilute the effect on cell survival or CRT emission. Cells were treated with only residual PBS (0 µL), only 5 µL remaining, or with 50 µL in the well and (A) cell survival and (B) CRT emission from B16F10 cells was compared to that of the untreated (UT) 24 h later. A horizontal dotted line indicates the mean value (% CRT+/PI-) from untreated cells.

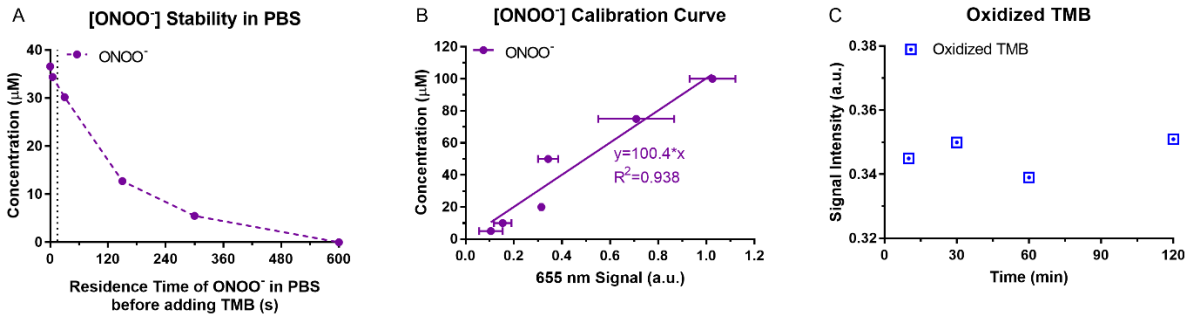

Figure S7.5. $ONOO^-$ was stable in PBS within time frames used in cell treatment studies. (A) Solutions of $ONOO^-$ were prepared in PBS and incubated at room temperature before addition of TMB. Oxidized TMB was then measured with UV-Vis spectrophotometry to determine the amount of $ONOO^-$ degradation. Within 15 s (represented as a vertical dotted line), the $ONOO^-$ decay was approximately 10%. (B) The concentration of $ONOO^-$ was determined from a calibration curve where oxidized TMB was measured after addition of various amounts of commercially available $ONOO^-$. (C) The product of $ONOO^-$ and TMB, oxidized TMB, was stable in PBS at room temperature for up to 2 h.

Table S7.1. Four groups were used for the pilot vaccination study

Groups	Plasma Treatment	Freeze/Thaw Cycle
1. Untreated Control	No	No
2. Plasma Only	Yes	No
3. Freeze-Thaw Control	No	Yes
4. Plasma+Freeze-Thaw	Yes	Yes

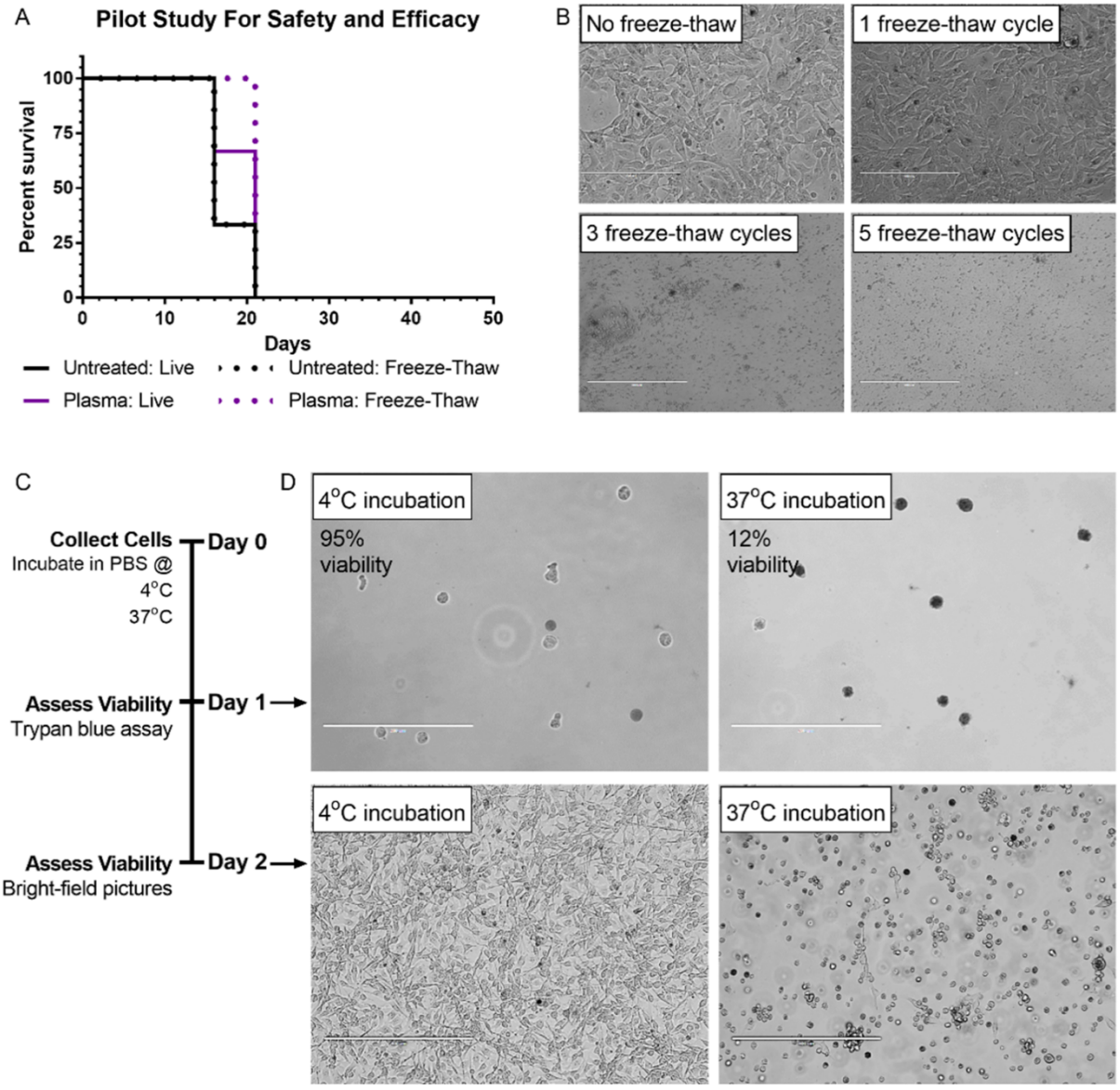

Figure S7.6. The method of preparing the vaccine was optimized. (A) A small pilot study (n=12) was performed to determine whether the experiment would reach the desired endpoint (50 days). Mice were vaccinated in the right flank with B16F10 cells (10^5 cells/mouse) either treated or untreated with DBD plasma (500 Hz). In one of the untreated groups and in one of the plasma groups, the vaccine underwent 1 freeze-thaw cycle in liquid nitrogen before injection. This was intended to eliminate or delay tumor growth at the vaccination site. The survival curve shows that no animal survived past 21 days. (B) Images taken on day 3 with the EVOS bright-field microscope (20x) showed that cells that underwent 1 freeze-thaw cycle (top right) continued to grow similar to that which did not (top left). Cells that underwent 3 (bottom left) or 5 (bottom right) freeze-thaw cycles, however, had significant reduction in cell viability and increase in cell debris (scale bar=200 µm). (C) We also attempted to reduce viability of cells in the whole-cell vaccine by incubating cells in PBS 24 h before injection. Cells were collected, washed twice with PBS, and resuspended at 10^6 cells/mL. Cells were aliquoted into Eppendorf tubes and incubated for 24 h in either 4°C or 37°C. On the next day (day 1), 10 µL of cell suspension was collected and the viability was analysed using the trypan blue exclusion assay. The remaining cell suspension was seeded into 6-well plates and 500 µL of complete cell media was added. The cells were incubated at 37°C with 5% CO_2 overnight and imaged with the EVOS on day 2 to further assess viability. (D) Viability remained high in cells incubated at 4°C (top left) compared to that of cells incubated for 24 h at 37°C (top right). The dark colored cells in the images represent trypan blue positive cells, which were quantified with an automated cell counter, described in the methods. Images of the slides are taken with the EVOs at 20x (scale bar=200 µm). Incubation of the remaining cell suspension showed that cells first incubated at 4°C continued to grow and proliferate (bottom left), while the majority of those initially incubated at 37°C did not (bottom right). Images are taken with the EVOs at 10x (scale bar=400 µm).

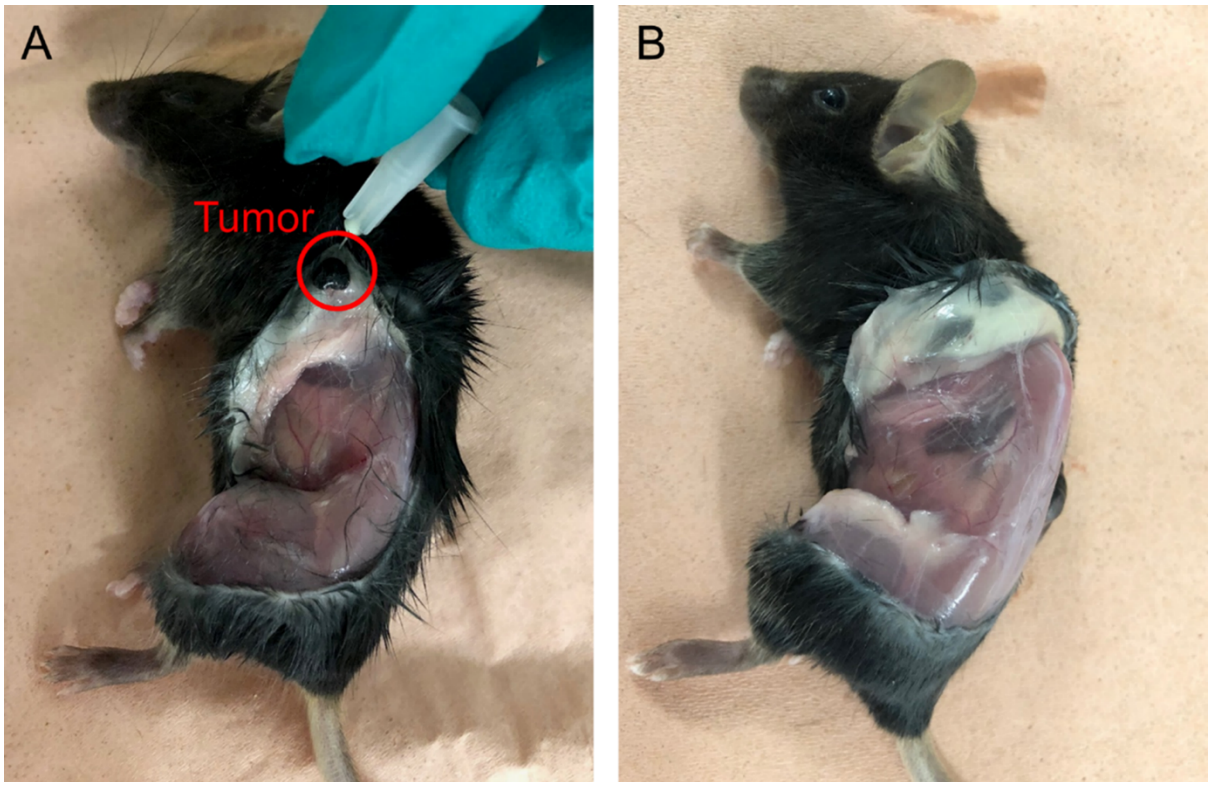

Figure S7.7. Necropsy of the mice that developed tumors at the vaccination site was performed when tumor burden exceeded the defined humane endpoints. (A) One mouse developed a tumor (circled in red) at the challenge site while (B) the other did not (dark areas on the mouse were checked and were a result of darker skin pigmentation).

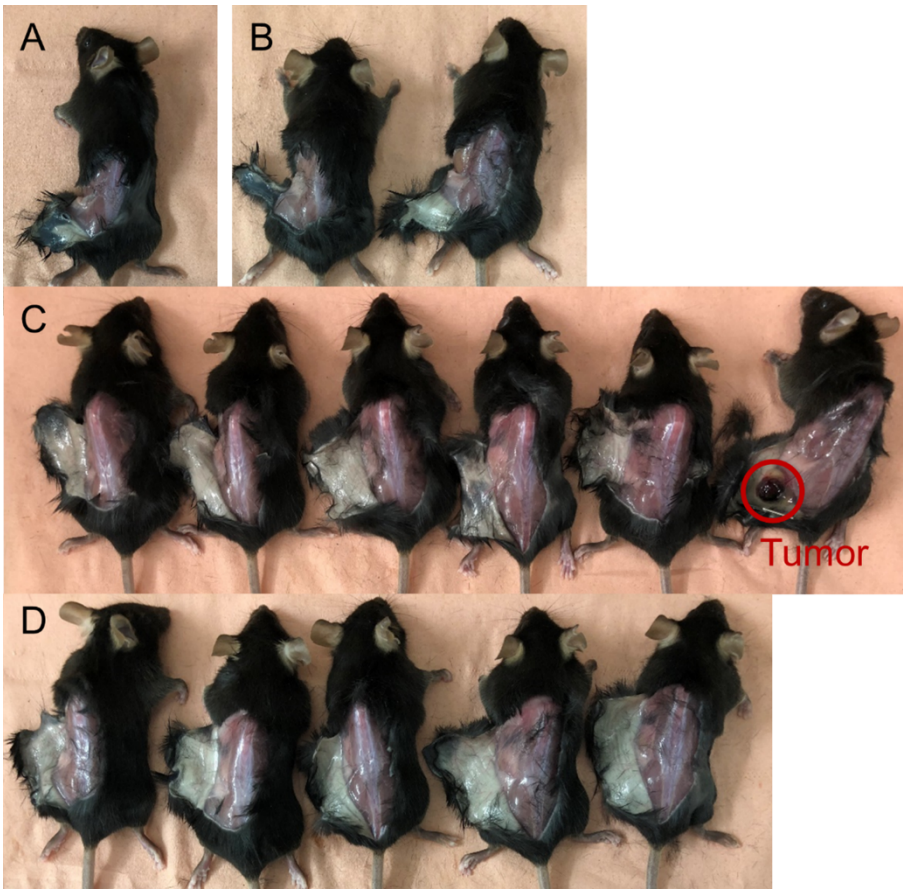

Figure S7.8. All remaining mice were sacrificed and necropsied together when the final mouse with a tumor reached humane endp Soints. The (A) Untreated group, (B) the PEF+RONS group, (C) the Plasma (500 Hz) group, and (D) the Mitoxantrone group all showed no tumor development at the live cancer challenge site apart from the (C) final mouse with a tumor which is circled in red.

Chapter VIII

GENERAL DISCUSSION

8.1 GENERAL DISCUSSION

Ever since its discovery two decades ago, researchers have tried to unravel the physiological function of Cygb. As part of the globin superfamily, Cygb's role in the maintenance of cellular oxygen supply was initially investigated. A physiological role in O_2 transport or storage typically requires O_2 binding with a P_{50} in the order of 1 Torr [1]. Although the apparent P_{50} of Cygb for O_2 increases from approximately 0.1 to 1 Torr (which is comparable to Mb) following reversible formation of a disulfide bridge between the Cys38 and Cys83 residues [2, 3] the intracellular concentration is considered too low to alter O_2 storage or diffusion [4]. Furthermore, in hexa-coordinated globins the distal HisE7 competes with O_2 for Fe^{2+}-binding, which increases O_2 affinity [5]. However, the rate of O_2 dissociation is generally too slow for oxygen transport.

Evolutionarily, the hexa-coordinative state is thought to be the original coordination state of the heme [6]. The conversion to the penta-coordinate state occurred after separation of the globin clade from Cygb and likely coincided with the rise of atmospheric oxygen levels and the evolution of complex life forms, which required the transportation of oxygen to tissues by means other than simple diffusion. Thus, the heme-coordination (and other features) of Cygb suggests that this globin may perform redox-regulated signaling functions or oxygen-sensing functions that mediate oxygen-dependent protein activities [2, 5, 7, 8].

In Chapter III, we investigated the molecular mechanism through which CYGB could be involved in redox regulation. Here, we showed that CYGB contains two redox-sensitive cysteine residues that enable the formation of intra- and/or intermolecular disulfide bridges. Previous studies have reported that CYGB is predominantly present as a monomer *in vivo*. We therefore chose to investigate the effect of the formation of an intramolecular disulfide bridge in between the cysteine amino acids of monomeric CYGB through computational simulations. The formation of an intramolecular disulfide bridge led to a minor shift of the E- and F-helix and substantially changed the position of the His117 residue, which resulted in the heme group becoming more accessible to external ligands. This is in accordance with other studies that showed the rearrangement of the secondary structure upon disulfide bridge formation [9-12]. In particular, the dissociation rate of the distal His81 from the heme iron is altered, leading to a more penta-coordinated state and increased heme reactivity. Thus, our investigations confirm, and further show, that the formation of an intramolecular disulfide bond affects the CYGB structure, thereby

opening the access to the heme group, through gate functioning of His117, which in turn could lead to a higher binding affinity. This supports the hypothesis that Cys38 and Cys83 serve as sensitive redox sensors that modulate the distal heme pocket reactivity and ligand binding of Cygb.

The cysteine redox switch and conformational changes from hexa- to penta-coordination provides additional functionalities to CYGB. This is evidenced perfectly by its intrinsic oxygen-dependent NOD and NiR activities. Cygb has been shown to have the highest rate of NO dioxygenation among globins [11, 13, 14]. However, the NO dioxygenation reaction rate drops dramatically under hypoxic conditions. Yet, at low oxygen levels, its NiR activity increases, thereby modulating NO homeostasis and vascular tone. Although hypoxia is often associated with reducing cellular conditions, mitochondrial ROS levels are increased, which could lead to oxidative stress [15, 16]. Under these conditions, the cysteine residues of Cygb can be oxidized and increase the NiR activity ~40-fold [17], further upregulating NO generation to a point that it may be physiologically relevant. This oxidoreductase activity could be catalytic if an effective reduction system exists to regenerate reduced heme species. The cytochrome b5/cytochrome b5 reductase system has been shown to fulfill this role [18].

Furthermore, CYGB expression can be induced by hypoxia through direct binding of hypoxia-sensitive transcription factors HIF-1, AP-1, and NFAT to their respective response elements on the Cygb promoter region [19]. Hypoxia-dependent regulation of CYGB mRNA levels was observed in various cell types and tissues [20-22]. In Chapter IV we showed the need for the proper selection and validation of reference genes for gene expression analysis using real-time qPCR, as it is highly dependent on cell type and experimental conditions. In A375 and Malme-3M melanoma cells, CYGB mRNA levels were elevated upon exposure to hypoxia. Differences in response between A375 and Malme-3M originated from different endogenous expression levels of CYGB. Immunoblotting confirmed that CYGB is strongly upregulated under hypoxic conditions in A375 cells. Interestingly, this upregulation in A375 cells was most likely HIF-2α-dependent. Consistent with absolute mRNA levels, Malme-3M cells exhibited higher CYGB protein levels than A375 cells, but no regulation could be observed under hypoxic conditions.

We further explored the molecular mechanism responsible for hypoxic induction of *CYGB* by employing a *CYGB* promoter-driven luciferase reporter assay. Whereas HIF-1α did not induce *CYGB* promoter-driven luciferase activation in A375 cells, HIF-2α overexpression did. Although

also a slight HIF-1α mediated activation could be observed, HIF-2α activation of the *CYGB* promoter was validated in non-melanoma cell line Hep3B. HIF-1α and HIF-2α share very similar characteristics, including their abilities to heterodimerize with HIF-1β and binding to the same DNA-binding consensus sequence (5'-RCGTG-3') [23]. Yet, cell type, duration, type of stimulation and culture conditions are reported to influence HIF-1α versus HIF-2α -mediated transcription [24-26]. Moreover, Smythies et al. showed that cell-specific gene induction by HIF-1α or HIF-2α arises by recruitment and association with other transcription factors that are enriched at HIF-1α or HIF-2α binding sites. Therefore, it is conceivable that in Hep3B and A375 cells, HIF-2α, rather than HIF-1α, by recruitment and binding of other transcription factors, positively regulates *CYGB* under hypoxic conditions in a cell type specific way.

As a redox-sensitive protein with proposed functions including RONS detoxification, signaling reactions, and NO homeostasis, we hypothesized that CYGB plays a cytoprotective role in melanoma cells. Therefore, the efficacy of therapies aimed at elevating RONS levels in cancer cells would be influenced by the presence of CYGB in melanoma cells. In Chapter V, we investigated the cytotoxic effect of indirect NTP treatment in two melanoma cell lines with divergent endogenous CYGB expression levels, and we explored the role of CYGB in determining treatment outcome. We confirmed that the treatment of PBS with NTP endows cytotoxicity that induces cell death in melanoma cells through apoptosis and that this cytotoxicity was mediated through the production of ROS. However, A375 and G361 melanoma cells were sensitive to a different degree towards NTP treatment. By establishing a CYGB-overexpressing A375 cell line and a CYGB-knockdown G361 cell line together with their corresponding isogenic controls, we showed that CYGB protects melanoma cells from ROS-induced apoptosis by the scavenging of ROS. Although we previously stated that it is unlikely that CYGB contributed directly to the scavenging of ROS due to the slow reaction rate of CYGB with H_2O_2, Zweier et al. recently demonstrated a potent SOD activity for CYGB. In SMCs subjected to oxidative stress, CYGB was shown to play a major role in the metabolism of $O_2^{\bullet-}$ and protects the cells against $O_2^{\bullet-}$ mediated cell death. This SOD function of Cygb may be particularly important for protection against oxidative stress in cells containing high levels of Cygb protein, such as liver stellate cells, pericytes of all organs, fibroblasts, or SMCs, in which Cygb concentrations have been reported to be as high as 5 μM [28]. In melanoma cells that still express CYGB at high levels, like G361 cells, we found

the concentration to be at least similar, if not higher, than as proposed for SMCs. Additionally, Cygb could aid cell survival after pPBS treatment by detoxifying RNS, through its NOD activity.

Interestingly, CYGB expression in A375 and G361 melanoma cells influenced the expression of NRF2 and HO-1. We proposed several mechanisms as to how NRF2 and HO-1 can be regulated by CYGB expression. However, the most exciting finding came from transcriptome analysis of G361 cells. We identified the lncRNA MEG3 as a possible mechanism through which NRF2 expression and its downstream target HO-1 can be regulated by CYGB. Strong evidence exists that MEG3 is a lncRNA tumor suppressor [29]. Therefore, the correlation between CYGB and MEG3 expression sheds a new light on the tumor-suppressive function of CYGB. How exactly CYGB contributes to MEG3 expression (or vice versa) and subsequent NRF2 expression would be an exciting new direction in CYGB research and could help elucidate the intricate tumor-suppressive role of CYGB, at least in melanoma.

Considering that CYGB expression is frequently downregulated (through hypermethylation) during melanomagenesis, it would be worthwhile to investigate whether CYGB expression correlates with MEG3 in CYGB high and low expressing melanoma cells. In A375 cells, MEG3 is almost undetectable. However, overexpression of CYGB did not alter MEG3 expression. It is plausible that CYGB regulates MEG3 expression indirectly through regulation of DNA methyltransferases, like DNA (cytosine-5-)-methyltransferase 1 [30].

The evidence that CYGB protects melanoma cells from ROS-induced apoptosis encouraged us to investigate the potential effect of CYGB on the cellular sensitivity towards RSL3-mediated ferroptosis in G361 melanoma cells that express highly abundant endogenous levels of CYGB.

Our findings in Chapter VI showed that an increased basal ROS level and higher degree of lipid peroxidation upon RSL3 treatment contributes to the increased sensitivity of CYGB knockdown G361 cells to ferroptosis. Furthermore, transcriptome analysis demonstrates the enrichment of multiple cancer malignancy pathways upon CYGB knockdown, supporting a tumor-suppressive role for CYGB. Remarkably, RSL3 treatment of CYGB knockdown cells also led to the activation of the NLRP3 inflammasome and pyroptosis pathways, which identified CYGB expression regulation as a critical determinant of the ferroptosis–pyroptosis therapy response.

Collectively, this suggests that CYGB is involved in the regulation of multiple modes of programmed cell death, including apoptosis, ferroptosis, and pyroptosis. How exactly CYGB is involved in determining the type of programmed cell death remains to be seen. However, a central role for the peculiar phospholipid cardiolipin (CL) can be proposed, as it was shown to play an integral part in the regulation of cell death and immune system proteins [31]. Under physiological conditions, CL is absent in the outer mitochondrial membrane (OMM) and is found in a similar amount in the inner and outer leaflet of the inner mitochondrial membrane (IMM). CL in the IMM acts as an anchor for cytochrome c (Cyt c) [32, 33]. Upon oxidative insult, Cyt c acquires peroxidase activity and oxidizes CL after which Cyt c detaches [34, 35]. Afterwards, CL translocates to the cytoplasmic side of the OMM where it facilitates mitochondrial pore formation and subsequent release of Cyt C and other proapoptotic macromolecules into the cytosol, thereby inducing apoptosis [31].

In contrast to apoptosis, which is generally considered to be an anti-inflammatory cell death, pyroptosis is associated with the release of pro-inflammatory molecules [36]. Recently, ferroptosis was shown to release immunogenic DAMPs, which could lead to ICD. However, conflicting evidence exists about the potential of ferroptosis as an ICD inducing modality [37, 38]. Besides mitochondrial ROS, highly damaged mitochondria are also a source of pro-inflammatory oxidized mitochondrial DNA [39]. Unless damaged and dysfunctional mitochondria are promptly removed by intracellular autophagocytosis (mitophagy), the NLRP3 inflammasome is activated [40]. During mitophagy, exposed CL serves as an ‘eat-me’ signal. In addition, there is increasing evidence that mitochondria function as docking sites for inflammasome assembly, through CL binding. CL was shown to bind directly to the LRR domain of NLRP3, and both NLRP3 and caspase-1 were found to bind to CL following priming by TLR4 agonist LPS [41, 42].

How exactly CL regulates inflammation and cell death remains unclear. However, it seems that different modifications of CL possess different immune and apoptotic activity [31]. Therefore, the cellular control of CL modification would serve as an important regulator of the immune system and cell death. CYGB could potentially be involved in this process via multiple mechanisms. Much like Cyt c, CYGB is a pseudo-peroxidase [34]. Under reducing conditions, CYGB has no peroxidase activity. However, in an oxidative environment, the heme iron is oxidized to its ferric state and, upon formation of an intramolecular disulfide bridge, is transformed to its

penta-coordinated state [10]. In this form CYGB possesses peroxidase activity. Moreover, in this conformation, CYGB can bind anionic lipids such as oleic acid and CL and oxidize them [43]. Thus, CYGB could induce modifications in CL through lipid peroxidation.

Another way CYGB could influence CL composition and exposure to the OMM is through its SOD and NOD activities. CYGB might have a general role in protecting electron transport proteins from NO toxicity [1]. In particular, NOD activity is important to prevent potent inhibition of the terminal oxidase of respiration cytochrome c oxidase [44]. Analogous to Mb, oxygenated CYGB would prevent NO-mediated inhibition of mitochondrial respiration and contribute to higher rates of oxidative phosphorylation [45]. This would explain the decreased oxygen consumption rate in CYGB knockdown G361 melanoma cells (Chapter VI). Moreover, inhibition of cytochrome c oxidase can effectively increase superoxide generation by the respiratory chain which, upon dismutation, forms H_2O_2 that could initiate apoptotic signaling through activation of Cyt c peroxidase activity and subsequent CL oxidation [46-48]. CYGB, through its dual SOD and NOD activities, could be instrumental in the regulation of mitochondrial function and provide protection from the detrimental effects of oxidative and nitrosative stress, especially in cells containing high levels of CYGB.

In future research, it would be of interest to investigate the (sub)cellular localization of CYGB, as it could help elucidate CYGBs function. Previous reports suggest cytoplasmic localization of CYGB in fibroblasts and their derivatives [49], while CYGB is also detected in the nucleus in neurons, various epithelial cells, hepatocytes, and connective tissue cells [50-52]. Fujita et al. demonstrated that in melanocytes and G361 melanoma cells CYGB is expressed in both the cytoplasm and nucleus. This is in accordance with our findings upon immunostaining of G361 cells. In A375 melanoma cells, only a weak signal could be detected. Transient overexpression of CYGB in A375 cells led to CYGB detection in both nucleus and cytoplasm.

In the last Chapter, we performed a thorough examination of the RONS generated by DBD plasma and sought to delineate the RONS that are responsible for plasma-induced ICD. The emission of surface CRT on two melanoma cell lines was used as a surrogate marker of ICD *in vitro*. A vaccination assay was performed to validate our findings *in vivo*. Our results show that alone, persistent RONS are not sufficient for DBD plasma-induced ICD and highlight the importance of the short-lived species. Furthermore, we observed that generating the desired RONS with the

plasma system is dependent on the plasma treatment energy and not on an individual treatment parameter (e.g., pulse frequency or application time). This study provides crucial information towards our fundamental knowledge of plasma-cell interactions which, through strategic optimization of DBD plasma parameters, would allow us to develop a clinical device for controlled delivery of RONS necessary for ICD.

Although the vaccination assay has been performed previously on a CT26 colorectal cancer model [54], we are first to demonstrate that NTP-created vaccine is safely prepared and offers complete protection. This strategy could be exploited for plasma-mediated control of non-superficial tumors. Together, these two *in vivo* vaccination studies offer conclusive evidence that direct application of NTP induces ICD in multiple cancers of different origins. It should be noted however that the perfusion of PTLs in the abdominal cavities of mice with metastatic pancreatic cancer showed similar signs of ICD [55, 56]. This is somewhat contradictory to the observations made in Chapter VII, as in PTLs the effect is largely due to more stable, long-lived species. A possible explanation might be that the concentrations of long-lived species that were present in the PTLs were greater than the ones we used here. We too saw a slight increase of CRT signal in cells that were treated with a mixture of persistent RONS. Therefore, with higher concentrations, ICD might also be induced.

In order to determine the effect of NTP on disease progression and/or remission, in-depth, mechanistic and longitudinal studies are needed. Moreover, further investigations into plasma delivery and administration protocols with other cancer types are also warranted for potential clinical translation. Ultimately, it is unlikely that NTP alone will be the solution to cancer therapy, but a combination of different therapies may be required. In the past, NTP has been combined with chemotherapy and even a therapeutic cancer vaccine [54, 57]. We also propose combining DBD plasma with other immunotherapeutic agents, particularly checkpoint inhibitors like PD-1/PDL-1 inhibitors, as ICD induction with DBD plasma may have a niche to further improve specific anti-cancer immune responses. For this to be effective, treatment schedules and combination orders should be tested. Strategies should be based on assisting different steps of the cancer-immunity cycle or attacking multiple hallmarks of tumor immune evasion [58, 59].

8.2 FUTURE PERSPECTIVES

CYGB is undoubtedly involved in the redox regulation of the cell through one of a multitude of different functions that have been assigned to the protein. Melanocytes and melanoma provide the perfect scenery to investigate the cellular role of CYGB further. For instance, it would be interesting to study the change in CYGB expression during melanocyte-to-melanoma transition in human patient-derived samples. Comparison of CYGB expression at different stages of melanoma development could help understand when CYGB levels are diminished and whether there is a correlation between the stage of melanoma and CYGB expression.

NTP treatment of melanoma has proven to be very effective in this thesis. However, CYGB expression also affected NTP cytotoxicity. Moreover, CYGB expression could potentially be a critical determinant of the ferroptosis – pyroptosis therapy response. NTP treatment, as an ICD inducer, holds future promise as a combination therapy with other immunotherapeutic agents (e.g., PD-1/PDL-1 inhibitors). As the knockdown of CYGB made melanoma cells more sensitive towards pyroptosis (a highly immunogenic form of cell death), it would be interesting to see whether CYGB expression influences immunogenicity of NTP treatment in melanoma. Through CYGB's involvement in multiple modes of programmed cell death, CYGB holds promise as a 'predictive biomarker' to assess the efficacy of certain cancer treatments aimed at inducing RONS-induced cell death. In future research, it would be of interest to investigate the (sub)cellular localization of CYGB, as it could help elucidate CYGBs function. For instance, analogous to Mb, a close relationship between CYGB and mitochondria could exist, where it provides protection against mitochondrial ROS through its NOD and SOD activities. Co-localization of mitochondria and CYGB would warrant further investigation into the proapoptotic, pro-, and anti-inflammatory functions of cytosolic-exposed CL and how they are regulated by CL chain saturation and oxidation and how CYGB could influence these modifications.

8.3 REFERENCES

1. Gell, D.A., *Structure and function of haemoglobins.* Blood Cells Mol Dis, 2018. **70**: p. 13-42.
2. Fago, A., et al., *Allosteric regulation and temperature dependence of oxygen binding in human neuroglobin and cytoglobin. Molecular mechanisms and physiological significance.* J Biol Chem, 2004. **279**(43): p. 44417-26.
3. Lechauve, C., et al., *Cytoglobin conformations and disulfide bond formation.* The FEBS Journal, 2010. **277**(12): p. 2696-2704.
4. Hankeln, T., et al., *Neuroglobin and cytoglobin in search of their role in the vertebrate globin family.* J Inorg Biochem, 2005. **99**(1): p. 110-9.
5. Kakar, S., et al., *Structure and reactivity of hexacoordinate hemoglobins.* Biophysical Chemistry, 2010. **152**(1): p. 1-14.
6. Burmester, T. and T. Hankeln, *Function and evolution of vertebrate globins.* Acta Physiol (Oxf), 2014. **211**(3): p. 501-14.
7. Hoogewijs, D., et al., *Androglobin: a chimeric globin in metazoans that is preferentially expressed in Mammalian testes.* Mol Biol Evol, 2012. **29**(4): p. 1105-14.
8. Storz, J.F., J.C. Opazo, and F.G. Hoffmann, *Gene duplication, genome duplication, and the functional diversification of vertebrate globins.* Mol Phylogenet Evol, 2013. **66**(2): p. 469-78.
9. Tsujino, H., et al., *Disulfide bonds regulate binding of exogenous ligand to human cytoglobin.* J Inorg Biochem, 2014. **135**: p. 20-7.
10. Beckerson, P., B.J. Reeder, and M.T. Wilson, *Coupling of disulfide bond and distal histidine dissociation in human ferrous cytoglobin regulates ligand binding.* FEBS Lett, 2015. **589**(4): p. 507-12.
11. Zhou, D., et al., *Oxygen binding and nitric oxide dioxygenase activity of cytoglobin are altered to different extents by cysteine modification.* FEBS Open Bio, 2017. **7**(6): p. 845-853.
12. Astudillo, L., et al., *Reduction of the internal disulfide bond between Cys 38 and 83 switches the ligand migration pathway in cytoglobin.* J Inorg Biochem, 2013. **129**: p. 23-9.
13. Zweier, J.L. and G. Ilangovan, *Regulation of Nitric Oxide Metabolism and Vascular Tone by Cytoglobin.* Antioxidants & Redox Signaling, 2019. **32**(16): p. 1172-1187.
14. Liu, X., et al., *Cytoglobin regulates blood pressure and vascular tone through nitric oxide metabolism in the vascular wall.* Nat Commun, 2017. **8**: p. 14807.
15. Chandel, N.S., et al., *Mitochondrial reactive oxygen species trigger hypoxia-induced transcription.* Proceedings of the National Academy of Sciences, 1998. **95**(20): p. 11715-11720.
16. Coimbra-Costa, D., et al., *Oxidative stress and apoptosis after acute respiratory hypoxia and reoxygenation in rat brain.* Redox Biology, 2017. **12**: p. 216-225.
17. Reeder, B.J. and J. Ukeri, *Strong modulation of nitrite reductase activity of cytoglobin by disulfide bond oxidation: Implications for nitric oxide homeostasis.* Nitric Oxide, 2018. **72**: p. 16-23.
18. Amdahl, M.B., et al., *Efficient Reduction of Vertebrate Cytoglobins by the Cytochrome b5/Cytochrome b5 Reductase/NADH System.* Biochemistry, 2017. **56**(30): p. 3993-4004.
19. Mathai, C., et al., *Emerging perspectives on cytoglobin, beyond NO dioxygenase and peroxidase.* Redox Biology, 2020. **32**: p. 101468.
20. Fordel, E., et al., *Cytoglobin expression is upregulated in all tissues upon hypoxia: an in vitro and in vivo study by quantitative real-time PCR.* Biochem Biophys Res Commun, 2004. **319**(2): p. 342-8.
21. Shaw, R.J., et al., *Cytoglobin is upregulated by tumour hypoxia and silenced by promoter hypermethylation in head and neck cancer.* Br J Cancer, 2009. **101**(1): p. 139-44.
22. Tian, S.F., et al., *Mechanisms of neuroprotection from hypoxia-ischemia (HI) brain injury by up-regulation of cytoglobin (CYGB) in a neonatal rat model.* J Biol Chem, 2013. **288**(22): p. 15988-6003.
23. Albadari, N., S. Deng, and W. Li, *The transcriptional factors HIF-1 and HIF-2 and their novel inhibitors in cancer therapy.* Expert Opin Drug Discov, 2019. **14**(7): p. 667-682.

24. Downes, N.L., et al., *Differential but Complementary HIF1α and HIF2α Transcriptional Regulation.* Molecular Therapy, 2018. **26**(7): p. 1735-1745.
25. Wenger, R.H., et al., *Frequently asked questions in hypoxia research.* Hypoxia (Auckl), 2015. **3**: p. 35-43.
26. Dengler, V.L., M. Galbraith, and J.M. Espinosa, *Transcriptional regulation by hypoxia inducible factors.* Crit Rev Biochem Mol Biol, 2014. **49**(1): p. 1-15.
27. Smythies, J.A., et al., *Inherent DNA-binding specificities of the HIF-1α and HIF-2α transcription factors in chromatin.* EMBO Rep, 2019. **20**(1).
28. Zweier, J.L., et al., *Cytoglobin has potent superoxide dismutase function.* Proc Natl Acad Sci U S A, 2021. **118**(52).
29. Zhou, Y., X. Zhang, and A. Klibanski, *MEG3 noncoding RNA: a tumor suppressor.* Journal of molecular endocrinology, 2012. **48**(3): p. R45-R53.
30. Shivapurkar, N., et al., *Cytoglobin, the newest member of the globin family, functions as a tumor suppressor gene.* Cancer Res, 2008. **68**(18): p. 7448-56.
31. Pizzuto, M. and P. Pelegrin, *Cardiolipin in Immune Signaling and Cell Death.* Trends Cell Biol, 2020. **30**(11): p. 892-903.
32. Vladimirov, G.K., et al., *Structure of the complex of cytochrome c with cardiolipin in non-polar environment.* Chemistry and Physics of Lipids, 2018. **214**: p. 35-45.
33. Nomura, K., et al., *Mitochondrial phospholipid hydroperoxide glutathione peroxidase inhibits the release of cytochrome c from mitochondria by suppressing the peroxidation of cardiolipin in hypoglycaemia-induced apoptosis.* Biochem J, 2000. **351**(Pt 1): p. 183-93.
34. Vlasova, II, *Peroxidase Activity of Human Hemoproteins: Keeping the Fire under Control.* Molecules, 2018. **23**(10).
35. Kagan, V.E., et al., *Cytochrome c acts as a cardiolipin oxygenase required for release of proapoptotic factors.* Nat Chem Biol, 2005. **1**(4): p. 223-32.
36. Broz, P., P. Pelegrín, and F. Shao, *The gasdermins, a protein family executing cell death and inflammation.* Nature Reviews Immunology, 2020. **20**(3): p. 143-157.
37. Wiernicki, B., et al., *Cancer cells dying from ferroptosis impede dendritic cell-mediated anti-tumor immunity.* Nature Communications, 2022. **13**(1): p. 3676.
38. Tang, D., O. Kepp, and G. Kroemer, *Ferroptosis becomes immunogenic: implications for anticancer treatments.* Oncoimmunology, 2020. **10**(1): p. 1862949-1862949.
39. West, A.P. and G.S. Shadel, *Mitochondrial DNA in innate immune responses and inflammatory pathology.* Nature Reviews Immunology, 2017. **17**(6): p. 363-375.
40. Zhou, R., et al., *A role for mitochondria in NLRP3 inflammasome activation.* Nature, 2011. **469**(7329): p. 221-225.
41. Iyer, S.S., et al., *Mitochondrial cardiolipin is required for Nlrp3 inflammasome activation.* Immunity, 2013. **39**(2): p. 311-323.
42. Elliott, E.I., et al., *Cutting Edge: Mitochondrial Assembly of the NLRP3 Inflammasome Complex Is Initiated at Priming.* J Immunol, 2018. **200**(9): p. 3047-3052.
43. Tejero, J., et al., *Peroxidase activation of cytoglobin by anionic phospholipids: Mechanisms and consequences.* Biochim Biophys Acta, 2016. **1861**(5): p. 391-401.
44. Brunori, M., et al., *Control of cytochrome c oxidase activity by nitric oxide.* Biochimica et Biophysica Acta (BBA) - Bioenergetics, 2004. **1655**: p. 365-371.
45. Kamga, C., S. Krishnamurthy S Fau - Shiva, and S. Shiva, *Myoglobin and mitochondria: a relationship bound by oxygen and nitric oxide.* (1089-8611 (Electronic)).
46. Poderoso, J.J., et al., *Nitric oxide inhibits electron transfer and increases superoxide radical production in rat heart mitochondria and submitochondrial particles.* (0003-9861 (Print)).
47. Brookes, P.S., et al., *Mitochondria: regulators of signal transduction by reactive oxygen and nitrogen species.* (0891-5849 (Print)).
48. Moncada, S. and J.D. Erusalimsky, *Does nitric oxide modulate mitochondrial energy generation and apoptosis?* (1471-0072 (Print)).

49. Schmidt, M., et al., *Cytoglobin is a respiratory protein in connective tissue and neurons, which is up-regulated by hypoxia.* (0021-9258 (Print)).
50. Emara, M., A.R. Turner, and J. Allalunis-Turner, *Hypoxic regulation of cytoglobin and neuroglobin expression in human normal and tumor tissues.* Cancer Cell International, 2010. **10**(1): p. 33.
51. Geuens, E., et al., *A globin in the nucleus!* J Biol Chem, 2003. **278**(33): p. 30417-20.
52. Hankeln, T., et al., *The cellular and subcellular localization of neuroglobin and cytoglobin -- a clue to their function?* IUBMB Life, 2004. **56**(11-12): p. 671-9.
53. Fujita, Y., et al., *Melanoma transition is frequently accompanied by a loss of cytoglobin expression in melanocytes: a novel expression site of cytoglobin.* PLoS One, 2014. **9**(4): p. e94772.
54. Lin, A.G., et al., *Non-thermal plasma induces immunogenic cell death in vivo in murine CT26 colorectal tumors.* OncoImmunology, 2018: p. 1-13.
55. Liedtke, K.R., et al., *A myeloid and lymphoid infiltrate in murine pancreatic tumors exposed to plasma-treated medium.* Clinical Plasma Medicine, 2018. **11**: p. 10-17.
56. Liedtke, K.R., et al., *Non-thermal plasma-treated solution demonstrates antitumor activity against pancreatic cancer cells in vitro and in vivo.* Scientific Reports, 2017. **7**(1): p. 8319.
57. Brullé, L., et al., *Effects of a non thermal plasma treatment alone or in combination with gemcitabine in a MIA PaCa2-luc orthotopic pancreatic carcinoma model.* PLoS One, 2012. **7**(12): p. e52653.
58. Hanahan, D. and R.A. Weinberg, *Hallmarks of cancer: the next generation.* Cell, 2011. **144**(5): p. 646-74.
59. Chen, D.S. and I. Mellman, *Oncology meets immunology: the cancer-immunity cycle.* Immunity, 2013. **39**(1): p. 1-10.

ACADEMIC CURRICULUM VITAE

PERSONALIA

Name	Joey De Backer
Address	Watervogelplein 2, 2050 Antwerpen
Email	joey.debacker@outlook.com
Phone	+32 486 08 95 41
Date of birth	11/10/1990
Nationality	Belgian
LinkedIn	www.linkedin.com/in/joey-de- backer-a994ba23a/

EDUCATION

2016 – 2022 **Doctor in Science: Biomedical Sciences**
University of Antwerp

2014 – 2016 **Master of Science in Biomedical Sciences (Molecular & Cellular)**
Graduated with great distinction
University of Antwerp

2009 – 2014 **Bachelor of science in Biology**
University of Antwerp

DISSERTATIONS

Doctoral thesis The versatile nature of cytoglobin, the Swiss-army knife among globins, with a preference for oxidative stress
Promotors: Prof. dr. Sylvia Dewilde, Prof. dr. Annemie Bogaerts, Prof. dr. Wim Vanden Berghe, Prof. dr. David Hoogewijs

Master thesis Plasma treatment of melanoma: CYGB expression as biomarker for therapeutic efficiency and malignancy
Supervisor prof. dr. Sylvia Dewilde, University of Antwerp

Bachelor thesis Prevalence of ground beetles on two slopes in Arolla, Switzerland
Supervisor prof. dr. Ruurd van Diggelen, University of Antwerp

COURSES

- Analysis of Grouped and Longitudinal data using Linear Mixed Models
  StatUA course, University of Antwerp (2017)

- R workshop
  StatUA, University of Antwerp (2018)

- 6th Young Professionals Workshop on Plasma Medicine - Frontiers in Redox Biology and Chemistry
  INP Greifswald, Rostock, Germany (2017)

- ECHO semester training for assistants
  University of Antwerp (2017)

- Laboratory Animal Sciences (FELASA C certificate)
  University of Antwerp (2016)

EDUCATIONAL ACTIVITIES

Teaching assistant of several practical courses focused on Protein Technology, Biochemistry, Molecular Biology, and Microbiology.

Supervision of students

Bachelor thesis

- Dries Luyten (Ba3 – Biochemistry and Biotechnology)
- Saar Adriaensen (Ba3 – Biochemistry and Biotechnology)

Master thesis

- Nathan Nijsmans (Master Biomedical Sciences): *De rol van cytoglobine in de selectiviteit van cold atmospheric plasma behandeling van melanoma*, 2016-2017
- Mathias Bosman (Master Biochemistry and Biotechnology): *Cytoglobin expression increases in response to a hypoxic environment and has a cytoprotective function in A375 and Malme3M melanoma cells*, 2018-2019
- Amber Driesen (Master Biochemistry and Biotechnology): *The other face of cytoglobin: Cytoglobin inhibits ferroptosis in malignant melanoma,* 2020-2021

Member

- OC B&B
- OC BMW since 2016
- OC FAR since 2019

Ombudspersoon

- Bachelor BMW (2016-2019)
- Bachelor FAR (2019-2022)

LAB SKILLS

Cell culture, protein expression and purification, DNA/RNA extraction, transfection, lentiviral transduction, gel electrophoresis, immunoblotting, flow cytometry, cell viability assays, oxidative stress assays, immunocytochemistry, PCR and qPCR, *in vivo* mouse studies, RNA-sequencing, bioinformatics.

PUBLICATIONS

2016 Vermeylen, S, De Waele, J, Vanuytsel, S, **De Backer, J**, Van der Paal, J, Ramakers, M, Leyssens, K, Marcq, E, Van Audenaerde, J, L. J. Smits, E, Dewilde, S, Bogaerts, A. 2016*. Cold atmospheric plasma treatment of melanoma and glioblastoma cancer cells*. Plasma Process Polym 13: 1195– 1205.

2018 **Joey De Backer**, Jamoliddin Razzokov, Dietmar Hammerschmid, Carl Mensch, Zainab Hafideddine, *et al*. *The effect of reactive oxygen and nitrogen species on the structure of cytoglobin: a potential tumor suppressor.* Redox Biol., 2018, 19, 1-10.

2019 Lin A, Gorbanev Y, **De Backer J**, et al. *Non-Thermal Plasma as a Unique Delivery System of Short-Lived Reactive Oxygen and Nitrogen Species for Immunogenic Cell Death in Melanoma Cells*. Adv Sci (Weinh). 2019;6(6):1802062. Published 2019 Jan 28. doi:10.1002/advs.201802062.

2019 Biscop E, Lin A, Boxem WV, Loenhout JV, Backer J, Deben C, Dewilde S, Smits E, Bogaerts AA. *Influence of Cell Type and Culture Medium on Determining Cancer Selectivity of Cold Atmospheric Plasma Treatment.* Cancers (Basel). 2019 Sep 1;11(9):1287. doi: 10.3390/cancers11091287.

2020 Attri P, Park JH, **De Backer J**, Kim M, Yun JH, Heo Y, Dewilde S, Shiratani M, Choi EH, Lee W, Bogaerts A. *Structural modification of NADPH oxidase activator (Noxa 1) by oxidative stress: An experimental and computational study*. Int J Biol Macromol. 2020 Nov 15;163:2405-2414. doi: 10.1016/j.ijbiomac.2020.09.120.

2021 **De Backer J***, Maric D*, Bosman M, Dewilde S, Hoogewijs D. *A reliable set of reference genes to normalize oxygen-dependent cytoglobin gene expression levels in melanoma*. Sci Rep. 2021 May 25;11(1):10879. doi: 10.1038/s41598-021-90284-6. * *Shared co-authorship*

2021 Attri P, Kaushik NK, Kaushik N, Hammerschmid D, Privat-Maldonado A, **De Backer J**, Shiratani M, Choi EH, Bogaerts A. *Plasma treatment causes structural modifications in lysozyme, and increases cytotoxicity towards cancer cells.* Int J Biol Macromol. 2021 Jul 1;182:1724-1736. doi: 10.1016/j.ijbiomac.2021.05.146.

2021 Lin A, Razzokov J, Verswyvel H, Privat-Maldonado A, **De Backer J**, Yusupov M, Cardenas De La Hoz E, Ponsaerts P, Smits E, Bogaerts A. *Oxidation of Innate*

Immune Checkpoint CD47 on Cancer Cells with Non-Thermal Plasma. Cancers (Basel). 2021 Feb 2;13(3):579. doi: 10.3390/cancers13030579.

2022 Vanderhaeghen T, Timmermans S, Watts D, Paakinaho V, Eggermont M, Vandewalle J, Wallaeys C, Van Wyngene L, Van Looveren K, Nuyttens L, Dewaele S, Vanden Berghe J, Lemeire K, **De Backer J**, Dirkx L, Vanden Berghe W, Caljon G, Ghesquière B, De Bosscher K, Wielockx B, Palvimo JJ, Beyaert R, Libert C. *Reprogramming of glucocorticoid receptor function by hypoxia*. EMBO Rep. 2022 Jan 5;23(1):e53083. doi: 10.15252/embr.202153083.

2022 **De Backer J**, Lin A, Berghe WV, Bogaerts A, Hoogewijs D. *Cytoglobin inhibits non-thermal plasma-induced apoptosis in melanoma cells through regulation of the NRF2-mediated antioxidant response.* Redox Biol. 2022 Jul 14;55:102399. doi: 10.1016/j.redox.2022.102399.

2022 **De Backer J**, Maric D, Zuhra K, Bogaerts A, Szabo C, Vanden Berghe W, Hoogewijs D. *Cytoglobin Silencing Promotes Melanoma Malignancy but Sensitizes for Ferroptosis and Pyroptosis Therapy Response.* Antioxidants (Basel). 2022 Aug 10;11(8):1548. doi: 10.3390/antiox11081548.

2022 Lin A, **De Backer J**, Quatannens D, Cuypers B, Verswyvel H, De La Hoz EC, Ribbens B, Siozopoulou V, Van Audenaerde J, Marcq E, Lardon F, Laukens K, Vanlanduit S, Smits E, Bogaerts A. *The effect of local non-thermal plasma therapy on the cancer-immunity cycle in a melanoma mouse model.* Bioeng Transl Med. 2022 Apr 21;7(3):e10314. doi: 10.1002/btm2.10314.

RESEARCH STAYS ABROAD

University of Fribourg, Switzerland at the research group Integrative oxygen physiology of prof. dr. David Hoogewijs. Period: 20.01.2019 – 14.02.19.

University of Fribourg, Switzerland at the research group Integrative oxygen physiology of prof. dr. David Hoogewijs. Period: 27.09.2021 – 13.02.2022

DANKWOORD

Als laatste nog een klein woordje dank.

Af en toe hoor je wel eens de term *eeuwige student* vallen. Iemand die al jaren bezig is met afstuderen. Zeer toepasselijk om het begin van mijn academische carrière te beschrijven. Specifieke plannen had ik niet. Go with the flow, toch? Onder dat motto koos ik ervoor om eens te polsen bij Sylvia of ik mijn masterthesis niet in haar onderzoeksgroep kon doen. Aangezien ik na een bachelor biologie koos om een master te doen in de biomedische wetenschappen kende ik de professoren niet. Mijn keuze voor Sylvia was er dus eentje puur op gevoel. Tijdens de hoorcolleges kwam ze over als iemand met enorm veel kennis, passie voor het vak, maar ook iemand zeer toegankelijk. Tijdens mijn tijd als een masterstudent op T1 en S4 leerde ik de zeer leuke groep mensen kennen die deel uitma(a)k(t)en van de PPES onderzoeksgroep. Ik was dan ook zeer vereerd toen Sylvia me vroeg of ik het eventueel niet zou overwegen om een doctoraat te starten. Ik had er nooit bij stilgestaan. Maar ik had er meteen wel zin in. Ik heb deze unieke kans met beide handen gegrepen en ik heb er geen seconde spijt van gehad. Soms vraag ik me af of ik het ooit overwogen zou hebben mocht Sylvia het mij nooit hebben gevraagd. Waarschijnlijk niet.

Daarom zal mijn eerste woordje dank gericht zijn aan Sylvia. Jij gaf mij de kans om dit doctoraat uit te voeren. Jij geloofde in mij en daar zal ik u altijd dankbaar voor zijn. Het blijft onwezenlijk te denken dat je er al even niet meer bent. Ik hoop dat ik u trots heb gemaakt met de wetenschappelijke resultaten die we hebben behaald. Het zou fantastisch zijn geweest om samen met u nog meer te discussiëren en te filosoferen over de functie van cytoglobine. Ik ben ervan overtuigd dat samen met u we nóg meer te weten hadden gekomen over cytoglobine. Je wordt enorm hard gemist op S4.

Naast Sylvia, waren er nog een aantal andere bollebozen nauw betrokken bij mijn doctoraat. Annemie, uw optimisme en liefde voor plasma is zeer aanstekelijk. Ik wist dat als er iets was waarmee je kon helpen ik het altijd mocht vragen. Je was zeer begaan met mijn doctoraat. Bedankt daarvoor. Wim, bedankt om mij te adopteren in de epigenetica-tak van PPES. Altijd goedlachs en vol met ideeën. David, van in het begin, op de O_2BIP in Hamburg, kwam je over als een zeer intelligente, gedreven wetenschapper. Maar ook (minstens even belangrijk) als een toffe, chille gast. Twee keer ben ik naar Fribourg gekomen om wat experimenten uit te voeren in jou onderzoeksgroep. Eerste keer was maar zeer kort maar genoeg om een al goede band te

vormen, zowel op wetenschappelijk als op persoonlijk vlak. De tweede keer verbleef ik wat langer in Fribourg en daar hebben we enorm veel verwezenlijkt. Het was exact wat ik nodig had om mijn doctoraat succesvol af te ronden. Merci David voor uw gastvrijheid en voor al uw raad. Fribourg, en bij uitbreiding Zwitserland, zal altijd een beetje voelen als thuiskomen.

En nu is het tijd om mijn lieve collega's wat in de bloemetjes te zetten. Jullie waren allemaal één voor één elk op jullie eigen manier een belangrijke reden waarom ik zo'n leuke tijd heb gehad. Werk voelde nooit aan als werk (en ik hoor sommige nu denken: 'gij werken?').

Allereerst den enige, den echte, Herald. Je bent een manusje-van-alles. Als er iets was dat ik niet wist stond je altijd klaar. Je was altijd bereid om dingen voor mij te bestellen. Je deinsde er ook niet voor terug om mee te gaan in een van de vele absurde ideeën of vragen die ik in den bureau dropte (ga ze hier niet vertellen, maar *je weet zelluf*).
Marie-Louise, de OG van de PPES. Jammer dat je op pensioen moest (of weer eens in de lappenmand lag) want ik had het absoluut niet erg gevonden om wat langer me jou op S4 door te brengen. Je nam geen blad voor de mond en je was altijd eerlijk. Dat heb ik wel graag. Ik heb vaak moeten lachen met jou. Ga de uitstapjes naar de muizen nooit vergeten alsook de eerste keer dat ik de vaatwasser uitlaadde en het overtollige water op de maatcilinders rustig wegkapte op de vloer waarop je zei: 'doede gij da thuis oek?'.
Stijn, mijn mentor, je hebt me zeer goed bijgestaan tijdens mijn masterthesis. Maar ook tijdens het begin van mijn doctoraat was je er altijd om te helpen. Merci ook dat je tijdig klaar was met jou doctoraat zodat ik uw mandaat kon overnemen. Zoals Marie-Louise zou zeggen: 'goei planning'. An, mijn bureaugenoot, je doorzettingsvermogen sierde jou. Het is makkelijk om de moed te verliezen wanneer je alles probeert maar je geen (goede) resultaten krijgt. Maar je bent toch blijven doorzetten. Een zeer mooie eigenschap. Dietmar, you will probably never read this but thank you for all the help with the mass spectrometry shizzle. Without you there would've never been a first manuscript. Thanks for everything! Evi, altijd opgewekt en vol goede moed om baanbrekend onderzoek te doen. Altijd zelfzeker. We hebben veel gelachen samen. Het was heel leuk om jou als collega te hebben. Zoë, van iedereen ben jij sowieso dé wetenschapper pur sang. Jij bent ook de enigste persoon die ik ken die liever oudbakken brood eet dan vers brood. Zainab, wij hebben goed gelachen samen. Net zoals Herald altijd wel te vinden om eens te filosoferen over een of andere absurditeit die ter sprake kwam.

Dan mijn twee fantastische collega's Eva en Karen of Karen en Eva. Jullie zaten opgeschept met mij (sorry hé) om samen enkele practica te geven. Jullie hebben mij enorm veel geholpen en ik heb veel geleerd van jullie. Door jullie was mijn taak als assistent des te makkelijker. Ook al waren het soms enorm uitputtende dagen in het practicum heb ik er nooit met tegenzin gestaan. Ik ben fier dat ik deel heb mogen uitmaken van de geïntegreerde practica. Zonder twijfel de beste en leukste practica. Bedankt voor alles. Ik ga het missen!

Wie moet ik dan nog bedanken? Niemand he? Ah jawel! Onze prinses van den bureau, Claudio. '*You got 99 problems but a frown ain't one.'* Somt het perfect op hé? Het was leuk om samen te werken met jou. Je bent heel gedreven en je bent goed in wat je doet. Keep up the good work! Claudia, de eindstreep is in zicht. Doorheen de jaren heb ik u toch wat meer ontspannen zien worden. Zo moet het. Het was altijd leuk babbelen met jou. Ik ben ervan overtuigd dat het schrijven van je thesis vlot zal verlopen. Als ik dat kan, dan kan jij dat zeker.
Claudina, thanks for bringing the Latin vibes to the work floor. I like your kind and warm personality. I wish you all the best in your future ventures with the PamGene. Amber, veel success met je doctoraat. Komt allemaal wel goed.

Special thanks also to Abraham. You came to Belgium 5 years ago with a typical American attitude, which is fine. But it pleases me to know that you embraced the European way of working also (read: enjoy some well-earned time off). We found out together that DBD plasma can induce ICD in mice. Many lives, mostly mice, were sacrificed. We allegedly destroyed the FACSAria one time at 11PM. But they can't prove it. Through working together with you I learned you are a very dedicated, motivated, and honest scientist. But also, a very good friend. All the best with the OrBITS.
Edgar, my friend. You are a genius. Just keep being you. We will see each other soon somewhere in the world. Maybe on that yacht? Also, think about that SharkAway idea. I'm serious.
Buiten de Drie Eiken werkmuren zijn er nog vele andere mensen die ik wil bedanken. Mijn goede vrienden (ik ga geen namen noemen; jullie weten wie jullie zijn) wil ik bedanken om mijn vrienden te zijn.

Ik wil ook mijn familie bedanken. Ik weet dat jullie allemaal heel trots zijn op wat ik doe. Den eerste van de familie die naar de universiteit gaat. Mama en papa, merci om mij te maken tot

wie ik ben. Ik ben heel trots dat jullie mijn ouders zijn. Tita, spijtig dat je er al even niet meer bent. Mijn grootste supporter. Je had het graag meegemaakt. Merci om te zijn wie je was en mij altijd te steunen. Je bent de beste. Popy, je bent een doorzetter. We hebben elkaar beter leren kennen sinds de Tita er niet meer is en daar ben ik blij om. Topanga, Dominic bedankt om een deel uit te maken van onze gekke familie. Ik zou geen andere broer en zus willen wensen. Ik wil ook nog graag Chantal en Jan bedanken. Ik heb zoveel fantastische herinneringen aan Paranam, Palm Village en Suriname in zijn geheel. Jullie hebben mij altijd met open armen ontvangen en gezorgd dat ik niets tekort kwam. Overgetelijke momenten heb ik daar beleefd. Ik kom snel nog eens op bezoek. Verder wil ik ook mijn schoonfamilie bedanken. Ik heb me altijd welkom gevoeld. Bedankt daarvoor.

Als laatste, mijn Lisa natuurlijk. Al meer dan 10 jaar mijn steun en toeverlaat. Echt geklaagd over mijn doctoraat heb ik niet, denk ik? Maar ik weet dat als ik toch eens mijn frustratie zou hebben geuit je er zou zijn voor mij om te luisteren. Merci om naar mijn wetenschappelijk gebrabbel te luisteren en te proberen (met de nadruk op proberen) niet in slaap te vallen wanneer we toch eens opteren voor een natuurdocumentaire te kijken. Ik prijs me zeer gelukkig dat ik jou heb. Thanks boo.